

# **2D/ 3D Quantitative Ultrasound of the Breast**

By

**Haidy Gerges Nasief**

A dissertation submitted in partial fulfillment of the requirements for the degree of

Doctor of Philosophy

(Medical Physics)

At the

UNIVERSITY OF WISCONSIN-MADISON

2017

The dissertation is approved by the following members of the Final Oral Committee:

Timothy J. Hall, Professor, Medical Physics

James A. Zagzebski, Emeritus Professor, Medical Physics

Mai A. Elezaby, Assistant Professor, Radiology

James E. Holden, Emeritus Professor, Medical Physics

Walter F. Block, Professor, Medical Physics

Tomy Varghese, Professor, Medical Physics

Paul Campagnola, Professor, Biomedical Engineering/Medical Physics

© Copyright by Haidy G Nasief 2017

All Rights Reserved

## Abstract

Breast cancer is the second leading cause of cancer death of women in the United States, so breast cancer screening for early detection is common. The purpose of this dissertation is to optimize quantitative ultrasound (QUS) methods to improve the specificity and objectivity of breast ultrasound. To pursue this goal, the dissertation is divided into two parts: 1) to optimize 2D QUS, and 2) to introduce and validate 3D QUS. Previous studies had validated these methods in phantoms. Applying our QUS analysis on subcutaneous breast fat demonstrated that QUS parameter estimates for subcutaneous fat were consistent among different human subjects. This validated our *in vivo* data acquisition methods and supported the use of breast fat as a clinical reference tissue for ultrasound BI-RADS<sup>®</sup> assessments. Although current QUS methods perform well for straightforward cases when assumptions of stationarity and diffuse scattering are well-founded, these conditions often are not present due to the complicated nature of *in vivo* breast tissue. Key improvements in QUS algorithms to address these challenges were: 1) applying a “modified least squares method (MLSM)” to account for the heterogeneous tissue path between the transducer and the region of interest, ROI; 2) detecting anisotropy in acoustic parameters; and 3) detecting and removing the echo sources that depart from diffuse and stationary scattering conditions. The results showed that a Bayesian classifier combining three QUS parameters in a biased pool of high-quality breast ultrasound data successfully differentiated all fibroadenomas from all carcinomas. Given promising initial results in 2D, extension to 3D acquisitions in QUS provided a unique capability to test QUS for the entire breast volume. QUS parameter estimates using 3D data were consistent with those found in 2D for phantoms and *in-vivo* data. Extensions of QUS technology from 2D to 3D can improve the specificity of breast ultrasound, and thus, could lead to improved screening with this modality.

## Dedication

*I dedicate this thesis to my beloved family:*

*My parents (Amal Botros and Gerges Nasief) and my brother (Amir Gerges Nasief)*

*My Husband (Nezar Basily) and my Kids (Julie Basily and James Basily)*

*Thanks for being there in every moment in my life, without you I couldn't have accomplished anything in life. I owe every bit of my past, present and future success to you. I am so thankful for your unconditional love, prayers, care, understanding, support and sacrifices.*

## Acknowledgements

*I would like to take this opportunity to first and foremost thank my lord, Jesus Christ to whom I owe my very existence, for the many blessings bestowed upon me to complete the research successfully.*

*I would like to express my deep, heartfelt and sincere gratitude to my advisors: Dr. Timothy Hall and Dr. James Zagzebski for giving me the opportunity to do this research, sharing their knowledge, allowing me to learn from their expertise, and for providing invaluable guidance and insight throughout this research.*

*I would like to extend this gratitude to my committee member: Dr. Tomy Varghese, Dr. Mai Elezaby, Dr. Walter Block, Dr. James Holden, and Dr. Paul Campagnola for the time dedicated to reading this work and for their valuable input.*

*I would like to thank:*

- *My friends: Ivan, Sarah, Yuqi, Xiao, Quincy, Lindsey, Camille, Mariajose, Leah, Andrew, John, Christine, David, Akire and Margo, for great time and experience in WIMR.*
- *Dr. Ernest Madsen and Gary Frank, for their help with the construction of the tissue mimicking phantoms used in this research work.*
- *The staff of the Department of Medical Physics, JoAnn Kronberg, Deb Torgerson, Orhan Unal, Yacouba Traore, Charles Rienke and Lyddia Ruch-Doll, for their help and support.*

*Finally, I sincerely thank the National Institutes of Health for funding this research.*

# Table of contents

Abstract	i
Dedication	ii
Acknowledgements	iii
Table of contents	iv
List of Figures	viii
List of Tables	xxi
<b>Chapter 1: Introduction</b>	<b>1</b>
1.1. Conventional ultrasound	2
1.2. Breast Imaging Reporting and Database System	4
1.3. Quantitative ultrasound	6
1.4. References	13
<b>Chapter 2: 2D Quantitative Ultrasound (QUS) Methods</b>	<b>18</b>
2.1. The Reference Phantom Method (RPM)	19
2.2. Specific Attenuation estimation (ATT)	22
2.3. Backscatter Coefficient (BSC) estimation	23
2.4. Effective Scatter Diameter (ESD) estimation	25
2.5. Effective scatter diameter heterogeneity index (ESDHI) estimation	28
2.6. Data Acquisition for in-vivo human subjects (2D study)	28
2.7. Limitations to QUS Methods	33
2.8. References	34
<b>Chapter 3: QUS of Subcutaneous Breast Fat</b>	<b>40</b>
3.1. Data acquisition	41
3.2. QUS parameters of subcutaneous breast fat	42
3.3. Discussion	46
3.4. Conclusion	51
3.5. References	52

<b>Chapter 4: Modified least squares method</b>	<b>55</b>
4.1. The modified least squares method (MLSM)	56
4.2. Theoretical assessment of the MLSM method	60
4.2.1. Results for the theoretical assessment	61
4.3. Phantom data acquisition	62
4.3.1. Evaluation of the MLSM on uniform phantom	62
4.3.2. Evaluation of the MLSM in heterogeneous phantoms	64
4.3.3. Evaluation of the MLSM on a complex phantom (ACR)	69
4.3.4. Evaluation of the MLSM on stacked test-cylinder phantoms	72
4.4. In vivo Data acquisition	75
4.4.1. Evaluation of the MLSM on in vivo breast data	75
4.4.2. Evaluation of the MLSM on in vivo kidney data	77
4.5. Discussion	79
4.6. Conclusion	80
4.7. References	82
<b>Chapter 5: Detecting coherence and examining anisotropy</b>	<b>84</b>
5.1. Coherence-related QUS parameters estimation	87
5.1.1. Maximum collapsed average (maxCA) of the generalized spectrum	87
5.1.2. Signal amplitude Signal to Noise ratio (SNR)	90
5.1.3. Nakagami shape parameter (Nakagami m)	91
5.2. In vivo Data Acquisition	94
5.2.1. Results for coherence related QUS parameters	94
5.3. Potential of avoiding coherence	97
5.4. Examining anisotropy	101
5.4.1. Trend approach	101
5.4.2. T-test approach	102
5.4.3. Power law fit to attenuation approach	104
5.4.4. Backscatter power difference (BSPD) approach	108
5.5. Discussion	111
5.6. Conclusion	112
5.7. References	113

<b>Chapter 6: Bayesian classifier for differentiating breast masses</b>	<b>117</b>
6.1. QUS Parameter Estimation	119
6.2. Bayesian Classifier	123
6.3. First data set to classify breast masses	124
6.3.1. Results for the thirty-five subjects	126
6.4. Additional data set to classify breast masses	129
6.4.1. Results for the forty-three human subjects	131
6.5. Additional data set acquired during 3D data acquisition	138
6.5.1. Results for the forty-eight human subjects	140
6.6. Discussion	142
6.7. Conclusions	143
6.8. References	145
<b>Chapter 7: Implementing 3D QUS in the breast and comparing 3D with 2D QUS results</b>	<b>151</b>
7.1. The automated breast volume scanning (ABVS) system	152
7.2. The simple elastography (SE) phantom	154
7.2.1. Results for the SE phantom	156
7.3. Data Acquisition for the ACR phantom	156
7.3.1. Results for the ACR phantom	157
7.4. Thick slice formation	158
7.4.1. Results for thick slice formation	158
7.5. Data Acquisition for in-vivo 3D QUS	160
7.5.1. 3D QUS of in vivo subcutaneous breast fat (n= 8)	161
7.5.2. 3D QUS of in vivo fibroadenomas (n= 5)	163
7.6. 2D versus 3D QUS of the breast	168
7.6.1. Results for 2D versus 3D QUS of subcutaneous breast fat	169
7.6.2. Results for 2D versus 3D QUS for an in-vivo breast mass	172
7.7. The acoustic properties of subcutaneous breast fat under different compression scenarios	173
7.7.1. Results for 3D subcutaneous breast fat under different levels of compression	174
7.8. Discussion	176
7.9. Conclusions	177
7.10. References	178

<b>Chapter 8: Contributions and future work</b>	179
<b>Appendix A: Reproducibility of the QUS estimates</b>	182
A.1. Reproducibility of QUS estimates in a rodent-mimicking phantom and a rat tumor	182
A.2. Reproducibility of results on breast masses	186
A.3. References	188
<b>Appendix B: Additional examples for in vivo breast fat and masses</b>	189
B.1. QUS parameter estimates after optimization of the QUS methods	189
B.2. Detecting anisotropy	193
B.2.1. Power law method	195
B.2.2. BSPD method for detecting anisotropy in the power spectra of backscattered echo signals	199
B.3. Bayesian classifier GUI for 43 human subjects	200
B.4. 3D data	202

## List of Figures

<b>FIGURE 1.1.</b> CREATION OF A B-MODE IMAGE .....	3
<b>FIGURE 1.2.</b> CLINICAL IMAGES OF A FIBROADENOMA AND A CARCINOMA .....	5
<b>FIGURE 1.3.</b> A REGION OF INTEREST (ROI) FOR PARAMETER ESTIMATION WAS CHOSEN WITHIN A B-MODE IMAGE. THAT ROI WAS FURTHER PARTITIONED INTO POWER SPECTRUM ESTIMATION REGIONS (PSER), AND, DEPENDING ON THE PARAMETER BEING ESTIMATED, DATA FROM ONE OR MORE OF THOSE PSERS WAS USED IN A PARAMETER ESTIMATION REGION (PER). FOR EXAMPLE, BACKSCATTER COEFFICIENT ESTIMATION WAS PERFORMED ON EACH PSER, BUT ESTIMATING ATTENUATION REQUIRED ESTIMATING THE POWER LOSS AS A FUNCTION OF DEPTH AMONG A SEQUENCE OF PSERS IN A SINGLE PER. THE DOTS SIGNIFY THE CENTER OF EACH PSER.....	7
<b>FIGURE 2.1.</b> EXAMPLE OF THE RPM APPLICATION WHERE A REGION OF INTEREST (ROI) FOR PARAMETER ESTIMATION WAS CHOSEN WITHIN A B-MODE IMAGE. THAT ROI WAS FURTHER PARTITIONED INTO POWER SPECTRUM ESTIMATION REGIONS (PSER) AND THE RATIO OF THE ECHO SIGNAL POWER SPECTRA FROM THE TISSUE TO THE POWER SPECTRA FROM THE SAME DEPTH IN THE REFERENCE PHANTOM WAS USED. (NOTE THAT WE NEED TO BE AT LEAST ONE (ELEVATION) APERTURE AWAY TO AVOID COMPLEX NEARFIELD BEAM PATTERNS). .....	20
<b>FIGURE 2.2.</b> EXAMPLE OF THE BSC AND THE FORM FACTOR TO PREDICT THE ESD.....	27
<b>FIGURE 2.3.</b> DIAGRAM ILLUSTRATE THE SCANNING IN SUPINE POSITION AND BEAM STEERING .....	32
<b>FIGURE 3.1.</b> TYPICAL BREAST ULTRASOUND IMAGE FROM THIS STUDY SHOWING AN EXAMPLE OF BREAST FAT ROI SELECTION (RECTANGLE IN THE UPPER RIGHT) .....	41
<b>FIGURE 3.2.</b> ATTENUATION COEFFICIENT VS. FREQUENCY IN BREAST FAT FOR INDIVIDUAL SUBJECTS .....	43

<b>FIGURE 3.3.</b> THE MEAN ATTENUATION COEFFICIENT ESTIMATES (DOTS) OF BREAST FAT AMONG 24 SUBJECTS, THE STANDARD DEVIATIONS (DASHED LINE) AND THE COMBINED POWER LAW FIT FOR THE ATTENUATION COEFFICIENT VS. FREQUENCY. ....	44
<b>FIGURE 3.4.</b> SPECIFIC ATTENUATION AT 7MHZ FOR EACH SUBJECT. THE CIRCLES REPRESENT THE MEAN FOR EACH SUBJECT AND THE BARS SHOW THE CORRESPONDING STANDARD DEVIATIONS .....	44
<b>FIGURE 3.5.</b> ABSC ESTIMATES FOR BREAST FAT FOR EACH SUBJECT, SHOWN RELATIVE TO THE MEAN VALUE AMONG ALL SUBJECTS (SOLID LINE). THE DASHED LINES INDICATE THE UPPER AND LOWER RANGE OF VALUES .....	45
<b>FIGURE 3.6.</b> EFFECTIVE SCATTERER DIAMETER (ESD) ESTIMATES FOR BREAST FAT FOR EACH SUBJECT. THE SOLID LINE SHOWS THE MEAN VALUE AMONG ESD ESTIMATES .....	46
<b>FIGURE 3.7.</b> TOP: ATTENUATION COEFFICIENT VS. FREQUENCY ESTIMATES FOR TWO CASES (CASE 1: UPPER LINE, CASE 2: LOWER LINE) OF UNEXPECTED BEHAVIOR OF ATTENUATION VS. FREQUENCY. BOTTOM: ASSOCIATED B-MODE IMAGES (CASE 1 ON THE LEFT; CASE 2 ON THE RIGHT) WITH THE ROI (OUTLINED BOXES) WITHIN WHICH THE ATTENUATION COEFFICIENTS WERE ESTIMATED.....	47
<b>FIGURE 3.8.</b> SPECIFIC ATTENUATION AT 7MHZ REPORTED IN FIG 3.4 FOR BREAST FAT (DATA POINTS), COMPARED TO MEAN VALUES FOR THE SAME PARAMETERS FOR EX VIVO BREAST FAT REPORTED BY D'ASTOUS AND FOSTER .....	48
<b>FIGURE 3.9.</b> ATTENUATION COEFFICIENT VS. FREQUENCY FOR BREAST FAT COMPARING IN VIVO BREAST MEASUREMENTS TO PREVIOUSLY REPORTED RESULTS .....	49

<b>FIGURE 3.10.</b> ATTENUATION COEFFICIENT VS. FREQUENCY FOR BREAST FAT, COMPARING EX VIVO RESULTS OF D’ASTOUS AND FOSTER, FOSTER ET AL., AND THE IN VIVO RESULTS REPORTED IN THIS STUDY .....	50
<b>FIGURE 3.11.</b> BSC VS. FREQUENCY FOR BREAST FAT AS REPORTED BY D’ASTOUS AND FOSTER, ANDERSON ET AL., AND OUR ESTIMATES REPORTED HERE .....	51
<b>FIGURE 4.1.</b> SCHEMATIC OF THE MODIFIED LEAST SQUARES METHOD (MLSM) DESCRIBING THE EXTRA STEPS BEYOND THE LEAST SQUARES METHOD .....	59
<b>FIGURE 4.2.</b> THE MODIFIED LEAST SQUARES METHOD (MLSM) FOR ATTENUATION ESTIMATION, WHERE THE SOLID CURVED LINE IS THE UNDERLYING ATTENUATION COEFFICIENT VS. FREQUENCY TO BE ESTIMATED. IN A) THE FIRST FREQUENCY SUBBAND IS CHOSEN, B) A LINEAR FIT IS APPLIED TO THE FIRST SUBBAND, C) THE PROCESS IS REPEATED FOR MULTIPLE SUBBANDS OVERLAPPING BY 50% WHERE THE RESULTING VALUE FOR THE ATTENUATION COEFFICIENT IN THE PREVIOUS SUBBAND SERVES AS THE STARTING POINT FOR THE NEXT SUBBAND, D) A POWER LAW ATTENUATION FIT AMONG THE PIECEWISE LINEAR FITS FROM EACH SUBBAND IS OBTAINED. $F_L$ AND $F_H$ STANDS FOR LOWER AND HIGHER FREQUENCY LIMITS RESPECTIVELY .....	60
<b>FIGURE 4.3.</b> THEORETICAL ASSESSMENT OF THE MLSM VERSUS THE LSM FOR A HIGHER FREQUENCY DEPENDENCE OF ATTENUATION IN THE SAMPLE AND THE CORRESPONDING POWER LAW AND LINEAR FITS RESULTING FROM THE MLSM AND THE LSM RESPECTIVELY. ....	61
<b>FIGURE 4.4.</b> EFFECTIVE ATTENUATION COEFFICIENT AT 6 MHZ DIVIDED BY THE FREQUENCY FOR THE UNIFORM PHANTOM .....	64

<b>FIGURE 4.5.</b> A SCHEMATIC OF THE THREE LAYERED PHANTOMS: A) SHOWS THE PHANTOM WITH CONSTANT BACKSCATTER AND LAYERED ATTENUATION B) SHOWS THE PHANTOM WITH CONSTANT ATTENUATION AND LAYERED BACKSCATTER LEVELS .....	65
<b>FIGURE 4.6.</b> EFFECTIVE ATTENUATION COEFFICIENT AT 6 MHz DIVIDED BY THE FREQUENCY FOR THE LAYERED ATTENUATION PHANTOM.....	67
<b>FIGURE 4.7.</b> EFFECTIVE ATTENUATION COEFFICIENT AT 6 MHz DIVIDED BY THE FREQUENCY FOR THE CONSTANT ATTENUATION PHANTOM.....	68
<b>FIGURE 4.8.</b> BSC ESTIMATES FOR THE VARIABLE BSC PHANTOM FROM FARAN'S THEORY, LSM, LAB MEASUREMENTS AND MLSM .....	68
<b>FIGURE 4.9.</b> SCHEMATIC OF THE ACR PHANTOM.....	69
<b>FIGURE 4.10.</b> B-MODE IMAGE OF THE ACR PHANTOM .....	71
<b>FIGURE 4.11.</b> EFFECTIVE ATTENUATION COEFFICIENT AT 6 MHz DIVIDED BY THE FREQUENCY FOR THE ACR PHANTOM.....	71
<b>FIGURE 4.12.</b> EFFECTIVE ATTENUATION COEFFICIENTS AT 6 MHz DIVIDED BY THE FREQUENCY FOR THE STACKABLE CYLINDERS .....	73
<b>FIGURE 4.13.</b> BSC ESTIMATED AFTER CORRECTING FOR ATTENUATION WITH VALUES FROM THE MLSM VERSUS OTHER METHODS AND LAB VALUES.....	74
<b>FIGURE 4.14.</b> EXAMPLE OF IN-VIVO BREAST DATA SCANNED WITH A SIEMENS S2000 AND AN 18L6 TRANSDUCER (SUBJECT 10 IN TABLE 7.2) .....	76
<b>FIGURE 4.15.</b> EXAMPLES OF THE ATTENUATION CORRECTED POWER SPECTRA WITH FAT VALUES VERSUS MLSM VALUES FOR A ROI IN THE SUBCUTANEOUS FAT IN A HUMAN SUBJECT WITH AN INFILTRATING DUCTAL CARCINOMA (IDC1 IN CHAPTER 6).....	77
<b>FIGURE 4.16.</b> B-MODE IMAGE OF THE SCANNED KIDNEY .....	78

<b>FIGURE 4.17.</b> ESD MAP AND THE DISTRIBUTION OF THE SCATTER SIZE OF THE GLOMERULI FOR IN-VIVO KIDNEY PATIENT.....	79
<b>FIGURE 5.1.</b> DIFFERENT SCATTERING SCENARIOS THAT CAN BE PRESENT IN IN-VIVO BREAST TISSUE (FIGURE FROM ROSADOMENDEZ, 2014) <sup>12</sup> .....	86
<b>FIGURE 5.2.</b> DIAGRAM ILLUSTRATING THE AMOUNT OF CORRELATION BETWEEN TWO DIFFERENT FREQUENCY COMPONENTS FOR TWO CASES: (A) A STATIONARY SIGNAL AND (B) A NON-STATIONARY SIGNAL (FIGURE FROM ROSADOMENDEZ, 2014) <sup>12</sup> .....	88
<b>FIGURE 5.3.</b> THE GENERALIZED SPECTRUM AND THE COLLAPSED AVERAGE (FIGURE FROM ROSADO-MENDEZ <sup>12</sup> ) .....	89
<b>FIGURE 5.4.</b> PLOTS OF THE INDIVIDUAL QUS PARAMETER ESTIMATES FOR EACH SUBJECT ORDERED FROM SMALLEST TO LARGEST ROI SIZE. THE SAME ROI WAS USED FOR ALL PARAMETER ESTIMATES FOR AN INDIVIDUAL SUBJECT (E.G., FA1 IS THE FIBROADENOMA WITH THE SMALLEST ROI). FIBROADENOMAS (FA) ARE SHOWN SEPARATELY FROM CANCERS. CANCERS ARE GROUPED TOGETHER BY TYPE: INVASIVE DUCTAL CARCINOMA (IDC); INVASIVE LOBULAR CARCINOMA (ILC); INTRACYSTIC PAPILLARY CARCINOMA(IPC), AND DUCTAL CARCINOMA IN SITU (DCIS). THE SOLID HORIZONTAL LINES SHOW THE MEDIAN VALUE OF THAT PARAMETER (SEPARATELY FOR FIBROADENOMAS AND CARCINOMAS), AND THE DASHED LINES SHOW THE INNER QUARTILE RANGE OF VALUES.....	96
<b>FIGURE 5.5.</b> MAPS FOR THE MAXCA, SNR AND NAKAGAMI M FOR ONE OF THE SUBJECTS (FA20 IN CHAPTER 6).....	97
<b>FIGURE 5.6.</b> ROIS CHOSEN IN THE ATS PHANTOM AND THE CORRESPONDING LATERAL MEAN OF THE SPECIFIC ATTENUATION COEFFICIENTS AT 6 MHZ VERSUS DEPTH.....	99

<b>FIGURE 5.7.</b> LATERAL MEAN OF THE ATTENUATION COEFFICIENT DIVIDED BY THE FREQUENCY AT 6 MHz VERSUS DEPTH FOR ROI'S IN AN ATS 539 PHANTOM. PLOT AND ATTENUATION COEFFICIENT/FREQ IMGE ON THE LEFT WERE GENERATED FROM THE ROI IN THE BACK GROUND, THE MIDDLE FOR AN ROI THAT INCLUDED THE MONOFILAMENT LINE TARGET, AND THE RIGHT FOR THE SAME ROI AFTER ELIMINATING THE SIGNALS FROM THE MONOFILAMENT LINE TARGET AND THE CORRESPONDING ATTENUATION MAPS .....	100
<b>FIGURE 5.8.</b> EXAMPLE OF THE ATTENUATION COEFFICIENT VERSUS FREQUENCY AT DIFFERENT BEAM STEERING ANGLES FOR ONE HUMAN SUBJECT .....	102
<b>FIGURE 5.9.</b> EXAMPLE OF THE T-TEST RESULT FOR ONE HUMAN SUBJECT SHOWS THE ANGLES THAT HAVE BEEN EXAMINED AND THE P-VALUES OBTAINED FROM THE T-TEST WHEN EXAMINING ATTENUATION ESTIMATES OBTAINED AT THESE ANGLES. THE P-VALUE FOR EACH PAIR EXAMINED IS SHOWN UNDERNEATH THE PAIR NAME. N5: REPRESENTS ATTENUATION ESTIMATES OBTAINED FROM THE NEGATIVE 5-DEGREE VIEW; N10: REPRESENTS ATTENUATION ESTIMATES OBTAINED FROM THE NEGATIVE 10-DEGREE VIEW; P5: REPRESENTS ATTENUATION ESTIMATES OBTAINED FROM THE POSITIVE 5-DEGREE VIEW; P10: REPRESENT ATTENUATION ESTIMATES OBTAINED FROM THE POSITIVE 10-DEGREE VIEW; AND 0: REPRESENT ATTENUATION ESTIMATES OBTAINED FROM THE CENTRAL DEGREE VIEW.....	104
<b>FIGURE 5.10.</b> AN EXAMPLE OF A POWER LAW FIT TO THE ATTENUATION COEFFICIENT VERSUS FREQUENCY AT ONE BEAM STEERING ANGLE .....	105
<b>FIGURE 5.11.</b> ILLUSTRATION OF ANISOTROPY EXAMINATION METHOD .....	105

<b>FIGURE 5.12.</b> EXAMPLE OF THE ATTENUATION COEFFICIENT ESTIMATED AT DIFFERENT ANGLES, IN BOTH RADIAL AND ANTI-RADIAL DIRECTIONS, FOR AN INTRACYSTIC PAPILLARY CARCINOMA (IPC IN CHAPTER 6) .....	106
<b>FIGURE 5.13.</b> ATTENUATION COEFFICIENT VERSUS FREQUENCY SHOWN IN FIGURE 5.12 WITH THE CORRESPONDING POWER LAW FIT (APPLIED IN THE SAME WAY AS FIGURE 5.10), THE NUMERICAL VALUE AT 6 MHZ AND THE NORMALIZED VALUE TO THE CENTRAL DEGREE VIEW, AND A PLOT OF THE NORMALIZED DATA TO THE ZERO-DEGREE VIEW FOR THE POWER LAW FIT AT 6 MHZ, IN BOTH RADIAL AND ANTI-RADIAL DIRECTION FOR ALL BEAM STEERING ANGLES FOR THE INTRACYSTIC PAPILLARY CARCINOMA (IPC IN CHAPTER 6).....	107
<b>FIGURE 5.14.</b> NORMALIZED DATA TO THE ZERO-DEGREE VIEW FOR THE POWER LAW FIT AT 6 MHZ FOR A FIBROADENOMA (FA22 IN CHAPTER 6).....	108
<b>FIGURE 5.15.</b> NBSPD FOR ONE ISOTROPIC AND ONE ANISOTROPIC TUMOR .....	109
<b>FIGURE 6.1.</b> THE GENERALIZED SPECTRUM AND THE COLLAPSED AVERAGE (FIGURE FROM ROSADO-MENDEZ <sup>34</sup> ) .....	122
<b>FIGURE 6.2.</b> SCHEMATIC OF THE BAYESIAN CLASSIFIER .....	125
<b>FIGURE 6.3.</b> GUI FOR BAYESIAN CLASSIFIER .....	126
<b>FIGURE 6.4.</b> PERFORMANCE OF THE BAYESIAN CLASSIFIER.....	128
<b>FIGURE 6.5.</b> PLOTS OF THE INDIVIDUAL QUS PARAMETER ESTIMATES FOR EACH SUBJECT ORDERED FROM SMALLEST TO LARGEST ROI SIZE. THE SAME ROI WAS USED FOR ALL PARAMETER ESTIMATES FOR AN INDIVIDUAL SUBJECT (E.G., FA1 IS THE FIBROADENOMA WITH THE SMALLEST ROI). FIBROADENOMA (FA) ARE SHOWN SEPARATELY FROM CANCERS. CANCERS ARE GROUPED TOGETHER BY TYPE: INVASIVE DUCTAL CARCINOMA (IDC); INVASIVE LOBULAR CARCINOMA (ILC). THE SOLID HORIZONTAL LINES SHOW THE	

MEDIAN VALUE OF THAT PARAMETER (SEPARATELY FOR FIBROADENOMA AND CARCINOMA), AND THE DASHED LINES SHOW THE INNER QUARTILE RANGE OF VALUES ..... 133

**FIGURE 6.6.** LOG-AVERAGE BACKSCATTER COEFFICIENT VERSUS MAXCA FOR FIBROADENOMAS, CARCINOMAS AND FAT ..... 134

**FIGURE 6.7.** RELATIONSHIP BETWEEN NAKAGAMI M AND ESD FOR FIBROADENOMA, CARCINOMA AND FAT ..... 135

**FIGURE 6.8.** ROC CURVES ILLUSTRATING THE PERFORMANCE OF VARIOUS CLASSIFIERS BASED ON COMBINATIONS OF QUS PARAMETERS; AUC=1 FOR ATT, ESD, ESDHI ..... 137

**FIGURE 6.9.** PLOTS OF BEST 3 PARAMETERS COMBINATION ..... 137

**FIGURE 7.1.** THE ABVS SYSTEM SHOWING A SIEMENS S2000 ULTRASOUND SYSTEM AND AN AUTOMATED BREAST VOLUME SCANNER (ABVS) ATTACHMENT. .... 153

**FIGURE 7.2.** ILLUSTRATION OF DATA ACQUISITION AND C-SCAN FORMATION. DATA WAS ACQUIRED BY TRANSLATING THE TRANSDUCER OVER THE SURFACE OF THE PHANTOM, AND THE C-SCAN IMAGE WAS GENERATED BY SELECTING DATA AT A CONSTANT DEPTH (CUT AT THE GREEN LINES) ..... 154

**FIGURE 7.3.** THE SIMPLE ELASTOGRAPHY PHANTOM AND A B-MODE IMAGE OF THE PHANTOM SHOWING THE SPHERE IN THE MIDDLE OF THE PHANTOM ..... 155

**FIGURE 7.4.** SHOWN FROM THE LEFT TO RIGHT ARE THE ACQUISITION VIEW WITH THE LOCATION WHERE THE C-SCAN WAS GENERATED OUTLINED, THE B-MODE C-SCAN WITH ATTENUATION OVERLAY WITH THE SPHERE OUTLINED, AND THE B-MODE C-SCAN WITH THE SPHERE OUTLINED. .... 156

**FIGURE 7.5.** THE SCHEMATIC OF THE ACR PHANTOM ..... 157

<b>FIGURE 7.6.</b> IMAGE OF THE ACR PHANTOM OBTAINED WITH THE ABVS SCANNER. LEFT CONVENTIONAL B-MODE IMAGE THROUGH A SPECULATED MASS; CENTER B-MODE C-SCAN; RIGHT B-MODE C-SCAN WITH ATT OVERLAY (THE COLORBAR SHOWS VALUES FROM 0-2 DB/CM MHZ).....	158
<b>FIGURE 7.7.</b> VARYING THE SLICE THICKNESS OF ATTENUATION MAPS OF THE SE PHANTOM. ....	159
<b>FIGURE 7.8.</b> ATT MAPS ESTIMATED AND ATT MAP OVERLAID ON THE B-MODE IMAGE OF ONE SLICE VERSUS 5 SLICES THICK FOR THE SE PHANTOM.....	159
<b>FIGURE 7.9.</b> B-MODE IMAGE OF A MASS (IDC10 IN CHAPTER 6) AND THE SURROUNDING SUBCUTANEOUS FAT .....	161
<b>FIGURE 7.10.</b> THICK SLICE FORMATION OF ESD (4MM) .....	163
<b>FIGURE 7.11.</b> AN EXAMPLE OF ATTENUATION AND ESD ESTIMATED FOR ONE HUMAN SUBJECT WITH A FIBROADENOMA (OUTLINED IN YELLOW) SCANNED WITH THE ABVS SYSTEM .....	164
<b>FIGURE 7.12.</b> ESD C-SCAN OF ONE HUMAN SUBJECT (SUBJECT 5, IN TABLE 7.1) SCANNED WITH THE ABVS SYSTEM. LEFT, B-MODE; CENTER, ESD; RIGHT, OVERLAY OF B-MODE AND ESD IMAGES. ....	165
<b>FIGURE 7.13.</b> ATT AND ESD ESTIMATES FOR ONE SLICE OF A TUMOR WITH A CLIP (SUBJECT 4 IN TABLE 7.1) .....	166
<b>FIGURE 7.14.</b> THICK SLICE FORMATION FOR THE FOR THE ESD ESTIMATES IN SUBJECT 4. ....	167
<b>FIGURE 7.15.</b> A) B-MODE C-SCAN, ATT C-SCAN AND B-MODE C-SCAN WITH ATT OVERLAY ABOVE THE CLIP, B) THE TOP ROW: SHOWS B-MODE C-SCAN, ESD C-SCAN AND B-MODE C-SCAN WITH ESD OVERLAY ABOVE THE CLIP, THE MIDDLE ROW SHOWS THE B-MODE C-SCAN, ESD C-SCAN AND B-MODE C-SCAN WITH ESD OVERLAY TAKEN AT THE CLIP, AND	

THE BOTTOM ROW THE B-MODE C-SCAN, ESD C-SCAN AND B-MODE C-SCAN WITH ESD OVERLAY TAKEN AFTER AVOIDING IT .....	168
<b>FIGURE 7.16.</b> A) ATT, ESD, AND BSC VERSUS FREQUENCY ESTIMATED IN 2D FOR SUBCUTANEOUS BREAST FAT, B) 3D QUS PARAMETERS ESTIMATED FOR SUBCUTANEOUS BREAST FAT (IN SUBJECT 5 TABLE 7.1), FOR EACH SUBPLOT THE TOP FIGURES SHOW THAT ATTENUATION COEFFICIENT VERSUS FREQUENCY AND THE BOTTOM FIGURES SHOW THE ESD MAPS AND THE BSC VERSUS FREQUENCY .....	169
<b>FIGURE 7.17.</b> BSC ESTIMATED USING DATA OBTAINED WITH THE 18L6 VERSUS ABVS TRANSDUCERS AND PREVIOUSLY PUBLISHED DATA FOR OUR PREVIOUS IN-VIVO STUDY <sup>3</sup> , D'ASTOUS AND FOSTER <sup>6</sup> , AND ANDERSON ET AL. <sup>7</sup> .....	170
<b>FIGURE 7.18.</b> ATT AND ESD FOR A FIBROADENOMA (SUBJECT 1 IN TABLE 7.1) ESTIMATED USING A) 2D VERSUS B) 3D DATA. FOR EACH SUBPLOT THE TOP FIGURES SHOW THAT ATTENUATION COEFFICIENT VERSUS FREQUENCY AND THE BOTTOM FIGURES SHOW THE ESD MAPS. ....	172
<b>FIGURE 7.19.</b> A) ATTENUATION COEFFICIENT VERSUS FREQUENCY AND B) BSC ESTIMATES FOR SUBCUTANEOUS FAT (FOR SUBJECT 5 IN TABLE 7.1) UNDER DIFFERENT COMPRESSION SCENARIOS. L1 REFERS TO THE FIRST COMPRESSION LEVEL (2.4%), L2 IS THE SECOND COMPRESSION LEVEL (5.3%), ETC.) .....	174
<b>FIGURE 7.20.</b> MEAN AND STANDARD DEVIATION FOR THE BSC OF SUBCUTANEOUS FAT AT 3 DIFFERENT COMPRESSION LEVELS. ....	175
<b>FIGURE 7.21.</b> BSC RESULTS FOR 3D SCANS OF SUBCUTANEOUS FAT UNDER DIFFERENT COMPRESSION LEVELS. ALSO SHOWN ARE OUR PREVIOUSLY PUBLISHED 2D RESULTS, RESULTS FROM D'ASTOUS AND FOSTER <sup>6</sup> , AND ANDERSON ET AL. RESULTS. <sup>7</sup> .....	175

<b>FIGURE 7.22.</b> A) ESD AND B) ESDHI VERSUS PERCENT AVERAGE ACCUMULATED STRAIN.....	176
<b>FIGURE A.1.</b> SCHEMATIC OF THE CUSTOM MADE, RODENT-LESION MIMICKING PHANTOM .....	183
<b>FIGURE A.2.</b> ATTENUATION MAPS AND ATTENUATION ESTIMATES VERSUS FREQUENCY FOR SPHERE A AND B OF THE RODENT PHANTOM. THE ATT ESTIMATED FOR EACH SPHERE IS SHOWN IN THE FIGURE (WHITE TEXT) AND THE EXPECTED VALUE IS SHOWN FOR EACH SPHERE IN BLACK.....	183
<b>FIGURE A.3.</b> ROI FOR SPHERE A AND THE BACKGROUND OF THE RODENT PHANTOM WITH THE TRANSDUCER IN CONTACT AND THROUGH A SALINE PATH .....	184
<b>FIGURE A.4.</b> POWER SPECTRA OF THE SAMPLE AND THE REFERENCE AND THE ATTENUATION CORRECTED POWER SPECTRA FOR THE REFERENCE WITH THE TRANSDUCER IN CONTACT AND THROUGH A SALINE PATH.....	185
<b>FIGURE A.5.</b> BSC OF SPHERE A USING THE BACKGROUND OF THE RODENT PHANTOM AS THE REFERENCE PHANTOM MATERIAL (WITH TRANSDUCER IN CONTACT AND BACKED OFF WITH A SALINE PATH) .....	185
<b>FIGURE A.6.</b> A) B-MODE OF THE RAT TUMOR PHANTOM, AND B) THE BACKSCATTER COEFFICIENT VERSUS FREQUENCY ESTIMATED FOR THE RAT TUMOR. ....	186
<b>FIGURE A.7.</b> EXAMPLE SHOWING THE REPRODUCIBILITY OF DATA AMONG DIFFERENT USERS FOR DIFFERENT HUMAN SUBJECTS (ACA: ADENOCARCINOMA, IDC: DUCTAL CARCINOMA, FA: FIBROADENOMA). NUMBERS REPRESENTED IN THE TABLES SHOW THE ATT ESTIMATED FROM EACH USER IN $\text{DB} \cdot \text{CM}^{-1} \text{MHZ}^{-1}$ .....	187
<b>FIGURE B.1.</b> QUS OF SUBCUTANEOUS BREAST FAT A) ESD MAP, B) POWER SPECTRA FOR THE SAMPLE AND THE REFERENCE, C) ATTENUATION COEFFICIENT VERSUS FREQUENCY, AND D) BSC VERSUS FREQUENCY.....	190

<b>FIGURE B.2.</b> QUS PARAMETER ESTIMATION FOR CENTRAL DEGREE VIEW FOR A FIBROADENOMA (FA23) A) THE B-MODE IMAGE, B) THE POWER SPECTRA OF THE SAMPLE AND THE REFERENCE, C) ESD MAP, D) ATTENUATION VERSUS FREQUENCY, E) FORM FACTOR FROM MEAN BSC, F) BSC VERSUS FREQUENCY .....	191
<b>FIGURE B.3.</b> QUS PARAMETERS ESTIMATED AND CREATION OF LARGE PARAMETRIC IMAGES OF ESD OF A FIBROADENOMA (FA21).....	192
<b>FIGURE B.4.</b> LARGE PARAMETRIC IMAGES OF ESD OF TWO CARCINOMAS (ACA AND IDC 8) AND 2 FIBROADENOMA (FA 15 AND FA25) .....	192
<b>FIGURE B.5.</b> BEAM STEERED B-MODE IMAGES FROM -10 TO 10 DEGREES CAPTURED FROM THE S2000 IN RESEARCH MODE FOR AN INFILTRATING DUCTAL CARCINOMA .....	193
<b>FIGURE B.6.</b> BEAM STEERED B-MODE IMAGES FROM -10 TO 10 DEGREES WITH AN INCREMENT OF 5 DEGREES FOR A DUCTAL CARCINOMA IN SITU (DCIS1) CAPTURED FROM THE S2000 IN CLINICAL MODE FOR A FIBROADENOMA .....	194
<b>FIGURE B.7.</b> EXAMPLE OF BEAM STEERED B-MODE IMAGES (STEERED FROM -20 TO 20 DEGREES) GENERATED OFFLINE FROM THE RF DATA ACQUIRED FROM THE S2000 IN RESEARCH MODE FOR A FIBROADENOMA (FA20 IN CHAPTER 6) .....	194
<b>FIGURE B.8.</b> QUS PARAMETER ESTIMATED FOR DIFFERENT BEAM STEERING ANGLES FOR AN ADENOCARCINOMA (ACA IN CHAPTER 6), A) BSC VERSUS FREQUENCY, B) TABLE SHOWING ESD AND ESDHI ESTIMATES FOR -5 TO +5 DEGREES, C) TABLE SHOWING BSC ESTIMATES FOR -5 TO +5 DEGREES, D) POWER SPECTRA FOR -5, 0, AND +5 DEGREES, AND E) B-MODE IMAGES FOR -5, 0, AND +5 BEAM STEERING ANGLES .....	195
<b>FIGURE B.9.</b> SHOWS AN EXAMPLE OF ATTENUATION COEFFICIENT VERSUS FREQUENCY FOR DIFFERENT BEAM STEERING ANGLES FOR AN INTRACYSTIC PAPILLARY CARCINOMA (IPC)...	196

<b>FIGURE B.10.</b> SHOWS AN EXAMPLE OF POWER LAW FITS TO ATTENUATION FOR DIFFERENT BEAM STEERING ANGLES FOR THE INTRACYSTIC PAPILLARY CARCINOMA (IPC) SHOWN IN FIGURE B.10 .....	197
<b>FIGURE B.11.</b> THE RESULTANT NORMALIZED ATT TO THE CENTRAL DEGREE VIEW (SHOWN IN TABLE B.2) WITH THE STANDARD ERROR VALUES FOR THE IPC .....	199
<b>FIGURE B.12.</b> EXAMPLES FOR THE BSPD METHOD IN DETECTING ANISOTROPY .....	200
<b>FIGURE B.13.</b> EXAMPLE OF THE GUI BUILT FOR THE BAYESIAN CLASSIFIER .....	201
<b>FIGURE B.14.</b> EXAMPLE OF THE GUI BUILT FOR THE BAYESIAN CLASSIFIER DIFFERENTIATING A FIBROADENOMA (FA3 IN TABLE 6.2, SEE CHAPTER 6) .....	201
<b>FIGURE B.15.</b> EXAMPLE OF THE GUI BUILT FOR THE BAYESIAN CLASSIFIER DIFFERENTIATING A CARCINOMA (IDC 2 IN TABLE 6.3, SEE CHAPTER 6) .....	202
<b>FIGURE B.16.</b> QUS PARAMETERS ESTIMATED USING THE ABVS SYSTEM AND THE ESD C-SCAN FOR A FIBROADENOMA (ABVS 1401, SUBJECT 1, TABLE 7.2) .....	202

## List of Tables

<b>TABLE 3.1.</b> AVERAGE VALUES OF THE ATTENUATION COEFFICIENT MODELED AS A LINEAR FUNCTION OF FREQUENCY (ATT), THE BACKSCATTER COEFFICIENT (BSC) MODELED AS A POWER LAW AND THE AVERAGE BACKSCATTER COEFFICIENT (ABSC) OF BREAST FAT VERSUS LITERATURE VALUES .....	49
<b>TABLE 4.1.</b> PROPERTIES OF THE CONSTANT ATTENUATION AND CONSTANT BACKSCATTER THREE-LAYER PHANTOMS.....	66
<b>TABLE 4.2.</b> LAB ATTENUATION VALUES FOR ACR PHANTOM.....	70
<b>TABLE 4.3.</b> LAB ATTENUATION OF THE STACKED TEST CYLINDERS.....	72
<b>TABLE 5.1.</b> A SUMMARY OF THE RESULTS OBTAINED FROM THE BSPD VERSUS POWER LAW FIT METHOD, SHOWING THE FINAL JUDGING OBTAINED FROM THE POWER LAW FIT METHOD (ISOTROPIC: YES, OR NO) AND THE MEAN BSPD (MBSPD) OBTAINED FROM THE BSPD METHOD.....	110
<b>TABLE 6.1.</b> QUS PARAMETER VALUES FOR THE 35 HUMAN SUBJECTS .....	127
<b>TABLE 6.2.</b> QUS PARAMETER VALUES OF FIBROADENOMAS INCLUDED IN THIS STUDY PRESENTED THE ORDER THEY ARE DISPLAYED IN THE FIGURES. THE SEQUENTIAL ORDER IN WHICH THEY WERE RECRUITED INTO THE STUDY ARE SHOWN IN THE “SUBJECT ORDER” COLUMN. ....	131
<b>TABLE 6.3.</b> QUS PARAMETER VALUES OF MALIGNANT MASSES INCLUDED IN THIS STUDY PRESENTED THE ORDER THEY ARE DISPLAYED IN THE FIGURES. THE SEQUENTIAL ORDER IN WHICH THEY WERE RECRUITED INTO THE STUDY ARE SHOWN IN THE “SUBJECT ORDER” COLUMN. ACA = ADENOCARCINOMA; DC = DUCTAL CARCINOMA; DCIS = DUCTAL CARCINOMA IN SITU; LC = LOBULAR CARCINOMA; LCIS = LOBULAR CARCINOMA IN SITU; IPC = INTRACYSTIC PAPILLARY CARCINOMA. SUBJECT 38 WAS REPORTED AS DCIS	

INVOLVING INTRADUCTAL PAPILLOMA AND INVOLVING DUCTS ADJACENT TO PAPILLOMA; SUBJECT 42 WAS REPORTED AS INFILTRATING DUCTAL CARCINOMA NOTTINGHAM GRADE 2, LCIS CLASSICAL TYPE, METASTATIC BREAST DUCTAL CARCINOMA. ....	132
<b>TABLE 6.4.</b> AREA UNDER THE RECEIVER OPERATING CHARACTERISTIC CURVES FOR VARIOUS 2- PARAMETER AND 3-PARAMETER COMBINATIONS OF QUS PARAMETERS FORMING A NAÏVE BAYESIAN CLASSIFIER TO DIFFERENTIATE FIBROADENOMAS FROM CARCINOMAS. THE 95% CONFIDENCE INTERVALS WERE COMPUTED SEPARATELY FOR THE CASE WHEN FIBROADENOMA WAS TRUE-POSITIVE .....	136
<b>TABLE 6.5.</b> PROPERTIES OF THE REFERENCE PHANTOM .....	138
<b>TABLE 6.6.</b> QUS PARAMETER VALUES OF FIBROADENOMAS INCLUDED IN THE ABVS STUDY.....	141
<b>TABLE 6.7.</b> COMPARISON OF THE MEDIAN AND INTERQUARTILE RANGES ESTIMATED FOR FIBROADENOMAS IN THE 43-HUMAN SUBJECT POOL VERSUS THE 48-HUMAN SUBJECT POOL	142
<b>TABLE 7.1.</b> QUS PARAMETERS OF 5 BREAST MASSES SCANNED WITH THE ABVS SYSTEM.....	164
<b>TABLE 7.2.</b> 2D VERSUS 3D QUS OF SUBCUTANEOUS FAT .....	171
<b>TABLE 7.3.</b> QUS PARAMETERS ESTIMATED FOR 5 FIBROADENOMAS IN 2D AND 3D .....	173
<b>TABLE B.1.</b> EXAMPLE FOR THE SIGMA N AND SIGMA ALPHA 0 OBTAINED FOR DIFFERENT BEAM STEERING ANGLES .....	198
<b>TABLE B.2.</b> ATT VALUES AT 6 MHZ AND THE NORMALIZED VALUES TO THE CENTRAL DEGREE VIEW FOR THE IPC SHOWN ABOVE.....	198
<b>TABLE B.3.</b> THE BSPD METHOD TO DETECT ANISOTROPY IN THE POWER SPECTRA OF BACKSCATTERED ECHO SIGNALS .....	200
<b>TABLE B.4.</b> SUBJECT ID USED IN CHAPTER 7 AND THE SUBJECT ID FROM RECRUITMENT FOR SUBCUTANEOUS FAT AND BREAST MASSES .....	203

## Chapter 1: Introduction

Breast cancer is the second most common cancer and the second leading cause of cancer death among women in the United States.<sup>1</sup> The common screening tests for breast cancer include clinical breast exams, breast self-exams, and mammography. Mammography is considered the primary imaging modality for screening asymptomatic women. The American college of radiology recommends annual mammograms for women of age 40 and over. Mammography is based on the detection of x-rays transmitted through the breast on a radiographic film or a digital detection device. However, it suffers from limitation due to its projective nature. The registration of the absorption and scattering of the x-rays in a two-dimensional image from the internal structures of the breast can reduce the conspicuity of any abnormality that might exist within it. For women with a family history of breast cancer or certain other risk factors, magnetic resonance imaging (MRI) is recommended in addition to mammograms.<sup>2</sup>

Another supplemental imaging modality for breast cancer detection is ultrasound. Generally, ultrasound is not used as a sole imaging modality, but it is often used to evaluate suspicious breast masses imaged on mammography, and is most useful in assessing very dense breasts, where x-ray mammography has a low sensitivity. Additionally, ultrasound is used as a tool to guide biopsy procedures that utilize minimally invasive techniques. Ultrasound plays an important role in breast cancer diagnosis and has become a valuable tool used in conjunction with mammography because the equipment is widely available, is cost-effective, and provides unique soft tissue information.

Breast cancer mortality rates have declined due to the possibility of detecting the disease at an early stage and because of the improvement in treatment options. Several studies reported that ultrasound screening in women with dense breasts and negative mammograms has increased

the cancer detection rate from 2.8 to 4.6 cancers per 1,000 women.<sup>3-7</sup> Berg et al.<sup>8</sup> studied 2662 women, among which there were 4814 incidence screens (annual ultrasound screening procedures for second and third years of study). In that group, the authors observed sensitivity and specificity for mammography alone of about 0.52 and 0.91, respectively. When ultrasound was included, the sensitivity for both modalities together increased to 0.76, but the specificity decreased to 0.84. When MRI was included with mammography plus ultrasound, the sensitivity increased to 1.0, but the specificity decreased to 0.65. Clearly, improvements in the specificity of breast ultrasound could have a significant impact on image-based breast mass classification.

## **1.1. Conventional ultrasound**

Conventional ultrasound works in a pulse echo mode, where a short acoustic pulse interacts with the tissue within a volume called the “resolution cell.” An echo-signal is generated within this volume when there are changes in density and/or compressibility. Following transmission of the pulse, the received scattered pressure (echoes) from various depths are converted by the ultrasound transducer into an electronic signal called the radiofrequency (RF) echo signal. B-mode images are created by sweeping a pulsed beam across a region of interest and displaying the amplitudes of echo signals on a 2D matrix (see Figure 1.1). The echo arrival time and the ultrasound beam axes are used to position the signals in their proper location.

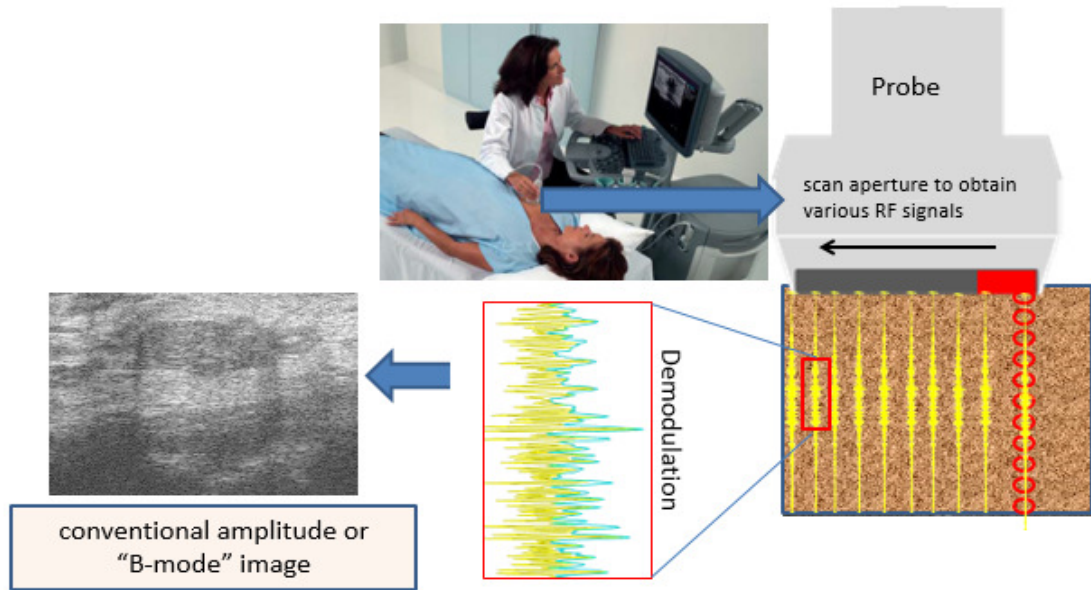


*Figure 1.1. Creation of a B-mode image*

Subjective image analysis is commonly performed in medical ultrasound. Conventional ultrasound can be a qualitative, low-specificity modality because image brightness and other features of displayed echo signals depend on the skill of the operator, the scanner configuration, and the transmission path that the acoustic pulse traverses on its way to the tissue of interest. Thus, it suffers from inter- and intra-observer variability in the evaluation of these images, and this reduces the objectivity of the imaging modality. The subjectivity and the fact that images of the same lesion may vary from system to system results in ultrasound having a rather low specificity for classifying breast masses. This leads to an increased false positive detection rate, requiring core biopsy to provide a definitive diagnosis. This results in a high rate of biopsy of benign tumors, causing unnecessary stress and cost to the patient and the healthcare system.

## 1.2. Breast Imaging Reporting and Database System

To aid with the communication of image interpretation, the American College of Radiology published and trademarked the Breast Imaging Reporting and Database System (BI-RADS®). This system defines a common lexicon to describe various features related to the appearance of breast masses and their surrounding tissue in the ultrasound image. Per this system, a mass is described based on its shape, posterior acoustic features (does the mass shadow or enhance?), and internal echo pattern (is the mass hyper-, hypo-, or iso-echoic comparing its brightness to the surrounding subcutaneous fat, internal reference point). For instance, malignant tumors usually have spiculated margins, an irregular shape, hypo-echogenicity, shadowing, duct extension, and an alignment that is nonparallel to the surrounding tissue layers. On the contrary, benign tumors more often have circumscribed margins, an oval shape, gentle bi- or tri-lobulations and parallel orientation.<sup>9</sup> The BIRADS lexicon descriptors provide a final classification scheme which assigns the lesion to one of seven different groups. Such standardization helps improve patient care by implementing common terminology for diagnostic descriptions and thus, leads to proper follow-up tests and procedures.<sup>10</sup> However, some cases are still ambiguous to the US BI-RADS lexicon, and this limits its effectiveness in describing a mass. For instance, the two tumors presented in Figure 1.2 (a fibroadenoma and a carcinoma) are both described by the same BI-RADS descriptors (hypo-echoic and shadowing).

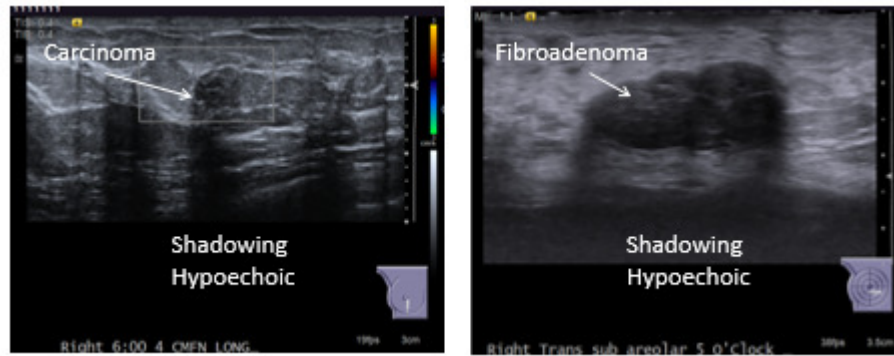


**Figure 1.2.** Clinical images of a fibroadenoma and a carcinoma

Most US BI-RADS descriptors are subjective and qualitative; thus, inter-observer variability for some descriptors still are present.<sup>11-13</sup> Several studies have evaluated inter-observer variability when interpreting sonographic features of solid breast masses. Arger et al.<sup>14</sup> found that the interpretations of four different readers were comparable when standardized descriptors of breast masses were applied. Similarly, Rahbar et al.<sup>15</sup> found that ultrasound features can be effective when differentiating benign from malignant masses. However, the authors stressed that interpreter variability needs to be dealt with. Abdullah et al.<sup>16</sup> presented an evaluation of the assessments of 267 breast masses made by five radiologists who used the BIRADS terminology and showed that observers achieved only fair agreement in describing the margins of the lesion and low agreement in describing small masses, which limits the early detection and diagnostic power. Distinguishing benign from malignant breast masses by way of imaging tests continues to be an important medical challenge. Thus, increasing the specificity of pulse-echo ultrasound will increase its diagnostic power and can reduce the rate of biopsies with negative results. This could ultimately reduce the emotional distress of patients and the amount of resources and time devoted to the detection and diagnosis of breast cancer.<sup>17-18</sup>

### 1.3. Quantitative ultrasound

To overcome the low specificity of B-mode imaging, various methods of quantitative ultrasound (QUS) are being devised. QUS methods enable accurate, clinically-based estimates of acoustic properties of tissues by accounting for instrumentation and wave propagation dependencies that affect pulse-echo data. The quantification is based on the premise that the development of a disease often affects the regional cellular microenvironment. Therefore, tissue microstructure (glands, collagen bundles in connective tissue, etc.) suffers modifications in its mechanical properties. The goal of QUS is to estimate acoustic properties of tissue by providing system- and observer-independent parameters. This would reduce the subjectivity of the sonographic analysis and, therefore, increase its objectivity, and hopefully its specificity.<sup>19-20</sup>

QUS techniques and methods can be grouped into three general modalities: 1) backscatter-based QUS, 2) flow-based QUS (Doppler-shift based techniques used to study blood flow and vascularity in tumors), and 3) elasticity-based QUS (quantify the elastic and viscous properties of the tissue). The backscatter-based QUS extracts the information about the structural and physical properties of the tissue microstructure from the statistical analysis of the scattering process either in the time domain (deriving envelope statistics or carrying out image texture analysis) or in the frequency domain (using spectral analysis of the RF signals). It relies on models describing the interaction of the acoustic pulse with the underlying tissue to solve the inverse problem of estimating a tissue property by comparing a quantity measured in the ultrasound signals with a model for the physical interaction.

In QUS, the estimation of parameters starts with the selection of a region of interest (ROI) over which the parameter of interest will be analyzed. Within the ROI, a parameter estimation region (PER), defining an area used to estimate a parameter of interest, is selected. The PER

contains a set of segments of adjacent RF signals, which represent samples of the resolution cell volume. An ROI may contain one or many parameter estimation regions depending on the task to be performed. For example, estimating attenuation requires estimating the power loss as a function of depth among a sequence of power spectral density estimation regions (PSER) in a single PER for attenuation as shown in Figure 1.3. To create a parametric image, the PER is moved across the ROI to estimate the parameter in various spatial locations. Thus, a 2D array of local values of the parameter of interest is obtained and then color-encoded to create a final parametric image.

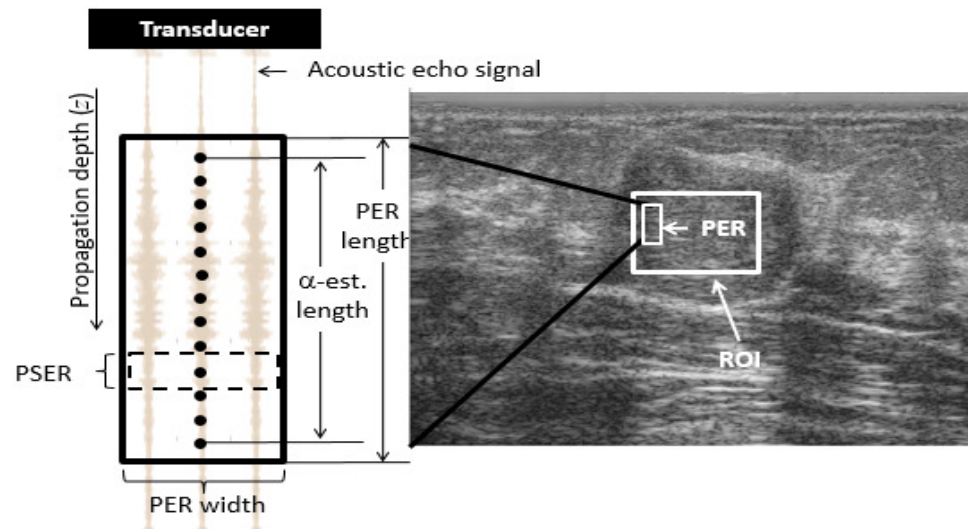


**Figure 1.3.** A region of interest (ROI) for parameter estimation was chosen within a B-mode image. That ROI was further partitioned into power spectrum estimation regions (PSER), and, depending on the parameter being estimated, data from one or more of those PSERs was used in a parameter estimation region (PER). For example, backscatter coefficient estimation was performed on each PSER, but estimating attenuation required estimating the power loss as a function of depth among a sequence of PSERs in a single PER. The dots signify the center of each PSER.

Researchers have demonstrated that QUS parameters have potential to provide important diagnostic information.<sup>21,22</sup> The most commonly estimated acoustic properties are the attenuation coefficient, which quantifies the spatial rate at which an ultrasound beam loses energy while traversing a tissue, and the backscatter coefficient (BSC), which is a material property that

quantifies the fraction of the ultrasound energy that is reflected back to the transducer. The attenuation coefficient is often reported in terms of the specific attenuation, ATT, which is the slope of the attenuation coefficient vs. frequency at a particular frequency. The BSC is parametrized in terms of the frequency-average BSC, ABSC, which quantifies echogenicity on an absolute scale, and the effective scatterer diameter, ESD, which is obtained by fitting a scattering model to the BSC vs. frequency and describes the spatial correlation function of echo signal sources.

Previous studies that investigated QUS breast imaging techniques produced promising results. For example, D'Astous and Foster<sup>23</sup> found that the attenuation coefficient and its frequency-dependence were different among infiltrating ductal cancer (IDC), breast parenchyma, and fat (3-8 MHz). They also found differences among these tissues in the magnitude and frequency-dependence of the backscatter coefficient (BSC). Further, they demonstrated that a 2-parameter analysis (attenuation and BSC) was sufficient to separate the 3 distinct tissue types they studied. More recently, Nam, et al.<sup>18</sup> demonstrated that estimates of the product of the acoustic attenuation coefficient and the lesion size (along the acoustic beam direction) correlated well with the assessment of the ultrasound BI-RADS<sup>®</sup> descriptor 'posterior acoustic features'. Although nearly all tumors in their study were classified as 'hypoechoic' (relative to nearby fat; internal clinical reference point), most cancers had lower average BSC estimates than fibroadenomas. Tadayyon et al. and Sannachi et al.<sup>24,25</sup> also demonstrated the potential of using QUS for evaluation of locally advanced breast cancers. Using a set of QUS parameters, they were able to differentiate between histologic Grade 1 versus Grades II and III tumors with 86% accuracy, and their QUS parameters could provide early measures of tumor response to neoadjuvant chemotherapy, in as little as one week after treatment began. Attenuation, which has been studied in the breast,<sup>15, 18, 23-</sup>

<sup>26</sup> was also used to differentiate fatty from normal liver<sup>27, 28</sup> and to detect changes in bone.<sup>29-30</sup> Spectral analysis of echo signals has also been used to differentiate between benign and malignant masses in the eye<sup>31</sup> and between normal and cancerous lymph nodes.<sup>32-33</sup> It also has been used to estimate cancer probability to guide biopsies in the prostate.<sup>34</sup> The ESD, derived from backscattered echo signals has been used to monitor changes in glomerular and arteriole sizes in kidneys.<sup>35-36</sup> More recently, Oelze et al.,<sup>37</sup> showed that the ESD can be used to differentiate rat mammary fibroadenomas from 4T1 mouse carcinomas. Other investigators have implemented different approaches to breast QUS that do not provide system-independent results. For example, Garra et al.<sup>38</sup> digitized the video output of an ultrasound scanner and analyzed the statistics of the B-mode image texture of breast scans. Although their patient population was small, they used low frequency (5 and 7.5 MHz) transducers, and they had comparatively poor-quality data, they could correctly identify 78% of the fibroadenomas, 73% of the cysts, and 91% of the fibrocystic nodules while maintaining high sensitivity for cancer. Using similar data acquisition, image texture parameters and an artificial neural network, Chen et al.<sup>39</sup> obtained a diagnostic accuracy of 95%, demonstrating that measures of texture statistics have merit for differentiating among breast diseases. Texture statistics vary because of variations in frequency-dependent scattering (BSC, ESD, and ESD heterogeneity index, as well as system-dependent functions). Thus, the success of these techniques may carry over to system-independent breast QUS techniques.

The purpose of this dissertation is to optimize QUS methods, to improve the specificity and objectivity of breast ultrasound. QUS derives estimates of acoustical properties of tissue, such as the attenuation coefficient and the backscatter coefficient, by computing echo signal power spectra and applying algorithms that account for transducer and system dependencies of the echo data. However, inhomogeneous tissue paths to the region of interest and the presence of echo

sources within this region that depart from diffuse and stationary scattering conditions assumed in the power spectra determinations can bias these estimates. We believe that recently described signal processing approaches, including techniques that evaluate for any coherent scattering in an echo signal wave train, can better characterize this complex tissue.

Until now our QUS applications in human breast have been applied to 2D data obtained using conventional, handheld array transducers. Thus, only data from select acquisition planes are acquired and processed. New 3D ultrasound breast imaging technology being introduced for B-mode imaging, can help overcome this limitation. Application of 3D acquisitions in QUS would provide a unique capability to acquire and process data from the entire breast volume. Our hypothesis is that extending current QUS technology from 2D to 3D acquisitions will improve performance and further improve the specificity of breast ultrasound.

To address these issues, we were guided by the following specific aims:

1. Optimize 2D QUS methods as they apply to breast diagnosis. In QUS parameter estimation, the region of interest is assumed to be homogeneous and of adequate size (>5 mm in diameter), the echo signals within a parameter estimation region are assumed to be from a stationary random process, and scattering is assumed to be incoherent. These assumptions frequently are not met in the human tissue. Our plan was to overcome these QUS parameter estimation limitations with the following sub-aims:
  - a. Test for sources of coherence within power spectrum estimation regions, and examine potential for anisotropy in acoustic parameters. We tested for the presence of echo signal coherence in *in vivo* breast tumors. We also developed methods to test for isotropic scattering properties which, if present, would justify the use of spatial compounding for reduced parameter estimate variance.

- b. Evaluate a new, “modified least squares” algorithm for computing attenuation compensation over complex overlying tissue paths between the transducer and the region of interest within a breast mass. An existing least squares technique yields an “effective attenuation coefficient” along the acoustic path, and a backscatter coefficient within the ROI, but assumes that attenuation is proportional to frequency. The modified method developed here accounts for the more common condition in which the attenuation follows a power law frequency dependence.
2. Implement 3-D QUS in the breast. A group of subjects were scanned with an “automated breast volume scanner” (Siemens Acuson ABVS), acquiring raw (RF) echo data in 3D. QUS algorithms that showed promise in distinguishing fibroadenomas from carcinomas in 2D were adapted and tested using phantoms to analyze 3D data sets provided by this system. The purpose here was to explore a systematic extension of current methods from 2D data acquisition and analysis to 3D in an attempt to introduce unique image planes and to better characterize tumor heterogeneity.
3. Compare 2D vs 3D QUS in the breast. We compared QUS parameter estimates obtained from human subjects scanned using the 18L6 transducer with those obtained from the ABVS scanner for subcutaneous fat and for any lesion that might present.

This dissertation is organized as follows: Chapter 1 introduced the rationale behind the use of quantitative ultrasound. Chapter 2 presents a description of QUS methods utilized to estimate the specific attenuation, the backscatter coefficient, an effective scatterer diameter, and an effective scatterer diameter heterogeneity index. It also contains a description of data acquisition for the later chapters. Chapter 3 presents the acoustic properties of subcutaneous breast fat (internal clinical reference point) for *in vivo* human subjects. Chapter 4 presents a description of the

“modified least squares method” for compensation of attenuation over an inhomogeneous tissue path. Chapter 5 presents results of tests for the presence of echo signal coherence in *in vivo* breast tumors and for isotropic scattering properties which, if present, would justify the use of spatial compounding. Chapter 6 presents a Bayesian classifier to distinguish breast masses. Chapter 7 presents a systematic extension of current methods from 2D data acquisition and analysis to 3D allowing for presentation in unique image planes. We also compare QUS parameter estimates obtained from 2D data with those obtained from the 3D data for *in vivo* subcutaneous breast fat, and for any lesion that might present. Finally, Chapter 8 discusses contributions and future work. Appendix A includes summary of reproducibility of the QUS estimates and Appendix B includes additional examples for *in vivo* breast fat and masses.

## 1.4. References

1. American Cancer Society, "Breast cancer: Detailed guide: Key statistics." [Online].  
Available: <http://www.cancer.org/cancer/breastcancer/detailedguide/breast-cancer-key-statistics>.
2. American Cancer Society, "Breast cancer prevention and early detection." [Online].  
Available: <http://www.cancer.org/>
3. Gordon, P.B.; Goldberg, S.L., Malignant breast masses detected only by ultrasound. A retrospective review. *Cancer* **1995**, *76*, 626-630.
4. Kaplan, S.S., Clinical utility of bilateral whole-breast US in the evaluation of women with dense breast tissue. *Radiology* **2001**, *221*, 641-664.
5. Kolb, T.M.; Lichy, J.; Newhouse, J.H., Comparison of the performance of screening mammography, physical examination, and breast US and evaluation of factors that influence them: an analysis of 27,825 patient evaluations. *Radiology* **2002**, *225*, 165-175.
6. Buchbeger, W.; Nichoff, A.; Obrist, P.; Dekoekkoek-Doll, P.; Dunser, M., Clinically and mammographically occult breast lesions: detection and classification with high resolution sonography. *Semin Ultrasound CT MR* **2000**, *21*, 325-336.
7. Crystal, P.; Strano, S.D.; Shcharynski, S.; Koretz, M.J., Using sonography to screen women with mammographically dense breasts. *AJR Am J Roentgenol* **2003**, *181*, 177-182.
8. Berg, W.A.; Blume, J.D.; Cormack, J.B.; Mendelson, E.B., Operator dependence of physician-performed whole breast US: Lesion detection and characterization. *Radiology* **2006**, *241*(2), 355-365.

9. Sehgal, C.M.; Weinstein, S.P.; Arger, P.H.; Conant, E.F., A review of breast ultrasound. *J Mammary Gland Biol Neoplasia* **2006**, *11*, 113-123.
10. American College of Radiology. BI-RADS: Ultrasound, 1<sup>st</sup> ed. In: Breast imaging reporting and data system: BI-RADS atlas, 4<sup>th</sup> ed. Reston, Virginia: American College of Radiology; **2003**.
11. Baker, J.A.; Kornguth, P.J.; Soo, M.S.; Walsh, R.; Mengoni, P., Sonography of solid breast lesions: observer variability of lesion description and assessment. *Am J Roentgenol* **1999**, *172*, 1621-1625.
12. Lazarus, E.; Mainiero, M.B.; Schepps, B.; Koelliker, S.L.; Livingston, L.S., BI-RADS Lexicon for US and Mammography: Interobserver Variability and Positive Predictive Value. *Radiology* **2006**, *239*(2), 385-391.
13. Berg, W.A.; Blume, J.D.; Cormack, J.B.; Mendelson, E.B., Operator dependence of physician-performed whole breast US: Lesion detection and characterization. *Radiology* **2006**, *241*(2), 355-365.
14. Arger, P.H.; Sehgal, C.M.; Conant, E.F.; Zuckerman, J.; Rowling, S.E.; Patton, J.A., Interreader variability and predictive value of US descriptions of solid breast masses: pilot study. *Acad Radiol* **2001**, *8*, 335-342.
15. Rahbar, G.; Sie, A.C.; Hansen, G.C.; Prince, J.S.; Melany, M.L.; Reynolds, H.E.; Jackson, V.P.; Sayre, J.W.; Bassett, L.W., Benign versus malignant solid breast masses: US differentiation. *Radiology* **1999**, *213*, 889-894.
16. Abdullah, N.; Mesuroelle, B.; El-Khoury, M.; Kao, E.; Breast Imaging Reporting and Data System Lexicon for US: Interobserver agreement for assessment of breast masses, *Radiology*, **2009**; *252*, 665-672

17. Oelze. M.; Quantitative ultrasound techniques and improvements to diagnostic ultrasonic imaging, *IEEE International Ultrasonics Symposium Proceedings*, **2012**, 232-239
18. Nam, K.; Zagzebski, J.; Hall, T.; Quantitative assessment of in vivo breast masses using ultrasound attenuation and backscatter, *Ultrason. Imaging*, **2013**; 35, 147-162
19. Thijssen J.; Ultrasonic speckle formation, analysis and processing applied to tissue characterization, *Pattern Recognition Letters*, **2003**; 24, 659-675
20. Insana, M.; and Brown DG, Acoustic scattering theory applied to soft biological tissues, in *Ultrasonic Scattering in Biological Tissues*, Eds. *KK Shung and GA Thieme*, CRC Press: Boca Raton, FL, **1993**
21. J. J. Anderson, M.-T. Herd, M. R. King, A. Haak, Z. T. Hafez, J. Song, M. L. Oelze, E. L. Madsen, J. A. Zagzebski, W. D. O'Brien et al., "Interlaboratory comparison of backscatter coefficient estimates for tissue-mimicking phantoms," *Ultrasonic imaging*, vol. 32, no. 1, pp. 48–64, 2010.
22. K. Nam, I. M. Rosado-Mendez, L. A. Wirtzfeld, G. Ghoshal, A. D. Pawlicki, E. L. Madsen, R. J. Lavarello, M. L. Oelze, J. A. Zagzebski, W. D. OBrien et al., "Comparison of ultrasound attenuation and backscatter estimates in layered tissue-mimicking phantoms among three clinical scanners," *Ultrasonic imaging*, vol. 34, no. 4, pp. 209–221, 2012.
23. D'Astous, F.; Foster, F.; Frequency dependence of ultrasound attenuation and backscatter in breast tissue, *Ultrason Med. & Biology*, vol. 12, no. 2, **1986**; 795–808.
24. Tadayyon, H.; Sadeghi-Naini, A.; Czarnota, G.; Noninvasive characterization of locally advanced breast cancer using textural analysis of quantitative ultrasound parametric images, *Translational Oncology*, vol. 7, no. 6, **2014**; 759–767.

25. Sannachi, L.; Tadayyon, H.; Sadeghi-Naini, A.; Tran, A.; Gandhi, S.; Wright, F.; Oelze, M.; Czarnota, G.; Non-invasive evaluation of breast cancer response to chemotherapy using quantitative ultrasonic backscatter parameters, *Medical Image Analysis*, vol. 20, no. 1, **2015**, 224–236.
26. Golub, R.M.; Parsons, R.E.; Sigel, B.; Feleppa, E.J.; Justin, J.; Zaren, H.A.; Rorke, M.; Sokil-Melgar, J.; Kimitsuki, H., Differentiation of breast tumors by ultrasonic tissue characterization. *J Ultrasound Med* **1993**, 12(10), 601-608.
27. Fujii, Y.; Taniguchi, N.; Itoh K; Shigeta, K.; Wang, Y.; Tsao, W.; et al., A new method for attenuation coefficient measurement in the liver: comparison with the spectral shift central frequency method. *J Ultrasound Med*, **2002**, 21(7), 783–788.
28. Narayana, A.; Ophir, J.; On the frequency dependence of attenuation in normal and fatty liver, *IEEE Trans. Son. Ultrason.* **1983**, SU-30, 379–383.
29. Wear, K.A. Characterization of trabecular bone using the backscattered spectral centroid shift. *IEEE Trans Ultrason Ferroelectr Freq Control*, **2003**, 50(4), 402-407.
30. Sasso, M.; Haiat, G.; Yamato, Y.; Naili, S.; Matsukawa, M., Dependence of ultrasonic attenuation on bone mass and microstructure in bovine cortical bone. *J Biomech* **2008**, 41(2), 347-355.
31. Liu, T.; Lizzi, F.L.; Silverman, R.H.; Kutcher, G.J., Ultrasonic tissue characterization using 2-D spectrum analysis and its application in ocular tumor diagnosis. *Med Phys* **2004**, 31(5), 1032-1039.
32. Feleppa, E.J.; Machi, J.; Noritomi, T.; Tateishi, T.; Oishi, R.; Yanagihara, E.; Jucha, J., Differentiation of Metastatic from benign lymph nodes by spectrum analysis in vitro. *Proc IEEE Ultrason Symp* **1997**, 2, 1137-1142.

33. Mamou, J.; Coron, A.; Hata, M.; Machi, J.; Yanagihara, E.; Laugier, P.; Feleppa, E.J., Three-dimensional high-frequency characterization of excised human lymph nodes. *Proc IEEE Ultrason Symp* **2009**, 45-48.
34. Feleppa, E.J.; Urban, S.; Kalisz, A.; Lizzi, F.L.; Fair, W.R.; Porter, C.R., Advanced ultrasonic imaging of the prostate for guiding biopsies and for planning and monitoring therapy. *Proc IEEE Ultrason Symp* **2000**, 2, 1399-1403.
35. Insana M.; Wood J.; Hall T.; Identifying Acoustic Scattering Sources In Normal Renal Parenchyma In Vivo By Varying Arterial And Ureteral Pressures, *Ultrasound Med Biol*,**1992**; 18(6/7): 587-599.
36. Hall T.; Insana M.; Harrison L.; Cox G.; Ultrasonic measurement of glomerular diameters in normal adult human. *Ultrasound Med Biol* **1996**; 22(8):987-997.
37. Oelze, M.L.; O'Brien, W.D.; Blue, J.P.; Zachary, J.F., Differentiation and characterization of rat mammary fibroadenomas and 4T1 mouse carcinomas using quantitative ultrasound imaging. *IEEE Trans Med Imaging* **2004**, 23(6), 764-771.
38. Garra, B.; Krasner, B.; Horii, S.; Ascher, A.; Mun, S.; Zeman, R.; Improving the distinction between benign and malignant breast lesions: the value of sonographic texture analysis, *Ultrasonic Imaging*, **1993**, 15(4), 267–285.
39. Chen, J.; Zagzebski, J.; Madsen, E.; et al., Tests of backscatter coefficient measurement using broadband pulses, *IEEE Transactions on Ultrasonics, Ferroelectrics, and Frequency Control*, **1993**, 40(5), 603–607.

## Chapter 2: 2D Quantitative Ultrasound (QUS) Methods

This research focuses on the backscatter-based QUS, which relies on models describing the interaction between an acoustic pulse emitted by a transducer and the underlying tissue. The short acoustic pulse emitted from the surface of the ultrasound probe transverses the tissue, and a part of its energy is absorbed as thermal energy.<sup>1</sup> This process affects the amplitude and the frequency content of the acoustic pulse. The pulse interacts instantaneously with structures within a volume of the tissue, referred to as the resolution cell, which is defined laterally and elevationally by the size and the shape of the transducer's aperture and axially by the number of cycles and the wavelength of the pulse.<sup>2-4</sup> An echo is generated within the resolution cell if there is a local change in the acoustic impedance, which may be manifested by microscopic heterogeneities (scatterers)<sup>5</sup> or by large interfaces. Such heterogeneities will elastically re-irradiate a scattered wave with a frequency content depending on the incident pulse and the tissue microstructures. The most commonly estimated acoustic properties are the specific attenuation coefficient (ATT), which quantifies the spatial rate at which an ultrasound beam loses energy while traversing a particular tissue, the backscatter coefficient (BSC), which is a material property that quantifies "echogenicity" on an absolute scale, and an effective scatter diameter (ESD), which is a method to quantify the frequency-dependence of the BSC and describe the spatial correlation function for the echo signal sources.

Our laboratory has joined efforts with other laboratories and demonstrated the possibility of estimating system-independent specific attenuation coefficients and backscatter coefficients in tissue mimicking phantoms and rodent models of breast tumors.<sup>6-8</sup> Once the echo signal data were acquired, offline analysis was performed using MATLAB (Mathworks, Natick, MA) to estimate the QUS parameters of interest. Echo signal power spectra were calculated as a function of depth

for data segments within the region of interest. Power spectra are typically computed by averaging periodograms within windowed regions of the RF echo signal whose axial extent were about 3-5mm. To calculate power spectra, 4 mm x 4 mm power spectrum estimation regions (PSER), overlapping by 75% both axially and laterally, were defined. For each RF line within the PSER, the Fourier transform was computed using a multi-taper technique with a time-half bandwidth product (NW) of 4.<sup>8-9</sup> The results for beam lines within the PSER were then averaged.

## **2.1. The Reference Phantom Method (RPM)**

The RPM developed by Yao et al.<sup>10</sup> is widely used to obtain estimates of the attenuation coefficient and the backscatter coefficient from data obtained with array-based ultrasound imaging systems. In this method, a well-characterized reference phantom with independently-measured sound speed, attenuation coefficients, and backscatter coefficients throughout the frequency range of interest is scanned immediately after scanning the subject. Faran's scattering theory, introduced in 1951, was applied to predict the backscatter coefficients in the phantom (with glass sphere scattering sources) used in this study.<sup>11</sup> Faran's scattering theory for spheres was tested by various researches who showed that the measured backscatter coefficients agreed with predicted values.<sup>12;13;14;15;16;17;18</sup> To predict the scattering cross section of the phantom, the first twenty-five terms of the Faran model were used. The inputs to the model include the sphere diameter distribution, the number of spheres per unit volume, the Poisson's ratio of the spheres, the speed of sound of both the spheres and the surrounding background material, and the mass density of the spheres and the background material. The reference phantom is used to account for system-dependent factors, including diffraction. The RPM method was tested in multiple research studies and demonstrated good agreement between theory and experiments as well as agreement among

different imaging systems.<sup>6-8</sup> The RPM requires a stationary random process and an adequate size for the PER ( $> 5\text{mm} \times 5\text{mm}$ , when scanning with the 18L6 linear array transducer, and 10 MHz center frequency) to get reliable parameter estimates. It is most applicable for diffuse or incoherent scattering conditions. This means that the number of scatterers within each resolution cell is large, and their positions are random. RPM utilizes the ratio of the echo signal power spectra from the tissue to the power spectra from the same depth in the reference phantom as shown in Figure 2.1

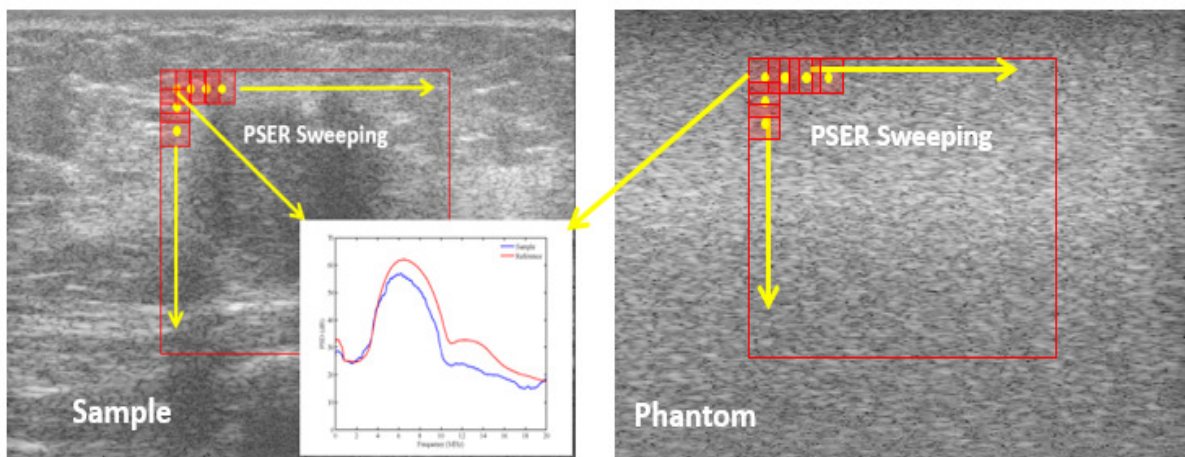


**Figure 2.1.** Example of the RPM application where a region of interest (ROI) for parameter estimation was chosen within a B-mode image. That ROI was further partitioned into power spectrum estimation regions (PSER) and the ratio of the echo signal power spectra from the tissue to the power spectra from the same depth in the reference phantom was used. (Note that we need to be least one (elevation) aperture away to avoid complex nearfield beam patterns).

The power spectrum of the backscattered RF echo signals using the first-order Born approximation (assuming scattering from soft tissue is weak enough to ignore multiple scattering), and provided that the distance from the transducer to the region of interest (ROI) is greater than the transducer aperture can be written as,<sup>10</sup>

$$S(f, z) = G(f, z) \cdot D(f, z) \cdot A(f, z) \cdot B(f) \quad (2-1)$$

where,  $f$  denotes frequency and  $z$  represents the depth of the PER.  $S(f,z)$  is the power spectrum of the backscattered echo signal,  $B(f)$  is the backscatter coefficient (BSC; assumed to be homogeneous) vs. frequency within the PER.  $G(f,z)$  represents the combined effects from transmitting and receiving with a transducer and depends on such factors as the transducer design, pulsing characteristics and receiver gain.  $D(f, z)$  accounts for diffraction effects.  $A(f, z)$  represents the total attenuation over the path from the transducer surface to the depth of interest.

Thus, for uniform samples, the ratio of the echo signal power spectrum from a sample to that from a reference medium can be described as:

$$\frac{S_{sam}(f, z)}{S_{ref}(f, z)} = \frac{G_{sam}(f, z)D_{sam}(f, z) B_{sam}(f) \exp(-4\alpha_{sam}(f)z)}{G_{ref}(f, z)D_{ref}(f, z) B_{ref}(f) \exp(-4\alpha_{ref}(f)z)} \quad (2-2)$$

where, the subscripts *sam* and *ref* denote the sample and reference medium respectively. The total attenuation  $A(f,z)$  in Eq. (2-1) is modeled as  $\exp(-4\alpha(f)z)$ , where  $\alpha(f)$  is the attenuation coefficient in the medium.

Assuming that the speed of sound is approximately the same in the sample and the reference, and that for array systems, the speed of sound used in the system beam-former (electronic focusing system) is the same as that of the sample and reference medium. The above equation can be simplified to

$$RS(f, z) = \frac{S_{sam}(f, z)}{S_{ref}(f, z)} = \frac{BSC_{sam}}{BSC_{ref}} \exp(-4(\alpha_{eff, sam}(f) - \alpha_{ref}(f))z) \quad (2-3)$$

where  $RS(f, z)$  represents the ratio of the power spectra from the sample and reference,  $\alpha_{eff, sam}$  is the effective attenuation in the sample (the average of the sample attenuation coefficient  $\alpha_{sam}(f, z)$  considering all intervening tissues) down to a depth  $z$ , such that:

$$\alpha_{eff, sam}(f) = \frac{1}{z} \int_0^z \alpha_{sam}(f, z') dz' \quad (2-4)$$

## 2.2. Specific Attenuation estimation (ATT)

The reduction in the amplitude of the ultrasound wave as it propagates through the tissue is referred to as attenuation. This reduction is a function of frequency and propagation distance and thus, it can provide useful diagnostic information and can lead to a better interpretation of B-mode images. Attenuation estimation is performed using the backscattered echo signals that arise from scatterers within the ROI. Attenuation measurements have been done by many researchers either in the frequency domain or in the time domain. Although time-domain techniques are easier to implement and faster than frequency-domain techniques, their use results in difficulties in compensating for local variations (i.e., diffraction effects) in the ultrasound field along the beam propagation path. Thus, more frequency-domain techniques have been investigated and developed. The two fundamental approaches to estimate the attenuation in the frequency domain are the spectral difference method and the spectral shift method. In this thesis, we will focus on the spectral difference method to track the reduction of the echo signal power spectra along the beam propagation path assuming that the scattering properties (i.e., the backscatter coefficient) of the sample are unchanged over the PER. The ATT is estimated using the RPM, where a rectangular parameter estimation region is identified as mentioned before and the echo signal power spectra are calculated as a function of depth for data segments within this region for both the sample and the reference. For a homogenous parameter estimation region, assuming linear frequency dependence for attenuation, the ratio of the echo signal power spectrum from the sample to the power spectrum of echoes from the reference phantom is given by:<sup>10</sup>

$$RS(f, z) = \frac{S_{sam}(f, z)}{S_{ref}(f, z)} = \frac{b_{sam} f^{n_{sam}}}{b_{ref} f^{n_{ref}}} \exp(-4(\alpha_{eff,sam}(f) - \alpha_{ref}(f))z) \quad (2-5)$$

where, the term  $b f^n$  represents the backscatter coefficient, modeled here as a power law in frequency for both media. The maximum frequency band that was at least 10 dB above the noise floor was selected.

Yao et al.<sup>10</sup> showed that the log of the ratio of the echo signal power spectrum from the sample to that of the reference, vs. depth, can be fit to a straight line. The slope of this line is proportional to the difference in attenuation coefficients between the sample and the reference phantom at the frequency analyzed. Since the attenuation and backscatter coefficients of the reference are known, then the attenuation and the backscatter coefficients of the sample can be determined using RPM equations.

$$\alpha_{sam}(f) = -\frac{\ln\left(\frac{S_{sam}(f, z)}{S_{ref}(f, z)}\right)\Big|_{z_2} - \ln\left(\frac{S_{sam}(f, z)}{S_{ref}(f, z)}\right)\Big|_{z_1}}{4(z_2 - z_1)} + \alpha_{ref}(f), \quad (2-6)$$

where,  $z_1$  and  $z_2$  are depths of PSER<sub>1</sub> and PSER<sub>2</sub>, and  $z_2 > z_1$ .

The specific attenuation coefficient<sup>19</sup>, ATT, was estimated from the local attenuation coefficient  $\alpha_{sam}(f, z)$ , i.e., the attenuation coefficient of the tissue within a single PER centered at depth  $z$  within the ROI (Fig. 1.1). Assuming that attenuation and backscatter are constant within the PER,  $\alpha_{eff, sam} = \alpha_{sam}$ . Thus,  $\alpha_{sam}(f, z)$  is obtained by quantifying the local rate of change of the power spectrum ratio as a function of depth at each frequency.<sup>5</sup> ATT is obtained from the slope of a linear fit to the local attenuation vs. frequency, i.e.,  $\alpha_{sam}(f) = ATT \times f$ .<sup>13</sup>

### 2.3. Backscatter Coefficient (BSC) estimation

The BSC is defined as the differential scattering cross section per unit volume for a scattering angle of 180°. Similar to attenuation estimations, the BSCs were estimated as a function

of frequency using the Reference Phantom Method<sup>10</sup> applied to the RF echo signals. However, since the power spectrum is calculated using a gating window of finite length, proper attenuation correction is necessary (especially if the medium has a large attenuation coefficient and a long gating window is used) before estimating the BSC.

The reference phantom method developed by Yao et al.<sup>10</sup> exhibits high accuracy in estimating QUS parameters when the ROI is homogenous. However, this approach can induce bias in correcting for the attenuation along the path from the transducer to the PER when the tissue is inhomogeneous. Attenuation compensation has been studied by a variety of researchers. A simple approach assumed a constant value for the attenuation and used that value to account for losses in signal amplitude with depth. A slightly more sophisticated approach was to measure the thickness of each tissue layer in the path and use published values for attenuation coefficients in each material to account for attenuation, as Wear, et al. did.<sup>22</sup> Lu et al.<sup>23</sup> proposed a dual spectrum method to measure an effective attenuation coefficient of body wall in liver assuming unchanging frequency dependence over the frequency analysis range.

Nam et al.<sup>24</sup> proposed a least squares method to estimate the effective attenuation between the ultrasound transducer and the PSER using power spectrum of RF echo signals from the sample and a reference phantom, and fit the ratio to 3-parameter model that quantifies the attenuation and backscatter properties of the media. The least squares method enables the determination of attenuation when the path is acoustically non-uniform, and has provided accurate measurements of the total attenuation and the backscatter coefficient versus frequency.<sup>24</sup> However, the least squares method assumes a linear relationship between attenuation and frequency, which can reduce the accuracy of the method if this assumption is invalid. Recent experiments<sup>7</sup> suggest that the attenuation coefficient for breast tissue likely is not linearly proportional to frequency. To take this

into consideration, a modification of the Nam method, termed the “Modified Least Squares Method” (MLSM), was applied in this study and is discussed in detail in Chapter 4.

Estimation of the BSC using the RPM technique requires knowledge of the intervening tissue effective attenuation  $\alpha_{\text{eff, sam}}$ . Applying the MLSM leads to a power law fit to values of  $\alpha_{\text{eff, sam}}$  from overlapping bandwidths to describe the frequency dependence of  $\alpha_{\text{eff, sam}}$ . Once  $\alpha_{\text{eff, sam}}$  is estimated for each PER, the BSC for that PER is estimated as a function of frequency using the RPM, by multiplying the BSC of the reference phantom with the ratio of the attenuation-corrected power spectrum from the sample to that of the reference as follows:

$$BSC_{\text{sam}}(f) = \frac{S_{\text{sam}}(f, z) \exp(4(\alpha_{\text{eff, sam}}(f))z)}{S_{\text{ref}}(f, z) \exp(4(\alpha_{\text{ref}}(f))z)} Bsc_{\text{ref}}(f) \quad (2-7)$$

where the variables were defined in Eqns. 2-3 – 2-6.

For each subject, an average backscatter coefficient (ABSC) was computed by averaging the BSC over the frequency bandwidth used for attenuation coefficients providing an objective estimate of “echogenicity”.

## 2.4. Effective Scatter Diameter (ESD) estimation

An “effective scatter diameter” (ESD) is estimated over regions of interest to characterize the frequency dependence of scattering. Conventional B-mode processing computes the envelope of the radiofrequency echo signal to modulate the intensity of the display, ignoring the phase information in the echo signal. However, there is important information in both the magnitude and the frequency dependence of the signal that can provide insight about the characteristic of a tumor.<sup>26-27</sup>

The ESD is a parameterization for a model for the spatial correlation function of the inhomogeneities in the medium.<sup>5</sup> Based on the single-scattering theory,<sup>27</sup> the form factor connects

the BSC and the correlation function for the medium. The BSC function, for a sparse media when scattering is weak can be expressed in terms of the spatial correlation function for acoustic impedance inhomogeneities as:<sup>29</sup>

$$BSC(k) = Ck^4 \int_{-\infty}^{\infty} b_{\gamma}(\Delta\mathbf{r}) e^{-i2\mathbf{k}\cdot\Delta\mathbf{r}} d\Delta\mathbf{r}, \quad (2-8)$$

where, C is independent of frequency and represent a combination of tissue properties and experimental parameters.  $\mathbf{k}$  is the scattering vector (points in the direction of insonification with magnitude equal to the wave number).  $b_{\gamma}(\Delta\mathbf{r})$  is the correlation function of the medium, which is assumed to be statistically stationary.

The acoustic form factor is proportional to the Fourier transform of the correlation function, and describes the size, geometry, and organization of the scatterers<sup>5</sup>. The acoustic form factor F is defined as a ratio of the backscatter coefficient for a test material having scatterers of finite size to that of similar material containing point scatterers

$$F(2k) = \sigma_b / \sigma_0 \quad (2-9)$$

where,  $k$  is the wave number,  $\sigma_b$  is the backscatter coefficient of the test material, and  $\sigma_0$  is the backscatter coefficient of a similar material consisting of point scatterers.

The common form factor models are the fluid sphere, spherical shell, exponential, and Gaussian models. This approach works best when  $0.6 < ka < 1.2$  ( $a$  is the scatterer radius). For biological tissue, we assume scattering occurs from a continuously varying impedance distribution. Thus, a Gaussian model is often used to study scattering structures of biological tissue.<sup>28, 31-32</sup>

The correlation function for a Gaussian model is<sup>5</sup>:

$$b_{\gamma}(\Delta\mathbf{r}) = e^{-\Delta r^2 / 2d} \quad (2-10)$$

where,  $d$  is a characteristic dimension of the correlation coefficient and the relationship between the effective scatterer radius and  $d$  is<sup>29</sup>:

$$2a = (12\sqrt{2\pi})^{1/3} d \approx 3.1d = d_1 d. \quad (2-11)$$

where,  $d_1$  is a constant depending on the form factor model.

Then, the BSC is given by<sup>29</sup>:

$$BSC(k) = C' k^4 e^{-2k^2 d^2} \quad (2-12)$$

Figure 2.2 show the BSC versus frequency and the acoustic form factor from the estimated BSC fitted to a Gaussian form factor model.

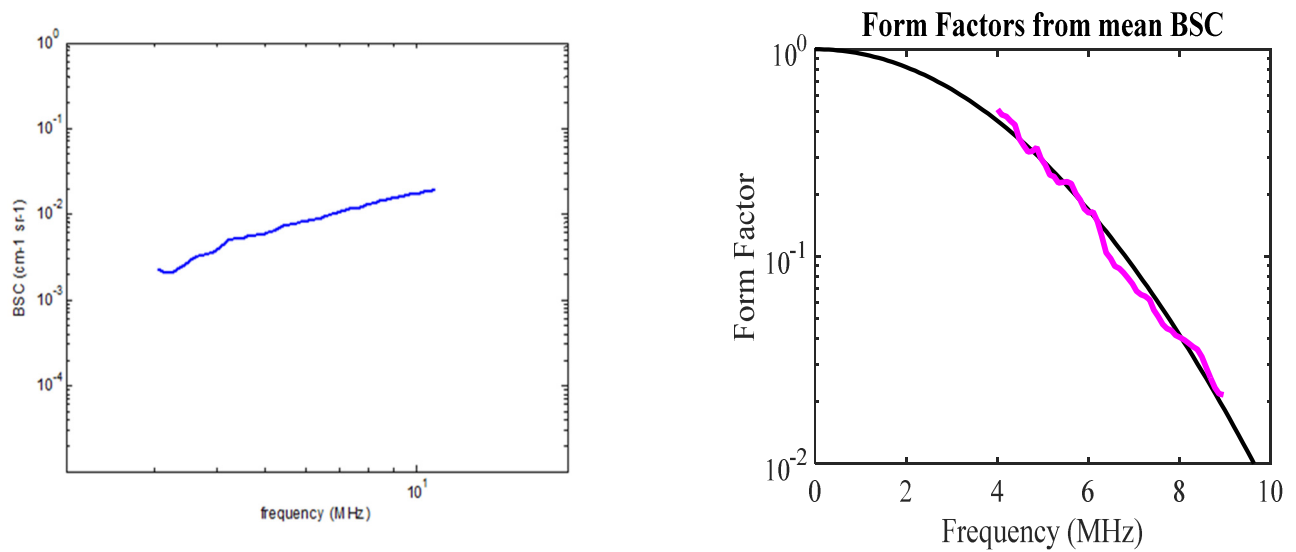


**Figure 2.2.** Example of the BSC and the form factor to predict the ESD

ESD is determined by comparing the frequency dependence of the estimated form factor with that of the form factor model.<sup>5</sup> For a Gaussian model, the ESD can be estimated as follows<sup>32-</sup>

$$\hat{a}^2 = \frac{-d_1^2 c^2 \sum_{\omega_{\min}}^{\omega_{\max}} (y(\omega)\omega^2 - \overline{y\omega^2})}{80 \sum_{\omega_{\min}}^{\omega_{\max}} (\omega^2 - \overline{\omega^2})^2} \quad (2-13)$$

where,  $y(\omega) = 10 \ln(BSC(\omega)/\omega^4)$ ,  $\omega$  represents angular frequency,  $c$  is the speed of sound, and  $d_1 = 3.1$  from Eq. (2-11).

## 2.5. Effective scatter diameter heterogeneity index (ESDHI)

### estimation

This newly introduced parameter ESDHI was used to characterize the spatial variability of ESD estimates among PERs (heterogeneity of the spatial correlation of acoustic impedance inhomogeneities) within the ROI. ESDHI was computed as the standard deviation of the ESD within the ROI, ignoring any spatial correlations among estimates from overlapping windows, as follows:<sup>34</sup>

$$\sigma = \sqrt{\frac{1}{N} \sum_{i=1}^N (x_i - \mu)^2} \quad (2-14)$$

where,  $N$  is number of PERs within the ROI,  $x_i$  is the ESD value for each PER and  $\mu$  is the mean of the ESD values.

## 2.6. Data Acquisition for in-vivo human subjects (2D study)

Radiofrequency echo data were acquired from 120 women scheduled for ultrasound-guided biopsies of previously detected breast tumors following a University of Wisconsin Institutional Review Board (IRB)-approved, Health Insurance Portability and Accountability Act (HIPAA)

-compliant protocol. These patients typically had screening and diagnostic mammograms and had a lesion sufficiently suspicious to warrant biopsy. The only specific exclusion criterion, other than age (at least 18 years old to provide informed consent) is that the lesion should be less than 20 mm in major dimension (half the width of the typical ultrasound field of view). We restricted the analysis to breast masses diagnosed by core biopsy as either fibroadenoma or carcinoma, and whose size was larger than 5 mm axially based on ultrasound images. This minimum lesion size restriction was imposed to limit the bias and the variance in the attenuation estimates.<sup>36</sup>

There were two subgroups of subjects. Fifty-one subjects were scanned using a custom elasticity imaging mode on a Siemens Antares (Siemens Medical Solutions USA, Inc., Malvern, Pennsylvania) equipped with a VFX13-5 linear array transducer (9 MHz center frequency). Radiofrequency echo signal data were recorded while the sonographer applied small deformations using the transducer, with an inter-frame axial strain of about 1%. Each frame consisted of either 256 or 312 acoustic scan lines. Echo signals also were recorded from a reference phantom using the same transducer and system settings.

The reference phantom was made with 6.4g of 3-45 $\mu$ m-diameter glass spheres homogeneously distributed in a 1600cc gel background. The background material consisted of an emulsion containing 70% safflower oil.<sup>36</sup> The acoustic attenuation and sound speed of this reference phantom (speed of sound of 1492 m/s at 2.5MHz and an attenuation coefficient from 2-10 MHz versus frequency slope of 0.54 dB $\cdot$ cm<sup>-1</sup> MHz<sup>-1</sup>) were measured on 2.5-cm thick test samples poured at the time of reference phantom fabrication. A narrowband through-transmission technique<sup>37</sup> was used to estimate sound speed and attenuation by transmitting 30-cycle acoustic pulses of different frequencies (2.5, 5, 7.5, and 10MHz) through the test cylinder

immersed in water. Acoustic pulses traversed the sample and reached a corresponding receiving transducer whose signal was read by a digital oscilloscope (500MHz, Model LT342, LeCroy, Chestnut Ridge, NY). The amplitude change and temporal shift of the detected waveforms, compared to waveforms recorded in the absence of the test cylinder, were used to determine the attenuation and the speed of sound of the material in the sample, respectively.

The same test cylinder was also used in laboratory measurements of backscatter coefficients for the phantom. Backscatter coefficients (BSCs) were measured using a broadband reference reflector method using single element focused transducers.<sup>40</sup> The test cylinder and the transducer were immersed in a tank of degassed water at room temperature. The transducer was connected to a pulse-receiver (Model 5052UA, Panametrics/Olympus, Waltham, MA). The test cylinder was placed at the focal plane of the transducer, and a set of RF echoes signals was acquired by automatically moving the sample (under stepper motor control; Aerotech Unidex 11 motion system, Aerotech, Inc, Pittsburg, PA) in a plane parallel to the surface of the test sample, at steps of 4mm. The RF echo signals were gated to consider only echoes from within the sample near the focal distance of the transducer. Echo signals from a planar interface (acrylic plate), were also acquired to account for the transmit-receive frequency response of the transducer-pulse-receiver system. Assuming a long duration gate (15 pulse-echo correlation lengths), the backscatter coefficient is given by the ratio of the square modulus of the Fourier transform of the gated RF signal averaged over all the collected signals, and divided by a term that accounts for the system's frequency response, the shape of the gating function, and the acoustic field integrated over the test cylinder volume.<sup>5</sup>

The second subgroup of subjects included sixty-nine women scanned using a Siemens S2000 system (Siemens Medical Solutions USA, Inc., Malvern, PA) with an 18L6 linear array

transducer (10 MHz center frequency). Subjects were scanned in a supine position in both radial and antiradial direction, and beams were steered from -10 to 10 degrees with an increment of 5 degrees as shown in Figure 1.4. The system was equipped with the Axius Direct Ultrasound Research Interface<sup>39</sup> that allowed acquisition of beam-formed RF echo signals following time-gain compensation but before envelope detection and post-processing. For each subject, multiple planes of RF data were collected, with the image plane centered on the mass and depicting surrounding subcutaneous fat. The transmit focus was placed below the mass, usually at approximately 6 cm. To minimize any effects of nonlinear propagation, the transmit power was well below its maximum setting, resulting in mechanical index (MI) values between 0.4-0.8 for these transmit focal depths.

Similarly, an equivalent reference phantom was scanned with the same transducer and system settings for these cases. The reference phantom material is an emulsion of 70% safflower oil immersed in a gelatin-water mixture composed of propylene glycol, deionized water, dry gelatin and 7.5 grams of Germall Plus<sup>®</sup> to preserve it. The phantom also contains 6.4 g of 3000E glass beads (Potter industries, Malvern, PA) per 1600 cc oil in gelatin emulsion. The volume of the phantom is about 1.6 liters and the mass density is 1.04 g/cm<sup>3</sup>. The tissue mimicking reference material was cast into an acrylic box with a 25 $\mu$ m-thick Saran<sup>™</sup> film scanning window (Dow Chemical, Midland MI, USA)

The sound speed of the reference phantom is 1492m/s at 2.5MHz; the attenuation coefficient vs. frequency,  $\alpha(f)$ , is represented by  $\alpha(f) = 0.54f$  dB/cm, where  $f$  is the frequency in MHz, and the backscatter coefficient at 5MHz is 1.37E-03cm<sup>-1</sup>sr<sup>-1</sup> and has been used by multiple researchers.<sup>39-44</sup>

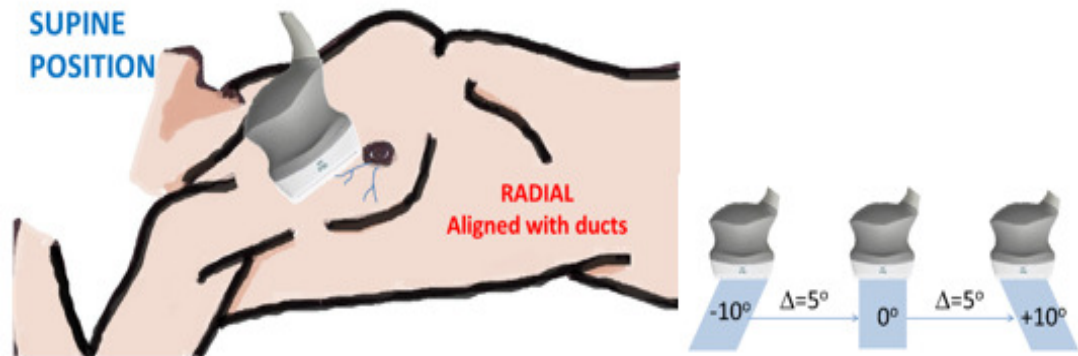


**Figure 2.3.** Diagram illustrate the scanning in supine position and beam steering

Since the scattering sources in the reference phantoms were tiny compared to the acoustic wavelength (the spatial correlation function for the scattering sources was effectively a delta function), the autocorrelation of the echo signals from the reference phantom provides a measure of the spatial resolution in B-mode imaging and QUS measurements. The axial and lateral correlation lengths when scanning with the 18L6 transducer at 10MHz for the zero-degree scan direction was assessed by imaging the reference phantom described. The width of the autocorrelation function at a correlation value of 0.2 for these conditions were 0.13 mm, (axial) and four adjacent acoustic scan lines, (lateral). In the axial direction, we define the “pulse echo correlation length” as the full width of the two-sided correlation function, i.e., twice the one-sided axial correlation length or 0.26mm. The lateral correlation length remained the same for the positive and negative 5 degree scans. The axial correlation length for the negative five degrees and positive five degrees’ scans (0.28 mm and 0.24 mm, respectively) was not significantly different from the zero-degree scan. These results suggest that data from small steering angles can be utilized to obtain more independent realizations of the echo signal power spectrum, as needed for small tumors.

## 2.7. Limitations to QUS Methods

Although current QUS methods perform well for straightforward cases (when the assumptions of stationarity and diffuse scattering are valid), QUS is more challenging when assumptions are violated due to the complicated nature of *in-vivo* breast tissue. Challenges related to the limited size of some masses (necessitating a small ROI), an acoustically inhomogeneous ROI, and a heterogeneous tissue path between the transducer and the ROI, all complicate the use of the RPM in evaluating breast masses.<sup>45</sup> Also, choosing a homogeneous ROI is complicated since this is totally subjective, may differ from one observer to the next, and some amount of signal coherence may be present due to the presence of periodic structures, low scatter density or strong isolated reflectors. This can affect the precision of estimation and limit the reproducibility of the results. Another challenge is the frequency dependence of attenuation, which is often assumed to be linear. However, recent studies suggest that for breast tissue the attenuation coefficient likely is not proportional to frequency.<sup>7</sup> Thus, attenuation could distort the spectral characteristics of the interrogating pulses and echo signals in an unexpected fashion. Also, acoustic properties within the tumor are typically assumed to be isotropic, and data from various angles can be averaged to reduce the variance of parameter estimates. However, anisotropy in attenuation estimates could introduce bias and variance in the QUS parameter estimates. Therefore, the next chapters address these challenges in order to optimize our QUS methods.

## 2.8. References

1. Insana, M.; Brown, D.; Acoustic scattering theory applied to soft biological tissues, in *Ultrasonic Scattering in Biological Tissues*, Eds. *KK Shung and GA Thieme*, CRC Press: Boca Raton, FL, **1993**
2. Fink, M.; Cardoso, J.; Diffraction effects in pulse-echo measurements, *IEEE Trans. Son. Ultrason.* **1984**; SU-31: 313-329
3. Wagner, R.; Smith, S.; Sandrik, J.; Lopez, H.; Statistics of speckle in ultrasound B-scans, *IEEE Trans. Sonics Ultrason.*, **1983**; 30, 157-164
4. Wagner, R.; Insana, M.; Brown, D.; Statistical properties of radio-frequency and envelope-detected signals with applications to medical ultrasound, *J. Opt. Soc. Am.*, **1987**; 4, 910-922
5. Insana, M.; Wagner, R.; Brown, D.; Hall, T.; Describing small-scale structure in random media using pulse echo ultrasound, *J. Acoust. Soc. Am.*, **1990**; 8, 180-192
6. Nam, K.; Rosado-Mendez, I.; Wirtzfeld, L.; et al. Ultrasonic attenuation and backscatter coefficient estimates of rodent tumor mimicking structures: comparison of results among clinical scanners. *Ultrason Imag.* **2011**; 33:233–50.
7. Wirtzfeld, L.; Nam, K.; Yassin, L.; et al., Techniques and Evaluation From a CrossPlatform Imaging Comparison of Quantitative Ultrasound Parameters in an In Vivo Rodent fibroadenoma Model, *IEEE Trans UltrasonFerroelectrFreq Control*, **2013**; 60(7)
8. Rosado-Mendez, I.; Nam, K.; Hall, T.; et al., Task-Oriented Comparison of Power Spectral Density Estimation Methods for Quantifying Acoustic Attenuation in Diagnostic Ultrasound Using a Reference Phantom Method, *Ultrason imaging* 35 (3), 214-234

9. Percival, D.; Walden, A.; Spectral Analysis for Physics Applications: Multitaper and Conventional Univariate Techniques. *New York, NY: Cambridge University Press; 1993.*
10. Yao, L.; Zagzebski, J.; Madsen, E.; Backscatter coefficient measurements using a reference phantom to extract depth-dependent instrumentation factors. *Ultrason Imaging* **1990**, 12, 58-7
11. Faran, J.; Sound scattering by solid cylinders and spheres. *J Acoust Soc Am* **1951**, 23, 405-418.
12. Zagzebski, J.; Lu, Y.;and Yao,L.;Quantitative ultrasound imaging: in vivo results in normal liver, *Ultrasonic imaging*, **1993**, 15(4) , 335–351.
13. Nam, K. ; Zagzebski, J.; Hall, T.;Quantitative assessment of in vivo breast masses using ultrasound attenuation and backscatter, *Ultrasonic imaging*, **2013**, 35(2), 146–161.
14. Burke, T.; Goodsitt, M.; Madson, E.; Zagzebski, J., Angular distribution of scattered ultrasound from a single steel sphere in agar gelatin: a comparison between theory and experiment. *Ultrason Imaging* **1984**, 6, 342-347.
15. Madsen, E.; Insana, M.; Zagzebski, J., Methods of data reduction from accurate determination of acoustic backscatter coefficients. *J Acoust Soc Am* **1984**, 76, 913-923.
16. Insana, M.; Madsen, E.; Hall, T.; Zagzebski, J., Tests of the accuracy of a data reduction method for determination of acoustic backscatter coefficients. *J Acoust Soc Am* **1986**, 79, 1230-1236.
17. Hall, T.; Madsen, E.; Zagzebski, J.; Boote, E., Accurate depth-independent determination of acoustic backscatter coefficients with focussed transducers, *J Acoust Soc Am* **1989**, 85, 2410-241

18. Davors, W.; Zagzebski, J.; Madsen, E.; Frequency-dependent angular scattering of ultrasound by tissue-mimicking materials and excised tissue, *J Acoust Soc Am* **1986**, 80, 229.
19. IEC TS 62736, Ultrasonics - Pulse-echo scanners – Simple methods for periodic testing to verify stability of an imaging system’s elementary performance, Technical Specification, IEC Edition 1.0 **2016-07**
20. Insana, M.; Hall, T.; Cook, L., Backscatter coefficient estimation using array transducers. *IEEE Trans Ultrason Ferroelec Freq Control* **1994**, 41, 714-723.
21. Hall, T.; Insana, M.; Harrison, L.; Cox, G., Ultrasonic measurement of glomerular diameters in normal adult humans. *Ultrasound Med Biol* **1996**, 22, 987-997.
22. Wear, K.; Characterization of trabecular bone using the backscattered spectral centroid shift. *IEEE Trans UltrasonFerroelectrFreq Control*. **2003**; 50(4):402–407. [PubMed: 12744396]
23. Lu, Z.; Zagzebski, J.; Madsen, E.; Dong, F.; A method for estimation an overlying layer correction in quantitative ultrasound imaging. *Ultrason Imaging*. **1995**; 17(4):269–290.
24. Bigelow, T.; Oelze, M.; O’Brien, W.; Estimation of total attenuation and scatterer size frombackscattered ultrasound waveforms. *J AcoustSoc Am*. **2005**; 117(3):1431–1439.
25. Nam, K.; Zagzebski, J.; Hall, T.; Simultaneous Backscatter And Attenuation Estimation using A Least Squares Method With Constraints, *Ultrasound Med. Biol.*, **2011**, 37(12), 2096–2104,
26. O’Donnell, M.; Miller, J., Quantitative broadband ultrasonic backscatter: an approach to nondestructive evaluation in acoustically inhomogeneous materials. *J Appl Phys* **1981**, 52, 1056-1065.

27. Lizzi, F.; Ostromogilsky, M.; Feleppa, E.; Rorke, M.; Yaremko, M., Relationship of ultrasonic spectral parameters to features of tissue microstructure. *IEEE Trans Ultrason Ferroelec Freq Control* **1986**, 33(3), 319-329.
28. Lizzi, F.; Ostromogilsky, M.; Feleppa, E.; Rorke, M.; Yaremko, M., Relationship of ultrasonic spectral parameters to features of tissue microstructure. *IEEE Trans Ultrason Ferroelec Freq Control* **1986**, 33(3), 319-329.
29. Gerig, A.; Zagzebski, J.; Varghese, T., Statistics of ultrasonic scatterer size estimation with a reference phantom. *J Acoust Soc Am* **2003**, 113(6), 3430-3437.
30. Nassiri, D.; Hill, C., The use of angular scattering measurements to estimate structural parameters of human and animal tissues. *J Acoust Soc Am* **1986**, 79, 2048-2054.
31. Nicholas, D., Evaluation of backscattering coefficients for excised human tissues: Results. interpretation and associated measurements. *Ultrasound Med Biol* **1979**, 8, 17-22.
32. Bamber, J., Theoretical modeling of the acoustic scattering structure of human liver. *Acoust Lett* **1979**, 3, 114-119.
33. Oelze, M.; O'Brien, Jr., W., Method of improved scatterer size estimation and application to parametric imaging using ultrasound. *J Acoust Soc Am* **2002**, 112(6), 3053-3063.
34. Nasief, H.; Rosado-Mendez, I.; Zagzebski, J.; Hall, T.; A Quantitative Ultrasound-Based Multi-Parameter Classifier for Breast Masses, under review .
35. Rosado-Mendez I.; Nam, K.; Hall, T.; Zagzebski, J.; Task-oriented comparison of power spectral density estimation methods for quantifying acoustic attenuation in diagnostic ultrasound using a reference phantom method, *Ultrason Imaging*. **2013**, Jul;35(3):214-234. doi: 10.1177/0161734613495524.

36. Madsen, E.; Hobson, M.; Shi, H.; Varghese, T.; Frank, G.; Stability Of Heterogeneous Elastography Phantoms Made From Oil Dispersions In Aqueous Gels. *Ultrasound Med. & Bio.* **2006**; 32(2):261-270. doi:10.1016/j.ultrasmedbio.2005.10.009.
37. Madsen, E.; Dong, F.; Frank, G. ; Garra, B. ; Wear, K.; Wilson, T.; Zagzebski, J.; Miller, H.; Shung, K.; Wang, S.; et al. Interlaboratory comparison of ultrasonic backscatter, attenuation, and speed measurements. *J Ultrasound Med.* **1999** Sep; 18(9): 615–631.
38. Shelby, S. ; Michael, F. ; Jeremy, J. ; Christian, H.; Mohammad, A.; Helmut, E.; An ultrasound research interface for a clinical system. *IEEE Trans Ultrason Ferroelectr Freq Control.* **2007** Jan; 54(1): 198–210
39. Rubert, N.; Varghese, T.; Mean scatterer spacing estimation using multi-taper coherence, *IEEE Trans. Ultrason. Ferroelectr. Freq. Control*, **2013**; 60, 1061-1073
40. Wagner, R.; Smith, S., Sandrik, J.; and Lopez, H.; Statistics of Speckle in Ultrasound B-Scans *IEEE Transactions on Sonics and Ultrasonics* 30(3):156- 163 · June **1983** DOI: 10.1109/T-SU.1983.31404 · Source: *IEEE Xplore*
41. Wagner, R.; Smith, S., Sandrik, J.; and Lopez, H.; Statistics of speckle in ultrasound B-scans, *IEEE Trans. Sonics Ultrason.*, **1983**; 30, 157-164
42. Thuthill, T.; Sperry, R.; Parker, K.; Deviations from Rayleigh statistics in ultrasonic speckle, *Ultrason. Imaging*, **1988**; 10, 81-89
43. Shankar, P.; A Model for ultrasonic scattering from tissues based on the K distribution, *Phys. Med. Biol.*, **1995**; 40(10), 1643-1659
44. Varghese, T.; Donohue, K.; Estimating mean scatterer spacing with the frequency-smoothed spectral autocorrelation, *IEEE Trans. Ultrason. Ferroelectr. Freq. Control* **1995**, 432: 451-46

45. Rosado-Mendez, I.; Nasief, H.; Nam, K.; Zagzebski, J.; Hall, T.; Challenges in Quantitative Ultrasound of the Breast, **2012**, *UITC meeting*

## Chapter 3: QUS of Subcutaneous Breast Fat

*This chapter is published as:*

Nasief, H. G., Rosado-Mendez, I. M., Zagzebski, J. A., & Hall, T. J. (2015). ACOUSTIC PROPERTIES OF BREAST FAT. *Journal of Ultrasound in Medicine: Official Journal of the American Institute of Ultrasound in Medicine*, 34(11), 2007–2016

Interpretation of ultrasound images to diagnose solid breast masses generally includes comparing B-mode image features of a mass with those of surrounding fat and parenchymal tissue. In the US-BIRADS lexicon,<sup>1</sup> internal echo patterns of masses are categorized as anechoic, hypoechoic, iso-echoic, hyper-echoic, or complex. Although these descriptors are closely related to the backscatter properties of breast masses, the evaluation of these features is qualitative, subjective, and coarsely assigned (most breast tumors are described as ‘hypoechoic’ but there is no mention of ‘how hypoechoic’).

Clinicians utilize breast fat as a standard for comparison of the echogenicity and the attenuation (shadowing) features of masses. Although it serves as a source for comparison, there is little data in the literature demonstrating the range of acoustic properties of *in vivo* breast fat. Foster et al.<sup>2</sup> measured attenuation coefficients and backscatter coefficients at 13 MHz for excised breast specimens that included fat. Edmonds et al.<sup>3</sup> measured attenuation coefficient vs. frequency slopes for excised breast tissues, including fat, over the 3-8 MHz range. D’Astous and Foster<sup>4</sup> developed a novel tissue analysis system to measure attenuation and backscatter coefficients for excised breast tissue specimens under controlled conditions. *In vivo* data were obtained by Anderson et al.<sup>5</sup> who measured BSCs of fibro-glandular and fatty breast tissue in the 5.25-13 MHz frequency range using the Reference Phantom Method. In this study, the acoustic properties of fat are estimated to test for consistency in our QUS parameter estimates and examine the use of fat as a clinical reference tissue for US-BIRADS descriptors.

### 3.1. Data acquisition

As mentioned in Chapter 2, 120 human subjects who were scheduled for core biopsy were recruited. However, for this data analysis, we excluded (obviously) heterogeneous fat lobules since radiologists compare echogenicity of a suspicious mass to that of fat using the average brightness, ignoring any specular reflectors or other heterogeneities that might be present. QUS parameter estimation techniques can provide reliable estimates for structures larger than about 5 mm (axially). In our study, criteria for analysis were image data that depicted large ( $> 1$  cm) and homogeneous (no noticeable internal specular reflectors) fat lobules. This resulted in 24 subjects selected for this analysis. A typical example is shown in Figure 3.1 in which a manually selected region of interest (ROI) within a fat lobule is outlined on the B-mode image.

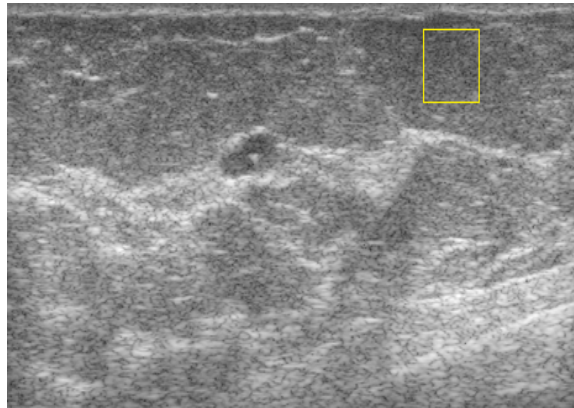


**Figure 3.1.** Typical breast ultrasound image from this study showing an example of breast fat ROI selection (rectangle in the upper right)

Data analysis was performed offline using routines written in MATLAB (the Mathworks, Natick, MA). Rectangular parameter estimation regions (PERs) were identified within a uniform ROI of a fat lobule selected as outlined above for each patient. Echo signal power spectra were calculated as a function of depth for data segments within this region for both the sample and reference phantom. To calculate a power spectrum, 4mm x 4mm power spectrum estimation

regions (PSER), overlapping by 75% both axially and laterally, were defined. For each RF line within the PSER, the Fourier transform was computed using a multi-taper technique with a time-half bandwidth product (NW) of 4.<sup>16-17</sup> The results for beam lines within the PSER were then averaged. For a homogenous PER, the ratio of the echo signal power spectrum from the sample to the power spectrum for the reference phantom was estimated using the RPM (see Chapter 2).

Attenuation was estimated using the RPM. Although the average speed of sound within the lobule as well as in any overlying tissues is not known (but estimated to be about 1460 m/s), having the transmit focus set distal to the ROI minimizes any bias in attenuation estimates caused by sound speed mismatches.<sup>18</sup> The maximum frequency band over which the echo signal power spectrum was at least 10 dB above the noise floor was selected for each subject. When reporting final results, the maximum frequency range common among all data sets was used. The BSC( $f$ ) and the average BSC (ABSC) for each subject was computed over the (6-12 MHz) frequency range used for attenuation estimation. The effective scatter diameter (ESD) was estimated over regions of interest within the fat lobules to characterize the frequency dependence of scattering. A Gaussian form factor was utilized to model soft tissue backscatter.<sup>19</sup> The ESD estimated here does not identify a microscopic scattering structure but simply parameterizes the frequency dependence of scattering.

### **3.2. QUS parameters of subcutaneous breast fat**

The attenuation coefficients versus frequency for the selected fat lobule in each patient are presented in Figure 3.2, while a summary plot for data over the 6-12 MHz range is presented in Figure 3.3. These are computed directly using the RPM. The results in Figure 3.2 exhibit significant variation in overall magnitude from one patient to another. For example, at 8 MHz,

breast fat attenuation coefficients ranging from 3.2 dB/cm up to 7.5 dB/cm were obtained. A similar range and variability is seen at other frequencies (above about 6 MHz).

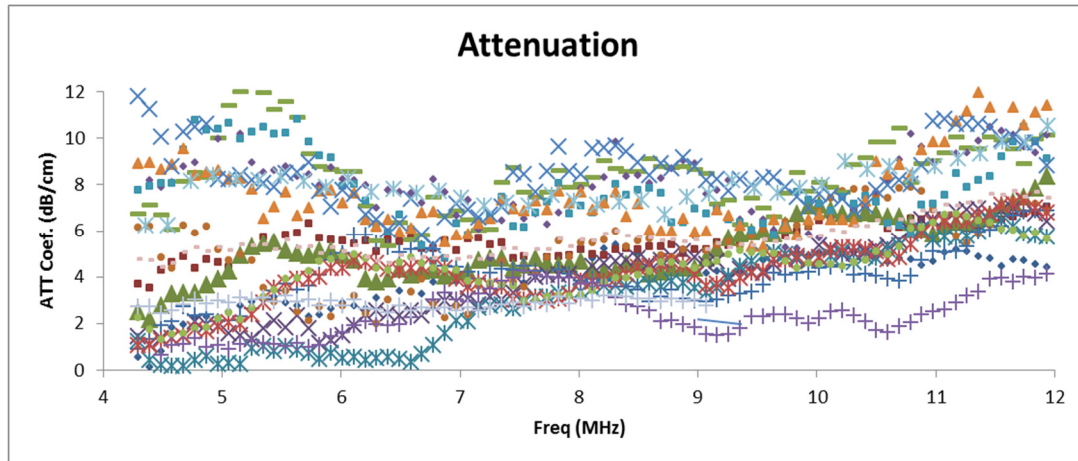


**Figure 3.2.** Attenuation coefficient vs. frequency in breast fat for individual subjects

The attenuation coefficient versus frequency data in the 4-6 MHz range exhibits unexpected behavior in that some patients' data suggest a decrease in attenuation with frequency over this range. It is likely that there exist non-apparent sources of echo signal coherence, such as interfaces or isolated strong scatterers, within the attenuation PERs that would violate assumptions used in attenuation estimation, and that these may be more prominent at lower frequencies. Thus, the summary plot for the attenuation results (Figure 3.3) excludes the 4-6 MHz frequency range. A power law fit for the attenuation for the combined data set (24 subjects) for the 6-12MHz frequency range resulted in  $\alpha(f) = 1.28 \text{ dB.cm}^{-1}\text{MHz}^{-0.73}$ . A plot of the mean attenuation coefficient vs. frequency is shown in Fig. 3.3.

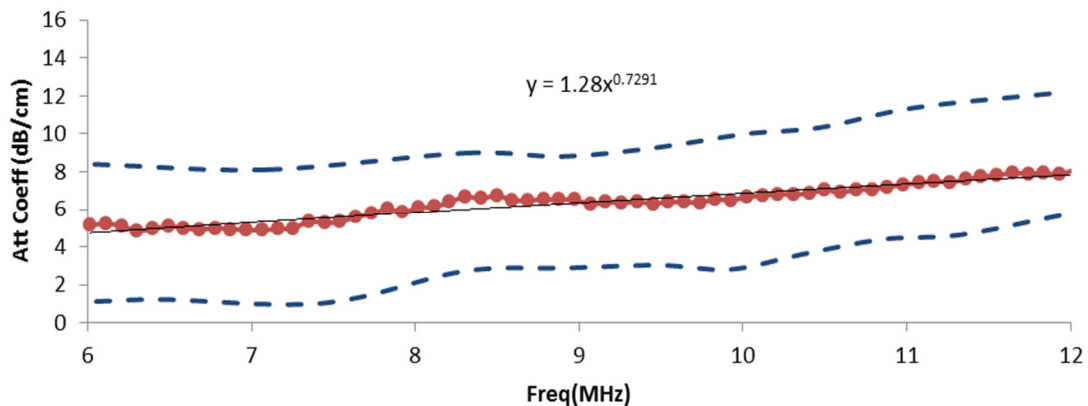


**Figure 3.3.** The mean attenuation coefficient estimates (dots) of breast fat among 24 subjects, the standard deviations (dashed line) and the combined power law fit for the attenuation coefficient vs. frequency.

As mentioned above, for each patient, attenuation coefficients were computed for several PERs within the ROI. For determining the variability among patients and to facilitate comparison with results of previous investigators, we fit the data to a straight line with zero intercept and estimated the slope of the attenuation coefficient vs. frequency at 7 MHz for each PER. We then computed an average and standard deviation of these values within the ROI from independent PERs. Results are presented in Figure 3.4 for each of the 24 subjects. The specific attenuation coefficient values at 7MHz among all subjects was  $0.73 \pm 0.23 \text{ dB}\cdot\text{cm}^{-1}\text{MHz}^{-1}$ .

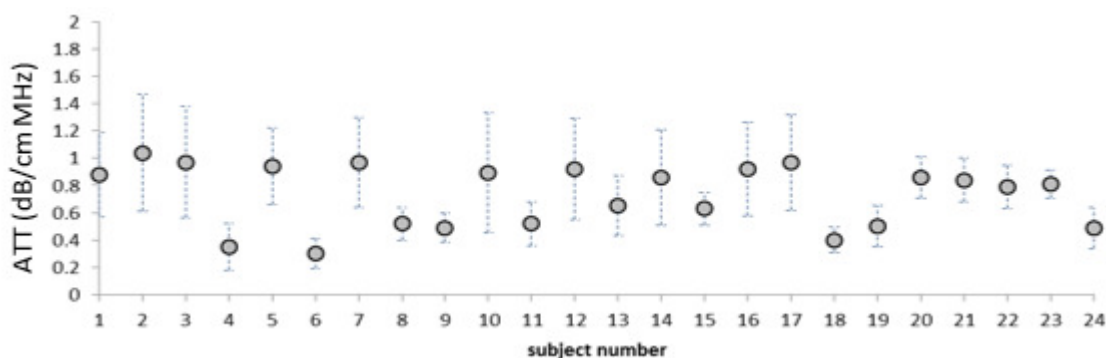


**Figure 3.4.** Specific attenuation at 7MHz for each subject. The circles represent the mean for each subject and the bars show the corresponding standard deviations

The mean BSC vs. frequency of the fat lobule over all patients follows a power law fit of  $(0.6 \pm 0.25) \times 10^{-4} \text{ sr}^{-1} \text{ cm}^{-1} \text{ MHz}^{-2.49}$ . The average backscatter coefficient (ABSC) in the 6-12 MHz range is  $0.0073 \pm 0.0023 \text{ cm}^{-1} \text{ sr}^{-1}$ . Individual ABSC's were plotted on a logarithmic scale to study deviations from the average value among subjects, and results are shown in Figure 3.5. The results showed that the ABSC range among subjects is about 10 dB. The lack of standardization of US imaging would make these brightness variations (from one subject to the next) hardly noticeable on a gray scale ultrasound image (given a 70dB dynamic range for the displayed echo used for breast imaging and free user control over average image brightness).

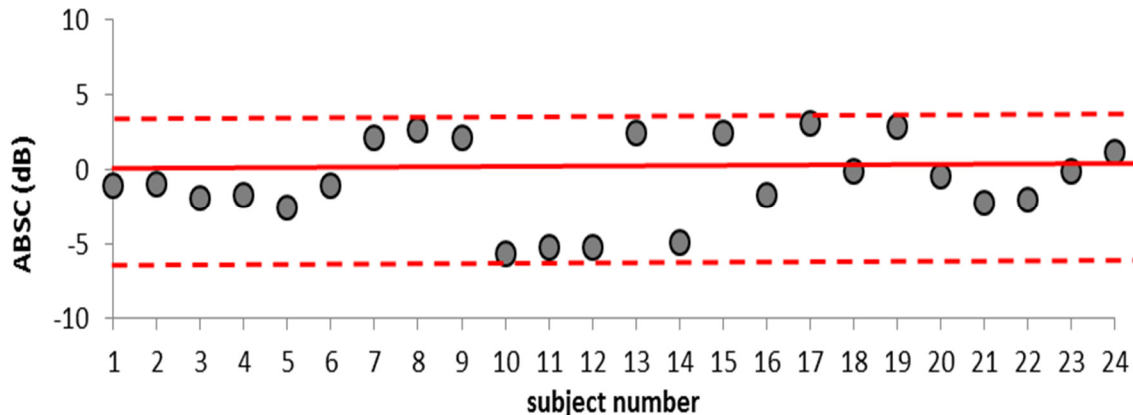


**Figure 3.5.** ABSC estimates for breast fat for each subject, shown relative to the mean value among all subjects (solid line). The dashed lines indicate the upper and lower range of values

Effective scatterer diameters were estimated to characterize the frequency dependence of backscatter. The mean ESD among all subjects is  $60.2 \pm 9.5 \mu\text{m}$ . Figure 3.6 shows ESD estimates for each subject compared to the mean value among estimates.

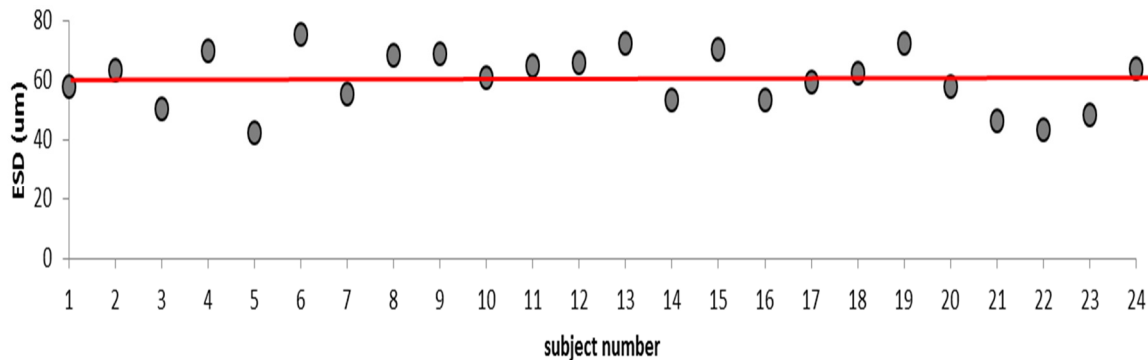


**Figure 3.6.** Effective scatterer diameter (ESD) estimates for breast fat for each subject. The solid line shows the mean value among ESD estimates

### 3.3. Discussion

The *in vivo* results for subcutaneous fat showed noticeable variability in attenuation estimates in the 4-6MHz frequency range. Intra-subject variability of about 6% was observed in attenuation estimates among the different ROIs selected within the same fat lobule. Attenuation estimate variance among subjects would likely have been smaller if larger ROIs were used and those ROIs were tested to demonstrate a lack of echo signal coherence and homogeneity of parameter estimates within the ROI. Attenuation is assumed to increase with frequency, but Figure 3.7 shows attenuation coefficient and B-mode images of two cases that do not follow this assumption. In one case, high attenuation values were estimated in the lower frequency band compared to the higher frequency band. In the other case, the attenuation estimates in the lower frequency band are very close to zero. In both cases, it is possible that sources of echo signal coherence were present in the ROI. Systematic analysis of echo signal data that first tests for the presence of echo signal coherence prior to QUS parameter estimates that assume incoherent scattering are currently being implemented and will be discussed in Chapter 5.

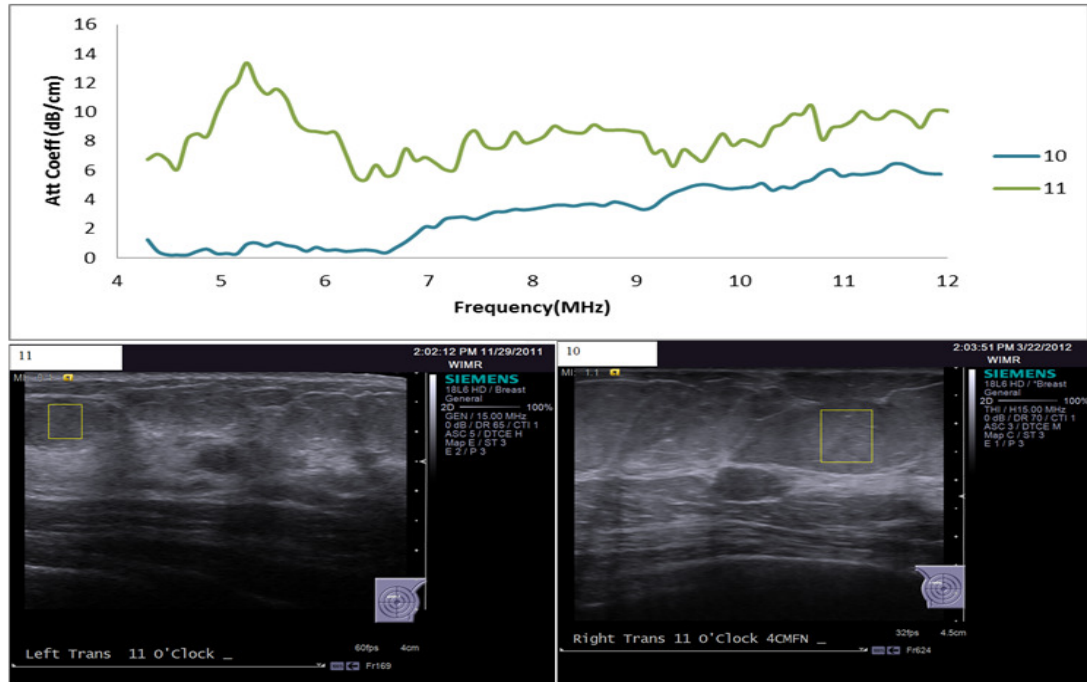


**Figure 3.7.** Top: attenuation coefficient vs. frequency estimates for two cases (case 1: upper line, case 2: lower line) of unexpected behavior of attenuation vs. frequency. Bottom: Associated B-mode images (case 1 on the left; case 2 on the right) with the ROI (outlined boxes) within which the attenuation coefficients were estimated.

Attenuation and backscatter coefficient estimates in this study were compared with previously published work. D'Astous and Foster<sup>4</sup> reported a mean attenuation coefficient vs frequency of  $0.16 \pm 0.03 \text{ dB} \cdot \text{cm}^{-1} \text{MHz}^{-1.7}$ , and a backscatter coefficient of  $(0.92 \pm 0.65) \times 10^{-4} \text{ sr}^{-1} \text{cm}^{-1} \text{MHz}^{-1.9}$  for ex vivo breast fat. Thus, their specific attenuation for fat at 7 MHz would be about  $0.62 \pm 0.12 \text{ dB} \cdot \text{cm}^{-1} \text{MHz}^{-1}$  (compared to  $0.73 \pm 0.23 \text{ dB} \cdot \text{cm}^{-1} \text{MHz}^{-1}$  for *in vivo* estimates in our study). Figure 3.8 shows our individual *in vivo* results for the attenuation coefficient versus frequency slope compared with the excised breast tissue estimates reported by D'Astous and Foster. Our values appear, on average, to be slightly higher than those of D'Astous and Foster, although the standard deviations among estimates certainly overlap.

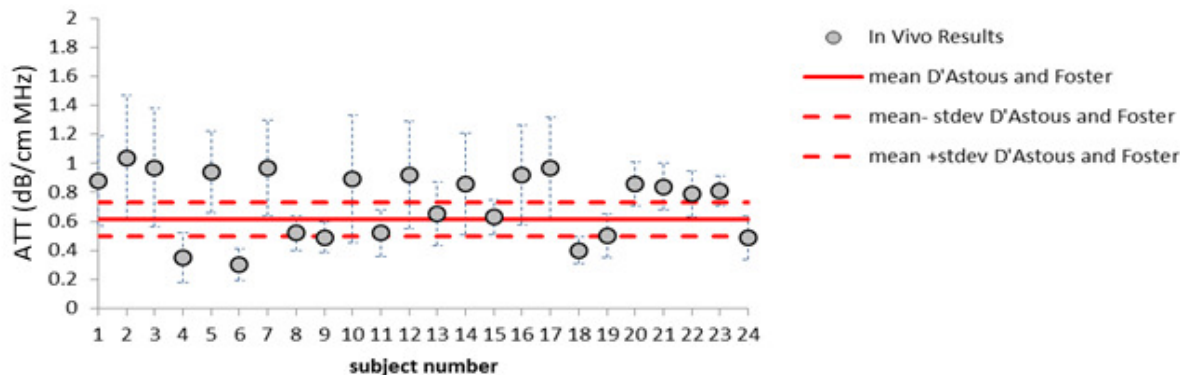


**Figure 3.8.** Specific attenuation at 7MHz reported in Fig 3.4 for breast fat (data points), compared to mean values for the same parameters for ex vivo breast fat reported by D'Astous and Foster

In other reports, Foster et al.<sup>2</sup> measured attenuation and backscatter coefficients for excised breast specimens at 13MHz; Edmonds et al.<sup>3</sup> measured attenuation coefficient vs. frequency slopes for fat over the 3-8MHz range; Anderson et al.<sup>5</sup> measured the backscatter coefficient of subcutaneous fat from 5.25 to 13 MHz; and Raju et al.<sup>19</sup> measured attenuation and backscatter coefficients of subcutaneous fat *in vivo* at the wrist and elbow in the range 14 to 34MHz. Table 4.1 shows the average values measured for the 24 subjects in the current study along with values reported by these researchers.

**Table 3. 1.** Average values of the attenuation coefficient modeled as a linear function of frequency (Att), the backscatter coefficient (BSC) modeled as a power law and the average backscatter coefficient (ABSC) of breast fat versus literature values

Data	Frequency (MHz)	ATT (dB·cm <sup>-1</sup> MHz <sup>-1</sup> )		BSC (bf <sup>n</sup> )		ABSC* (cm <sup>-1</sup> sr <sup>-1</sup> )	
		<u>mean</u>	<u>Stdev.</u>	b (x10 <sup>-4</sup> )	n	<u>mean</u>	<u>Stdev.</u>
D'Astous and Foster <sup>9</sup>	3-7	0.62	0.12	0.92±0.65	1.9	0.004	0.003
Anderson et al. <sup>10</sup>	5.25-13	-	-	0.259	3.4	0.003	0.003
Edmonds et al. <sup>8</sup>	3-8	2.00	0.65	-	-	-	-
Raju et al. <sup>38</sup>	14-34	1.84		-	-	0.073	0.072
Foster et al. <sup>7</sup>	13	1.1	0.3	1.4±0.6	-	0.014	0.006
Current study results	6-12	0.73	0.23	0.6±0.25	2.5	0.0073	0.002

\* ABSC shown corresponds to the frequency range stated in the table.

For visual comparisons between our *in vivo* data and the data from these previous studies, values are plotted on a logarithmic scale, and are shown in Figure 3.9. The plots suggest very consistent results among current and previously published data over the frequency ranges tested.

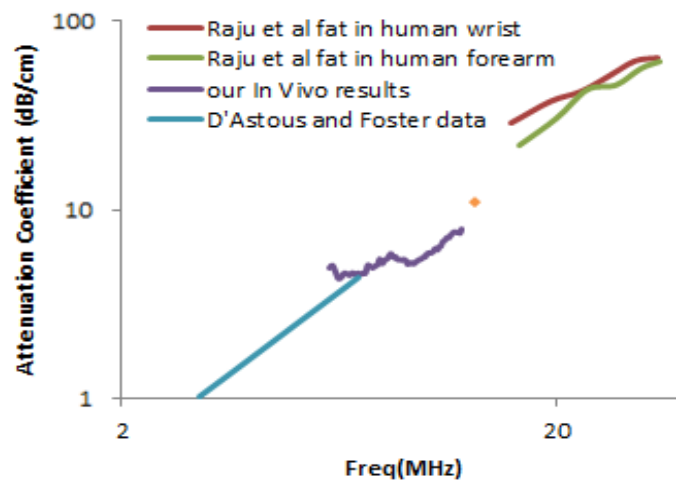


**Figure 3.9.** Attenuation coefficient vs. frequency for breast fat comparing *in vivo* breast measurements to previously reported results

Focusing on the data from breast tissues, Figure 3.10 shows the *ex vivo* results from D'Astous and Foster as well as from Foster et al. compared to our *in vivo* results. The regions shown are defined by the mean plus and the mean minus one standard deviation of the reported results.

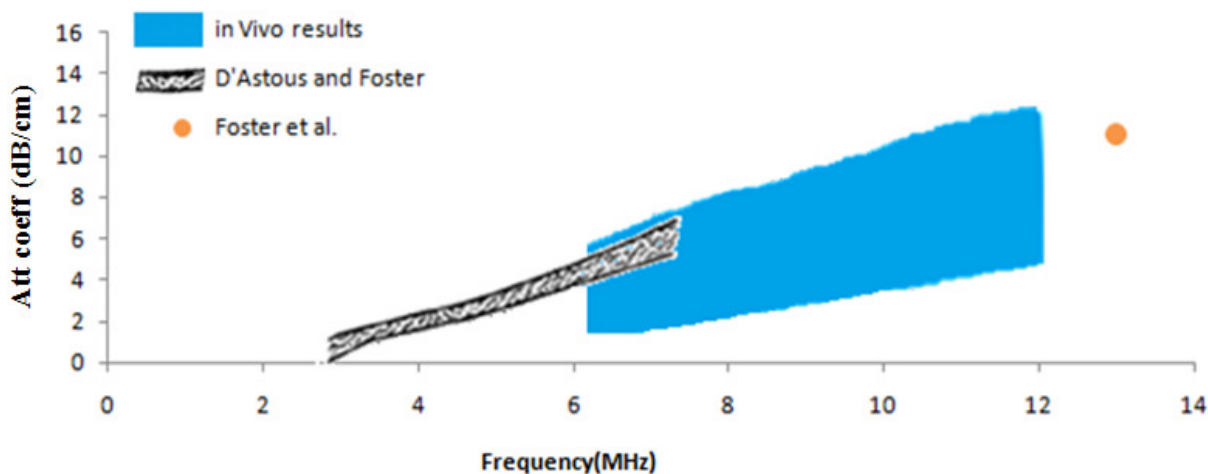


**Figure 3.10.** Attenuation coefficient vs. frequency for breast fat, comparing *ex vivo* results of D'Astous and Foster, Foster et al., and the *in vivo* results reported in this study

The measured BSC versus frequency for breast fat in this study exhibited close agreement among all 24 subjects both in magnitude and frequency dependence. A graphic comparison on a log-log plot of these results with those of D'Astous and Foster and those of Anderson et al. using 7.5 and 10 MHz transducers is presented in Figure 3.11. The upper and lower curves shown are defined by the mean plus and the mean minus one standard deviation of the reported results.

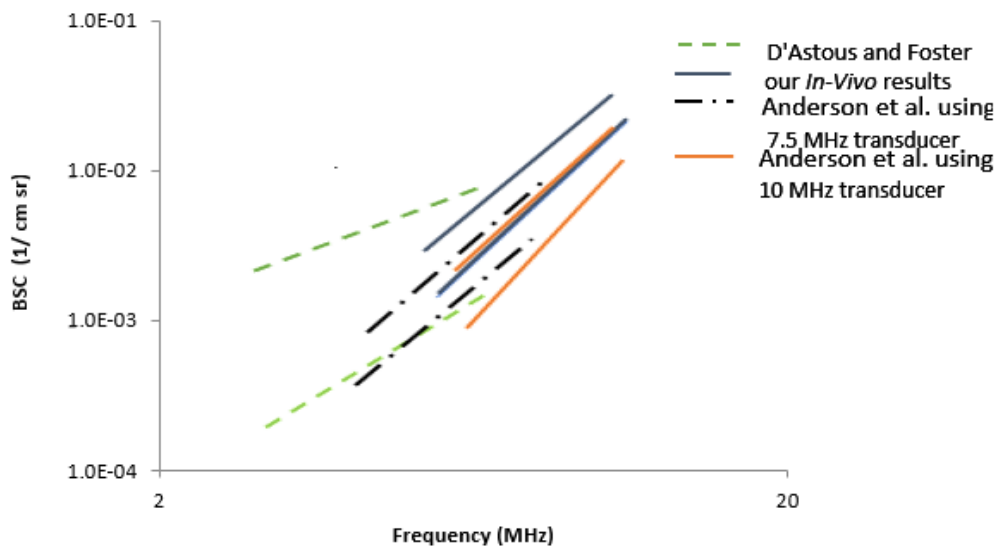


**Figure 3.11.** BSC vs. frequency for breast fat as reported by D’Astous and Foster, Anderson et al., and our estimates reported here

### 3.4. Conclusion

The results reported here show consistency in acoustic properties of breast fat among twenty-four subjects and with previously published data. These results demonstrate our QUS methods provide consistent parameter estimates among subjects, and those estimates are in agreement with previously reported values from other groups. The range of average backscatter coefficient in the 6-12 MHz frequency range for breast fat in each subject is within 5 dB of the mean ABSC value across subjects. This finding quantitatively supports the use of fat as a reference tissue for US-BIRADS. The consistency in the characteristics of breast fat encourages future use of quantitative measures, for example to specify the degree to which a mass is “hypo-echoic”. Similarly, reporting the specific attenuation, or some equivalent measure, may reduce the subjectivity in describing ‘posterior acoustic features’ which depend on both the attenuation in the mass and its dimension along the acoustic beam path. This could in turn improve BIRADS descriptors of ultrasound breast data.

### 3.5. References

1. Online American College of Radiology. BI-RADS: Ultrasound, 1st ed. Website. <http://www.acr.org/Quality-Safety/Resources/BIRADS/Ultrasound>. Accessed June **2014**.
2. Foster, F.; Strban, M.; Austin, G.; The Ultrasound Macroscopic: Initial Studies of Breast Tissue. *Ultrason Imaging* **1984**; 6(3):243-261.
3. Edmonds, P.; Mortensen, C.; Hill, J.; Holland, S.; Jensen, J.; Schattner, P.; et al. Ultrasound Tissue Characterization Of Breast Biopsy Specimens. *Ultrason Imaging* **1991**; 13(2):162-185.
4. D'Astous, F.; Foster, F.; Frequency-dependence of ultrasound attenuation and backscatter in breast-tissue. *Ultrasound Med Biol* **1986**; 12(10):795-808
5. Anderson, M.; Soo, M.; Trahey, G.; In vivo breast tissue backscatter measurements with 7.5- and 10-MHz transducers. *Ultrasound Med Biol* **2001**; 27(1):75–81.
6. Hanafy, A.; Limited diffraction broadband phased array transducer with frequency controlled two dimensional aperture capability, **1999**, patent no. US 5976091 A.
7. Brunke, S.; Insana, M.; Dahl, J.; Hansen, C.; Ashfaq, M.; Emert, H.; An ultrasound research interface for a clinical system. *IEEE Trans Ultrason Ferroelectr Freq Control* **2007**; 54(1):198-210.
8. Madsen, E.; Frank, G.; Carson, P.; Edmonds, P.; Frizzell, L.; Herman, B.; et al. Inter-laboratory comparison of ultrasonic attenuation and speed measurements. *J Ultrasound Med* **1986**; 5:569–576.

9. Madsen, E.; Hobson, M.; Shi, H.; Varghese, T.; Frank, G.; Stability of heterogeneous elastography phantoms made from dispersions in aqueous gels. *Ultrasound Med Biol* **2006**; 32(2):261–270.
10. Chen, J.; Zagzebski, J.; Madsen, E.; Tests of backscatter coefficient measurement using broadband pulses. *IEEE Trans Ultrason Ferroelectr Freq Control* **1993**; 40(5):603–607.
11. Wear, K.; Stiles, T.; Frank, G.; Madsen, E.; Cheng F.; Feleppa E.; et al. Interlaboratory comparison of ultrasonic backscatter coefficient measurements from 2 to 9 MHz, *J. Ultrasound Med.* **2005**; 24:1235–1250.
12. Madsen, E.; Zagzebski, J.; MacDonald, M.; Frank, G.; Ultrasound focal lesion detectability phantoms. *MedPhys* **1991**;18:1171.
13. Burlew, M.; Madsen, E.; Zagzebski, J.; Banjavic, R.; Sum, S.; A new ultrasound tissue-equivalent material. *Radiology* **1980**;134:517.
14. Insana, M.; Wagner, R.; Brown, D.; Hall, T.; Describing small-scale structure in random media using pulse-echo ultrasound. *J Acoust Soc Am* **1990**; 87(1):79-192.
15. Insana, M.; Hall, T.; Parametric ultrasound imaging from backscatter coefficient measurements: Image formation and interpretation. *Ultrason Imaging* **1990**;12:254.
16. Rosado-Mendez, I.; Nam, K.; Hall, T.; Zagzebski, J.; Task-oriented comparison of power spectral density estimation methods for quantifying acoustic attenuation in diagnostic ultrasound using reference phantom method. *Ultrason imaging* **2013**; 35(3):214-234
17. Percival, D.; Walden, A.; Spectral Analysis for Physics Applications: Multitaper and conventional univariate techniques. New York, NY: Cambridge University Press; **1993**.

18. Nam, K.; Rosado-Mendez, I.; Rubert, N.; Madsen, E.; Zagzebski, J.; Hall, T.; Ultrasound attenuation measurements using a reference phantom with sound speed mismatch. *Ultrason Imaging* **2011**; 33(4):251-63.
19. Raju, B.; Srinivasan, M.; High-frequency ultrasonic attenuation and backscatter coefficients of in vivo normal human dermis and subcutaneous fat. *Ultrasound Med Biol* **2001**; 27(11):1543–1556.

## Chapter 4: Modified least squares method

*A portion of this chapter is published as:*

*Nasief, H. G., Rosado-Mendez, I. M., Zagzebski, J. A., & Hall, T. J. (2015). ACOUSTIC PROPERTIES OF BREAST FAT. Journal of Ultrasound in Medicine: Official Journal of the American Institute of Ultrasound in Medicine, 34(11), 2007–2016*

In-vivo breast tissue is very complicated and heterogeneous; thus, a proper correction for attenuation over the inhomogeneous tissue path between the ultrasound transducer and a ROI within a breast mass is necessary to obtain reliable QUS estimates – especially when quantifying the frequency-dependence of scattering with the Effective Scatterer Diameter. Many algorithms have been developed over the years to compensate for the attenuation over the intervening tissue path, as mentioned in Chapter 2.<sup>1-5</sup> The most recent and perhaps most sophisticated approach for attenuation compensation was developed in our group by Nam et al.<sup>5</sup> They proposed a least squares method to estimate an effective attenuation coefficient between the ultrasound transducer and a ROI. The method uses the power spectrum of the RF echo signals from the ROI and the spectrum from a reference phantom. They fit the ratio of the two spectra to a 3-parameter tissue model that quantifies the attenuation and backscatter properties of the media. The least squares method enables the determination of attenuation when the path is acoustically non-uniform, providing an accurate estimate of the total attenuation to a PER and the backscatter coefficient versus frequency of the sample within the PER. In developing this method, the relation between attenuation and frequency was assumed to be linear. However, this relationship does not hold over a broad frequency range in most human tissue.<sup>6</sup> To take this into consideration, a modification of the Nam method, a “Modified Least Squares Method” (MLSM), is applied in this study. The MLSM is discussed in detail in this chapter.

The MLSM addresses the departure from linearity assumed in the LSM by dividing the echo signal frequency range into small, 2 MHz, overlapping sub-bands (where the linear frequency dependence of attenuation is a reasonable approximation). Thus, the assumption of a linear dependence of attenuation on frequency over the entire echo signal bandwidth is not necessary. This method was tested using a theoretical assessment, on uniform phantoms, on phantoms with layers having different attenuation and layers having different backscatter levels, on stacked phantoms with an attenuation frequency dependence different from  $f^1$ , and a phantom simulating subcutaneous fat and breast parenchyma. The method was also applied to derive in-vivo breast and kidney BSC data.

#### 4.1. The modified least squares method (MLSM)

This MLSM represents a modification to the Nam et al. least squares method<sup>5</sup> to estimate an “effective attenuation coefficient” over the path between the ultrasound transducer and the center of the PER, as mentioned above. The previous least squares method for estimating attenuation and backscatter coefficients begins by employing the first order Born approximation (assuming scattering from soft tissue is weak enough to ignore multiple scattering and the distance from the transducer to the PER is greater than the transducer aperture). Thus, the power spectra can be described using equations applied in the reference phantom technique<sup>7</sup> (see Chapter 2).

In the Nam method, ultrasound attenuation is approximated as a linear function of frequency:

$$\alpha(f) = \alpha_0 f + \alpha_1 \quad (4-1)$$

where  $\alpha_0$  is the attenuation coefficient versus frequency slope and,  $\alpha_1$  is a positive constant representing the intercept (set to zero in the Nam method).

Thus, the cumulative attenuation  $A(f, z)$  from the transducer to depth  $z$  and back to the transducer is approximated by

$$A(f, z) = \exp(-4\alpha_{0,eff} fz) \quad (4-2)$$

where  $\alpha_{0,eff}$  is an effective “specific attenuation coefficient” for the propagation path.

Similarly, the backscatter coefficient  $B(f)$  within the ROI is modeled as a power law,

$$B(f) = b f^n \quad (4-3)$$

where  $b$  is a constant and  $n$  represents the frequency dependence.

The method starts by computing the ratio of the echo signal power spectrum from the sample to the power spectrum of echoes from the reference phantom, given by Yao et al. as follows:<sup>7</sup>

$$RS(f, z) = \frac{S_{sam}(f, z)}{S_{ref}(f, z)} = \frac{b_{sam} f^{n_{sam}}}{b_{ref} f^{n_{ref}}} \exp(-4(\alpha_{o,eff,sam}(f) - \alpha_{o,ref}(f))z) \quad (4-4)$$

where subscripts *sam* and *ref* denote the sample and reference phantom respectively.

Computing the natural log of the ratio of the power spectra in Eq. 4-4, yields

$$\ln \frac{S_{sam}(f, z)}{S_{ref}(f, z)} = \ln \frac{b_{sam}}{b_{ref}} + (n_{sam} - n_{ref}) \ln f - 4(\alpha_{o,eff,sam} - \alpha_{o,ref}) f \cdot z \quad (4-5)$$

To simplify, we apply the following substitutions

$$X(f, z) = \ln \frac{S_{sam}(f, z)}{S_{ref}(f, z)}, \quad b = \ln \frac{b_{sam}}{b_{ref}}, \quad n = (n_{sam} - n_{ref}), \quad \alpha = (\alpha_{o,eff,sam} - \alpha_{o,ref}) \quad (4-6)$$

Thus,

$$X(f, z) = b + n \ln f - 4\alpha f z \quad (4-7)$$

Three equations in three unknowns are obtained by differentiating the right side of Eq. (4-8) below with respect to each of the three variables and setting the derivatives to 0. These equations are then fit to a three parameter least squares linear model (based on power law models for tissue

attenuation and backscatter) to solve for the unknowns,  $b$ ,  $n$  and  $\alpha$  that are consistent with the power spectrum data within the frequency band of interest (4-9 MHz). Thus,

$$[\hat{b}, \hat{n}, \hat{\alpha}] = \arg \min_{b, n, \alpha} \sum_{i=1}^K (X(f_i, z) - b - n \ln f_i + 4\alpha f_i z)^2 \quad (4-8)$$

where,  $\hat{b}, \hat{n}, \hat{\alpha}$  are the estimated parameters and  $K$  is the number of frequency components to be used for the least squares fitting.

Nam et al. apply Eq. 4-8 to the entire echo signal frequency spectrum. However, in the MLSM method used here, we divide the echo signal frequency band into subbands 2MHz wide with 50% overlap. A schematic of the steps the MLSM takes beyond the Nam et al. method is shown in Figure 4.1. By using relatively narrow frequency ranges for analysis, the approximation that attenuation is linearly dependent on frequency over that narrow frequency range is reasonably accurate. Starting at the lower band, i.e., where the echo signal power spectrum first exceeds the noise floor by 10 dB, values for  $\hat{b}, \hat{n}$ , and  $\hat{\alpha}$  are determined. The resulting value for the attenuation coefficient over the first subband then serves as a starting point,  $\alpha_1$  in Eq. 4-1, for a subsequent fit to the data over the next subband, as shown in Figure 4.2. The process continues over the interval for which the echo signal power spectrum exceeds the noise floor by 10 dB.

For each 2MHz frequency interval, the  $b$  and  $n$  estimates for backscatter coefficients are discarded. New values are estimated in each interval simply to obtain attenuation estimates that are robust to variations in echogenicity. The estimation results from each subband are then combined into a single power law attenuation model to smooth the piecewise linear function and obtain an estimate of the effective attenuation coefficient vs. frequency. This power law fit is used to describe the frequency dependence of  $\alpha_{\text{eff}, s}$  from 4–9 MHz. This modification to the Least Squares Method may lead to more reliable, system-independent QUS parameter estimates in the breast (and other tissues).

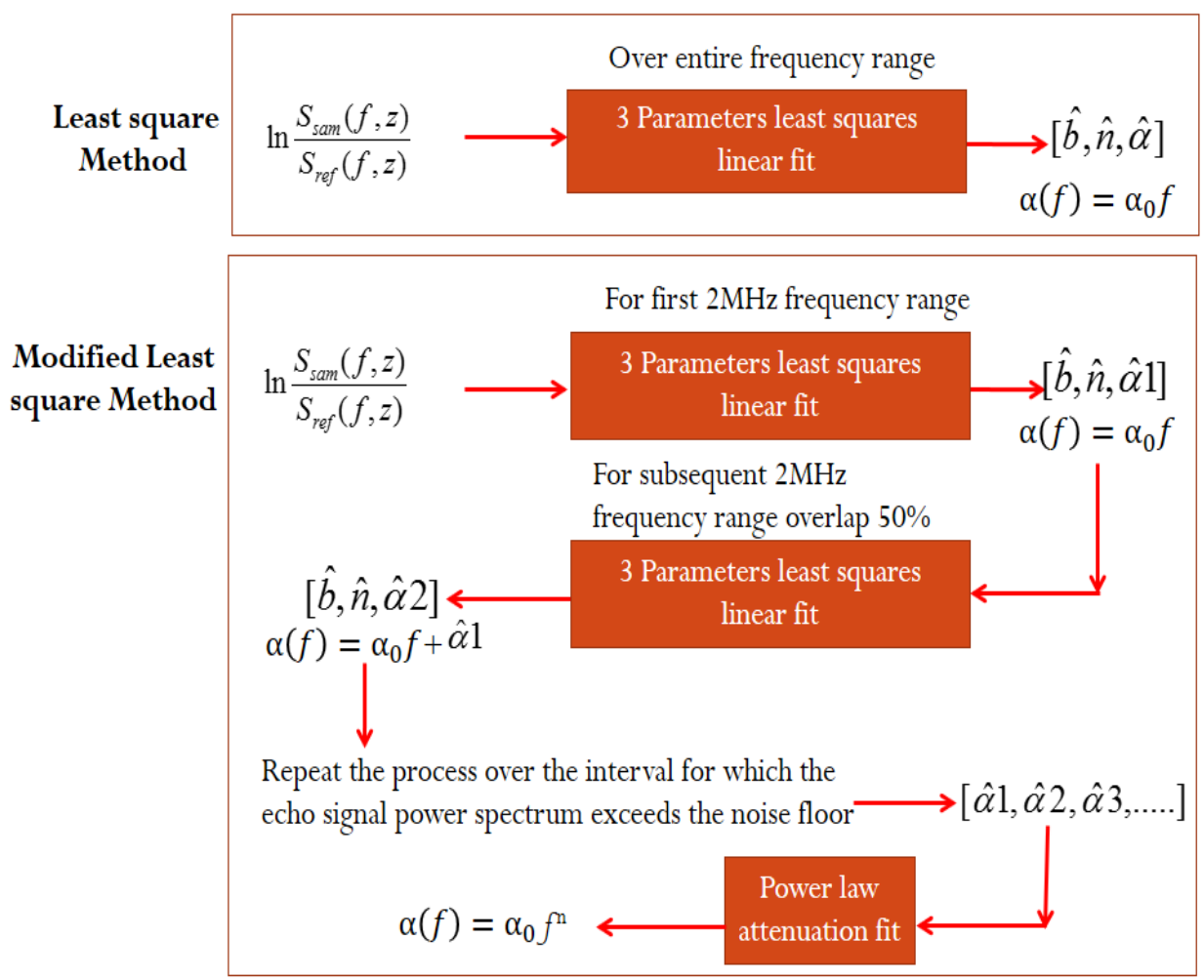


**Figure 4.1.** Schematic of the modified least squares method (MLSM) describing the extra steps beyond the least squares method

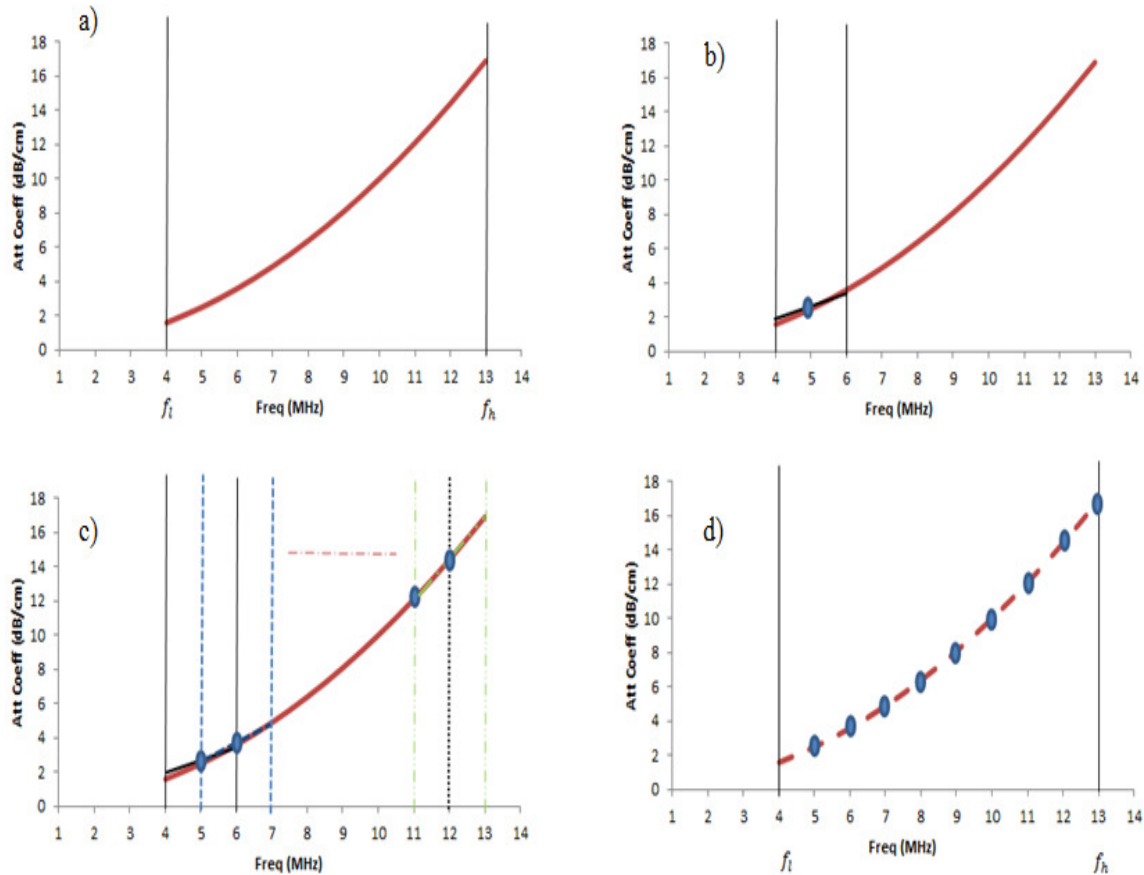


**Figure 4.2.** The modified least squares method (MLSM) for attenuation estimation, where the solid curved line is the underlying attenuation coefficient vs. frequency to be estimated. In a) the first frequency subband is chosen, b) a linear fit is applied to the first subband, c) the process is repeated for multiple subbands overlapping by 50% where the resulting value for the attenuation coefficient in the previous subband serves as the starting point for the next subband, d) a power law attenuation fit among the piecewise linear fits from each subband is obtained.  $f_l$  and  $f_h$  stands for lower and higher frequency limits respectively

## 4.2. Theoretical assessment of the MLSM method

To evaluate the method for a higher frequency dependence of attenuation, we performed a theoretical assessment using data from a modeled sample and reference. We set the attenuation properties of the sample to be  $0.3 f^{1.6}$ , and its backscatter coefficient to be  $5E-6 f^{2.25}$ . We set the reference phantom attenuation to be  $0.5 f^{1.1}$ , and its backscatter coefficient to be  $3E-6 f^{3.25}$ . We

assumed that the power spectra of the sample and the reference follow a Gaussian distribution (over the 3-12 MHz range), and that the speed of sound is the same in the sample and the reference (1540 m/s). We computed the ratio of the power spectra of the sample to that of the reference using the values assigned for each of them. We then plugged the values of the power spectral ratios and the reference information into the LSM and the MLSM methods and estimated the attenuation (assuming a 2-cm depth). The LSM is used with constraints on the allowable values for  $\alpha_{0 \text{ eff}}$ . We applied a broad constraint range (0.2-2 dB.cm<sup>-1</sup>MHz<sup>-1</sup>).

### 4.2.1. Results for the theoretical assessment

The results in Figure 4.3 show that for a higher frequency dependence of attenuation, the MLSM method was successful in estimating the attenuation coefficient ( $0.31 f^{1.58}$  vs. the expected value of  $0.3 f^{1.6}$ ). The MLSM was also successful in estimating the backscatter coefficient ( $5.23 \text{ E-}6 f^{2.55}$  vs. the expected value of  $5 \text{ E-}6 f^{2.25}$ ). The LSM method on the other hand, was not very successful in estimating the attenuation coefficients.

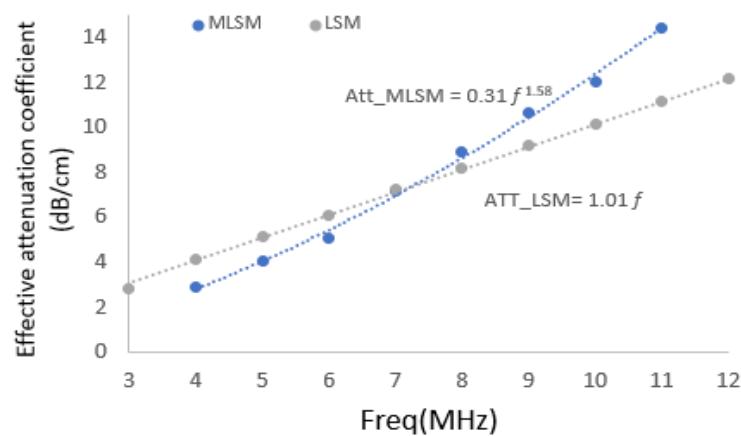


**Figure 4.3.** Theoretical assessment of the MLSM versus the LSM for a higher frequency dependence of attenuation in the sample and the corresponding power law and linear fits resulting from the MLSM and the LSM respectively.

### 4.3. Phantom data acquisition

Phantoms used in this study were scanned using a S2000 scanner (Siemens Medical Solutions USA, Inc, Malvern, PA) equipped with an 18L6 linear array transducer, with a nominal excitation frequency of 10MHz. The transmit focus was set below 5 cm and the power was set to 39%. Five separate frames of RF echo data, each consisting of 368 acoustic beamlines, were acquired with an elevational translation or rotation of the transducer between each frame to obtain statistically independent echoes. The system was equipped with the Axius Direct Ultrasound Research Interface<sup>8</sup> that allows acquisition of beam-formed RF echo signals following time-gain-compensation but before envelope detection and post processing. Data were available for each acoustic scan line, covering the entire B-mode image plane. Data analysis was performed off-line using routines written in MATLAB to estimate the effective attenuation over the intervening tissue path, to correct for attenuation before estimating the BSC and ESD parameters described in the previous chapter. For theoretical predictions of BSCs in the phantoms, the Faran scattering theory (see Chapter 2) was used, and the predictions computed were compared with the experimentally-estimated BSCs.

#### 4.3.1. Evaluation of the MLSM on uniform phantom

The MLSM was tested using two tissue mimicking phantoms with uniform attenuation and backscatter coefficients. Phantom 1 was used as the reference, and Phantom 2 was used as the sample. Both phantoms were made with 1-45 micrometer diameter glass bead scatterers.<sup>10</sup> The tops of Phantom 1 and Phantom 2 are covered with a 25 $\mu$ m thick Saran<sup>TM</sup> film (Dow Chemical, Midland MI, USA) and a plastic-coated aluminum foil (made by Gammex Inc., Middleton, WI, USA), respectively. The acoustic properties of the phantoms were measured using single-element

transducers and a narrow-band substitution method on test cylinders manufactured at the same time as the phantom components (as with reference phantoms; see Chapter 2). The sound speed of the phantoms was 1492 m/s at 2.5MHz. The measured attenuation coefficients for the reference phantom (phantom 1) and for the sample (phantom 2) were  $0.55 \text{ dB}\cdot\text{cm}^{-1}\text{MHz}^{-1}$  and  $0.54 \text{ dB}\cdot\text{cm}^{-1}\text{MHz}^{-1}$ , respectively. Backscatter coefficients were measured using a broadband reference reflector method and single-element focused transducers (see Chapter 2).

RF echo data were analyzed to estimate the effective attenuation coefficient ( $\alpha_{\text{eff, sam}}$ ) using both the LSM and the MLSM methods. The results were compared with those estimated from the RPM. The expected value for the local attenuation coefficient estimated from laboratory measurements ( $\alpha_{\text{L, sam}}=0.54 \text{ dB}\cdot\text{cm}^{-1}\text{MHz}^{-1}$ ) was used as basis of comparison, since for a uniform phantom, the effective attenuation coefficient ( $\alpha_{\text{eff, sam}}$ ) equals the local attenuation coefficient ( $\alpha_{\text{L, ref}}$ ) throughout. We estimated the effective attenuation coefficient over the frequency band of interest using the linear fit for the LSM method,  $\alpha_0 f$ , and the power law fit for the MLSM method,  $\alpha_0 f^n$ . The effective attenuation coefficient divided by frequency at 6MHz  $\{\alpha_{o,eff}/f \mid_6\}$  was then estimated. Since the RPM yields an estimate for the “local” attenuation coefficient, its results were converted to effective attenuation coefficients by summing overlying local attenuation increments to the analysis window and then dividing by the depth of the window.

#### ***4.3.1.1 Results for the uniform phantom***

Figure 4.4 shows  $\{\alpha_{o,eff}/f \mid_6\}$  versus depth resulting from the RPM, LSM and the MLSM. The “expected” values are those obtained from the laboratory measurements. The results show that  $\{\alpha_{o,eff}/f \mid_6\}$  estimated using the MLSM is in good agreement with the expected value ( $0.54 \text{ dB}\cdot\text{cm}^{-1}\text{MHz}^{-1}$ ) and the values obtained from the LSM and the RPM.

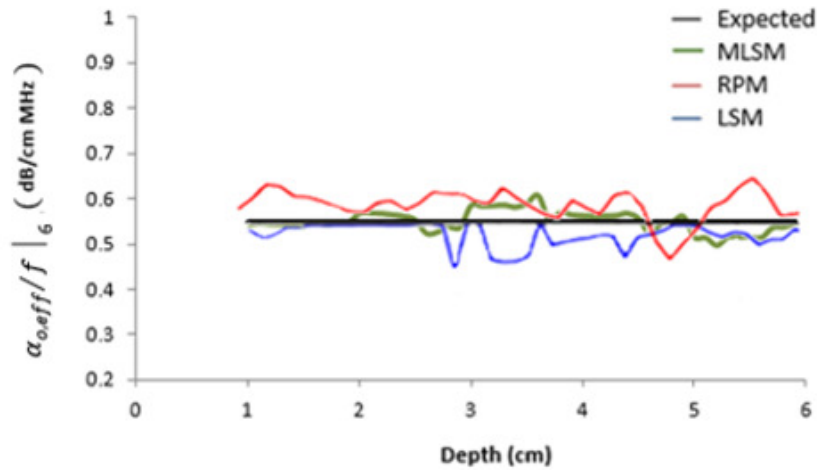


**Figure 4.4.** Effective attenuation coefficient at 6 MHz divided by the frequency for the uniform phantom

### 4.3.2. Evaluation of the MLSM in heterogeneous phantoms

To further test the method, two tissue mimicking phantoms with layers having different attenuation and backscatter coefficients were used to determine the sensitivity of the method to variations in backscatter and attenuation along the ultrasound beam paths. The first phantom, shown in Figure 4.5a, was designed to have three layers with equivalent backscatter properties, but with the middle layer having a higher attenuation coefficient ( $0.73 \text{ dB}\cdot\text{cm}^{-1}\text{MHz}^{-1}$ ) than the other two layers ( $0.48 \text{ dB}\cdot\text{cm}^{-1}\text{MHz}^{-1}$ ). The second three-layered phantom, shown in Figure 4.5b, was designed to have a uniform attenuation coefficient ( $0.52 \text{ dB}\cdot\text{cm}^{-1}\text{MHz}^{-1}$ ) in all layers but the middle layer has 6dB higher backscatter. The reference phantom data were acquired from the top layer of the constant backscatter phantom after rotating it 90 degrees to gain access to this uniform volume.

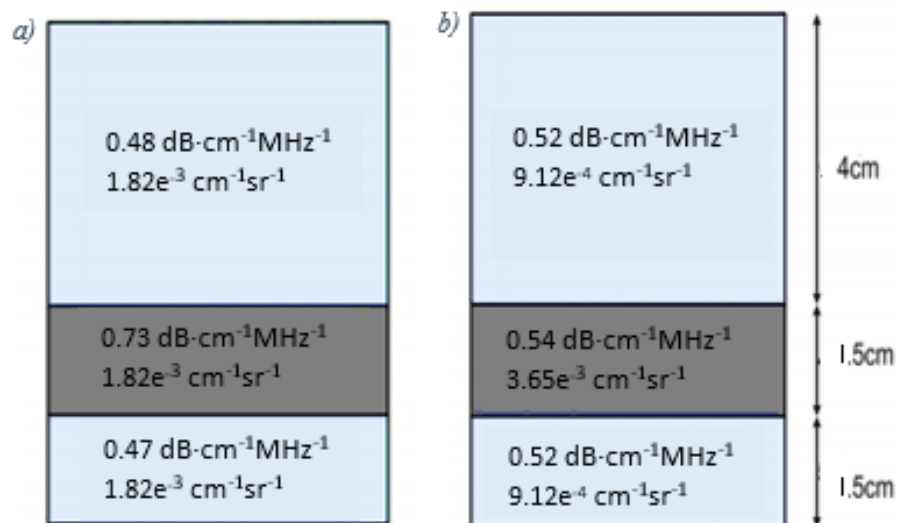


**Figure 4.5.** A schematic of the three layered phantoms: a) shows the phantom with constant backscatter and layered attenuation b) shows the phantom with constant attenuation and layered backscatter levels

Both phantoms consist of water based gel with condensed milk (to control attenuation)<sup>10</sup> and include 5-43 $\mu$ m glass spheres, with a median size of 24 $\mu$ m to provide scattering. The surface of each layer is bonded to the next, and the media have nearly identical mass densities and speeds of sound. Thus, the reflection losses at the interfaces are negligible. The phantoms are 9cm (lateral) x 9cm (elevation) x 7cm (axial) rectangular parallelepipeds and are stored in plastic containers filled with oil. The through-transmission estimates for the speed of sound, attenuation coefficients, and planar reflector-method backscatter coefficients (see Chapter 2) of the phantom layers were measured using 2.5cm-thick, 7.5cm-diameter test cylinders manufactured during construction of the phantoms. Attenuation coefficients were fit to linear functions of frequency, and the slopes of the attenuation coefficient vs. frequency (dB·cm<sup>-1</sup>MHz<sup>-1</sup>) were obtained over 3.5-10MHz. The characteristics of both phantoms are shown in Table 4.1.

**Table 4.1.** Properties of the constant attenuation and constant backscatter three-layer phantoms

Phantom	Scatterer diameter	Number density	Background material	Speed of sound	Attenuation
	in $\mu\text{m}$	in g/l		in m/s at 3.5 MHz	in (dB/cm MHz)
<b>Constant Backscatter Phantom</b>					
top	5 to 43	4	26% milk, 74%gel	1553	0.48
middle	5 to 43	4	50% milk, 50%gel	1564	0.73
bottom	5 to 43	4	26% milk, 74%gel	1555	0.47
<b>Constant Attenuation Phantom</b>					
top	5 to 43	2	3:1 gel to milk	1552	0.52
middle	5 to 43	8	3:1 gel to milk	1553	0.54
bottom	5 to 43	2	3:1 gel to milk	1552	0.52

**4.3.2.1. Results for heterogeneous phantoms**

The  $\{\alpha_{o,eff}/f \mid \epsilon\}$  in the first 4 cm of the variable attenuation coefficient phantom is the same as the local attenuation coefficient, after which there is a gradual increase (i.e. at the boundary between top and middle layer) in the measured and expected effective attenuation coefficient values due to the presence of a higher attenuation coefficient in the middle layer. This contributes to the total attenuation to any PER placed within this layer. This is followed by a decrease in the effective attenuation coefficient values after the bottom layer is reached as shown in Figure 4.6. The mean percent error of the MLSM (1.1%) was smaller than that of the LSM (1.8%) and the RPM (2.0%) for the phantom with constant backscatter and variable attenuation coefficient.

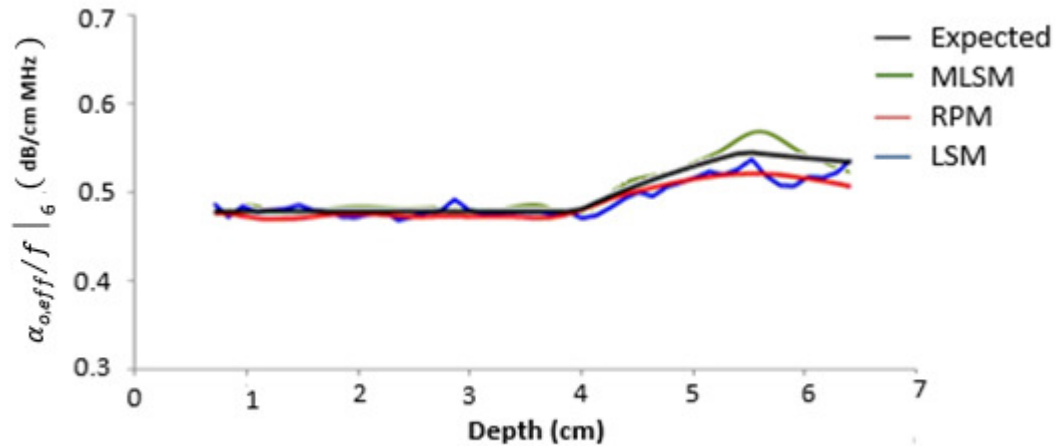


**Figure 4.6.** Effective attenuation coefficient at 6 MHz divided by the frequency for the layered attenuation phantom.

For the phantom with constant attenuation and a layered backscatter coefficient, errors were observed from the LSM and the RPM along the beam path. The bias presented in the LSM estimates (since the attenuation coefficient in the phantom material is not exactly proportional to  $f^1$ ,  $\alpha = \alpha_0 f^{1.16}$ ) was compensated for, by using the MLSM, resulting in smaller errors (estimates closer to the expected value). The homogeneity of backscatter assumed in the RPM is violated at the interfaces. Thus, a higher decrease in the attenuation estimates was noticed in the RPM beyond 4 cm due to large errors in local attenuation estimations occurring at the layer boundaries. A summary of the result is shown in Figure 4.7.

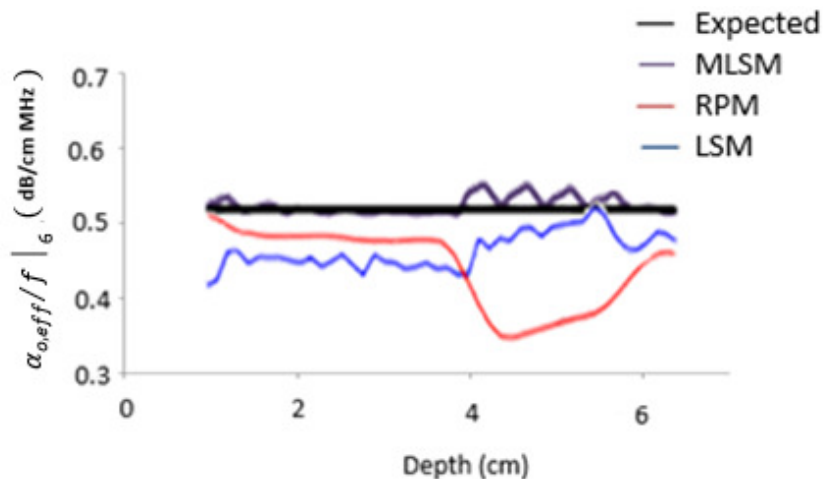


**Figure 4.7.** Effective attenuation coefficient at 6 MHz divided by the frequency for the constant attenuation phantom

BSCs were also estimated for the three-layer phantom with constant attenuation. Results for the middle and bottom layers are shown in Figure 4.8. The frequency dependencies of the measured backscatter coefficients obtained with the MLSM are in good agreement with results from the LSM, and both are in good agreement with the values predicted with Faran's theory and the lab values.

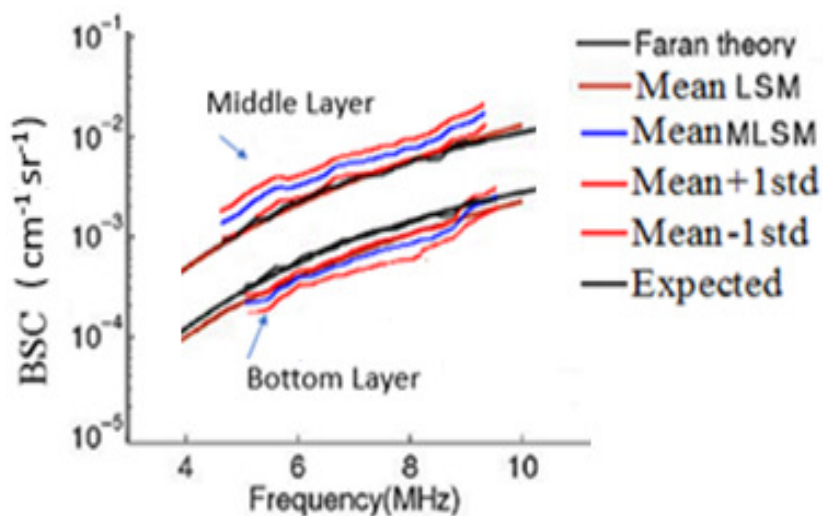


**Figure 4.8.** BSC estimates for the variable BSC phantom from Faran's theory, LSM, Lab measurements and MLSM

### 4.3.3. Evaluation of the MLSM on a complex phantom (ACR)

The method was further tested on a phantom that mimics breast tissue. The phantom was manufactured for the American College of Radiology (ACR).<sup>11</sup> It has masses of various sizes and shapes embedded in a simulated breast parenchyma, with a proximal layer of tissue-mimicking fat forming an irregular boundary, as shown in Figure 4.9. The simulated glandular parenchyma, and most lesions, contain solid particles of graphite (catalog no. 9039; Superior Graphite, Chicago, Ill) and glass beads (45–53  $\mu\text{m}$  in diameter; Potters Industries, Parsippany, NJ) dispersed in the gelatin. The fatty portions of the phantom contain oil droplets.

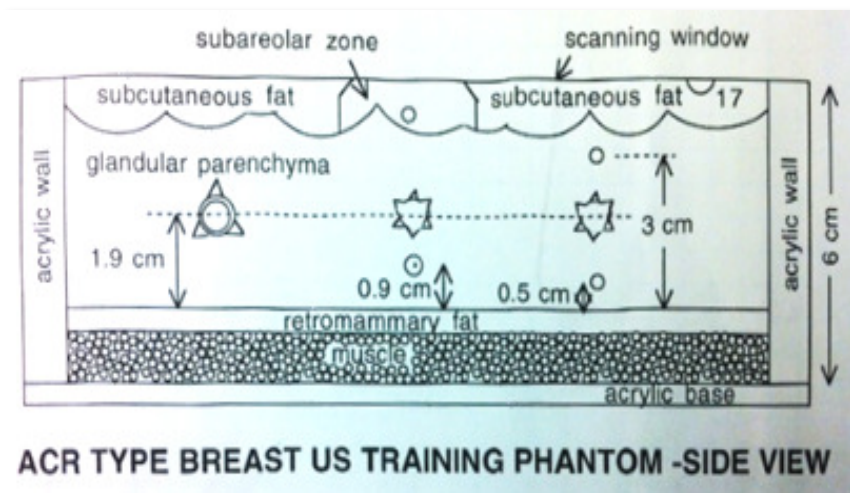


*Figure 4.9. schematic of the ACR phantom*

The phantom was scanned with a Siemens S2000 machine equipped with an 18L6 transducer at the same setting used for in vivo breast imaging to mimic the scanning condition for later experiments. The transmit focus was set to 4 cm and the transmit power was at 39%. There is no laboratory-measured BSC for the tissue mimicking fat, and it can't be predicted because of the presence of the oil droplets (with unknown size) in the base materials. Thus, we only compared attenuation estimates versus depth with lab values obtained using a narrow band substitution

technique on test samples manufactured at the time of the phantom (see Chapter 2). The laboratory-measured attenuation coefficients for the subcutaneous fat and the glandular parenchyma are shown in Table 4.2. The reference phantom was made with 6.4g of 3-45 $\mu$ m-diameter glass spheres homogeneously distributed in a 1600cc gel background. The background material consisted of an emulsion containing 70% safflower oil. The acoustic attenuation and sound speed of this reference phantom (speed of sound of 1492 m/s at 2.5MHz and an attenuation coefficient from 2-10 MHz versus frequency slope of 0.54 dB $\cdot$ cm<sup>-1</sup>MHz<sup>-1</sup>) were measured by single-element transducers on 2.5-cm thick test cylinders of the phantom materials that were poured at the time of its fabrication. A narrowband through-transmission technique was employed (see Chapter 2).

**Table 4.2.** Lab attenuation values for the ACR phantom

	Subcutaneous fat	Glandular Parenchyma
Power law attenuation fit	0.97 f <sup>0.87</sup>	0.28 f <sup>1.33</sup>
Linear attenuation fit	0.738 f	0.713 f
Speed of Sound (m/s)	1454	1567

#### 4.3.3.1. Results for the ACR phantom

The effective attenuation was estimated with the MLSM over a region spanning the subcutaneous fat and the glandular parenchyma as shown in Figure 4.10.

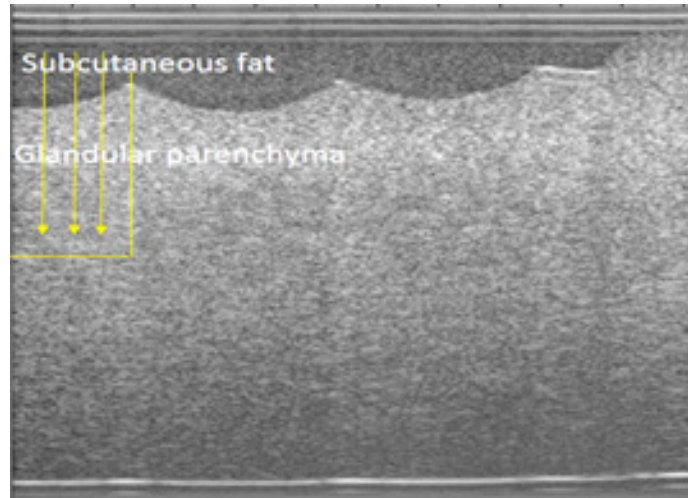


**Figure 4.10.** B-mode image of the ACR phantom

The effective attenuation estimated from the MLSM was compared with the lab value and with those obtained from the LSM. The results showed better agreement (over those obtained by the LSM) between the MLSM and the expected value. Data are plotted in Figure 4.11.

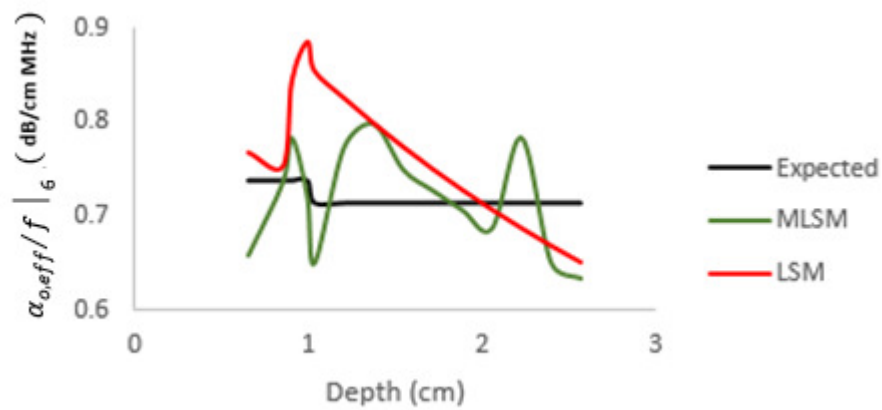


**Figure 4.11.** Effective attenuation coefficient at 6 MHz, divided by the frequency for the ACR phantom

#### 4.3.4. Evaluation of the MLSM on stacked test-cylinder phantoms

To further test attenuation estimates in layered media, we placed 3 test cylinders on top of each other in a water bath with their axes aligned. Each test cylinder contains material with a different frequency dependent attenuation that differs from  $f^1$ . A summary of the attenuation coefficient (from through-transmission measurements; see Chapter 2) for these materials is shown in Table 4.3. The stacked test cylinders were scanned with a Siemens S2000 equipped with a 6C1 curvilinear array transducer at the same setting used for *in vivo* kidney imaging to mimic those scanning conditions for comparison with later experiments. The focus was set to 2.0 cm and the transmit power was set to 63%. The effective attenuation was estimated with the MLSM for ROIs in each layer individually, and results were compared to the lab-measured attenuation values. The BSC was estimated after correcting for attenuation with the MLSM-measured attenuation values. Backscatter coefficient estimates obtained were compared to lab-measured BSC (measured using a broadband reference reflector method, see Chapter 2), and BSC estimated after correcting for attenuation with the LSM, and a “layer compensation method” (where a constant attenuation value is used to compensate for attenuation in each layer of material (tissue type) over the intervening tissue path).

**Table 4.3.** Lab Attenuation of the stacked test cylinders

	Layer 1	Layer 2	Layer 3
Attenuation coefficient	$0.313 f^{1.26}$	$0.502 f^{1.17}$	$0.288 f^{1.28}$

##### 4.3.4.1. Results for stacked cylinders

The effective attenuation estimated from the MLSM was compared with the lab value (over a 3-5 MHz range). The results for the MLSM and the expected value are shown in Figure 4.12.

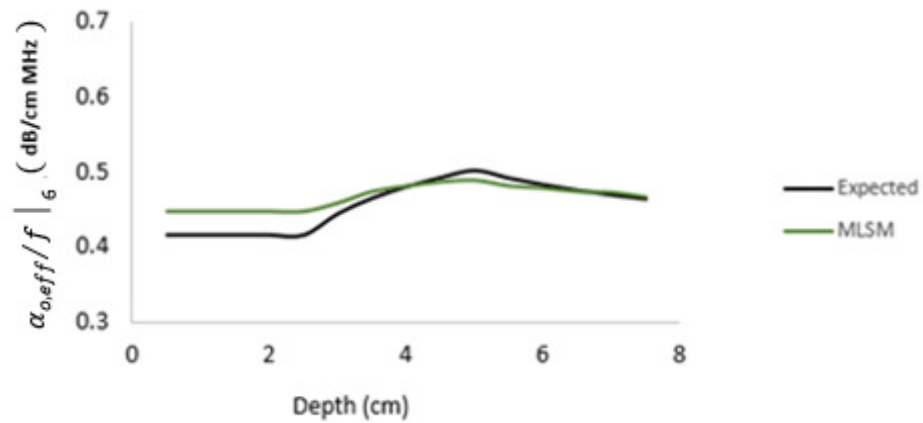


**Figure 4.12.** Effective attenuation coefficients at 6 MHz divided by the frequency for the stackable cylinders

Figure 4.13 shows the estimated BSC in each layer after correcting for attenuation with the MLSM, Nam's LSM, and the layer compensation method, and the lab backscatter measurements. The results show that the BSC estimated after correcting for attenuation with the MLSM is in good agreement in frequency dependence with the other methods.

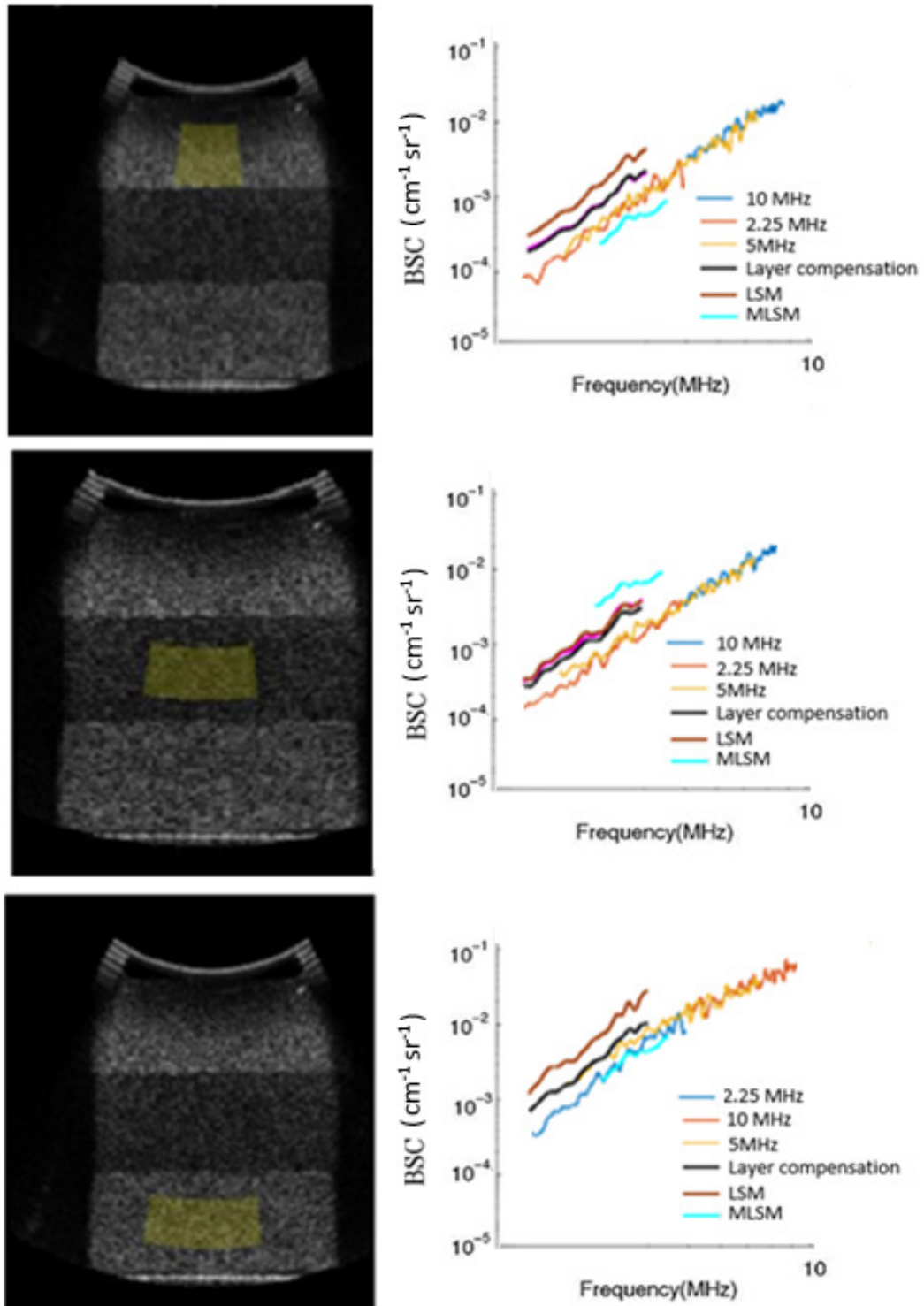


**Figure 4.13.** BSC estimated after correcting for attenuation with values from the MLSM versus other methods and lab values

## 4.4. *In vivo* Data acquisition

After testing the method on phantoms, we evaluated the MLSM on *in vivo* data from the breast and kidneys. Human subjects were scanned with a Siemens S2000 machine equipped with an 18L6 linear array transducer for *in vivo* breast data and a 6C1 curvilinear array transducer for the kidney data. A reference phantom was scanned at the same system settings to allow use of the Reference Phantom Method for estimating acoustic parameters. Offline analysis was done with routines written in MATLAB (Mathworks, Natick, MA). A rectangular parameter estimation region was identified. Echo signal power spectra were calculated as a function of depth for data segments within this region for both the sample and the reference phantom. The analysis bandwidth was selected such that the power spectral values were at least 10 dB above the noise floor. To calculate the echo signal power spectrum, a 4 mm x 4 mm power spectrum estimation region, overlapped by 75% both axially and laterally, and a multi-taper technique with a time-half bandwidth product (NW) of 4 was utilized (see Chapter 2).

### 4.4.1. Evaluation of the MLSM on *in vivo* breast data

In this preliminary study, 120 women scheduled for ultrasound-guided biopsy of previously detected breast tumors were recruited following a University of Wisconsin Institutional Review Board-approved, Health Insurance Portability and Accountability Act-compliant protocol (these are the same subjects and analysis methods used in Chapter 3). Subjects were scanned in the supine position in both radial (image plane aligned with breast ducts) and anti-radial (image plane perpendicular to ducts) planes.

To evaluate the MLSM on *in vivo* breast data, we selected 9 human subjects with homogeneous fat lobules and corrected for attenuation right below the fat lobule. A typical

example is shown in Figure 4.14. The attenuation-corrected power spectrum represents the power spectrum obtained after correcting for different attenuation values that can exist in the intervening tissue. It is obtained by multiplying the power spectrum by the exponential function of the attenuation,  $\exp(4 \alpha(f) z)$ . The accuracy of the MLSM was evaluated by comparing the attenuation-corrected power spectrum obtained using values estimated from this method versus the fat values ( $1.28 f^{0.73}$ ) from our previous study.<sup>12</sup>

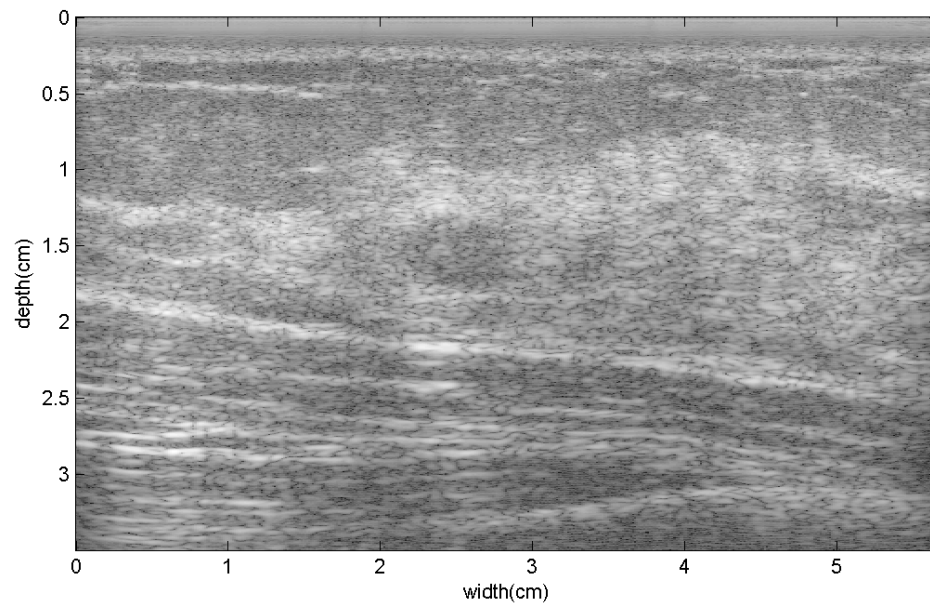


**Figure 4.14.** Example of in-vivo breast data scanned with a Siemens S2000 and an 18L6 transducer (subject 10 in table 7.2)

#### 4.4.1.1. Results for in-vivo breast data

Figure 4.15 shows the attenuation-corrected power spectra for the sample and the reference in a ROI within the fat lobule for a human subject with an infiltrating ductal carcinoma (IDC1 in Chapter 6). Attenuation compensation for the sample was done using the attenuation values of the subcutaneous breast fat<sup>12</sup> (light blue dots), and the attenuation values estimated using the MLSM (light blue line). The attenuation compensation for the reference was obtained by using

the lab-measured attenuation values. The results show that the attenuation-corrected power spectrum resulting from using the previously published fat values were in good agreement with those obtained after correcting for attenuation with values estimated using the MLSM.

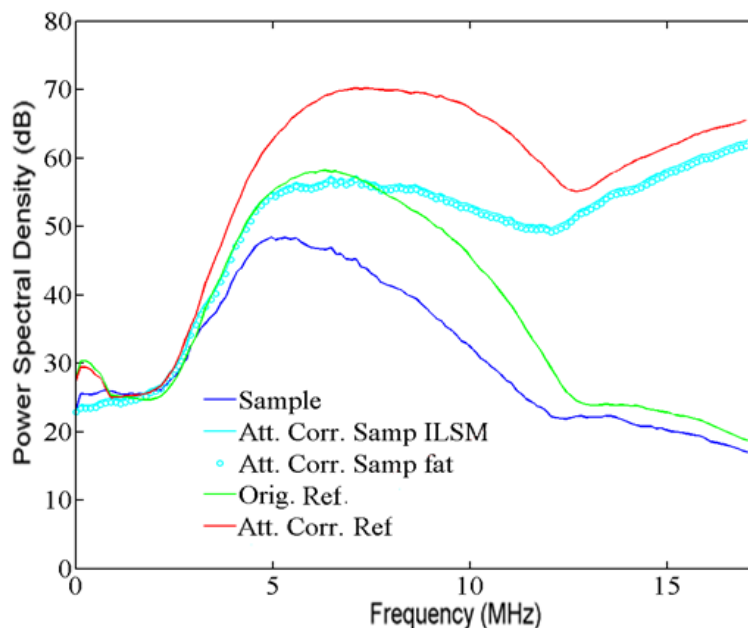


**Figure 4.15.** Examples of the attenuation corrected power spectra with fat values versus MLSM values for a ROI in the subcutaneous fat in a human subject with an infiltrating ductal carcinoma (IDC1 in Chapter 6).

#### 4.4.2. Evaluation of the MLSM on *in vivo* kidney data

To evaluate the method on echo signals acquired when scanning kidneys, we asked a nephrologist to scan a subject before a scheduled kidney transplant and provide us with the pathology-measured diameter of the glomeruli (Bowman's capsule; consistent with prior research<sup>12,13</sup>). With the patient lying on his/her side, scanning was performed with a Siemens S2000 equipped with a 6C1 curved array transducer. RF echo data was also obtained from a reference phantom. The reference phantom was made with 7.2g of 3000E beads distributed in a 1800cc agarose gel background. The sound speed, attenuation coefficient, and backscatter

coefficient of this reference phantom were established in the usual way (speed of sound of 1542 m/s at 2.5MHz and an attenuation coefficient from 2.5-10 MHz versus frequency slope of 0.51  $\text{dB}\cdot\text{cm}^{-1}\text{MHz}^{-1}$ ; see Chapter 2). Figure 4.16 shows a B-mode image of a kidney.

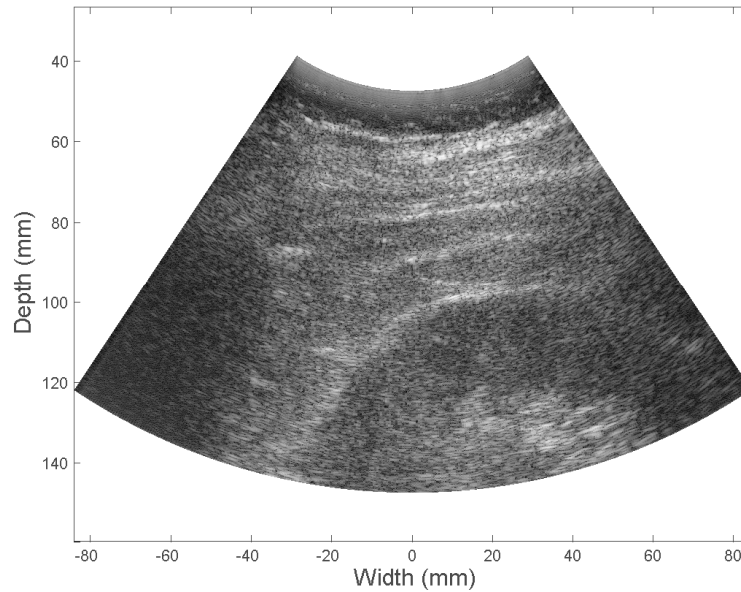


**Figure 4.16.** *B-mode image of the scanned kidney*

To evaluate the accuracy of the method, a blind estimation of the effective scatter diameter (ESD) was carried out after correcting for attenuation with the MLSM method. The ROI was chosen such that the acoustic beams were perpendicular to the kidney surface (i.e. parallel to the dominant nephron orientation) as previously reported for glomerular size estimation.<sup>12,13</sup>

#### **4.4.2.1. Results for in vivo kidney data**

The results in Figure 4.17 show an effective scatter diameter map and the distribution of the scatter sizes of the glomeruli estimated. The results show that the mean ESD was  $406 \pm 6 \mu\text{m}$  in good agreement with the pathology-measured glomerular size of 395-420  $\mu\text{m}$ .

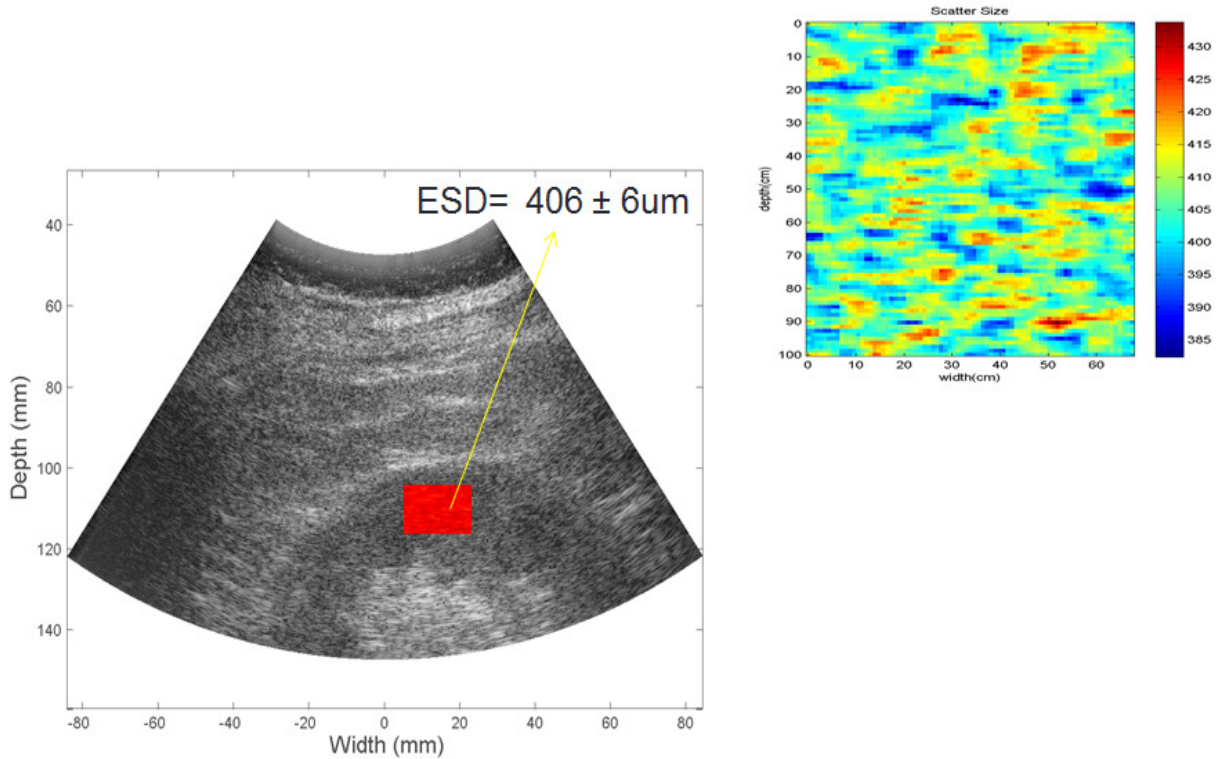


**Figure 4.17.** ESD map and the distribution of the scatter size of the glomeruli for in-vivo kidney patient

## 4.5. Discussion

It is important to account for ultrasound beam attenuation in the inhomogeneous tissue path between the transducer and a PER when determining backscatter coefficients in any tissue. The MLSM enables attenuation estimation for cases where the path is acoustically non-uniform. The method is effective even when the relationship between the attenuation and frequency is not linear. In this study, the MLSM was utilized to provide an estimate of the effective attenuation coefficient, defined as the total attenuation to the PER divided by the total path length. Theoretical assessment was performed and showed that the MLSM correctly estimated the attenuation values when the frequency dependence of attenuation in the sample was higher than  $f^1$ . Comparisons were made with results obtained from a reference phantom method and least squares method for uniform and

heterogeneous phantoms. The method was also evaluated on complex phantoms, including phantoms with a frequency dependence of attenuation that differs from  $f^1$ . Finally, we applied the technique to *in vivo* breast and kidney data.

As expected, attenuation coefficients measured using the RPM are in good agreement with actual values when the test sample is homogeneous with constant backscatter throughout the sample. However, the RPM estimates of attenuation and backscatter were erroneous when there was backscatter contrast along the beam path. The piece-wise linear frequency dependence approach with the MLSM solves the problem that causes the LSM to lose accuracy when the assumption of attenuation being proportional to frequency is not met (i.e. LSM assumes the attenuation coefficient is proportional to frequency. Errors result in its use when the frequency dependence of attenuation in the path between the transducer and region of interest differs from  $f^1$ ).

The MLSM applied to *in vivo* breast data showed a good agreement between the attenuation corrected power spectra versus those obtained from correction using the average values for fat. Also, applying the MLSM on *in vivo* kidney data resulted in good agreement in the ESD estimated and the pathology lab measurement of the glomeruli sizes. This shows promise for the case of estimating backscatter coefficients without prior knowledge of the attenuation along the beam path.

## 4.6. Conclusion

The MLSM method described here provided accurate estimates of the total attenuation along the beam path. The MLSM showed high accuracy for uniform phantoms, complex phantoms, phantoms with higher frequency dependence, and *in vivo* data. The MLSM provided

the closest estimates to the expected value compared to other methods. These promising initial results encourage further development and testing for *in vivo* use.

## 4.7. References

1. Oelze, M.; O'Brien, W.; Frequency-dependent attenuation-compensation functions for ultrasonic signals backscattered from random media. *J Acoust Soc Am* **2002**, 111(5), 2308-2319.
2. Wear, K.; Characterization of trabecular bone using the backscattered spectral centroid shift. *IEEE Trans UltrasonFerroelectrFreq Control*. **2003**; 50(4):402–407. [PubMed: 12744396]
3. Lu, Z.; Zagzebski, J.; Madsen, E.; Dong, F.; A method for estimation an overlying layer correction in quantitative ultrasound imaging. *Ultrason Imaging*. **1995**; 17(4):269–290.
4. Bigelow, T.; Oelze, M.; O'Brien, W.;. Estimation of total attenuation and scatterer size frombackscattered ultrasound waveforms. *J AcoustSoc Am*. **2005**; 117(3):1431–1439.
5. Nam, K.; Zagzebski, J.; and Hall, T.; Simultaneous Backscatter And Attenuation Estimation using A Least Squares Method With Constraints, *Ultrasound in Med. & Biol.*, **2011**, Vol. 37, No. 12, pp. 2096–2104.
6. Wirtzfeld, L.; Nam, K.; Yassin, L.; et al., Techniques and Evaluation From a CrossPlatform Imaging Comparison of Quantitative Ultrasound Parameters in an In Vivo Rodent fibroadenoma Model, *IEEE Trans UltrasonFerroelectrFreq Control*, **2013**; 60(7)
7. Yao, L.; Zagzebski, J.; Madsen, E., Backscatter coefficient measurements using a reference phantom to extract depth-dependent instrumentation factors. *Ultrason Imaging* **1990**, 12, 58-7
8. Brunke, S.; Insana, M.; Dahl ,J.; Hansen, C.; Ashfaq, M.; Emert, H.; An ultrasound research 5 interface for a clinical system. *IEEE Trans. Ultrason. Ferroelectr. Freq. Control* **2007**; 54:198-6 210

9. Kofler, J.; Madsen, E., Improved method for determining resolution zones in ultrasound phantoms with spherical simulated lesions. *Ultrasound Med Biol* **2001**, *27*, 1667-1676 .
10. Madsen, E.; Hobson, M.; Shi, H.; Varghese, T.; Frank, G.; Stability of heterogeneous elastography phantoms made from dispersions in aqueous gels. *Ultrasound Med Biol.* **2006**; *32*(2):261–270.
11. Madsen, E.; Berg, W.; Mendelson, E.; Frank, G.; Anthropomorphic breast phantom for quantification of investigators for ACRIN protocol 6666, *Radiology* **2006**, *239*(3), 869-874.
11. Nasief, H.; Rosado-Mendez, I.; Zagzebski, J.; Hall, T.; Acoustic Properties Of Breast Fat. *J. Ultrason. Med.*, 2015, *34*(11). <http://doi.org/10.7863/ultra.14.07039>
12. Hall, T. ; Insana, M. ;Harrison, L.; et al.; Ultrasonic measurement of glomerular diameters in normal adult humans. *Ultrasound in medicine & biology*, *22*(8), 987-997, **1996**.
13. Garra, B.; Insana, M.; Sesterhenn, I.; Hall, T.; Wagner, R.; et al. Quantitative ultrasonic detection of parenchymal structural change in diffuse renal disease. *Invest Radiol* **1994**; *29*:134-140.

## Chapter 5: Detecting coherence and examining anisotropy

*A Portion of chapter is published as:*

*Nasief, H.; Rosado-Mendez, I.; Zagzebski, J.; and Hall, T.; A Quantitative Ultrasound-Based Multi-Parameter Classifier for Breast Masses, IEEE, under review*

QUS provides quantitative parameters that relate to visual features in a B-mode image. In addition, it offers observer- and system- independent parameters that can enhance the overall diagnostic accuracy. The estimation of QUS parameters generally assumes that echo signals arise from diffuse (incoherent) scattering conditions, and thus, the signals may be classified as stationary. However, these assumptions are not always met in the human breast. Although we constrain our QUS analysis to homogeneous ROI's, some amount of signal coherence, not reliably detected by human interpreters, may be present due to, for example, periodic structures, a low scatterer number density or strong isolated reflectors. This can affect the precision of QUS parameter estimations and limit the reproducibility of the results.

Tissues are usually composed of both spatially structured and random distributions of heterogeneities in density and compressibility. Thus, the backscattered echo signals contain different levels of coherent and incoherent scattering. Several techniques have been proposed to quantify properties of the structured component. For instance, Insana et al.<sup>1</sup> proposed the intensity spectrum method, Varghese and Donohue,<sup>2</sup> proposed a spectral correlation method, Wear et al.<sup>3</sup> proposed autoregressive spectrum analysis and cepstrum estimation, and Pereira et al.<sup>4</sup> proposed a singular spectrum analysis. Most of these techniques focused on estimating parameters from situations in which the coherent component is caused by a quasi-periodic array of scatterers with resolved spacing.<sup>5</sup> Other researchers have investigated the ratio of the energy in the echo signal coming from the coherent component to the energy coming from the diffuse component.<sup>1,6,7,8</sup>

Different scattering scenarios can be present in in vivo data. In the case of diffuse scattering, the echo amplitudes are stationary. If for example, a quasi-periodic lattice of scatterers is present in addition to the randomly distributed scatterers, the mean scatterer spacing among the organized scatterers is less than the size of the resolution cell. Consequently, all the resolution cells within the parameter estimation region will have approximately the same underlying statistics (invariant with position). Therefore, the echo signal will still be stationary.

In the case of a quasi-periodic lattice of scatterers with mean scatterer spacing larger than the resolution cell, the periodically spaced scatterers are sampled by the mean scatterer spacing. Thus, the autocovariance function of the echo amplitude depends on the absolute position of the scatterers. Various studies have demonstrated that properties of the structured field of scatterers, such as the mean scatterer spacing, can be used to discriminate among different pathological processes.<sup>2-3,9</sup>

In the case where the acoustic pulse “meets” a structure with significantly larger scattering cross section than that of the diffuse component, such as a microcalcification in the breast or a tissue interface acting as a specular reflector, the autocovariance function of the echo amplitude depends on the absolute position of the resolution cell, thereby making the signal non-stationary.

Recent work in our group resulted in an algorithm that automatically decides whether at each location of the parameter estimation region there is a significant source of coherent scattering, and if so, what the nature of this source is, i.e., which of the cases in Fig. 5.1 best describes the scattering scenarios.<sup>10-11</sup> When a signal is stationary, the statistics of the echo signal are the same among the different samples within the region of interest. When a signal is non-stationary, the statistics will vary with the location of the PER. Thus, the identification and grouping process

identifies the presence of coherent scattering and characterizes its nature.<sup>10-11</sup> In this chapter, we will test for the presence of coherence and estimate QUS parameters that can describe the underlying scattering condition in breast tissue.

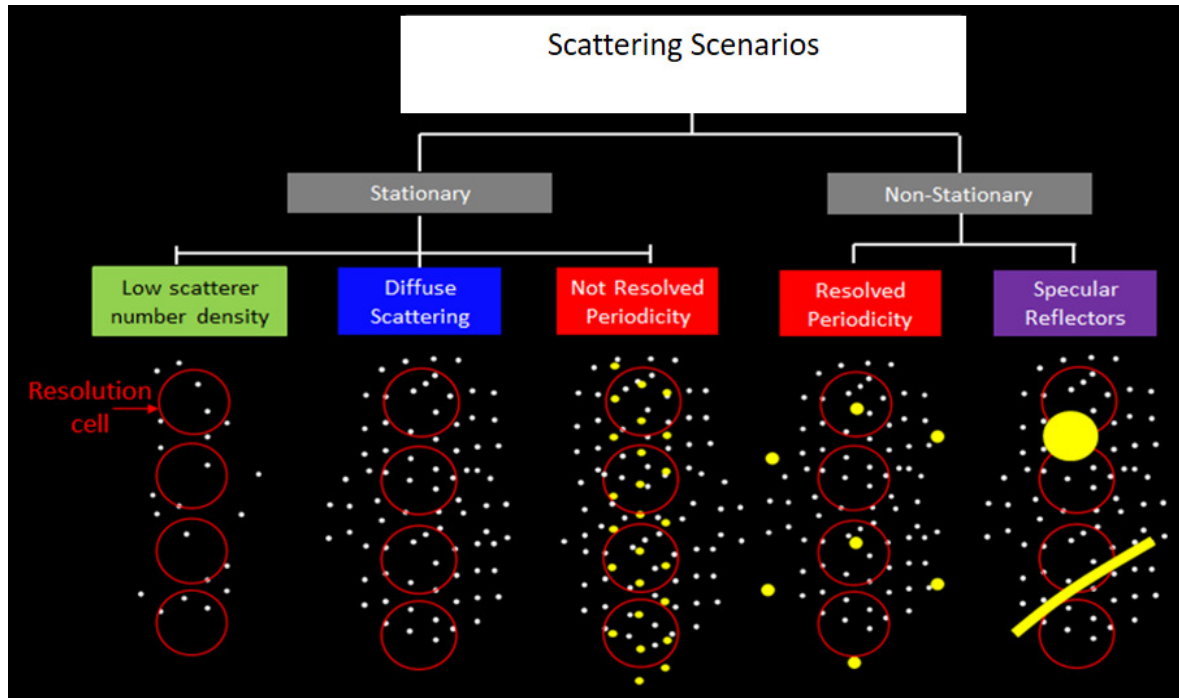


**Figure 5.1.** Different scattering scenarios that can be present in in-vivo breast tissue (Figure from Rosadomendez, 2014)<sup>12</sup>

Another QUS challenge arises from the fact that the QUS parameters estimated within a ROI inside the tumor boundaries are typically assumed to be isotropic, enabling data from various angles to be averaged to improve the precision of the estimates and reduce the variability. However, if anisotropy is present, averaging data from multiple angles of interrogation (spatial compounding) can increase bias and variance in parameter estimates. Therefore, examining parameter estimates as a function of angle of incidence is another critical step to estimate the

characteristics of tissue. In this chapter, we also introduce and describe methods that can be used to test for anisotropy in parameter estimates.

## 5.1. Coherence-related QUS parameters estimation

In this section, we outline methods to estimate potential QUS parameters (the maximum collapsed average of the generalized spectrum, the signal to noise ratio (SNR) of the echo signal envelope, and the Nakagami shape parameter,  $m$ ) that can be used to quantify coherent scattering from either stationary or nonstationary processes. A description of each of these QUS parameters is shown below.

### 5.1.1. Maximum collapsed average (maxCA) of the generalized spectrum

To quantify coherence within selected ROIs due to a non-stationary process, the generalized spectrum was utilized. Researchers have used the generalized spectrum and the shape of the “collapsed average” to determine the presence of such coherent sources.<sup>13-15</sup> To derive the generalized spectrum, the Fourier transform of the RF echo signal and its conjugate is computed.<sup>11,12</sup> These are plotted on the bi-frequency plane, as shown in Figure 5.2. The values assigned to points in this plane are related to the degree of correlation between frequency components  $f_i$  and  $f_j$ .<sup>9,14,16-17</sup> The elements off the main diagonal of the bi-frequency plane shown in Figure 5.2. depend on various factors, including the relative power of the coherent component to that of the incoherent component, and the pulse spectrum and how it is modified while it propagates through tissue.

In the case of a stationary process, there is no correlation among different frequency components, and this is represented by a zero value in the off-diagonal region of the generalized

spectrum (i.e. the expected value of the diffuse scatterer component does not contribute significantly to the off-diagonal values of the generalized spectrum). The covariance matrix of wide-sense stationary signals is diagonalized under Fourier transformation, and elements of its main diagonal correspond to the discrete power spectral density. Thus, the diagonal of the generalized spectrum in the bi-frequency plane ( $f_1=f_2$ ), has a real and positive value and is equivalent to the power spectral density, which is the average power of the stationary random process expressed as a function of frequency. However, when the signals are non-stationary, different frequency components become correlated, and the off-diagonal values of the generalized spectrum are different from zero. The detection of nonzero values in the off-diagonal elements is used to indicate the presence of non-stationary trends in the backscattered echo signal.<sup>17</sup>

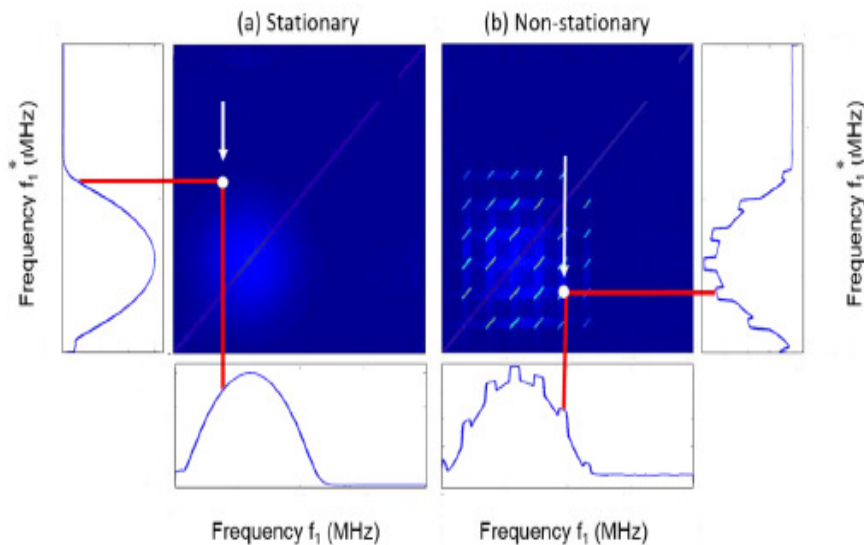


**Figure 5.2.** Diagram illustrating the amount of correlation between two different frequency components for two cases: (a) a stationary signal and (b) a non-stationary signal (Figure from Rosadomendez, 2014)<sup>12</sup>

A nonparametric approach, the “collapsed average” of the generalized spectrum, is used to test for coherence. The collapsed average representation is obtained by averaging the complex values of the generalized spectrum along diagonals, i.e., points with equal  $\Delta f = f_1 - f_2$ , where  $f_1$  and

$f_2$  are frequency values in the real and imaginary planes of the spectrum.<sup>18-22</sup> In the case of diffuse scattering, the frequency components of the contribution of these scatterers to the total echo signal are uncorrelated.<sup>8</sup> Thus, the off-diagonal values of the generalized spectrum are close to zero and the values of the collapsed average at  $\Delta f \neq 0$  are also close to zero.<sup>8,20</sup> When the echo signal arises from a non-stationary process, different frequency components of the signal spectrum become correlated and the off-diagonal values differ significantly from zero.<sup>2,8,18,23</sup> In the collapsed average, the peak at  $\Delta f = 0$  MHz corresponds to the main diagonal of the generalized spectrum as shown in Figure 5.3. The presence of peaks in the collapsed average at frequencies ( $\Delta f$ ) other than 0 MHz indicates the presence of non-stationary coherence. The maximum in the collapsed average of the generalized spectrum within a search region (defined by the available bandwidth) is then determined and examined as a potential QUS parameter to classify different tumor types (will be discussed later in Chapter 6).

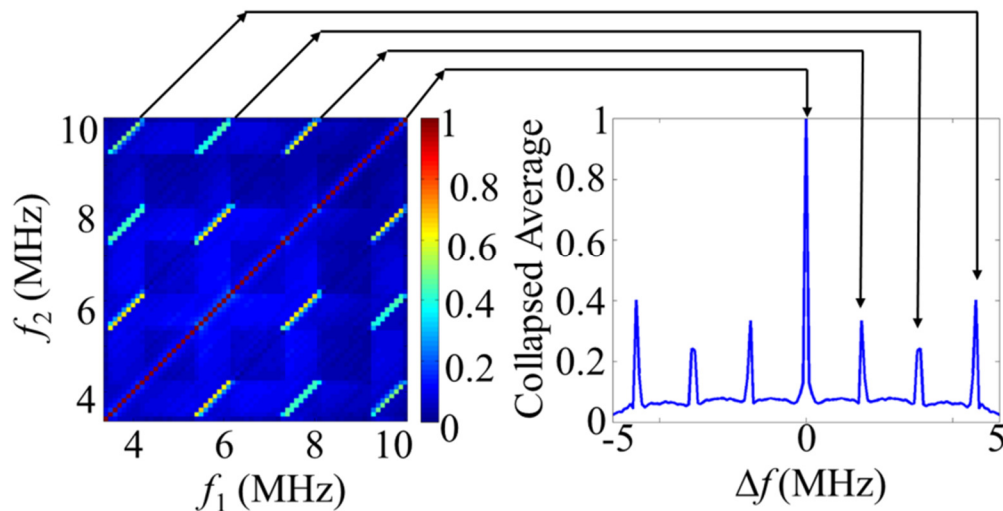


**Figure 5.3.** The generalized spectrum and the collapsed average (Figure from Rosado-Mendez<sup>12</sup>)

### 5.1.2. Signal amplitude Signal to Noise ratio (SNR)

To quantify coherence due to a stationary process, the signal to noise ratio (SNR) of the echo signal envelope was utilized as a model-free parameter to classify different scattering conditions. The signal displayed in the conventional B-mode image is the echo amplitude  $V(t)$  (after logarithmic compression). The demodulated signal  $y_d(t)$ , i.e., the signal from which the carrier sinusoid has been removed, can be expressed in terms of its amplitude  $V(t)$  and phase  $\xi(t)$ :<sup>24</sup>

$$y_d(t) = y(t)e^{-j2\pi f_c t} = V(t)e^{j\xi(t)} \quad (5-1)$$

Assuming that the number of scatterers within the resolution cell is asymptotically large, and that there is a uniform distribution of phase, under the assumption of the Central Limit Theorem, the real and imaginary parts of the demodulated signal  $y_d(t)$  are zero-mean Gaussian distributed random variables with the same variance. As a consequence, the probability density function of the amplitude  $V(t)$  of  $y_d(t)$  becomes a Rayleigh distributed random variable:<sup>6,24</sup>

$$P_{\text{Rayleigh}}(V) = \frac{V}{\sigma^2} \exp\left\{-\frac{V^2}{2\sigma^2}\right\} \quad (5-2)$$

where the variance  $\sigma^2$  is related to the mean of the squared scattering cross sections of the scatterers within the resolution cell.

The mean  $\mu_V$  and variance  $\sigma_V^2$  of the Rayleigh distributed amplitude  $V$  are:<sup>17</sup>

$$\begin{aligned} \mu_V &= \sqrt{\frac{\pi\sigma^2}{2}} \\ \sigma_V^2 &= \left(\frac{4-\pi}{2}\right)\sigma^2 \end{aligned} \quad (5-3)$$

Thus, the echo envelope amplitude signal-to-noise ratio (SNR) has a fixed value of: <sup>17,24</sup>

$$\text{SNR}_v = \frac{\mu_v}{\sigma_v} = \sqrt{\frac{\pi}{4-\pi}} = 1.913 \quad (5-4)$$

Based on the SNR, stationary echo signals can be divided into three cases. Diffuse scattering (e.g., echo signals from the reference phantom) are consistent with Rayleigh statistics, with the ratio of the mean echo envelope amplitude to its standard deviation equivalent to 1.91. Low scatterer number density conditions are “Pre-Rayleigh” with a SNR < 1.9. Unresolved periodicity is “post Rayleigh” with a SNR > 1.9.<sup>17</sup> Thus, the echo signal envelope SNR value for each tumor in the human subject population was determined. The differentiation in SNR values between various scattering conditions suggested testing it as a potential QUS parameter to classify different tumor types (as discussed in Chapter 6).

### 5.1.3 Nakagami shape parameter (Nakagami $m$ )

The homodyned-K distribution is the most general model for stationary backscattered echo signals. The parameters associated with it provide a direct quantification of structural properties of the array of scatterers. However, it lacks a closed-form expression for its mathematical representation which complicates the estimation of its parameters.<sup>25,26</sup> Methods for estimating its parameters have been improving in terms of the accuracy and precision since it was introduced by Dutt and Greenleaf in 1994.<sup>7</sup> For instance, Hruska and Oelze<sup>27</sup> proposed a method that relies on the closed-form expression of fractional moments of the homodyned-K distribution. In this method, theoretical expressions for the SNR, skewness, and kurtosis of fractional powers of the echo amplitudes are obtained for a range of values of the homodyned-K distribution parameters.

Then, the SNR, skewness and kurtosis are measured from echo data from the material (tissue) of interest. The measured and theoretical values of these parameters are compared. An important limitation of this method occurs when trying to estimate a  $k$  value, estimate of the ratio of coherent to incoherent backscatter signal energy, close to zero (if trying to identify a PER with diffuse scattering) as it results in a bias in the estimates.<sup>27</sup> Another complication that was found in this method was the difficulty in computing the theoretical values of the SNR, skewness, and kurtosis.

An alternative to the general homodyned-K distribution is the Nakagami distribution, which has been proposed as a good approximation to the homodyned-K.<sup>25,28-30</sup> Its advantages over the homodyned-K distribution are that the Nakagami distribution probability density function has a closed-form expression, thus making it mathematically tractable, and its parameter estimation is relatively easy. Thus, the Nakagami model was utilized here to analyze stationary features. The probability density function proposed by Nakagami et al.<sup>31</sup> has the following form:

$$P_{Nakagami}(A | m, \Omega) = \frac{2m^m}{\Gamma(m)\Omega^m} A^{2m-1} \exp\left\{-\frac{mA^2}{\Omega}\right\} \quad (5-5)$$

where the amplitude is  $A$ ,  $m$  is called the “shape parameter”, and  $\Omega$  is a “scaling parameter”.

Various papers have demonstrated the effectiveness of the Nakagami parameter ‘ $m$ ’ to distinguish zones with Post-Rayleigh and Pre-Rayleigh statistics from those with Rayleigh statistics.<sup>25-26,30</sup> Shankar et al.<sup>26</sup> demonstrated that the parameter  $m$  can distinguish zones with different scatterer concentrations as long as the Rayleigh limit has not been reached. Most of the applications of the Nakagami distribution in ultrasound estimate the Nakagami parameter ‘ $m$ ’ as the squared SNR ratio of the echo signal intensity.<sup>25-26,30,32</sup> However, the simplicity of the Nakagami probability density function makes it possible to define the maximum likelihood

estimator (MLE) for the shape parameter ‘ $m$ ’. The joint probability density function for a vector  $V$  composed of a set of  $K$  independent and identically distributed samples of the amplitude  $V$  is:

$$p(\mathbf{V} | m, \Omega) = \prod_{k=1}^K \frac{2m^m}{\Gamma(m)\Omega^m} V_k^{2m-1} \exp\left\{-\frac{mV_k^2}{\Omega}\right\} \quad (5-6)$$

The MLE estimators are obtained by finding the values of  $m$  and  $\Omega$  that maximize  $p(V|m, \Omega)$ . After taking the logarithm of  $p(V|m, \Omega)$  and the derivative with respect to  $\Omega$  we get:

$$\hat{\Omega} = \overline{V^2} \quad (5-7)$$

where the overbar indicates the sample average and the hat  $\hat{\cdot}$  indicates an estimate.

Repeating the same with  $m$  and substituting for  $\Omega$ , the MLE estimator can be obtained by minimizing the difference between

$$\ln \hat{m} - \psi(\hat{m}) = \ln \overline{V^2} - \overline{\ln V^2} \quad (5-8)$$

where  $\psi(x)$  is the digamma function of  $x$ .<sup>33</sup>

The function on the left side of Eq. 5-8 increases monotonically with ‘ $m$ ’. Thus, a simple binary search algorithm can be used to obtain the value of ‘ $m$ ’. Researchers demonstrated that the MLE estimator of ‘ $m$ ’ provided the minimum squared error of the  $m$  value when compared to other estimators, such as the one based on the squared SNR of the echo signal intensity. The value of ‘ $m$ ’ is mainly defined by scattering statistics:  $m = 1$  for Rayleigh statistics,  $m < 1$  for pre-Rayleigh statistics, and  $m > 1$  for post-Rayleigh conditions.<sup>32</sup> Thus, the MLE estimator of the Nakagami parameter ‘ $m$ ’ is used here to determine the value of ‘ $m$ ’ for each tumor. Like the SNR, the Nakagami shape parameter ‘ $m$ ’ can be a potential QUS parameter to classify different tumor types, and this is examined in Chapter 6.

## **5.2. *In vivo* Data Acquisition**

In this preliminary study, 43 subjects with biopsy proven breast masses were included in the analysis. Data acquisition of the *in vivo* subjects is described in detail in Chapter 2. The masses included 27 fibroadenomas, 10 invasive (or infiltrating) ductal carcinomas, 2 invasive lobular carcinomas, 1 adenocarcinoma, 1 intracystic papillary carcinoma, and 2 ductal carcinomas in situ. Once the echo signal data were acquired, the envelope of the RF data was utilized to estimate the QUS parameters of interest. Offline analysis was performed using MATLAB (Mathworks, Natick, MA). The full ROI was used as our PER for estimating the QUS parameters associated with coherence to get a single estimate.

### **5.2.1. Results for coherence related QUS parameters**

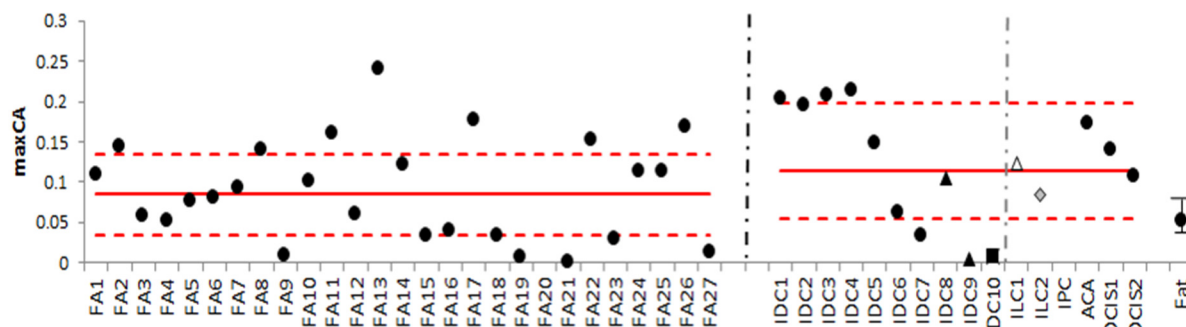
All subjects in this study had masses that were categorized as US-BIRADS 4 except subjects 23, 24, 33, and 40, whose masses were categorized as US-BIRADS 3, 5, 1, and 5, respectively. Pathology identification of the tumor type was based on core biopsy specimens. A summary of the results obtained from the 43 subjects for each of the parameters is shown in Table 5.1 below.

**Table 5.1.** Nakagami  $m$ , maxCA and SNR Values for each subject included in the study, FA: fibroadenoma, ACA: adenocarcinoma, IDC: infiltrating ductal carcinoma, ILC: invasive lobular carcinoma, IPC: intracystic papillary carcinoma, and DCIS: ductal carcinoma in situ

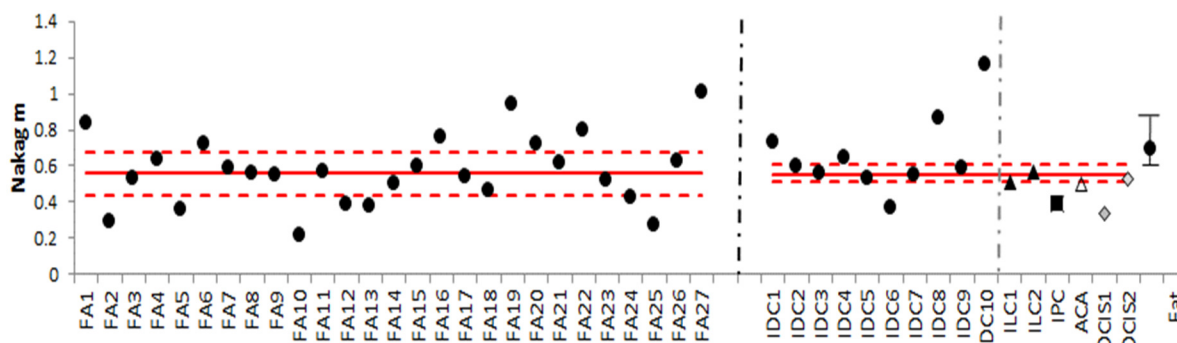
Fibroadenoma					carcinoma				
AITT dB-cm <sup>-1</sup> MHz <sup>-1</sup>	ESD ( $\mu$ m)	ESDHI ( $\mu$ m)	ABSC (cm <sup>-1</sup> sr <sup>-1</sup> )	Subject order	AITT dB-cm <sup>-1</sup> MHz <sup>-1</sup>	ESD ( $\mu$ m)	ESDHI ( $\mu$ m)	ABSC (cm <sup>-1</sup> sr <sup>-1</sup> )	subject order
0.74	82	14.2	0.0213	22	1.85	90	10.1	0.005	18
1.25	83	13.6	0.046	35	2.19	68	8.5	0.039	39
1.55	109	15.8	0.036	37	2.17	58	13.1	0.041	40
1.57	125	13.8	0.0019	9	0.85	54	14	0.115	36
0.68	60	14.2	0.0025	27	1.47	100	12.2	0.075	34
0.69	107	10.4	0.0076	28	1.48	69	12.3	0.007	11
1.94	147	12.1	0.048	41	0.63	96	2.4	0.006	25
0.71	144	4.1	0.0003	13	1.09	82	11.1	0.002	42
1	87	15.1	0.0094	15	2.2	87	6.2	0.001	17
0.85	112	13.6	0.009	21	1.03	80	11.3	0.002	19
0.76	87	10.9	0.003	30	0.74	95	5.1	0.016	26
1.24	119	11.8	0.039	31	0.52	87	6.2	0.015	24
1.19	117	15.3	0.046	43	0.5	59	7.5	0.028	33
1.92	166	11.8	0.0013	12	1.3	77	13.6	0.94	10
1.3	90	15.6	0.01	14	1.92	79	18.6	0.01	38
1.04	93	13.1	0.0212	32					
0.42	83	20	0.0143	16					
1.01	110	9.5	0.0003	29					
0.36	95	14.5	0.0221	23					
0.89	97	10.5	0.0092	20					

Summary plots of the individual QUS parameter estimates obtained from each subject are shown in Figure 5.4. Data are presented in these plots ordered from the smallest to largest ROI size to illustrate any potential trend in parameter estimates with ROI size. Parameter values for breast fat<sup>35</sup> are included in the plots (data point on the right of the plot) for comparison.

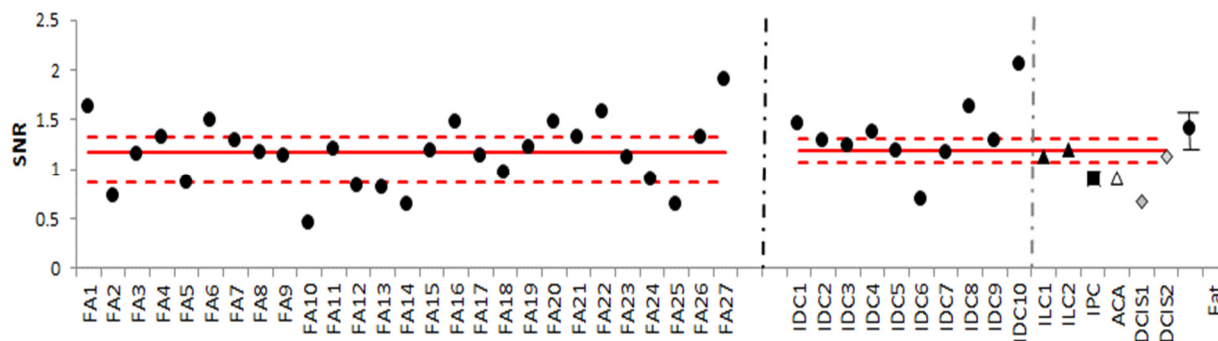
The median SNR estimate of the biopsy confirmed fibroadenomas ( $1.17 \pm 0.64$ ; median  $\pm$  inner-quartile range) was similar to the value in carcinomas ( $1.2 \pm 0.31$ ), and is close to the median value found for breast fat ( $1.4 \pm 0.25$ ). The median Nakagami  $m$  estimate among fibroadenomas ( $0.56 \pm 0.29$ ) was not different from the values in carcinomas ( $0.56 \pm 0.15$ ), and both were close to the median value found in breast fat ( $0.68 \pm 0.15$ ). The median maxCA estimate among fibroadenomas ( $0.09 \pm 0.09$ ) was comparable to the value in carcinomas ( $0.11 \pm 0.09$ ), and both are not significantly different from the median value found in breast fat ( $0.05 \pm 0.03$ ).



a) maxCA estimates for each subject ordered from smallest to largest ROI size



b) Nakagami m estimates for each subject ordered from smallest to largest ROI size



c) SNR estimates for each subject ordered from smallest to largest ROI size

**Figure 5.4.** Plots of the individual QUS parameter estimates for each subject ordered from smallest to largest ROI size. The same ROI was used for all parameter estimates for an individual subject (e.g., FA1 is the fibroadenoma with the smallest ROI). Fibroadenomas (FA) are shown separately from cancers. Cancers are grouped together by type: Invasive ductal carcinoma (IDC); Invasive lobular carcinoma (ILC); intracystic papillary carcinoma (IPC), and ductal carcinoma in situ (DCIS). The solid horizontal lines show the median value of that parameter (separately for fibroadenomas and carcinomas), and the dashed lines show the inner quartile range of values.

Maps were also generated for each of these parameters to show a color encoding representation of them. An example for one of the subjects (FA20 in Chapter 6) is shown in Figure 5.5. The color encoding maps show that the results from the three parameters agree with each other. For instance, the same area (outlined in the figure) that was color encoded as having diffuse scattering based on the maxCA (dark blue, color close to 0 value) had a SNR value close to 1.91 (green color) and a Nakagami  $m$  value close to 1 (green color)

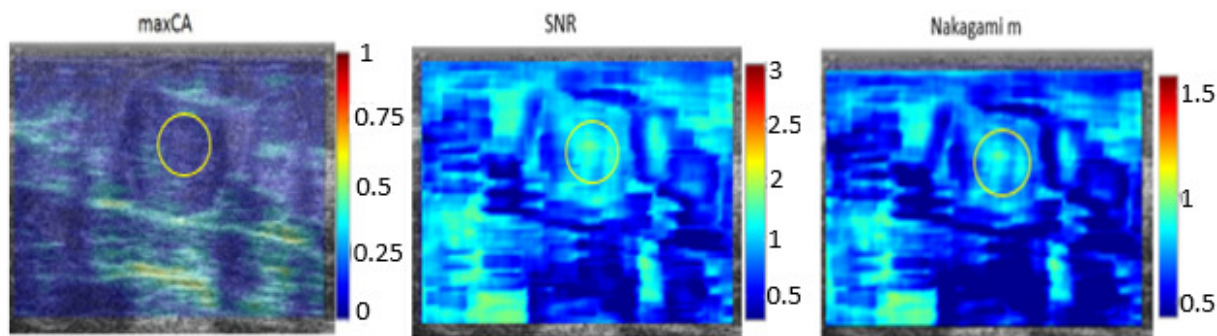


*Figure 5.5. Maps for the maxCA, SNR and Nakagami  $m$  for one of the subjects (FA20 in Chapter 6)*

### 5.3 Potential of avoiding coherence

The results in the previous section show that there is a large overlap between the coherence parameter values detected for fibroadenomas and carcinomas. These results demonstrate that none of these parameters, individually, can separate benign from malignant masses. However, these parameters are still useful to detect the presence of coherence as shown in Figure 5.4. Once an area of coherence is identified, we can eliminate the source of coherence and re-estimate the parameter value. Thus, tumors that were excluded due to their obvious B-mode image heterogeneity could be included after eliminating regions containing echo signal coherence.

To illustrate the idea, we scanned an ATS 539 phantom (ATS Laboratories, Inc, Bridgeport, CT). The phantom has 17, 0.1 mm monofilament line targets with 1 cm spacing between them. These targets were scanned to mimic the presence of strong isolated scatterers. The reference phantom used for this experiment is the same one used for second subgroup *of in vivo* data acquisitions (see Chapter 2). The phantom contains 6.4 g of 3000E glass beads. The sound speed of the phantom is 1492m/s at 2.5MHz; the attenuation coefficient vs. frequency,  $\alpha(f)$ , is represented by  $\alpha(f) = 0.54f$  dB/cm, where  $f$  is the frequency in MHz. The tissue mimicking reference material was cast into an acrylic box with a 25 $\mu$ m-thick Saran™ film scanning window (see Chapter 2).

We estimated the attenuation coefficient with the RPM in a) a ROI in the uniform background of the phantom, b) in a ROI including the monofilament line targets and c) in a ROI after avoiding monofilament line targets. To avoid the coherent structure, we started with the same ROI (1.8 cm x 1.5 cm) that included the coherent source (Figure 5.6b, B-mode image with the ROI outlined). Then, we manually selected a second smaller ROI (3mm x 3mm) that is centered around the coherent structure (Figure 5.6c, B-mode image with the ROI outlined). Once the PER of the smaller ROI was determined, and before eliminating power spectra from this location, the positions of the smaller ROI were examined to make sure it matches a PER in the larger ROI. If not, the process was repeated, by manually shifting the location of the smaller ROI, until a match is present. Then, we removed the power spectra generated from this small ROI before estimating the attenuation coefficient. Figure 5.6 a, b, and c show the different ROIs and the corresponding lateral mean of the specific attenuation coefficients at 6 MHz versus depth. In the case of the ROI with the coherent source (Figure 5.6b), applying the RPM to the backscattered echo data resulted in large errors in local attenuation estimations at the location of the coherent source. The homogeneity

of backscatter assumed in the RPM is violated at this location, and the effects are shown in Figure 5.6b. The high backscatter at this location results in the decrease and increase shown in the local attenuation coefficient versus depth values relative to the actual attenuation coefficients.

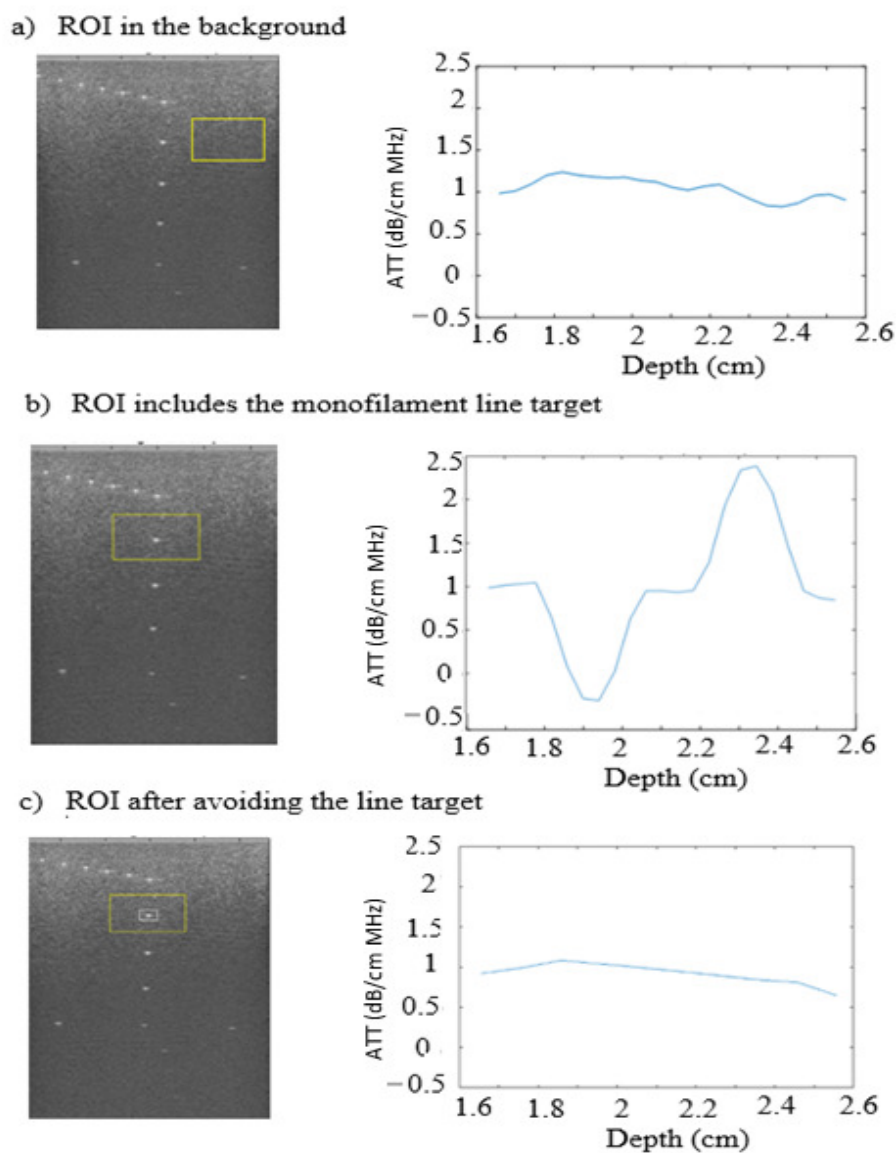


**Figure 5.6.** ROIs chosen in the ATS phantom and the corresponding lateral mean of the specific attenuation coefficients at 6 MHz versus depth.

The results in Figure 5.7 show the lateral mean of the specific attenuation coefficients at 6 MHz versus depth generated from the 3 different ROIs and the corresponding attenuation maps. To generate the map for the ROI where we avoided coherence, we performed interpolation to get the attenuation values in the area where power spectral estimates were eliminated due to the presence of coherence. The results show that eliminating potential sources of coherence is feasible. Further testing and application of this method on phantoms and in-vivo data is a proposed subject for future study.

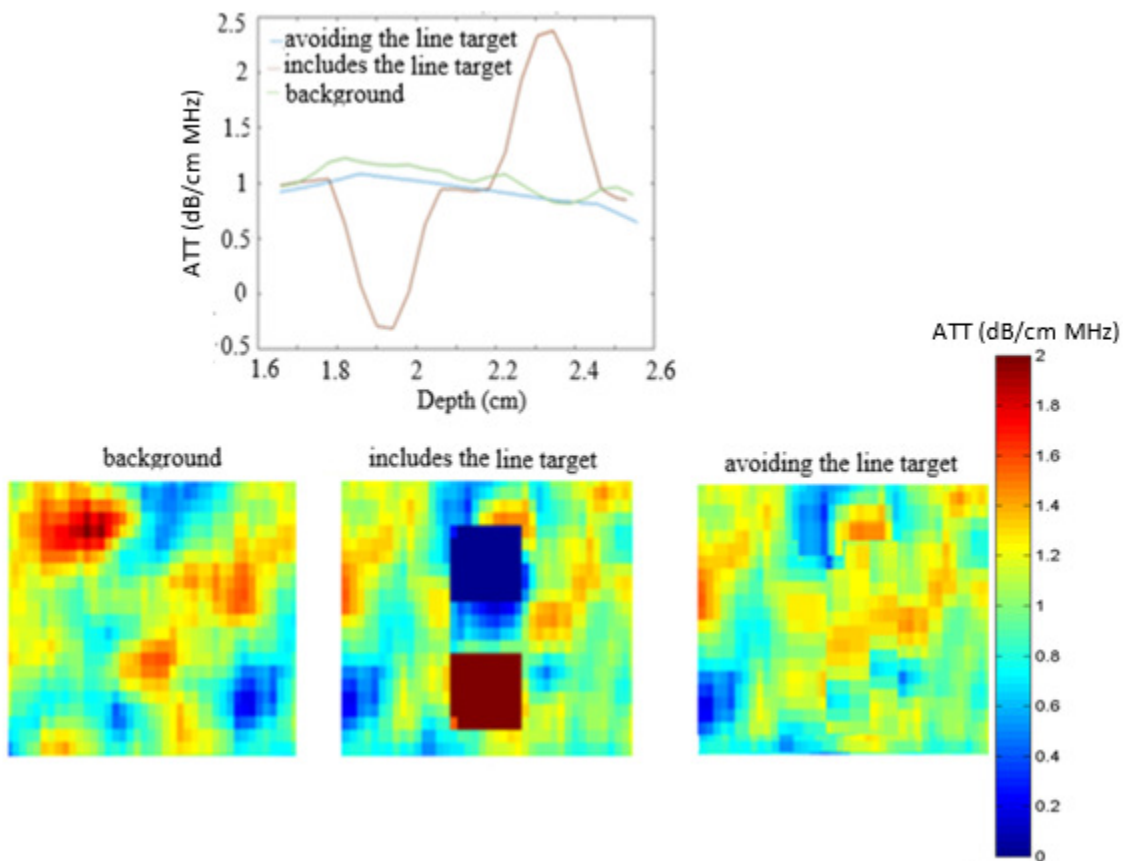


**Figure 5.7.** Lateral mean of the attenuation coefficient divided by the frequency at 6 MHz versus depth for ROI's in an ATS 539 phantom. Plot and attenuation coefficient/freq image on the left were generated from the ROI in the back ground, the middle for an ROI that included the monofilament line target, and the right for the same ROI after eliminating the signals from the monofilament line target and the corresponding attenuation maps

## 5.4. Examining anisotropy

As mentioned earlier, QUS assumes that the material properties within an ROI are isotropic. Thus, for an individual patient it is valid to average data obtained at different beam steering angles prior to estimating QUS parameters to reduce statistical variations. In this section, we introduce two different approaches to detect anisotropy. The first approach focuses on detecting anisotropy in attenuation estimates. The second approach quantifies the difference in backscattered power between the integrated echo signal power spectra of the sample being investigated and the reference phantom. Subjects included in this study are from the second subgroup (see data acquisition section in Chapter 2). The analysis was restricted to subjects with either a fibroadenoma or a carcinoma. A brief description of each of the methods utilized to detect anisotropy is shown below.

### 5.4.1. Trend approach

To test for isotropy in attenuation, we estimated the local attenuation coefficient using the RPM (see Chapter 2) for different beam steering angles (-10 to 10 degrees with an increment of 5 degrees) and for two different orientations (Anti-Radial: perpendicular to breast ducts, and Radial: aligned with ducts). Attenuation estimates were characterized as anisotropic if a trend was subjectively noticed in the estimates as we go from the positive to the negative scan angles in either the radial or the anti-radial scan planes. The bandwidth (consistent among all human subjects, i.e. 4-9 MHz) was selected such that the power spectral values were at least 10 dB above the noise floor. We started by plotting the attenuation coefficient versus frequency for each beam steering angle, then subjectively looked for a visual trend in the data to determine if there was a basis for pursuing this investigation objectively.

### 5.4.1.1. Result for the Trend approach

Figure 5.8 shows the presence of a trend in attenuation estimates from positive to negative scan angles. The attenuation estimates from the zero-degree echo signal data is in the middle followed by a decrease as we steer the beam over the negative angles and an increase over the positive beam steering angles (as illustrated by arrows in Figure 5.7, right schematic).

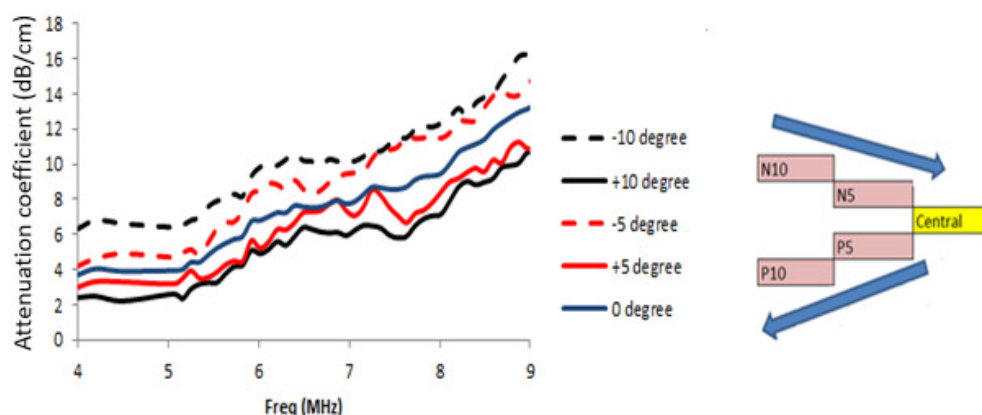


*Figure 5.8. Example of the attenuation coefficient versus frequency at different beam steering angles for one human subject*

### 5.4.2. T-test approach

Although the previous method provided a simple means for examining anisotropy, it was not always easy to judge whether a trend exists or not. Some of the attenuation estimates were noisy for some of the subjects, and that might be related to the presence of artifacts that were ignored in visual interpretation, but the power spectrum analysis was sensitive to, and therefore violate the assumptions used in the RPM. Thus, a more rigorous approach was examined. This approach applied the Student t-test assuming a normal distribution and 95% confidence ( $\alpha = 0.05$ ) to examine the combination of attenuation estimates (4-9 MHz) obtained from various

beam steering angles. The null hypothesis was that the attenuation coefficient estimates at any two steering angles come from populations with equal means. Thus, if estimates are equivalent (via t-test) at all steering angles, then the parameter estimates can be judged to be isotropic, and data from multiple angles can be averaged (“spatial compounding”) to obtain a lower attenuation estimate variance. In order to examine the null hypothesis, the t-test was applied for each pair of the beam steering angles. For example, attenuation estimates from the central and -5 degree views undergo the t-test and a p-value is obtained for this pair. Then, the process is repeated for values from central versus -10 degrees, and so on, until all angle pairs are examined. This provides a systematic test at which angle pair the null hypothesis was rejected.

#### ***5.4.2.1. Result for T-test approach***

The results in Figure 5.8 show an example of anisotropic attenuation estimates, where the t-test shows a significant difference ( $>0.05$ ) at one of the possible combinations of beam steering angles. Although the serial t-test suggests all attenuation estimates versus beam steering angle comes from equal mean ( $p < 0.05$ ) for a particular subject, the presence of an angle that violates the null hypothesis (i.e. N5 versus N10 with a  $p\text{-value}=0.064>0.05$ , highlighted in Figure 5.8) leads to judging that subject as anisotropic. Clearly this approach is suboptimal.

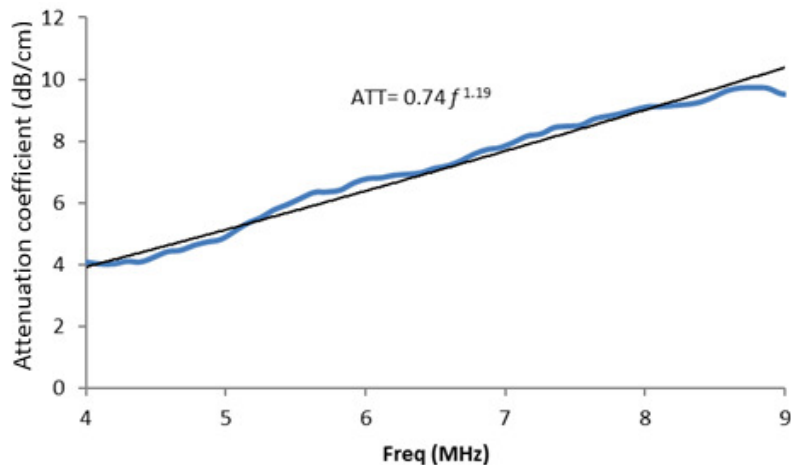
t-Test (Ho: Samples comes from population of equal means, alpha=0.05)

<b>0,N5</b>	<b>N5,n10</b>	<b>N10,P5</b>
2.45E-04	0.064	2.52E-09
<b>0,N10</b>	<b>N5,P5</b>	<b>N10,P10</b>
3.25E-08	1.38E-06	1.68E-14
<b>0,P5</b>	<b>N5,p10</b>	
3.057E-01	1.3E-11	
<b>0,p10</b>		
0.0076		

**Figure 5.9.** Example of the t-test result for one human subject shows the angles that have been examined and the p-values obtained from the t-test when examining attenuation estimates obtained at these angles. The p-value for each pair examined is shown underneath the pair name. N5: represents attenuation estimates obtained from the negative 5-degree view; N10: represents attenuation estimates obtained from the negative 10-degree view; P5: represents attenuation estimates obtained from the positive 5-degree view; P10: represent attenuation estimates obtained from the positive 10-degree view; and 0: represent attenuation estimates obtained from the central degree view

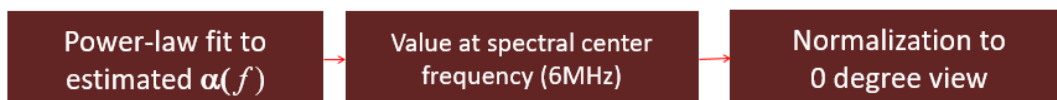
### 5.4.3. Power law fit to attenuation approach

The previous two methods can lead to a false conclusion of anisotropy if the attenuation coefficient estimates at any beam steering angle is noisy. To overcome this, we computed a power-law fit of attenuation versus frequency for each beam steering angle. The analysis bandwidth (4-9 MHz) was selected and an example of the power law fit to the attenuation values for one angle is shown in Figure 5.10.



**Figure 5.10.** An example of a power law fit to the attenuation coefficient versus frequency at one beam steering angle

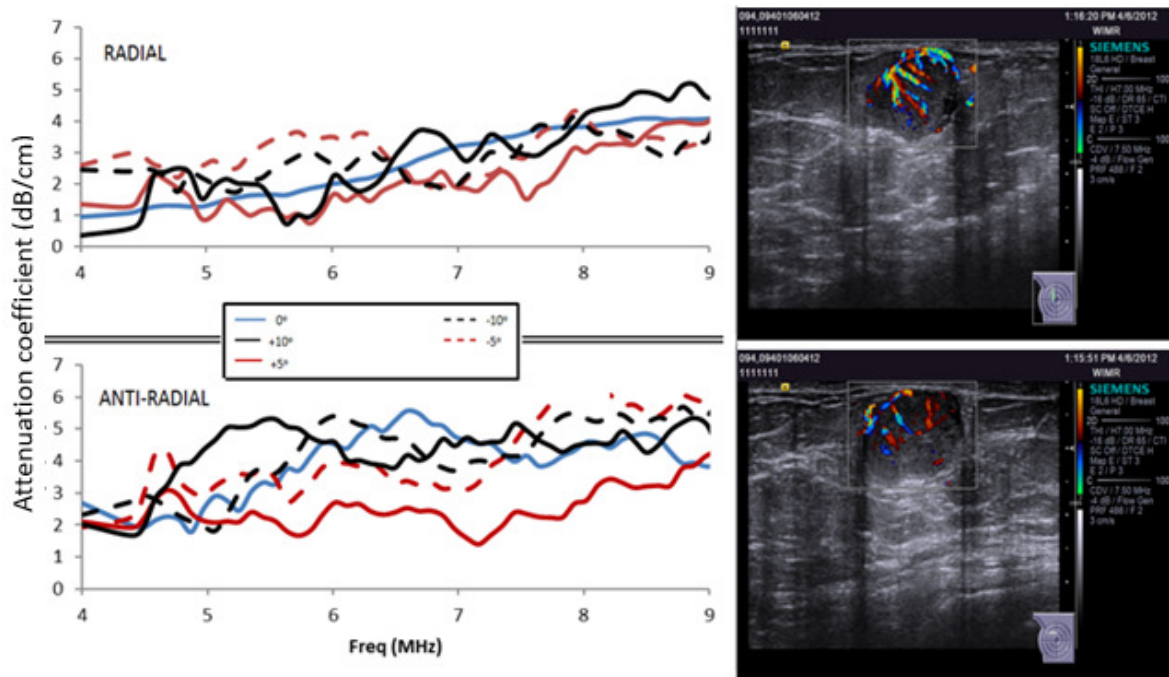
The specific attenuation value at 6 MHz using the power law fit among various steering angles was then determined and normalized (by division) with respect to the central view angle to determine angular dependence and test for anisotropy as illustrated in Figure 5.11.



**Figure 5.11.** illustration of anisotropy examination method

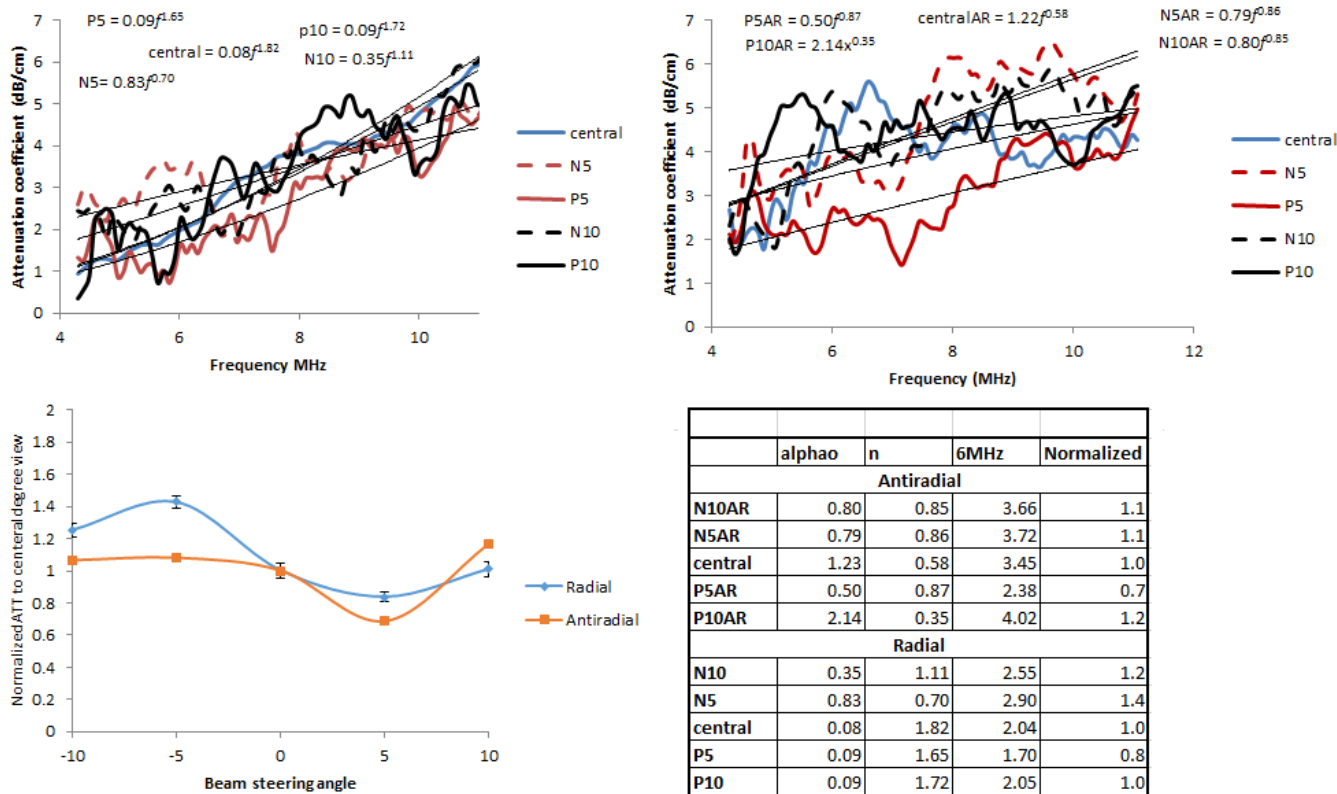
#### 5.4.3.1. Result for the Power law fit to attenuation approach

Figure 5.12 shows the attenuation estimated at different beam steering angles and the corresponding B-mode image, in both radial and antiradial directions for an intracystic papillary carcinoma (IPC in Chapter 6).



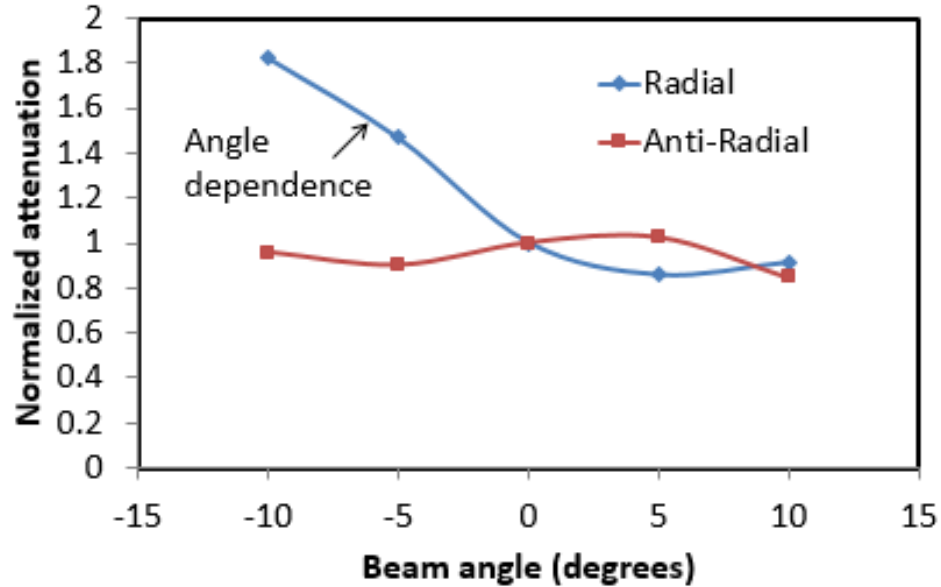
**Figure 5.12.** Example of the attenuation coefficient estimated at different angles, in both radial and anti-radial directions, for an intracystic papillary carcinoma (IPC in Chapter 6)

Figure 5.13 shows the attenuation coefficient versus frequency estimated for different beam steering angles and the power law fit ( $\alpha = \alpha_0 f^n$ ) for each beam steering angle. The figure also shows the numerical value at 6 MHz, the normalized value to the central degree view, and a plot showing the normalized data to the zero-degree view for the power law fit at 6 MHz, in both radial and anti-radial direction.



**Figure 5.13.** Attenuation coefficient versus frequency shown in Figure 5.12 with the corresponding power law fit (applied in the same way as Figure 5.10), the numerical value at 6 MHz and the normalized value to the central degree view, and a plot of the normalized data to the zero-degree view for the power law fit at 6 MHz, in both radial and anti-radial direction for all beam steering angles for the intracyclic papillary carcinoma (IPC in Chapter 6).

If the attenuation within a tumor was isotropic the normalized power law fit value would be the same at different beam steering angles and in both the radial and anti-radial directions. If a tumor exhibits anisotropy in one direction and is isotropic in the other direction, it was judged as anisotropic. An example of a fibroadenoma that shows anisotropy (FA22 in Chapter 6, was isotropic in one direction but anisotropic in the other direction and thus was judged as anisotropic) using the power law fit of the attenuation approach is shown in Figure 5.14. The results from this approach show that anisotropy was detected in a larger fraction of fibroadenomas (69%) than in carcinomas (50%).



**Figure 5.14.** Normalized data to the zero-degree view for the power law fit at 6 MHz for a fibroadenoma (FA22 in Chapter 6)

#### 5.4.4. Backscatter power difference (BSPD) approach

Another technique termed “the backscatter power difference approach” was developed in our lab for studying *ex vivo* cervix data, and it shows promise for detecting anisotropy in the power spectra of backscattered echo signals.<sup>37</sup> This approach quantifies the difference in backscattered power between the integrated echo signal power spectrum of the sample being investigated and the spectrum from the reference phantom.<sup>37</sup> Power spectra for both the sample and the reference are computed at the same depth  $z$  for different steered acoustic beams. The ratio of these power spectra at each steered angle  $\theta$ , is calculated and integrated over a bandwidth above the noise floor (4-9 MHz), such that<sup>37</sup>

$$\text{BSPD}(\theta) = \text{Backscattered Power Difference at } \theta^\circ = \frac{1}{\text{BW}} \int_{\text{BW}} 10 \log_{10} \frac{P_{\text{tissue}}(f, \theta^\circ)}{P_{\text{ref}}(f, \theta^\circ)} df \quad (5-11)$$

This value is then normalized over the maximum BSPD value (for all steering angles) by subtraction:

$$nBSPD(\theta) = BSPD_{max} - BSPD(\theta) \quad (5-12)$$

The nBSPD measures the loss in backscattered power as the acoustic beam is steered away from the angle with the highest BSPD. Thus, it should be system-independent due to the normalization to the echo signal power from a reference phantom.<sup>37</sup> Then the mean BSPD (mBSPD) is calculated.

#### 5.4.4.1. Results for the Backscatter power loss (BSPD) approach

If the tumor is isotropic, nBSPD estimates will be the same over all beam steering angles, illustrated by the nearly flat line of BSPD estimates shown in Figure 5.15. Thus, if the mBSPD value is close to zero, it is considered isotropic.

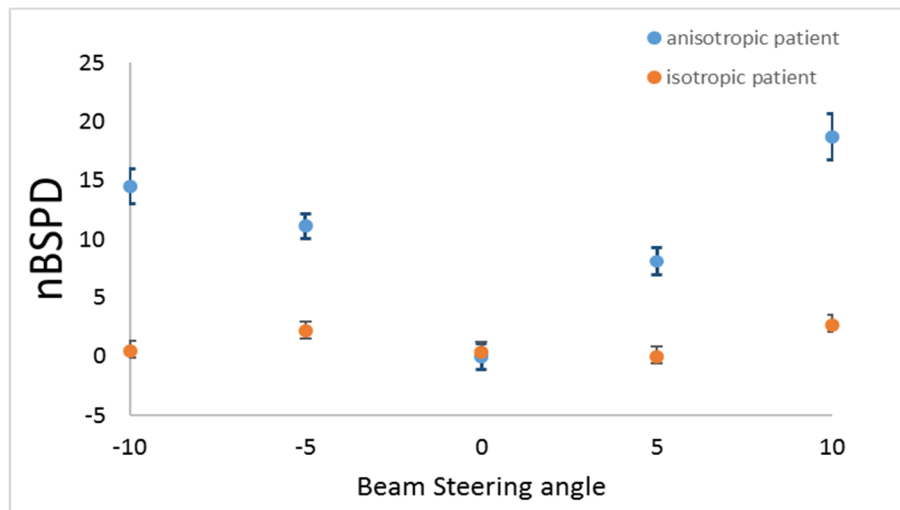


**Figure 5.15.** nBSPD for one isotropic and one anisotropic tumor

The results from the BSPD approach agreed with those from the power law fit of attenuation approach and detected anisotropy in the same tumors, which suggests that our QUS methods are

sensitive to detecting anisotropy. A summary of the results obtained from the two methods is shown in Table 5.1.

**Table 5.1.** A summary of the results obtained from the BSPD and the power law fit method for detecting anisotropy. For each subject, a decision on isotropy is obtained from the power law fit method (isotropic: yes, or no) and the mean BSPD (mBSPD) obtained from the BSPD method

Fibroadenoma						
BSPD approach			Power Law fit approach			subject ID
Radial	Antiradial	Isotropic	Radial	Antiradial	Isotropic	
mBSPD	mBSPD		isotropic	isotropic		
0.08	0.09	yes	yes	yes	yes	8
1.36	3.18	no	no	no	no	11
0.04	0.07	yes	yes	yes	yes	12
1.13	1.21	no	no	no	no	13
2.28	5.43	no	no	no	no	14
2.18	0.07	no	no	yes	no	15
0.03	0.05	yes	yes	yes	yes	19
2.01	1.09	no	no	no	no	20
0.07	0.08	yes	yes	yes	yes	24
0.03	0.02	no	yes	no	no	25
2.58	1.51	no	no	no	no	22
0.02	6.2	no	yes	no	no	21
0.16	0.26	no	no	no	no	23
Carcinoma						
Radial	Antiradial	Isotropic	Radial	Antiradial	Isotropic	subject ID
mBSPD	mBSPD		isotropic	isotropic		
0.51	1.63	no	no	no	no	9
0.06	0.03	yes	yes	yes	yes	10
0.08	0.01	yes	yes	yes	yes	16
3.16	2.23	no	no	no	no	17
0.06	0.08	yes	yes	yes	yes	18
0.06	1.86	no	yes	no	no	26
2.21	1.97	no	no	no	no	29
0.02	0.07	yes	yes	yes	yes	34

## 5.5. Discussion

The heterogeneous nature of the breast often leads to conditions where our QUS assumptions are not met. Thus, optimizing our QUS methods by overcoming challenges associated with tissue heterogeneity is critical. This could in turn lead to the inclusion of data sets from more tumors than those included in previous chapters. The results reported here showed that QUS parameters, such as the maximum collapsed average, the signal to noise ratio (SNR) of the echo signal envelope, and the Nakagami shape parameter did not differ significantly between fibroadenomas and carcinomas. However, these parameters agreed with each other and were useful in detecting the presence of coherence within the region of interest. Once the location of coherent scattering is detected, the power spectra from these locations can be eliminated to provide a better estimate of QUS parameters as illustrated in Section 5.3. This simple approach, as well as development of more sophisticated approaches, needs to be examined and tested using *in vivo* breast data in the future. This can also allow less dependence on selection of the ROI (if the area of coherence is detected and avoided) and thus, increase the reproducibility of the parameter estimates.

The results presented here also showed that more fibroadenomas (69%) exhibited anisotropy in attenuation (or simply backscattered power) than carcinomas (50%). Testing for anisotropy is important to determine whether we can spatially compound data from various angles to reduce the variance of the estimates. Although we limited this study to subjects that lacked obvious echo signal coherence within the tumor, as we beam steer the data, we need to note that when a subject is scanned at different beam steering angle, some structures (fat, parenchyma, etc.) might be imaged that were not present in the other beam steering angles and can affect the anisotropy detection.

## 5.6. Conclusion

Detecting coherence and deriving QUS parameters associated with it can lead to a more thorough estimate of the acoustic properties of breast tissue. Eliminating sources of coherence in the analyzed backscattered signal is feasible. This may increase the reproducibility of the parameter estimates. Both fibroadenomas and carcinomas appeared to exhibit anisotropy in attenuation, which was detected in both the anti-radial and radial directions. Attenuation anisotropy was detected more in fibroadenomas than in carcinomas. Since, *in vivo* breast tumors showed attenuation anisotropy, averaging attenuation estimates obtained at multiple beam-steering angles is not recommended.

## 5.7. References

1. Insana, M.; Wagner, R.; Garra, B.; Brown, D.; and Shawker, T.; Analysis of ultrasound image texture via generalized Rician statistics, *Optical Engineering*, **1986**; 25, 743-748
2. Varghese, T.; and Donohue, K.; Mean-scatterer spacing estimates with spectral correlation, *J. Acoust. Soc. Am.*, **1994**; 96, 3504-3515
3. Wear, K.; Wagner, R.; Insana, M.; and Hall, T.; Application of autoregressive spectral analysis to cepstral estimation of mean scatterer spacing, *IEEE Trans. Ultrason. Ferroelect. Freq. Control*, **1993**; 40, 50-58
4. Pereira, W.; and Maciel, C.; Performance of ultrasound echo decomposition using singular spectrum analysis, *Ultrasound Med. Biol.*, **2001**; 27, 1241-1248
5. Insana, M.; and Brown, D.; Acoustic scattering theory applied to soft biological tissues, in *Ultrasonic Scattering in Biological Tissues*, Eds. KK Shung and GA Thieme, CRC Press: Boca Raton, FL, **1993**
6. Wagner, R.; Insana, M.; and Brown, D.; Statistical properties of radio-frequency and envelope detected signals with applications to medical ultrasound, *J. Opt. Soc. Am.*, 1987; 4, 910-92
7. Dutt, V.; and Greenleaf, J.; Ultrasound echo envelope analysis using a homodyned K distribution signal model, *Ultrason. Imaging*, **1994**; 16, 265-28
8. Hruska, D.; and Oelze, M.; Improved parameter estimates based on the homodyned K Distribution,” *IEEE Trans. Ultrason. Ferroelect. Freq. Control*, **2009**; 56, 2471-2481
9. Donohue, K.; Huang, L.; Burks, T.; Forsberg, F.; and Piccoli, C.; “Tissue classification with generalized spectrum parameters, *Ultrasound Med. Biol.*, **2001**; 27, 1515-1524

10. Rosado-Mendez, I.; Drehfal, L.; Zagzebski, J.; Hall, T.; Analysis of Coherent and Diffuse Scattering Using a Reference Phantom, *IEEE Trans Ultrason Ferroelectr Freq Control*. 2016 Sep;63(9):1306-20. doi: 10.1109/TUFFC.2016.2547341. Epub **2016** Mar 25.
11. Zagzebski, J.; Rosado-Mendez, I.; and Nasief, Haidy G.; and Hall, T.; Quantitative ultrasound: Enhancing diagnosis using estimates of acoustic attenuation and backscatter, *AIP Conference Proceedings*, **2016**, 1747, 050001.
12. Rosado\_Mendez, I.; *Advanced Spectral Analysis Methods for Quantification of Coherent Ultrasound Scattering: Applications in the Breast*, University of Wisconsin Madison, PhD thesis, **2014**
13. Huang, L.; Donohue, K.; Genis, V.; Forsberg F.; Duct detection and wall spacing estimation in breast tissue, *Ultrason. Imaging*, **2000**; 22, 138-153
14. Donohue, K.; Fosberg, F.; Piccolli, C.; Goldberg, B.; Analysis and classification of tissue with scatterer structure templates, *IEEE Trans. Ultrason. Ferroelect. Freq. Control*, **1999**; 46, 300-310
15. Luchies, A.; Goshal, G.; O'Brien, W.; Oelze, M.; Quantitative ultrasonic characterization of diffuse scatterers in the presence of structures that produce coherent echoes, *IEEE Trans. Ultrason. Ferroelectr. Freq. Control*, **2012**; 59, 893-904
16. Rubert, N.; Varghese, T.; Mean scatterer spacing estimation using multi-taper coherence, *IEEE Trans. Ultrason. Ferroelectr. Freq. Control*, **2013**; 60, 1061-1073
17. Wagner, R.; Smith, S.; Sandrik, J.; and Lopez, H.; Statistics of Speckle in Ultrasound B-Scans *IEEE Transactions on Sonics and Ultrasonics* 30(3):156- 163 · June **1983** DOI: 10.1109/T-SU.1983.31404 ·

18. Shankar, P.; A Model for ultrasonic scattering from tissues based on the K distribution, *Phys. Med. Biol.*, **1995**; 40(10), 1643-1659
19. Varghese, T.; Donohue, K.; Estimating mean scatterer spacing with the frequency-smoothed spectral autocorrelation, *IEEE Trans. Ultrason. Ferroelectr. Freq. Control* **1995**, 432: 451-46
20. Gerr, N.; Allen, J.; The generalized spectrum and spectral coherence of harmonizable time series, *Digital Signal Processing*, **1994**; 4, 222-238
21. Huang, L.; Donohue, K.; Genis, V.; Forsberg F.; Duct detection and wall spacing estimation in breast tissue, *Ultrason. Imaging*, **2000**; 22, 138-153
22. Hurd, H.; Gerr, N.; Graphical methods for determining the presence of periodic correlation, *Journal of Time Series Analysis*, **1991**; 12, 337-350
23. Donohue, K.; Huang, L.; Genis, V.; Forsberg, F.; Duct size detection and estimation in breast tissue, Proc. IEEE, *Ultrasonics Symposium*, **1999**; 1363-1366
24. Thuthill, T.; Sperry, R.; and Parker, K.; Deviations from Rayleigh statistics in ultrasonic speckle, *Ultrason. Imaging*, **1988**; 10, 81-89
25. Tsui, P.; and Wang, S.; The effect of transducer characteristics on the estimation of Nakagmi parameter as a function of scatterer concentration, *Ultrasound Med Biol.*, **2004**; 30, 1355- 1363
26. Shankar, P.; A general statistical model for ultrasonic backscattering from tissues, *IEEE Trans. Ultrason. Ferroelect. Freq. Control*, **2000**; 47, 727-736
27. Hruska, D.; and Oelze, M.; Improved parameter estimates based on the homodyned K Distribution," *IEEE Trans. Ultrason. Ferroelect. Freq. Control*, **2009**; 56, 2471-2481

28. Destrempes, F.; and Cloutier, G.; A critical review and uniformized representation of statistical distributions modeling the ultrasound echo envelope, *Ultrasound Med. Biol.*, **2010**; 36, 1037-1051
29. Destrempes, F.; and Cloutier, G.; Review of envelope statistics model for quantitative ultrasound imaging and tissue characterization, in *Quantitative Ultrasound in Soft Tissues*, eds. Jonathan Mamou, and M. L. Oelze, Springer **2013**; 219-274
30. Tsui, P.; and Chang, C.; Imaging local scatterer concentrations by the Nakagami statistical model, *Ultrasound Med. Biol.*, **2007**; 33, 608-619
31. Nakagami, M.; Statistical character of short-wave fading, *J. Inst. Elec. Commun. Eng. Japan*, **1943**; 27, 146-151
32. Shankar, P.; Ultrasonic tissue characterization using a generalized Nakagami model, *IEEE Trans. Ultrason. Ferroelec. Freq. Control*, **2001**; 48, 1726-1730

## Chapter 6: Bayesian classifier for differentiating breast masses

*This chapter is published as:*

*Nasief, H.; Rosado-Mendez, I.; Zagzebski, J.; and Hall, T.; A Quantitative Ultrasound-Based Multi-Parameter Classifier for Breast Masses, IEEE, under review*

Distinguishing benign from malignant breast masses by way of imaging tests continues to be an important medical challenge. Non-invasive classification of tumor types can reduce the number of unnecessary biopsies. Researchers, including D'Astous and Foster,<sup>1</sup> demonstrated that a 2-parameter analysis (attenuation and BSC) was sufficient to separate infiltrating ductal cancer (IDC), breast parenchyma, and fat. Mortensen et al.<sup>2</sup> achieved 0.93 accuracy when using sound speed, attenuation, and backscatter parameters to build an artificial neural network to differentiate malignant from benign masses in 18 *ex-vivo* breast tissue samples. More recently, Nam et al.<sup>3</sup> demonstrated that estimates of the product of the acoustic attenuation coefficient and the lesion size (along the acoustic beam direction) correlated well with the assessment of the ultrasound BI-RADS descriptor 'posterior acoustic features'. Tadayyon et al. and Sannachi et al.<sup>4;5</sup> also demonstrated the potential of using multiple QUS parameters to differentiate between histologic Grade I versus Grades II and III tumors, finding a 0.86 accuracy in their studies. Other investigators have implemented different approaches to breast QUS that do not provide system-independent results. For example, Garra et al.<sup>6</sup> digitized the video output of an ultrasound scanner and analyzed the statistics of the B-mode image texture of breast scans. They correctly identified 78% of the fibroadenomas, 73% of the cysts, and 91% of the fibrocystic nodules while maintaining high sensitivity for cancer. Using similar data acquisition, image texture parameters and an artificial neural network, Chen et al.<sup>7</sup> obtained a diagnostic accuracy of 95% in identifying malignant lesions.

Algorithms and analysis tools utilizing a Bayesian classifier have been developed that combine parameter estimates to differentiate cancer types and predict their re-occurrence based on mammography data,<sup>8-11</sup> but none have been reported using quantitative ultrasound (although other network classifiers have been reported, as described above). For example, Nahr et al.<sup>12</sup> developed a kernel-based naïve Bayes (KBNB) classifier that exhibited good performance for early diagnosis of breast cancer. Features including the shape and size of the suspicious mass were used by the classifier to identify malignant breast masses. This approach assumed that the presence of a particular feature of a class is unrelated to the presence of any other feature. Zyout et al.<sup>13</sup> integrated a Bayesian classifier with a pattern synthesizing scheme to detect clustered microcalcifications in mammograms. They achieved a sensitivity and specificity of 91.3% and 98.6%, respectively for diagnosing cancer. Burnside et al.<sup>14</sup> built a Bayesian network that included BI-RADS descriptors for microcalcifications seen in mammograms. The classifier was reported to perform as well as a subspecialty-trained mammographer in estimating the probability of malignancy. One of the challenges with using Bayesian classifiers is that the computational complexity of these networks increases as the number of parameters involved increases. However, a Bayesian classifier is a good choice for combining a relatively small set of QUS parameters.

As mentioned earlier, quantitative ultrasound (QUS) methods enable accurate, clinically-based estimates of acoustic properties of tissues by accounting for instrumentation and wave propagation dependencies that affect pulse-echo data.<sup>15:16</sup> In Chapter 2, we provided a description of QUS parameters that are most commonly estimated, including the attenuation coefficient, which quantifies the spatial rate at which an ultrasound beam loses energy while traversing a particular tissue, and the backscatter coefficient (BSC), which quantifies the fraction of the ultrasound energy that is reflected back to the transducer. The attenuation coefficient is often reported in terms of the

specific attenuation coefficient, ATT, which is the attenuation coefficient at a particular frequency divided by that frequency. The BSC is parametrized in terms of the frequency-average BSC, ABSC, which quantifies echogenicity. A reference phantom method (RPM) was used to estimate the ATT and ABSC (the ABSC was estimated with the RPM, after correcting for the attenuation estimated using the MLSM; see Chapter 4). The effective scatterer diameter, ESD, which is obtained by fitting a form factor model to the measured form factor vs. frequency, and an effective scatterer diameter heterogeneity index (ESDHI) over regions of interest within each mass were also determined. In Chapter 5, we provided a description and results for QUS parameters that are related to the presence of coherence by computing the echo signal envelope signal to noise ratio (SNR), the Nakagami shape parameter,  $m$ , and the maximum collapsed average (maxCA) of the generalized spectrum. In this chapter, we examine the effect of combining these QUS parameters to differentiate breast carcinomas from fibroadenomas using a Bayesian classifier. A brief description of each parameter is provided. Initial test results are reported and limitations of the study are considered.

## 6.1. QUS Parameter Estimation

Once the echo signal data were acquired (see Chapter 2), offline analysis was performed using MATLAB (Mathworks, Natick, MA) to estimate QUS parameters. Power spectra were estimated within a selected region of interest (ROI) using a multitaper method<sup>17</sup> with a time-half bandwidth product of 4, and  $4 \times 4$  mm<sup>2</sup> power spectrum estimation regions overlapping by 90% both axially and laterally.<sup>18;19</sup> For tumors smaller than 6 mm in the axial direction, a  $3 \times 3$  mm<sup>2</sup> power spectrum estimation region was used, and beams steered  $\pm 5$  degrees were included to improve the statistics of power spectral estimation.<sup>20;21</sup> Only the bandwidth +10dB above the noise

floor (4-9MHz) was used in the estimation of the attenuation and the backscatter coefficients. The ROI size was (by subjective B-mode image assessment) the largest homogeneous region within the tumor boundary outlined by the sonographer at the time of the scan. Pathology identification of tumor type was based on core biopsy specimens. Attenuation and backscatter coefficients within the tumor were estimated using the reference phantom method (RPM).<sup>22</sup> This method has been tested in multiple studies demonstrating system-independent estimates in excellent agreement with theory and independent measurements.<sup>17;20;21;23</sup> The RPM utilizes the ratio of the echo signal power spectra from the tissue to the power spectra from the same depth in the reference phantom (see Chapter 2).

The lesion's QUS parameters were estimated as follows:

1) Specific attenuation coefficient, ATT: this parameter was estimated from the local attenuation coefficient  $\alpha_{L,s}(f, z)$ , i.e., the attenuation coefficient of the tissue within a single parameter estimation region (PER) centered at depth  $z$  within the ROI (see Chapter 2). Assuming that  $\alpha_s$  and BSCs are constant within the PER,  $\alpha_{L,s}(f, z)$  is obtained by quantifying the local rate of change of the power spectrum ratio as a function of depth at each frequency.<sup>24</sup> ATT is obtained from the slope of a linear fit to the local attenuation vs. frequency, i.e.,  $\alpha_{L,s}(f) = \text{ATT} \times f$ .<sup>25</sup>

2) Backscatter coefficient BSC: The estimation of BSC using the RPM requires knowledge of the intervening tissue effective attenuation. The modified least-squares approach<sup>26</sup> (see Chapter 4) was used to estimate the effective attenuation from 4–9 MHz. Once the effective attenuation was estimated for each PER, the BSC for that PER was estimated as a function of frequency using the reference phantom technique, by inserting the effective attenuation coefficient into the RPM equation (see Chapter 2). For each subject, ABSC was computed by averaging the BSC over the

4-9MHz frequency range used for attenuation coefficients providing an objective estimate of “echogenicity”.<sup>24</sup>

3) The effective scatterer diameter (ESD): this parameter was estimated by obtaining the acoustic form factor from the estimated BSC and fitting a Gaussian form factor model by means of square error minimization<sup>27:28</sup> (see Chapter 2).

4) A heterogeneity index of the ESD (ESDHI): this parameter was computed as the standard deviation of the ESD within the ROI, ignoring any spatial correlations among estimates. This latter parameter represents the spatial variability among the ESD estimates.

The estimation of ATT, BSC, and ESD is based on the assumption that echo signals arise from diffuse (incoherent) scattering conditions and that the underlying random process may be classified as stationary. However, these assumptions are not always met in the human breast. Although we constrain our QUS analysis to homogeneous ROI's, some amount of signal coherence, not reliably detected by human interpreters, may be present (see Chapter 5). This can affect the precision of QUS parameter estimations and limit the reproducibility of the results. This led to introducing QUS parameters that relate to coherence factors, listed as follows.

5) The maximum collapsed average (maxCA) of the generalized spectrum within a search region (defined by the available bandwidth): this is a nonparametric approach used to test for coherence due to a non-stationary process.<sup>29:30</sup> In the case of stationary signals, there is no correlation among different frequency components represented by points off the diagonal of the generalized spectrum. However, when the signals are non-stationary, different frequency components become correlated, and the off-diagonal values of the generalized spectrum are significantly different from zero. In the collapsed average, the peak at  $\Delta f = 0$  MHz corresponds to the main diagonal of the generalized spectrum as shown in Figure 6.1. The presence of peaks in

the collapsed average indicates the presence of a periodic component, and their corresponding frequency ( $\Delta f$ ) is inversely proportional to the separation of the periodic scatterers.<sup>31;32</sup> The maximum in the collapsed average of the generalized spectrum, away from the main diagonal, within the search region is determined. If that maximum value is larger than 95% of the values from equivalently-acquired reference phantom data, then non-stationary coherent scattering from resolved periodicity is declared<sup>33</sup> (see Chapter 5).

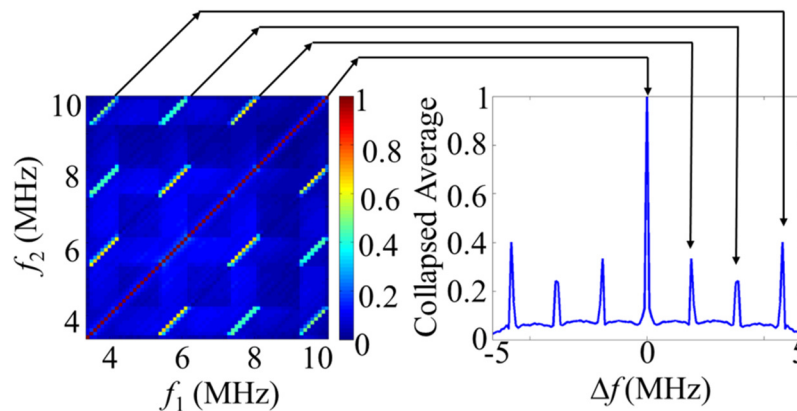


**Figure 6.1.** The generalized spectrum and the collapsed average (Figure from Rosado-Mendez<sup>34</sup>)

6) The signal to noise ratio (SNR) of the echo signal envelope: this represents a model-free parameter to quantify coherence due to a stationary process.<sup>34</sup> Based on the envelope SNR, stationary echo signals can be divided into three cases. Diffuse scattering with fully developed speckle (such as the case of echo signals from the reference phantom) is described with Rayleigh statistics, with the ratio of the mean echo envelope amplitude to its standard deviation equivalent to 1.91. Low scatterer number density conditions are described as “pre-Rayleigh” with a  $\text{SNR} < 1.9$ , and periodically-spaced scattering sources with sub-resolution spacing are described as “post-Rayleigh” with a  $\text{SNR} > 1.9$  (see Chapter 5).

7) The Nakagami shape parameter  $m$ : this represents a model-based parameter to analyze stationary features.<sup>35</sup> The Nakagami distribution probability density function has a closed-form

expression, thus making it mathematically tractable, and its parameter estimation is relatively easy. Also, the simplicity of the Nakagami probability density function makes it possible to define the maximum likelihood estimator (MLE) for the shape parameter  $m$ , whose value is mainly defined by scattering statistics:  $m = 1$  for Rayleigh statistics,  $m < 1$  for pre-Rayleigh statistics, and  $m > 1$  for post-Rayleigh (see Chapter 5).

## 6.2. Bayesian Classifier

Previous studies<sup>1;25;36</sup> suggest that no single acoustic parameter successfully differentiates benign from malignant breast masses. The challenge, then, is to test the classification performance of some combination of QUS parameters. The estimated specific attenuation coefficient (ATT), average backscatter coefficient (ABSC), effective scatterer diameter (ESD), ESD heterogeneity index (ESDHI), maximum collapsed average (maxCA), envelope signal to noise ratio (SNR), and Nakagami shape parameter (Nakagami  $m$ ) values for each breast mass were used to build Bayesian classifiers. To simplify the task, we grouped lesions in two classes: fibroadenomas (benign lesions) and carcinomas (including all types of malignant breast masses in our pool). A multivariate normal Bayesian classification uses a  $d$  dimensional feature vector  $x = [x_1, x_2, \dots, x_d]$ , where the features or components  $x_1, x_2, \dots, x_d$  are the set of  $d = 2$  or  $3$  QUS parameters defining the classifier. When the components of  $x$  are continuous random variables, the probability density function of  $x$  is  $p(x)$  and the class-conditional probability for class  $w_i$  is  $p(x|w_i)$ . The classification is done by applying Bayes' rule to compute the likelihood of class membership given some characteristic of that class such that,<sup>37</sup>

$$p(w|x) = \frac{p(x|w_i)p(w_i)}{p(x)} \quad (6.1)$$

where  $p(w_i)$  is a prior probability. Given multiple classes, each class  $w_i$  (here,  $i = 1$  corresponds to fibroadenomas, and  $i = 2$  to carcinomas), has its own mean vector  $m_i$  and covariance matrix  $c_i$ , such that the class-conditional probabilities are<sup>37</sup>

$$p(x|w_i) = 2\pi^{-d/2} |c_i|^{-1/2} \exp -1/2 (x - m_i)^T c_i^{-1} (x - m_i) \quad (6.2)$$

The strategy to move from probabilities to discriminants is to maximize  $\ln(p(w_i|x))$  which, from Eq. 4, is equivalent to maximizing  $\ln(p(x|w_i)) + \ln(p(w_i))$ , or

$$\max[\ln p(w_i) - 1/2 \ln|c_i| - 1/2 (x - m_i)^T c_i^{-1} (x - m_i)] \quad (6.3)$$

The expression  $(x - m_i)^T c_i^{-1} (x - m_i)$  can be thought of as  $\|(x - m_i)\|_{c_i^{-1}}^2$  which looks like a squared distance multiplied by the inverse covariance matrix  $c_i$ , which acts as a metric (stretching factor) on the space. Thus, the classification using multivariate normal distributions is simply a minimum (Mahalanobis) distance classifier. The results of the classification are assignments to the class with the highest probability (i.e. minimum distance to the centroid of the trained class).<sup>37-39</sup>

### 6.3. First data set to classify breast masses

A detailed description of the data acquisition for these human subjects is provided in Chapter 2. This study started with human subjects from the second subgroup recruited. This resulted in data from 35 human subjects and analyzed four QUS parameters (ATT, BSC, ESD, ESDHI). The data was divided into a training set, consisting of parameter estimates from 18 subjects, and a testing set, consisting of ultrasound parameters from 17 subjects. A 2-fold cross validation technique was used to assess how accurately the model might perform. Cross validation was done such that the 18 subjects for the training set were chosen randomly from the 35 patients, and testing was done on the rest. The whole process was repeated 10 times and the average

performance was recorded. To determine the best parameters to classify benign from malignant masses, multiple classifiers combining either 2 or 3 parameters (ATT, BSC, ESD and ESDHI) were examined. The schematic of the workflow of the Bayesian classifier is shown in Figure 6.2. The process started with acquiring B-mode images and RF echo data from the ultrasound machine, followed by offline analysis to estimate the QUS parameters of interest. Then, combinations of either 2 or 3 parameter pairs were used to define the centroid of each classification class (fibroadenoma or carcinoma). The new test set was classified based on the minimum distance to the centroid of each class.

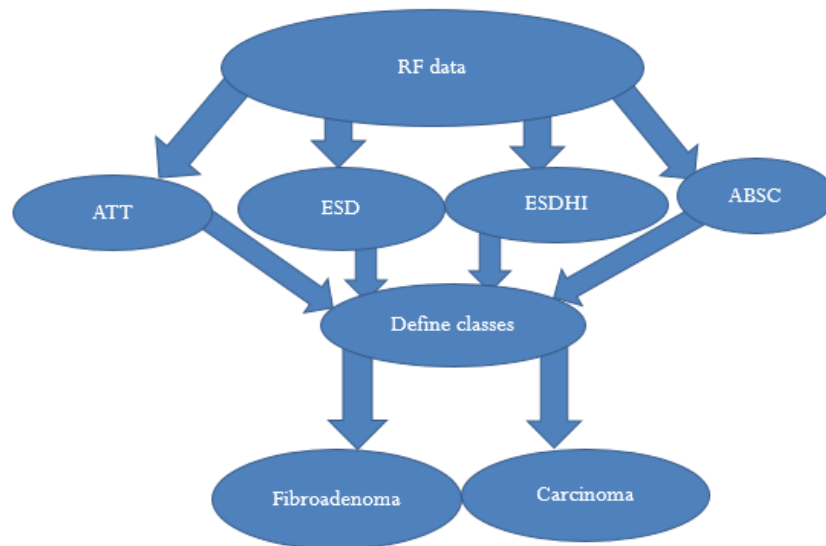


**Figure 6.2.** Schematic of the Bayesian Classifier

To simplify the classification process, facilitate data entry, and the plotting of the results, a graphical user interface (GUI) shown in Figure 6.3 was built using MATLAB. In this GUI, a user enters the values of the estimated QUS parameters and then hits the “plot” and “plot 3D” buttons to see the new data set plotted on the graphs corresponding to either 2 or 3 parameter

combinations. The classification result appears as either fibroadenoma or carcinoma in the category window.

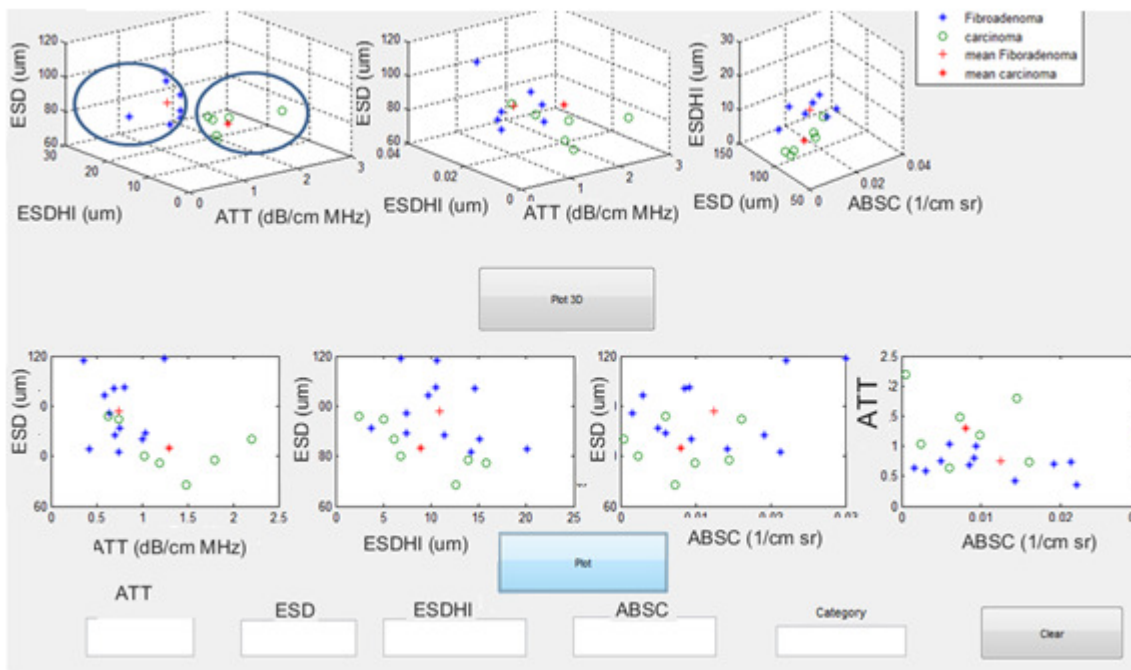


*Figure 6.3. GUI For Bayesian Classifier*

### 6.3.1. Results for the thirty-five subjects

For the 35 human subjects shown in Table 6.1, attenuation within pathology-confirmed fibroadenoma ranged from  $0.36\text{-}1.94\text{ dB}\cdot\text{cm}^{-1}\text{MHz}^{-1}$ , with a median value  $\pm$  interquartile range of  $1.01 \pm 0.53\text{ dB}\cdot\text{cm}^{-1}\text{MHz}^{-1}$ . Attenuation in carcinomas was somewhat higher than the mean attenuation of fibroadenomas, with a median value  $\pm$  interquartile range of  $1.3 \pm 0.51\text{ dB}\cdot\text{cm}^{-1}\text{MHz}^{-1}$ . Among fibroadenomas, the median ESD was  $102 \pm 30\text{ }\mu\text{m}$ , which is higher than the median of  $80.2 \pm 20\text{ }\mu\text{m}$  for carcinomas. The median ESDHI estimate among fibroadenomas ( $13.6 \pm 3.4\text{ }\mu\text{m}$ ) was slightly higher than the value among carcinomas ( $11.1 \pm 5.8\text{ }\mu\text{m}$ )

*Table 6.1. QUS parameter values for the 35 human subjects*

Fibroadenoma					carcinoma				
ATT dB-cm <sup>-1</sup> MHz <sup>-1</sup>	ESD ( $\mu$ m)	ESDHI ( $\mu$ m)	ABSC (sr <sup>-1</sup> cm <sup>-1</sup> )	Subject order	ATT dB-cm <sup>-1</sup> MHz <sup>-1</sup>	ESD ( $\mu$ m)	ESDHI ( $\mu$ m)	ABSC (sr <sup>-1</sup> cm <sup>-1</sup> )	Subject order
0.74	82	14.2	0.0213	22	1.85	90	10.1	0.005	18
1.25	83	13.6	0.046	35	2.19	68	8.5	0.039	39
1.55	109	15.8	0.036	37	2.17	58	13.1	0.041	40
1.57	125	13.8	0.0019	9	0.85	54	14	0.115	36
0.68	60	14.2	0.0025	27	1.47	100	12.2	0.075	34
0.69	107	10.4	0.0076	28	1.48	69	12.3	0.007	11
1.94	147	12.1	0.048	41	0.63	96	2.4	0.006	25
0.71	144	4.1	0.0003	13	1.09	82	11.1	0.002	42
1	87	15.1	0.0094	15	2.2	87	6.2	0.001	17
0.85	112	13.6	0.009	21	1.03	80	11.3	0.002	19
0.76	87	10.9	0.003	30	0.74	95	5.1	0.016	26
1.24	119	11.8	0.039	31	0.52	87	6.2	0.015	24
1.19	117	15.3	0.046	43	0.5	59	7.5	0.028	33
1.92	166	11.8	0.0013	12	1.3	77	13.6	0.94	10
1.3	90	15.6	0.01	14	1.92	79	18.6	0.01	38
1.04	93	13.1	0.0212	32					
0.42	83	20	0.0143	16					
1.01	110	9.5	0.0003	29					
0.36	95	14.5	0.0221	23					
0.89	97	10.5	0.0092	20					

The results also showed that the ESD versus the attenuation coefficient can be used to differentiate between carcinoma and fibroadenomas in most cases, such that patients with a mass that has high attenuation and low ESD likely have a carcinoma and those with the opposite characteristic have a fibroadenoma. Our preliminary data showed that a classifier incorporating ultrasound ATT, ESD, and ESDHI suggesting that a Bayesian classifier might differentiate benign from malignant tumors. The Bayesian classifier shows a high classification rate, with performance of the 2 and 3 parameter combinations shown in Figure 6.4. The best performance with a parameter pair (ATT, ESD) was about 80% correct classification which increased to about 100% with three

parameters (ATT, ESD, ESDHI) as shown in Figure 6.4. However, more verification studies are needed, to include a larger data set and more tumor types.

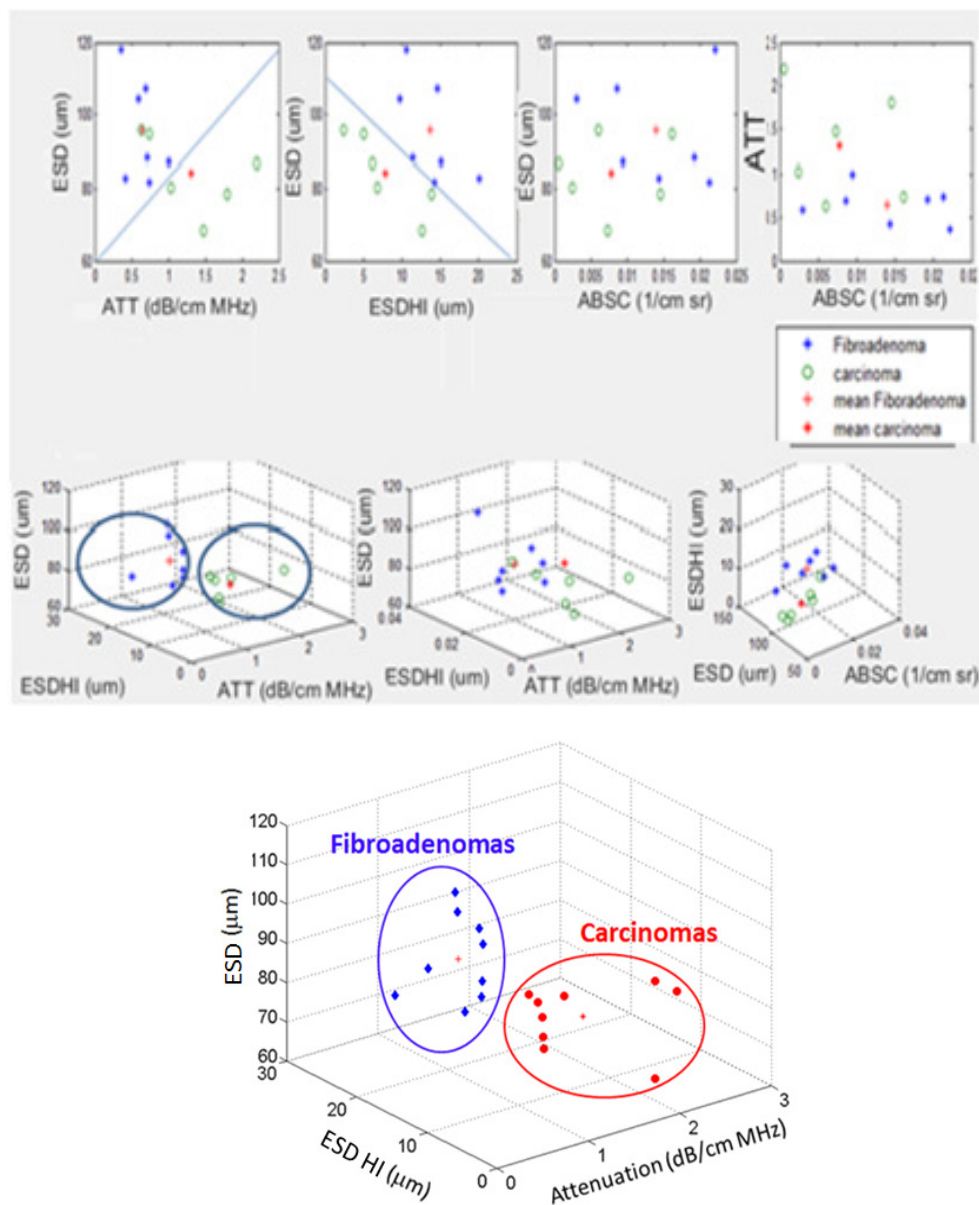


**Figure 6.4.** Performance of the Bayesian classifier

## 6.4. Additional data set to classify breast masses

We expanded the number of human subjects available to train and test the Bayesian classifier by including subjects that were scanned under an elasticity imaging modality (first subgroup, see Chapter 2). This resulted in an additional 7 fibroadenomas and 1 carcinoma. Thus, a total of 43 subjects including 27 fibroadenomas, 10 invasive (or infiltrating) ductal carcinomas, 2 invasive lobular carcinomas, 1 adenocarcinoma, 1 intracystic papillary carcinoma, and 2 ductal carcinomas in situ were used for the analysis (these are the same subjects used for the data analysis in Chapter 5). We not only increased the number of human subjects, but we also expanded our testing to include the QUS parameters related to coherence (see Chapter 5). This resulted in seven QUS parameters to be tested. However, given the limited number of subjects, combinations of either 2 or 3 parameter pairs were tested each time.

To make sure that all data sets were used for training and testing, instead of using the 2-fold cross validation technique, we applied MATLAB functions and a leave one out cross validation method. The MATLAB built-in functions were utilized to 1) specify the cross validation type and partition to be “leave one out” (the entire data set was used for training except one tumor that was left out for testing, and that process was repeated for each tumor, and that entire process was repeated 10 times, i.e., 10 random seeds;  $n_{\text{boots}}=10$ ); 2) estimate the prior probabilities from the relative frequencies of the classes and obtain the posterior probabilities of each feature assuming a multivariate normal (Gaussian) distribution fit to the model features; 3) classify breast masses using the ‘Mahalanobis’ distance approach; and 4) create an empirical ROC curve, provide the area under the computed ROC curve (AUC), and estimate the 95% confidence intervals to judge the overall performance of each classifier.

The creation of this classifier started by partitioning the data using the MATLAB function “cvpartition” in which we specified the cross-validation type and partition to be “leave one out”. Data were arranged such that each row of the training set corresponded to a specific class (either fibroadenoma or carcinoma) and columns corresponded to features (estimated QUS parameter). Once the training set was specified, the naïve Bayes classifier was created using the MATLAB function “NaïveBayes.fit” assuming a multivariate normal (Gaussian) distribution fit to the model features. The prior probabilities were estimated from the relative frequencies of the classes using the MATLAB function “FreqDist”. The MATLAB function “posterior” was used to obtain the posterior probabilities of each feature. Two MATLAB functions, “predict” and “classify”, were used to classify the test data into one of the classes of the Bayesian classifier. The ‘mahalanobis’ distance option was selected in the classify function. The MATLAB function “confusionmat” was used to obtain the confusion matrix determined by known and predicted groups. Cross validation was performed using the MATLAB function “crossval” that used the partitions created by the “cvpartition” function. This function computed the squared errors between the fit and the corresponding response test set and returned the overall mean across all test sets for the predictions. Overall performance of each classifier was judged based on the empirical ROC curve created using the MATLAB function “perfcurve”. That function returned the X and Y coordinates of an ROC curve for a vector of classifier predictions, the thresholds on classifier scores for the computed values of X and Y, and the area under the computed ROC curve along with 95% confidence intervals for that performance.

### 6.4.1. Results for the forty-three human subjects

A summary of the QUS parameter estimates obtained from the 43 subjects for each of the parameters is shown in Tables 6.2 (fibroadenomas) and 6.3 (carcinomas). Subjects are ordered from the smallest to largest ROI size. All subjects in this study were categorized as US-BIRADS 4 except subjects 23, 24, 33, and 40 which were categorized as US-BIRADS 3, 5, 1, and 5, respectively.

**Table 6.2.** QUS parameter values of fibroadenomas included in this study presented the order they are displayed in the figures. The sequential order in which they were recruited into the study are shown in the “subject order” column.

Class	ATT (dB-cm <sup>-1</sup> MHz <sup>-1</sup> )	ESD (μm)	ESDHI (μm)	ABSC (cm <sup>-1</sup> sr <sup>-1</sup> )	SNR	Nakagami <i>m</i>	maxCA	ROI size (mm <sup>2</sup> )	subject order
FA1	0.74	81.8	14.2	0.0213	1.63	0.83	0.109	5×5	22
FA2	1.25	83.4	13.6	0.0460	0.71	0.29	0.144	5×5	35
FA3	1.55	109.4	15.8	0.0360	1.15	0.53	0.057	5×5	37
FA4	1.57	124.8	13.8	0.0019	1.31	0.64	0.052	6×6	9
FA5	0.68	59.7	14.2	0.0025	0.85	0.35	0.076	6×6	27
FA6	0.69	107.2	10.4	0.0076	1.49	0.72	0.080	6×6	28
FA7	1.94	147.1	12.1	0.0480	1.28	0.59	0.093	5×8	41
FA8	0.71	143.6	4.1	0.0003	1.17	0.56	0.139	7×6	13
FA9	1.00	87.0	15.1	0.0094	1.13	0.55	0.008	7×6	15
FA10	0.85	112.3	13.6	0.0090	0.45	0.21	0.101	8×6	21
FA11	0.76	86.5	10.9	0.0030	1.21	0.57	0.161	8×6	30
FA12	1.24	119.0	11.8	0.0390	0.83	0.39	0.060	7×7	31
FA13	1.19	116.7	15.3	0.0460	0.80	0.38	0.239	6×9	43
FA14	1.92	165.5	11.8	0.0013	0.63	0.50	0.121	8×7	12
FA15	0.67	96.1	17.5	0.0170	1.19	0.59	0.033	9×7	3
FA16	1.30	90.1	15.6	0.0100	1.47	0.76	0.040	9×7	14
FA17	1.04	93.2	13.1	0.0212	1.13	0.54	0.177	8×10	32
FA18	1.05	127.5	10.6	0.0020	0.97	0.46	0.033	14×7	8
FA19	1.20	145.0	10.6	0.0064	1.80	0.88	0.006	10×10	1
FA20	0.42	82.9	20.0	0.0143	1.48	0.72	0.094	12×9	16
FA21	0.76	112.5	8.5	0.0013	0.63	0.32	0.001	15×9	2
FA22	1.01	109.8	9.5	0.0003	1.57	0.79	0.152	16×9	29
FA23	1.69	131.2	12.9	0.0090	1.02	0.47	0.029	15×10	7
FA24	1.14	105.5	11.1	0.0030	1.51	0.72	0.112	15×12	5
FA25	0.36	95.3	14.5	0.0221	0.64	0.27	0.114	16×12	23
FA26	0.71	85.6	11.5	0.0120	1.52	0.73	0.169	15×15	6
FA27	0.89	96.8	10.5	0.0092	1.89	1.01	0.013	15×15	20

**Table 6.3.** QUS parameter values of malignant masses included in this study presented the order they are displayed in the figures. The sequential order in which they were recruited into the study are shown in the “subject order” column. ACA = adenocarcinoma; DC = ductal carcinoma; DCIS = ductal carcinoma in situ; LC = lobular carcinoma; LCIS = lobular carcinoma in situ; IPC = intracystic papillary carcinoma. Subject 38 was reported as DCIS involving intraductal papilloma and involving ducts adjacent to papilloma; Subject 42 was reported as infiltrating ductal carcinoma Nottingham Grade 2, LCIS classical type, metastatic breast ductal carcinoma.

Class	ATT $\text{dB}\cdot\text{cm}^{-1}\text{MHz}^{-1}$	ESD ( $\mu\text{m}$ )	ESDHI ( $\mu\text{m}$ )	ABSC ( $\text{cm}^{-1}\text{sr}^{-1}$ )	SNR	Nakagami $m$	maxCA	ROI size ( $\text{mm}^2$ )	subject order
IDC1	1.85	90.1	10.1	0.005	1.45	0.73	0.204	5×5	18
IDC2	2.19	68.3	8.5	0.039	1.28	0.59	0.195	5×5	39
IDC3	2.17	57.9	13.1	0.041	1.24	0.56	0.206	5×5	40
IDC4	0.85	54.0	14.0	0.115	1.36	0.64	0.213	6×5	36
IDC5	1.47	100.3	12.2	0.075	1.19	0.53	0.149	5×7	34
IDC6	1.48	68.6	12.3	0.007	0.69	0.37	0.061	8×6	11
IDC7	0.63	95.9	2.4	0.006	1.17	0.54	0.034	7×6	25
IDC8	1.09	81.9	11.1	0.002	1.62	0.86	0.105	8×8	42
IDC9	2.2	86.7	6.2	0.001	1.29	0.59	0.004	13×10	17
IDC10	1.03	80.2	11.3	0.002	2.06	1.16	0.009	12×12	19
ILC1	0.74	94.7	5.1	0.016	1.13	0.51	0.123	5×5	26
ILC2	0.52	87.2	6.2	0.015	1.20	0.57	0.084	8×6	24
IPC	0.50	58.5	7.5	0.028	0.91	0.40	0.084	14×12	33
ACA	1.30	77.4	13.6	0.094	0.91	0.50	0.172	6×5	10
DCIS1	1.92	79.1	18.6	0.001	0.68	0.34	0.140	5×5	38
DCIS2	2.20	62.8	15.9	0.016	1.54	0.79	0.107	7×6	4

Summary plots of the QUS parameter estimates obtained from each subject for ATT, ESD, ESDHI and ABSC are shown in Fig. 6.5. Summary plots of the QUS parameter estimates obtained from each subject for maxCA, Nakagami  $m$ , and SNR are shown in Chapter 5. Similar to the arrangements in Tables 6.2 and 6.3, results are presented in these plots ordered from the smallest to largest ROI size to illustrate any potential trend in parameter estimates with ROI size. Parameter values for breast fat (described in Chapter 4; data point on the far right of each plot)<sup>10</sup> are included in the plots for comparison.

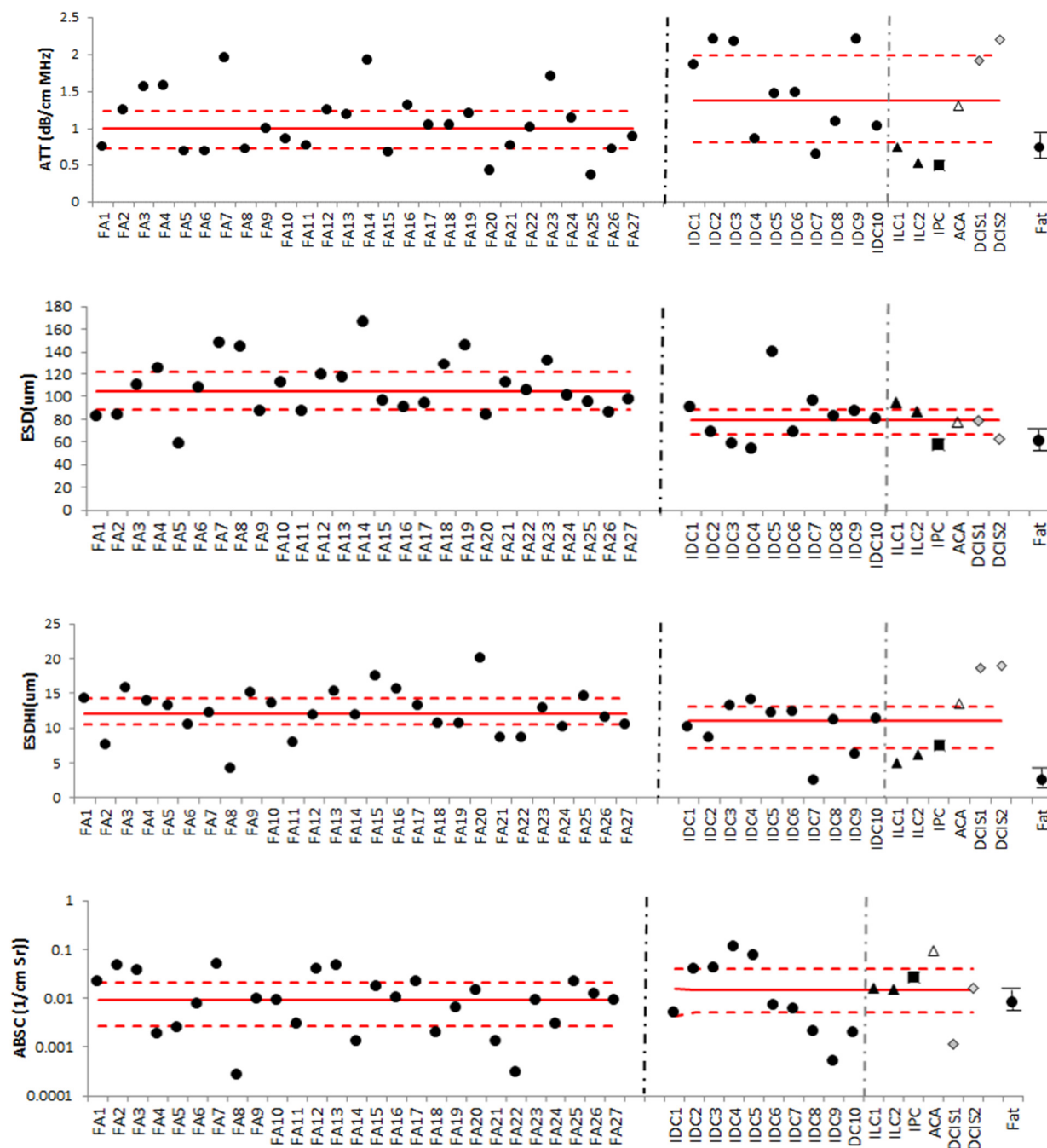


**Figure 6.5.** Plots of the individual QUS parameter estimates for each subject ordered from smallest to largest ROI size. The same ROI was used for all parameter estimates for an individual subject (e.g., FA1 is the fibroadenoma with the smallest ROI). Fibroadenoma (FA) are shown separately from cancers. Cancers are grouped together by type: Invasive ductal carcinoma (IDC); Invasive lobular carcinoma (ILC). The solid horizontal lines show the median value of that parameter (separately for fibroadenoma and carcinoma), and the dashed lines show the inner quartile range of values

The median ATT estimate among pathology-confirmed fibroadenomas ( $1.01 \pm 0.52$  dB·cm<sup>-1</sup>MHz<sup>-1</sup>; median  $\pm$  innerquartile range) was slightly lower than the median ATT among carcinomas ( $1.38 \pm 1.16$  dB·cm<sup>-1</sup>MHz<sup>-1</sup>), but both are higher than the median value for breast fat ( $0.82 \pm 0.40$  dB·cm<sup>-1</sup>MHz<sup>-1</sup>). The ATT for breast parenchyma and structural tissue reported by D'Astos and Foster ( $0.87 \pm 0.29$  dB·cm<sup>-1</sup>MHz<sup>-1.5</sup>) was smaller than the median values in fibroadenomas and carcinomas, but larger than that of breast fat.<sup>1</sup> The median ABSC estimate among fibroadenomas ( $0.92 \times 10^{-2} \pm 1.85 \times 10^{-2}$  cm<sup>-1</sup>sr<sup>-1</sup>) was slightly lower than the median ABSC estimate among carcinomas, ( $1.55 \times 10^{-2} \pm 3.5 \times 10^{-2}$  cm<sup>-1</sup>sr<sup>-1</sup>), and both were higher than the median value for breast fat ( $0.78 \times 10^{-2} \pm 0.72 \times 10^{-2}$  cm<sup>-1</sup>sr<sup>-1</sup>). This seemed counter-intuitive because most lesions appeared hypoechoic with respect to surrounding fat. Furthermore, the backscatter coefficient for breast parenchyma and structural tissue reported by D'Astos and Foster<sup>1</sup> was  $0.53 \times 10^{-2} \pm 0.26 \times 10^{-2}$  cm<sup>-1</sup>sr<sup>-1</sup>. A possible explanation is that this higher average backscatter coefficient might be due to the presence of coherent structures within the ROI. This is addressed in Figure 6.6, which shows a scatter plot of the logarithm of ABSC versus maxCA for fibroadenomas (blue points), carcinomas (orange points), and breast fat (black point). The positive correlation ( $R^2=0.49$ ) among these two variables supports this explanation.

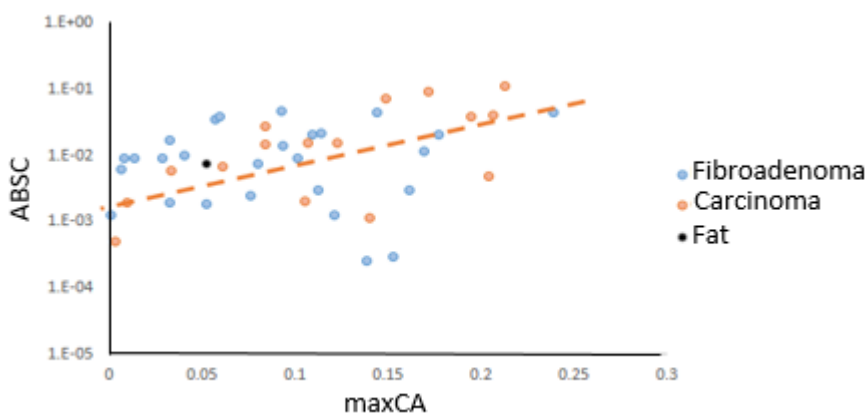


**Figure 6.6.** *log-average backscatter coefficient versus maxCA for fibroadenomas, carcinomas and fat*

The median ESD estimate among fibroadenomas ( $107.2 \pm 33.3 \mu\text{m}$ ) was slightly higher than the median ESD among carcinomas ( $79.6 \pm 21.1 \mu\text{m}$ ), and both are larger than the median value found in breast fat ( $61.6 \pm 14.0 \mu\text{m}$ ). The median ESDHI estimate among fibroadenomas ( $12.1 \pm 3.8 \mu\text{m}$ ) was similar to the value among carcinomas ( $11.2 \pm 6.0 \mu\text{m}$ ), and both were larger than the median value found in breast fat ( $4.15 \pm 0.33 \mu\text{m}$ ). The median maxCA estimate among fibroadenomas ( $0.09 \pm 0.09$ ) was comparable to the value in carcinomas ( $0.11 \pm 0.09$ ), and both are not significantly different from the median value found in breast fat ( $0.05 \pm 0.03$ ). The median envelope SNR estimate among fibroadenomas ( $1.17 \pm 0.64$ ) was similar to the value in carcinomas ( $1.2 \pm 0.31$ ), and is close to the median value found for breast fat ( $1.4 \pm 0.25$ ). The median Nakagami  $m$  estimate among fibroadenomas ( $0.56 \pm 0.29$ ) was not different from the values in carcinomas ( $0.56 \pm 0.15$ ), and both were close to the median value found in breast fat ( $0.68 \pm 0.15$ ). The relationship between the ESD and the Nakagami parameter  $m$  was also examined to make sure there is no trend in the data (i.e. the ESD estimates represents the tissue of interest and is not related to coherence) as suggested by Figure 6.7.

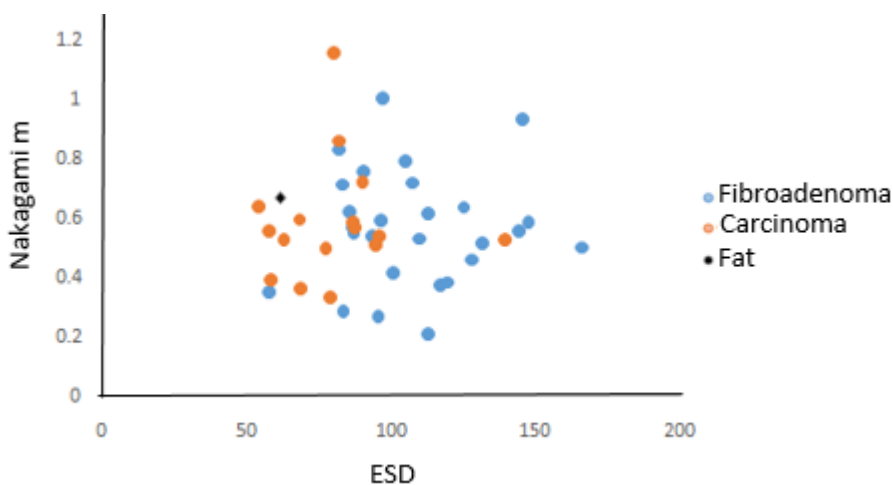


**Figure 6.7.** Relationship between Nakagami  $m$  and ESD for fibroadenoma, carcinoma and fat

Table 6.4 lists ROC AUC values and the corresponding 95% confidence intervals for various two-parameter and three-parameter combinations used for Bayesian classifiers. The best two parameter classification performance (largest AUC values) was obtained with ESD and ESDHI (AUC=0.94), and the best three-parameter classification performance was obtained with ATT, ESD, and ESDHI (AUC=1.0), followed by ABSC, ESD, and ESDHI (AUC=0.99) as shown in Figure 6.8.

**Table 6.4.** Area under the receiver operating characteristic curves for various 2-parameter and 3-parameter combinations of QUS parameters forming a naïve Bayesian classifier to differentiate fibroadenomas from carcinomas. The 95% confidence intervals were computed separately for the case when fibroadenoma was true-positive

<b>2 Parameters</b>	<b>AUC</b>	<b>95% Confidence interval</b>
ESD, ESDHI	0.94	[0.88,1.00]
ESD, ATT	0.92	[0.92,0.99]
ESD, ABSC	0.91	[0.82,0.97]
ESD, maxCA	0.90	[0.81,0.97]
ESD, Nakagm	0.89	[0.82,0.98]
ESD, SNR	0.89	[0.70,0.92]
<b>3 Parameters</b>		
ESD, ESDHI, ATT	1.00	[1.00,1.00]
ESD, ESDHI, ABSC	0.99	[0.96,1.00]
ESD, ESDHI, maxCA	0.95	[0.93,1.00]
ESD, Att, Nakagm	0.94	[0.83,0.98]
ESD, Att, SNR	0.94	[0.83,1.00]

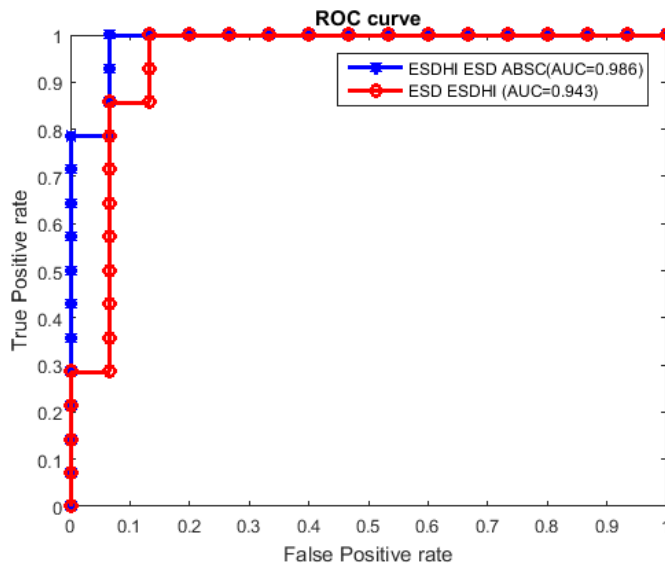


**Figure 6.8.** ROC curves illustrating the performance of various classifiers based on combinations of QUS parameters;  $AUC=1$  for ATT, ESD, ESDHI

The differentiation between fibroadenomas and carcinomas with ATT, ESD, and ESDHI can be observed in Figure 6.9, which shows each fibroadenoma (red) and each carcinoma (blue) in a 3D space defined these parameters.

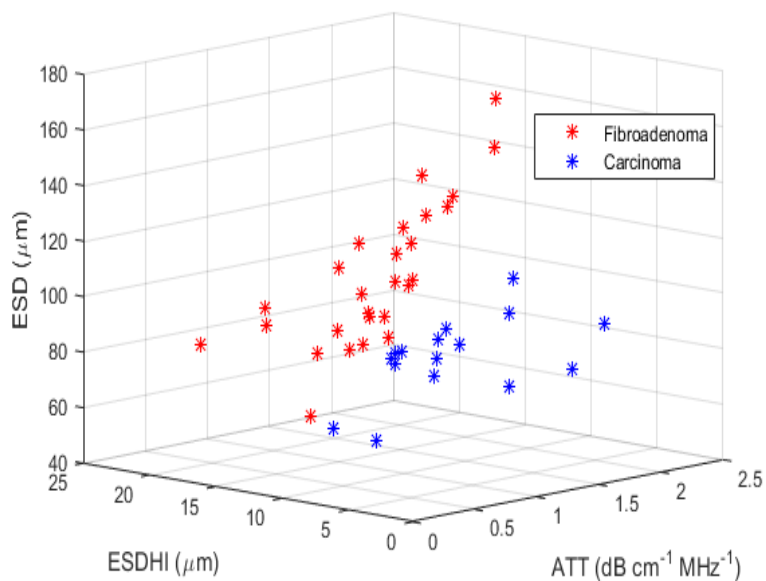


**Figure 6.9.** Plots of best 3 parameters combination

## 6.5. Additional data set acquired during 3D data acquisition

For this subgroup, human subjects recruited (n=15) did not necessarily have suspicious breast mass. The protocol used in the study was UW HSC IRB-approved and HIPAA-compliant. Subjects who were at least 18 years old (to provide informed consent) were recruited. 2D and 3D RF echo signal data were acquired from these subjects, the motivation for scanning these subjects was to test the 3D QUS parameter estimation and compare it with 2D estimates. Here we are only reporting the 2D estimates, the 3D estimates are reported in Chapter 7. 2D acquisition was performed in the same manner mentioned in Chapter 2 (for the second subgroup) with a Siemens S2000 machine equipped with an 18L6 transducer. The reference phantom data was the same phantom described in Chapter 2 for the second subgroup. A summary of the properties of the phantom is provided in Table 6.5.

**Table 6.5.** *Properties of the reference phantom*

Speed of sound (m/s)	1492
Attenuation coefficient ( $\text{dB}\cdot\text{cm}^{-1}\text{MHz}^{-1}$ )	0.54
Scattering sources	3000E glass beads

This group included an additional 5 fibroadenomas. However, some of these subjects had a previous biopsy or had somewhat heterogeneous tumors or had a biopsy clip within the tumor. For a subject with a clip, the power spectra from the clip location was removed (see Chapter 5) to avoid echo signal coherence, in order to avoid the QUS parameter estimate bias that can result from the presence of the clip. Since this data set did not well-conform to our selection criteria, we started by training the classifier with a random selection of an equal

number of fibroadenomas and carcinomas (to eliminate the effect of prior probability on the performance of the classifier). The idea of this experiment was to assess the ability of the classifier to correctly classify these tumors if only unbiased, high quality data (i.e. follow our QUS assumptions) was used for training. This resulted in 32 human subjects (the data was selected such that all carcinomas were included (n=16) and an equal number of fibroadenomas were randomly selected) used for training the classifier.

To obtain the AUC of the ROC curve and its confidence interval for the classifier built with each combination of QUS parameters, a 'Leave-one-out' training strategy was implemented using standard MATLAB functions. For this purpose, the ensuing steps were followed: 1) Construction of measurements matrix: A 'measurement' matrix was composed of 32 rows (number of subjects) containing the measurement vector. A measurement vector refers to the set of two (i.e., ESD and ESDHI) or three (i.e., ESD, ESDHI and ATT) QUS parameters for one subject used in the classification. 2) Creation of data partitions for 'Leave-one-out' cross validation: The measurement matrix was used as an input to the `cvpartition` function with the 'Leave Out' option. These steps created partition objects with 32 training sets and 32 corresponding test measurements. Each training set/test pair was obtained by using one measurement vector as the test subject and the remaining 31 vectors as the training set. This was repeated 32 times by drawing a different measurement vector, without replacement. 3) Creation of classifiers: 32 Naïve Bayesian classifiers were created with the function `NaiveBayes.fit`, using each of the 32 training sets. 4) Test of the classifiers: Each of the 32 classifiers was applied to the corresponding test measurement vector using the `predict` function. This resulted in 32 scores (class to which each of the 32 measurement vectors was assigned by the classifier, either fibroadenoma or carcinoma). 5) Construction of the ROC

curve: The 32 scores were used to obtain the ROC curve using the `perfcurve` function in MATLAB. This function also provided an estimate of the area under the ROC curve (AUC) and its confidence interval using a bootstrap approach by setting the 'Nboot' option to a value `nboot`. This creates `nboot` ROC curves, each one achieved by sampling with replacement the scores 32 times. This led to `nboot` AUC estimates of the AUC, from which the mean and confidence intervals were obtained. Here, we used `nboot=10`.

Once the classifier was trained the rest of the human subject data ( $n=15$ ) were used to test the classifier's ability to classify unknown data. It is important to keep in mind that if there were enough subjects, once a classifier was built any new data set would be entered in the GUI and classified as either a fibroadenoma or a carcinoma, but would not be used to retrain the classifier. Thus, the QUS parameter estimates from each of these subjects were entered into the GUI, and a classification category was obtained.

An additional experiment was performed to determine the effect of such biased pool of data on the AUC of the ROC curve. Here we used the entire data (48 human subjects) to train and test the classifier performance and determine the area under the ROC curve for the best performing 2 and 3 parameters sets to see whether any performance reduction would occur when these additional 5 data sets were included.

### **6.5.1. Results for the forty-eight human subjects**

The results for QUS parameter estimates for the additional five subjects (scanned with 18L6 transducer to obtain 2D data at the same time the 3D data were acquired) are summarized in Table 6.6.

**Table 6.6.** QUS parameter values of fibroadenomas included in the ABVS study

	ATT (dB/cm MHz)	ESD ( $\mu\text{m}$ )	ESDHI ( $\mu\text{m}$ )	ABSC (1/cm sr)	SNR	Nakagami m	maxCA
1	1.31	119.2	10.1	0.006	1.5	1.03	0.01
2	1.61	84	16	0.01	1.3	1	0.1
3	0.78	168	10	0.12	1.4	0.9	0.03
4	0.95	86.2	17	0.03	1.1	1.05	0.05
5	1.09	163	19	0.0003	1.69	0.85	0.012

For the forty-eight human subjects, the median ATT estimate among pathology-confirmed fibroadenomas ( $1.03 \pm 0.49 \text{ dB}\cdot\text{cm}^{-1}\text{MHz}^{-1}$ ; median  $\pm$  innerquartile range) was slightly lower than the median ATT among carcinomas ( $1.38 \pm 1.16 \text{ dB}\cdot\text{cm}^{-1}\text{MHz}^{-1}$ ). The median ABSC estimate among fibroadenomas ( $0.93 \times 10^{-2} \pm 1.84 \times 10^{-2} \text{ cm}^{-1}\text{sr}^{-1}$ ) was slightly lower than the median ABSC estimate among carcinomas, ( $1.55 \times 10^{-2} \pm 3.5 \times 10^{-2} \text{ cm}^{-1}\text{sr}^{-1}$ ). The median ESD estimate among fibroadenomas ( $108.3 \pm 37.9 \mu\text{m}$ ) was slightly higher than the median ESD among carcinomas ( $79.6 \pm 21.1 \mu\text{m}$ ). The median ESDHI estimate among fibroadenomas ( $13 \pm 4.5 \mu\text{m}$ ) was similar to the value among carcinomas ( $11.2 \pm 6.0 \mu\text{m}$ ). The median maxCA estimate among fibroadenomas ( $0.078 \pm 0.081$ ) was comparable to the value in carcinomas ( $0.11 \pm 0.09$ ). The median SNR estimate among fibroadenomas ( $1.2 \pm 0.55$ ) was similar to the value in carcinomas ( $1.2 \pm 0.31$ ). The median Nakagami m estimate among fibroadenomas ( $0.59 \pm 0.32$ ) was not different from the values in carcinomas ( $0.56 \pm 0.15$ ). A comparison of these results with previous results estimated for the fibroadenomas in the 43 human subjects pool is shown in Table 6.7.

**Table 6.7.** Comparison of the median and interquartile ranges estimated for fibroadenomas in the 43-human subject pool versus the 48-human subject pool

	Fibroadenoma	
median $\pm$ IQR	Results from the 43 human subjects	Results from the 48 human subjects
ATT	$1.01 \pm 0.52 \text{ dB}\cdot\text{cm}^{-1}\text{MHz}^{-1}$	$1.03 \pm 0.49 \text{ dB}\cdot\text{cm}^{-1}\text{MHz}^{-1}$
ABSC	$0.92 \times 10^{-2} \pm 1.85 \times 10^{-2} \text{ cm}^{-1} \text{sr}^{-1}$	$0.93 \times 10^{-2} \pm 1.84 \times 10^{-2} \text{ cm}^{-1} \text{sr}^{-1}$
ESD	$107.2 \pm 33.3 \mu\text{m}$	$108.3 \pm 37.9 \mu\text{m}$
ESDHI	$12.1 \pm 3.8 \mu\text{m}$	$13 \pm 4.5 \mu\text{m}$
maxCA	$0.09 \pm 0.09$	$0.078 \pm 0.081$
Nakagami m	$0.56 \pm 0.29$	$0.59 \pm 0.32$
SNR	$1.17 \pm 0.64$	$1.2 \pm 0.55$

The results show that when unbiased pool of data is used for training the classifier, the rest of the subjects were classified correctly. When the biased pool of data was included in the classifier training, the best two parameter classification performance (largest AUC values), was obtained with the ESD and the ESDHI (AUC=0.92 with confidence interval of [0.87, 0.97]), and the best three-parameter classification performance was obtained with ATT, ESD, and ESDHI (AUC=0.98 with confidence interval of [0.94, 1]). This reduction in the AUC is due to the fact that with the leave-one-out method, each time you train the classifier, a new centroid is identified based on the data in the training set. This can affect the classification of the tumors when using the minimum distance to the centroid method. However, when the classifier is trained with an unbiased, high quality pool of data, and the remainder of the data set was tested using the GUI, all tumors were classified correctly (since the biased data set did not contribute to the calculation of the centroid of each class).

## 6.6. Discussion

A multi-parameter Bayesian classifier appears to be an effective approach for combining QUS parameters to increase the specificity of breast ultrasound and to identify those lesions that

are least likely to be carcinomas. We also expect these acoustic parameters to vary with treatment (such as chemotherapy), potentially making the approach useful for monitoring treatment.<sup>12</sup> The results reported here demonstrate the need to further test this approach to noninvasive breast tissue classification. In this study, the limited number of samples in our preliminary results enables these classifiers to be only marginally trained and tested. Thus, a larger data set is needed to allow testing performance when additional parameters are added to the classifier. For example, parameters related to the linear and nonlinear elastic properties of breast tissue have shown promise for tissue classification.<sup>40;41</sup> To robustly test a 5-parameter classifier to select among two categories (benign and carcinoma), and assuming that 10 subjects are needed in each category per parameter, at least 50 subjects per category (at least 100 subjects in total) would be needed. Classifier performance reported here is biased (optimistically) because the data entering into the study were preselected as either fibroadenomas (the only benign disease included) or carcinomas (all cancer types combined into a single class). That reduction in task complexity greatly simplifies the performance requirements compared to the clinical task of breast mass characterization. Further, the tumors selected for inclusion had reasonably large regions that were (subjectively) homogeneous. This likely reduced variability in parameter estimates and improved classifier performance. Classification into these categories (“carcinoma” and “fibroadenoma”) is insufficient for clinical practice. A more useful classification would include all cancer types, all benign breast masses, and various types of normal tissue.

## 6.7. Conclusions

A Bayesian classifier based on three system-independent QUS parameters (ATT, ESD, and ESDHI) was effective for differentiating between fibroadenomas and cancerous masses in the

breast. Performance of the classifier incorporating these features resulted in an area under the ROC curve of 1.0. A larger study is needed to increase the diversity of benign diseases included and more rigorously test performance.

## 6.8. References

1. F. D'Astous and F. Foster, "Frequency dependence of ultrasound attenuation and backscatter in breast tissue," *Ultrasound in medicine & biology*, vol. 12, no. 2, pp. 795–808, **1986**.
2. Mortensen, P. Edmonds, Y. Gorfu, J. Hill, J. Jensen, P. Schattner, L. Shifrin, A. Valdes, S. Jeffrey, and L. Esserman, "Ultrasound tissue characterization of breast biopsy specimens: Expanded study," *Ultrasonic Imaging*, vol. 18, no. 3, pp. 215–230, **1996**.
3. K. Nam, J. A. Zagzebski, and T. J. Hall, "Quantitative assessment of in vivo breast masses using ultrasound attenuation and backscatter," *Ultrasonic imaging*, vol. 35, no. 2, pp. 146–161, 2013.
4. H. Tadayyon, A. Sadeghi-Naini, and G. Czarnota, "Noninvasive characterization of locally advanced breast cancer using textural analysis of quantitative ultrasound parametric images," *Translational Oncology*, vol. 7, no. 6, pp. 759–767, **2014**.
5. L. Sannachi, H. Tadayyon, A. Sadeghi-Naini, W. Tran, S. Gandhi, F. Wright, M. Oelze, and G. Czarnota, "Non-invasive evaluation of breast cancer response to chemotherapy using quantitative ultrasonic backscatter parameters," *Medical Image Analysis*, vol. 20, no. 1, pp. 224–236, **2015**.
6. B. Garra, B. Krasner, S. Horii, A. Ascher, S. Mun, and R. Zeman, "Improving the distinction between benign and malignant breast lesions: the value of sonographic texture analysis," *Ultrasonic Imaging*, vol. 15, no. 4, pp. 267–285, **1993**.
7. Chen, D.; and Hsiao, Y.; "Computer-aided diagnosis in breast ultrasound," *Journal of Medical Ultrasound*, vol. 16, no. 1, pp. 46 – 56, **2008**.

8. E. S. Burnside, D. L. Rubin, J. P. Fine, R. D. Shachter, G. A. Sisney, and W. K. Leung, "Bayesian network to predict breast cancer risk of mammographic microcalcifications and reduce number of benign biopsy results: initial experience 1," *Radiology*, vol. 240, no. 3, pp. 666–673, **2006**.
9. C. E. Kahn, L. M. Roberts, K. A. Shaffer, and P. Haddawy, "Construction of a bayesian network for mammographic diagnosis of breast cancer," *Computers in biology and medicine*, vol. 27, no. 1, pp. 19–29, **1997**.
10. D. Dumitru, "Prediction of recurrent events in breast cancer using the naive bayesian classification," *Annals of the University of Craiova-Mathematics and Computer Science Series*, vol. 36, no. 2, pp. 92–96, **2009**.
11. J. Gadewadikar, O. Kuljaca, K. Agyepong, E. Sarigul, Y. Zheng, and P. Zhang, "Exploring bayesian networks for medical decision support in breast cancer detection," *African Journal of Mathematics and Computer Science Research*, vol. 3, no. 10, pp. 225–231, **2010**.
12. J. Nahar, Y.-P. P. Chen, and S. Ali, "Kernel-based naive bayes classifier for breast cancer prediction," *Journal of biological systems*, vol. 15, no. 01, pp. 17–25, **2007**.
13. I. Zyout, I. Abdel-Qader, and C. Jacobs, "Bayesian classifier with simplified learning phase for detecting microcalcifications in digital mammograms," *Journal of Biomedical Imaging*, vol. 2009, p. 30, **2009**.
14. E. S. Burnside, D. L. Rubin, J. P. Fine, R. D. Shachter, G. A. Sisney, and W. K. Leung, "Bayesian network to predict breast cancer risk of mammographic microcalcifications and reduce number of benign biopsy results: initial experience 1," *Radiology*, vol. 240, no. 3, pp. 666–673, **2006**.

15. J. J. Anderson, M.-T. Herd, M. R. King, A. Haak, Z. T. Hafez, J. Song, M. L. Oelze, E. L. Madsen, J. A. Zagzebski, W. D. O'Brien et al., "Interlaboratory comparison of backscatter coefficient estimates for tissue-mimicking phantoms," *Ultrasonic imaging*, vol. 32, no. 1, pp. 48–64, **2010**.
16. K. Nam, I. M. Rosado-Mendez, L. A. Wirtzfeld, G. Ghoshal, A. D. Pawlicki, E. L. Madsen, R. J. Lavarello, M. L. Oelze, J. A. Zagzebski, W. D. OBrien et al., "Comparison of ultrasound attenuation and backscatter estimates in layered tissue-mimicking phantoms among three clinical scanners," *Ultrasonic imaging*, vol. 34, no. 4, pp. 209–221, **2012**.
17. I. M. Rosado-Mendez, K. Nam, T. J. Hall, and J. A. Zagzebski, "Task-oriented comparison of power spectral density estimation methods for quantifying acoustic attenuation in diagnostic ultrasound using a reference phantom method," *Ultrasonic imaging*, vol. 35, no. 3, pp. 214–234, **2013**.
18. K. Nam, I. M. Rosado-Mendez, L. A. Wirtzfeld, A. D. Pawlicki, V. Kumar, E. L. Madsen, G. Ghoshal, R. J. Lavarello, M. L. Oelze, T. A. Bigelow et al., "Ultrasonic attenuation and backscatter coefficient estimates of rodent-tumor-mimicking structures: comparison of results among clinical scanners," *Ultrasonic imaging*, vol. 33, no. 4, pp. 233–250, **2011**.
19. L. A. Wirtzfeld, K. Nam, Y. Labyed, G. Ghoshal, A. Haak, E. Sen-Gupta, Z. He, N. R. Hirtz, R. J. Miller, S. Sarwate et al., "Techniques and evaluation from a cross-platform imaging comparison of quantitative ultrasound parameters in an in vivo rodent fibroadenoma model," *Ultrasonics, Ferroelectrics, and Frequency Control, IEEE Transactions on*, vol. 60, no. 7, pp. 1386–1400, **2013**.

20. A. Gerig, Q. Chen, J. Zagzebski, and T. Varghese, "Correlation of ultrasonic scatterer size estimates for the statistical analysis and optimization of angular compounding," *Journal of the Acoustical Society of America*, vol. 116, no. 3, pp. 1832–1841, 2004.
21. W. Liu, J. A. Zagzebski, T. Varghese, A. L. Gerig, and T. J. Hall, "Spectral and scatterer-size correlation during angular compounding: Simulations and experimental studies," *Ultrasonic Imaging*, vol. 28, no. 4, pp. 230–244, 2006.
22. L. X. Yao, J. A. Zagzebski, and E. L. Madsen, "Backscatter coefficient measurements using a reference phantom to extract depth-dependent instrumentation factors," *Ultrasonic Imaging*, vol. 12, no. 1, pp. 58–70, **1990**.
23. K. Nam, I. M. Rosado-Mendez, L. A. Wirtzfeld, G. Ghoshal, A. D. Pawlicki, E. L. Madsen, R. J. Lavarello, M. L. Oelze, J. A. Zagzebski, W. D. O'Brien et al., "Comparison of ultrasound attenuation and backscatter estimates in layered tissue-mimicking phantoms among three clinical scanners," *Ultrasonic Imaging*, vol. 34, no. 4, pp. 209–221, **2012**.
24. Insana, M.; Wagner, R.; Brown, D.; and Hall, T.; Describing small-scale structure in random media using pulse-echo ultrasound, *The Journal of the Acoustical Society of America*, vol. 87, no. 1, pp. 179–192, **1990**.
25. Nam, K.; Zagzebski, J.; and Hall, T.; Quantitative assessment of in vivo breast masses using ultrasound attenuation and backscatter, *Ultrasonic Imaging*, vol. 35, no. 2, pp. 146–161, **2013**.
26. Nasief, H.; Rosado-Mendez, I.; Zagzebski, J.; and Hall, T.; Acoustic properties of subcutaneous breast fat, *Journal of Ultrasound in Medicine*, vol. 34, no. 11, pp. 2007–2016, **2015**.

27. Insana, M.; and Hall, T.; Characterizing The Microstructure Of Random-Media Using Ultrasound, *Physics In Medicine and Biology*, vol. 35, no. 10, pp. 1373–1386, OCT **1990**.
28. Insana, M.; and Hall, T.; Parametric ultrasound imaging from backscatter coefficient measurements: Image formation and interpretation, *Ultrasonic Imaging*, vol. 12, no. 4, pp. 245–267, **1990**.
29. Rubert, N.; and Varghese, T.; Scatterer number April 29, 2017 DRAFT 8 density considerations in reference phantom based attenuation estimation, *Ultrasound in medicine & biology*, vol. 40, no. 7, pp. 1680–1696, **2014**.
30. Omari, E.; Varghese, T.; Madsen, E.; and Frank, G.; Evaluation of the impact of backscatter intensity variations on ultrasound attenuation estimation, *Medical physics*, vol. 40, no. 8, **2013**.
31. Luchies, A.; Ghoshal, G.; O'Brien, W.; and Oelze, M.; Reducing the effects of specular scatterers on QUS imaging using the generalized spectrum, *Proceedings - IEEE Ultrasonics Symposium*, no. 1, pp. 728–731, **2010**.
32. Luchies, A.; and Oelze, M.; “Backscatter Coefficient Estimation Using Tapers with Gaps,” *Ultrasonic Imaging*, vol. 37, no. 2, pp. 117–134, **2015**.
33. Rosado-Mendez, I. ; Drehfal, L.; Zagzebski, J.; and Hall, T.; Analysis of Coherent and Diffuse Scattering Using a Reference Phantom, *IEEE transactions on ultrasonics, ferroelectrics, and frequency control*, vol. 63, no. 9, pp. 1306– 1320, **2016**.
34. Rosado-Mendez, I. ; Advanced spectral analysis methods for quantification of coherent ultrasound scattering: Applications in the breast. University of Wisconsin, **2014**.

35. Zagzebski, J.; Rosado-Mendez, I.; Nasief, H.; and Hall, T.; Quantitative Ultrasound (QUS): Enhancing Diagnosis using Estimates of Acoustic Attenuation and Backscatter Properties of Tissue, *MEDICAL PHYSICS: Fourteenth Mexican Symposium on Medical Physics*, vol. 1747, no. 1, p. 050001, **2016**.
36. Mortensen, C. ; Edmonds, P. ; Gorf, Y. ; Hill, J. ; et al.; Ultrasound tissue characterization of breast biopsy specimens: Expanded study, *Ultrasonic Imaging*, vol. 18, no. 3, pp. 215– 230, **1996**.
37. Donohue, K.; Huang, L.; Georgiou, G.; Cohen, F.; Piccoli, C. ; and Forsberg, F. ; Malignant and benign breast tissue classification performance using a scatterer structure preclassifier. *IEEE Transactions on Ultrasonics, Ferroelectrics, and Frequency Control*, vol. 50, no. 6, pp. 724–729, **2003**.
38. Huang, L.; Donohue, K.; Genis, V.; and Forsberg, F.; Duct detection and wall spacing estimation in breast tissue. *Ultrasonic Imaging*, vol. 22, no. 3, pp. 137–152, **2000**.
39. Wagner, R.; Smith, S.; Sandrik, J.; and Lopez, H.; Statistics of speckle in ultrasound bscans, *IEEE Transactions on Sonics and Ultrasonics*, vol. 30, no. 3, pp. 156–163, **1983**.
40. Shankar, P.; Dumane, V. ; Reid, J.; Genis, V.; Forsberg, F.; Piccoli, C.; and Goldberg, B.; Classification of ultrasonic b-mode images of breast masses using nakagami distribution, *IEEE Transactions on Ultrasonics, Ferroelectrics, and Frequency Control*, vol. 48, no. 2, pp. 569–580, 2001.
41. Destrempes, F. ; and Cloutier, G. ; Review of envelope statistics models for quantitative ultrasound imaging and tissue characterization, in *Quantitative Ultrasound in Soft Tissues*. Springer, 2013, pp. 219–274

## **Chapter 7: Implementing 3D QUS in the breast and comparing 3D with 2D QUS results**

*Portion of this chapter is published as:*

*Wang, Y.; Nasief, H.; Kohn, S.; Milkowski, A.; Clary, T.; Barnes, S.; Barbone, P.; and Hall, T.; Three-dimensional ultrasound elasticity imaging on an automated breast volume scanning system, Ultrasonic imaging, accepted for publication, May 2017.*

Breast tissue classification is very important in diagnosing cancer. As mentioned earlier, QUS parameters such as the specific attenuation coefficient (ATT), the backscatter coefficient (BSC), and the effective scatter diameter (ESD) can give important insight into the characteristics of focal breast masses. In the previous chapter, we described a Bayesian classifier that showed promising preliminary results as a non-invasive tool to differentiate between fibroadenomas and carcinomas using combinations of QUS parameters. In this chapter, we explore extension of QUS to data acquired using 3D imagers. Given the performance of the Bayesian classifier for 2D data sets, we anticipated that the extension of QUS to data acquired using an automated breast volume scanning (ABVS) system might also provide a powerful tool for detecting and classifying breast masses. The ABVS scanner was chosen because it can scan the whole breast, and may represent a practical way of automated ultrasound screening, under consideration in many centers for dense breast.

Presented here is a systematic extension of current 2D data acquisition and analysis methods to 3D in an attempt to provide better spatial sampling of breast tumors and display unique image planes to better characterize tumors (C-scan image plane, constant depth plane). C-scan images allow visualization of the tumor relative to breast ductal structures and thus, they could provide more insight into the structural modification by a breast tumor. For instance, a benign tumor tends to lie within ductal structures. Also, the shape of a mass in the C-scan view may offer

insight regarding its nature, since carcinomas, unlike most fibroadenomas, tend to have irregular boundaries that can be hard to detect using 2D scans.

Our preliminary 2D results for human classification showed that values for the effective scatterer diameter along with the specific attenuation can be used to differentiate between carcinoma and fibroadenoma in most cases, such that patients with high attenuation and low effective scatterer diameter are likely to have a carcinoma and those with the opposite characteristic are more likely to have a fibroadenoma (see Chapter 6). Given the promising preliminary results in 2D, we focused our initial 3D C-scan image formation on ATT and ESD. QUS algorithms were adapted and tested using phantoms, *in vivo* subcutaneous fat, and *in vivo* breast masses to analyze 3D data sets provided by this system. The analysis was done off line on each slice to estimate QUS parameters in the same manner described in Chapter 2. Parametric 2D images were then stacked together to generate a volume and C-scan images were displayed from this volume. Using 3D data, we also estimated the acoustic properties of subcutaneous breast fat under different levels of deformation (increased surface stress) to explore whether there may be variation in acoustic properties as a function of accumulated strain. Finally, we varied the thickness of the reconstructed slices to reduce statistical variations beyond the reductions achieved using 2D processing of single scan plane acquisition.

## **7.1. The automated breast volume scanning (ABVS) system**

The system consists of two parts, a Siemens S2000 ultrasound system and an automated breast volume scanner (ABVS) attachment (see Figure 7.1). The ABVS is composed of a support tower, an arm, and a transducer pod assembly containing a 154mm long, 768-element 1D array ultrasound transducer (14L5BV). The transducer excitation frequency was set to 11MHz, the

maximum field of view was 154 mm x 168 mm, the maximum display depth was 60 mm. Elevational transducer motion was controlled by a motor inside the pod assembly that sweeps the transducer in the elevational direction within the pod.

The commercial system uses an open-mesh screen that couples the transducer to the breast. In this study, that screen assembly was replaced with a compliant, fluid-filled coupling bag. A motor in the tower was added to lift or lower counterweights which offset the weight of the arm and transducer pod assembly, thus allowing the arm to move vertically, up or down. Both directions were tested in this study. However, the downward movement was utilized for most of the subjects. The S2000 was programmed to control the motion of the counterweights and transducer pod.



**Figure 7.1.** *The ABVS system showing a Siemens S2000 ultrasound system and an automated breast volume scanner (ABVS) attachment.*

Data were acquired using the AXIUS Direct ultrasound research interface<sup>1</sup> to obtain RF data sampled at 40 MHz for each scan line in the 3D volume. Image and RF echo signal data were acquired throughout planes each separated by 0.3 mm for phantoms and 0.2 mm for human

subjects. For each slice, the specific attenuation coefficients were measured (using a 6mmx6mm PER) with the Reference Phantom Method (see Chapter 2). Secondly, the backscatter coefficients were estimated (using a 4mmx4mm PER) with the Reference Phantom Method after compensating for attenuation using a modified least squares method (see Chapter 4). ESDs were estimated from the BSC using a Gaussian form factor model (see Chapter 2). Measured values from independent 2D parametric images were stacked together to generate a volume, then C-scan images (constant depth, see Figure 7.2) of ESDs and ATT were generated.

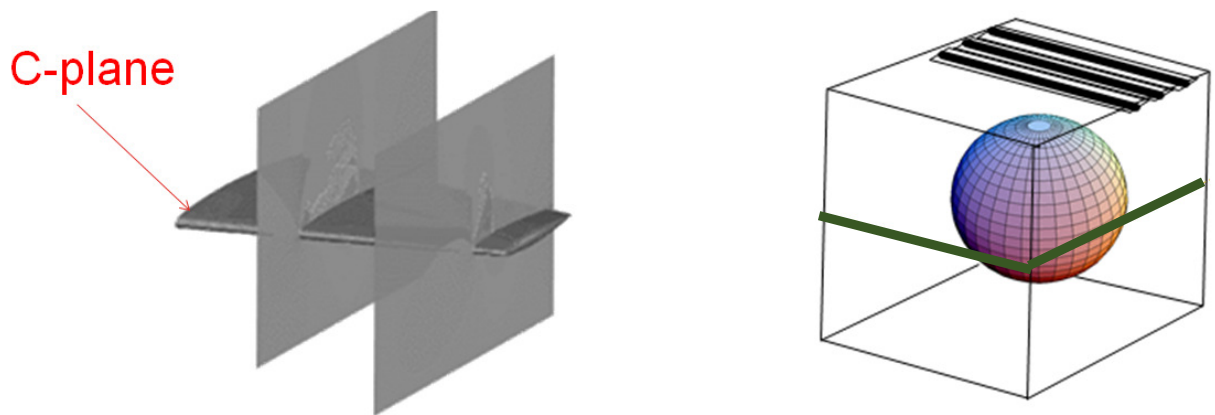


**Figure 7.2.** *Illustration of data acquisition and c-scan formation. Data was acquired by translating the transducer over the surface of the phantom, and the C-scan image was generated by selecting data at a constant depth (cut at the green lines)*

## 7.2. The simple elastography (SE) phantom

RF echo signals were acquired from a phantom composed of agar gel (a 5-cm cube with a 1 cm diameter sphere at its center with ATT contrast, see Figure 7.3). The speed of sound and attenuation coefficient of the phantom were measured (in test cylinders) using a narrow band substitution technique (see Chapter 2). The speed of sound in the sphere was 1533 m/sec at 2.5 MHz, and the attenuation coefficient versus frequency slope was  $0.48 \text{ dB} \cdot \text{cm}^{-1} \text{MHz}^{-1}$ . The speed

of sound in the background was 1518 m/sec at 2.5 MHz and the attenuation coefficient was  $0.09 \text{ dB} \cdot \text{cm}^{-1} \text{MHz}^{-1}$ .

The reference phantom used here, termed the black curved phantom, had the same composition as the phantom described in Chapter 2 for in-vivo data (second subgroup). However, this reference phantom was immersed in oil and had a dome shape to better conform to the fluid-filled bag. This phantom has tiny glass bead scattering sources (3000E beads; nominally 5-20  $\mu\text{m}$  diameter). The acoustic properties of the reference phantom were determined as described in Chapter 2. The sound speed of the phantom is 1517m/s at 2.5MHz; the attenuation coefficient vs. frequency,  $\alpha(f)$ , is represented by  $\alpha(f) = 0.51f \text{ dB/cm}$ , where  $f$  is the frequency in MHz. Both the sample and the reference were scanned using a fluid-filled bag to couple the transducer to the surface of the phantom being imaged. During the data acquisition, 250 frames of RF data were acquired. The elevational separation between slices was 0.3 mm. Data from 53 slices covering the sphere and the surrounding background material (15.9 mm) were analyzed.

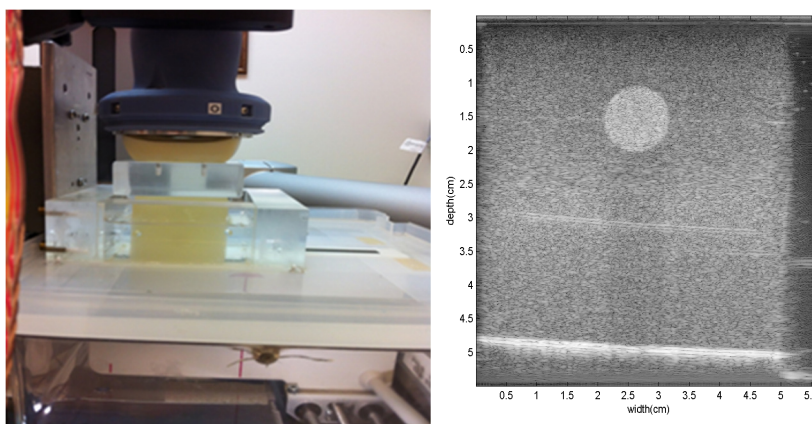


**Figure 7.3.** *The simple elastography phantom and a B-mode image of the phantom showing the sphere in the middle of the phantom*

### 7.2.1. Results for the SE phantom

The results showed that there was a bias of about 20% in ATT ( $0.6 \text{ dB}\cdot\text{cm}^{-1}\text{MHz}^{-1}$  vs. the expected value of  $0.48 \text{ dB}\cdot\text{cm}^{-1}\text{MHz}^{-1}$ ). Higher apparent attenuation values were found at the edges of the inclusion, as shown in Figure 7.4. This might be due to refraction or to backscatter artifacts that sometimes plague the RPM method in estimating attenuation. Figure 7.4 shows a B-mode image from the acquisition view and the location where C-scan image was generated. Also shown are a B-mode C-scan with the sphere outlined in yellow, and the B-mode C-scan with attenuation overlay.

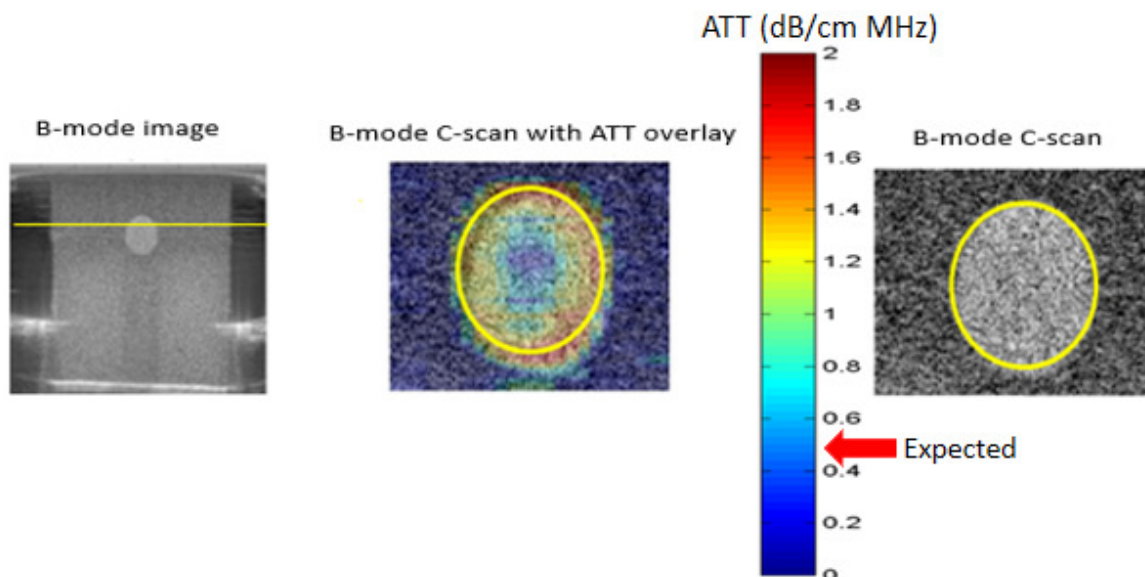


**Figure 7.4.** Shown from the left to right are the acquisition view with the location where the c-scan was generated outlined, the B-mode C-scan with attenuation overlay with the sphere outlined, and the B-mode C-scan with the sphere outlined.

### 7.3. Data Acquisition for the ACR phantom

This phantom was manufactured in our lab for the American College of Radiology (ACR)<sup>5</sup>, and has masses of various sizes and shapes embedded in a simulated breast parenchyma, with a proximal layer of tissue-mimicking fat forming an irregular boundary. A schematic of this

phantom is shown in Figure 7.5 (this is the same phantom used in Chapter 4). For this study, we were interested in a hypoechoic, highly attenuating mass (spanning 1.2 cm). The lab attenuation coefficient of this mass was  $1.42 \text{ dB}\cdot\text{cm}^{-1}\text{MHz}^{-1}$ . The phantom was scanned with the Siemens S2000 ABVS system. The same reference phantom described in the previous section was used for this study.

During the data acquisition, 200 frames of RF data were acquired. However, data from 45 slices covering the tumor and surrounding tissue mimicking material, extending over a 13.5 mm elevational dimension, were analyzed. For each slice, ATT was estimated. Both an “acquired plane” view and a C-scan of the B-mode and the B-mode with ATT overlay were constructed.

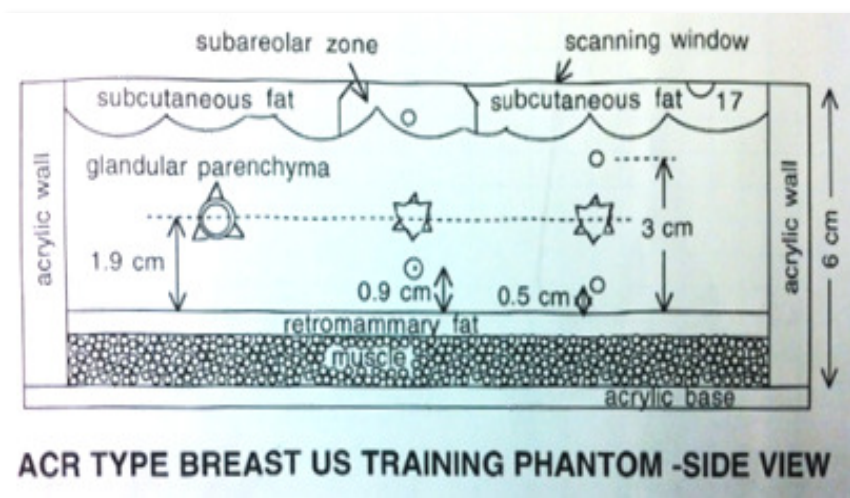


*Figure 7.5. The schematic of the ACR phantom*

### 7.3.1. Results for the ACR phantom

The results showed that ATT C-scans of the hypoechoic, highly attenuating mass exhibited a 20% overestimation in the average attenuation values ( $1.7 \text{ dB}\cdot\text{cm}^{-1}\text{MHz}^{-1}$  vs. an expected value of  $1.42 \text{ dB}\cdot\text{cm}^{-1}\text{MHz}^{-1}$ ).

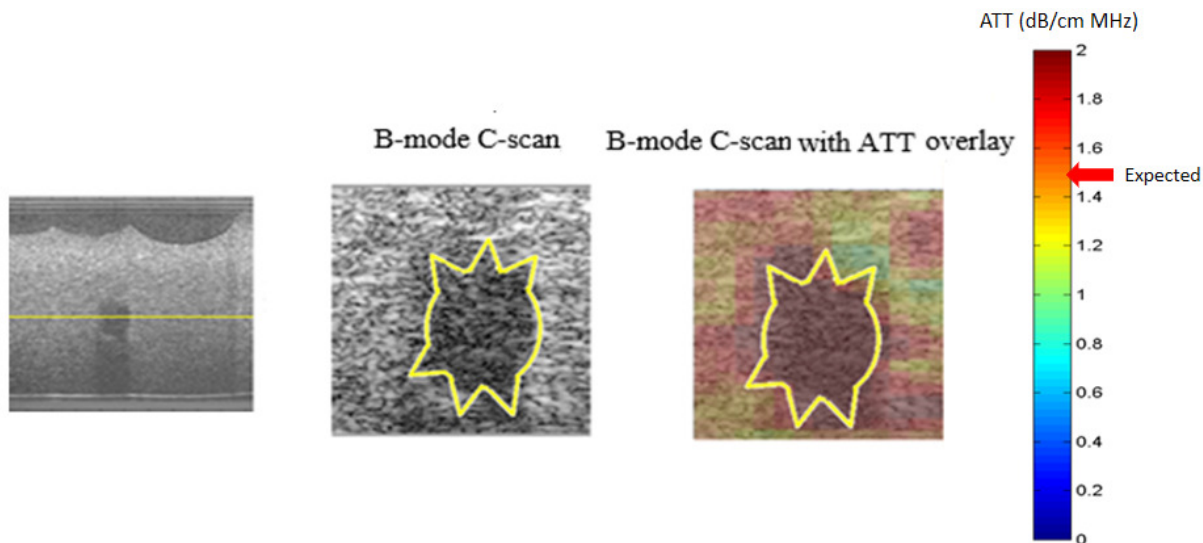


**Figure 7.6.** Image of the ACR phantom obtained with the ABVS scanner. Left conventional B-mode image through a speculated mass; center B-mode C-scan; right B-mode C-scan with ATT overlay (the colorbar shows values from 0-2 dB/cm MHz).

## 7.4. Thick slice formation

To reduce statistical variations beyond the reductions achieved using 2D processing of single scan plane acquisition, we varied the thickness of the reconstructed slices of the SE phantom. To do so, the ATT estimated from an increasing number of slices (2, 3, 5, 7, 9, and 11 slices) were averaged to generate a map of this parameter. The ROI selected (4cm x 3 cm) for the analysis included the 1 cm sphere as shown in Figure 7.2.

### 7.4.1. Results for thick slice formation

The maps generated using different slice thicknesses are shown in Figure 7.7. The maps generated using 1 and 5 slice thickness overlaid on B-mode images are shown in Figure 7.8.

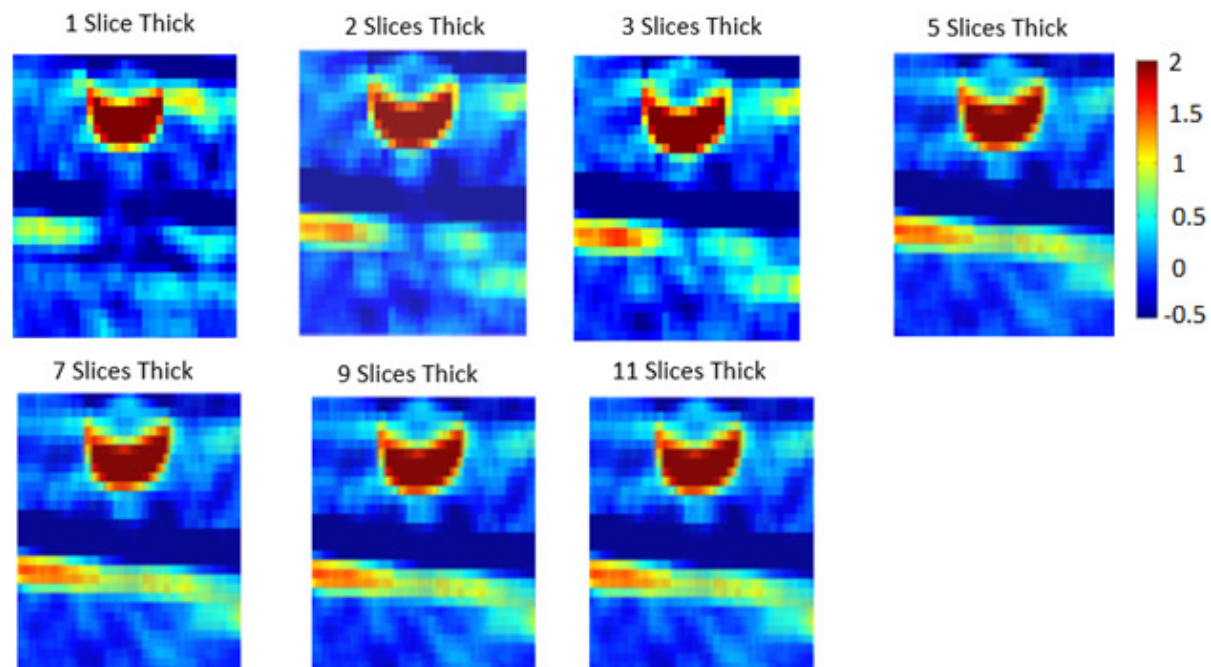


*Figure 7.7. Varying the slice thickness of attenuation maps of the SE phantom.*

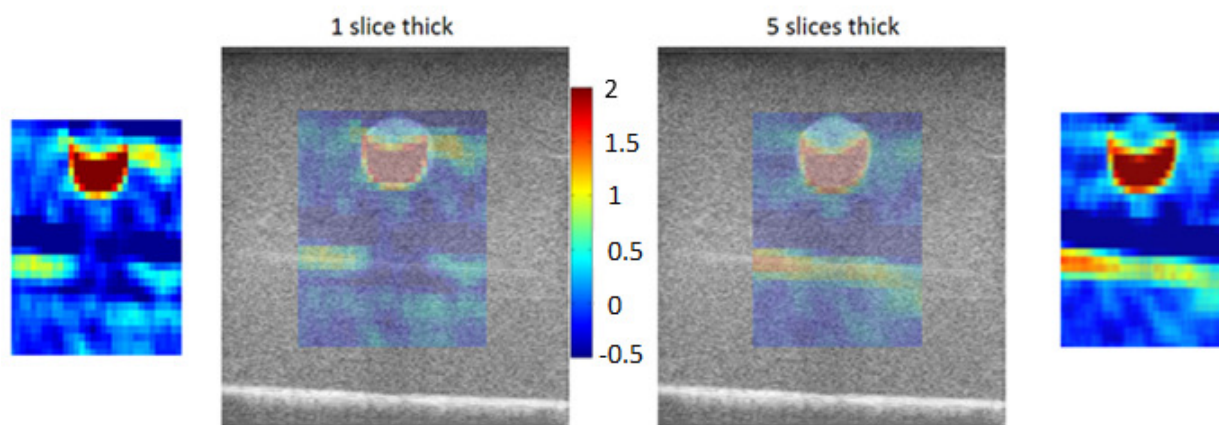


*Figure 7.8. ATT maps estimated and ATT map overlaid on the B-mode image of one slice versus 5 slices thick for the SE phantom*

## 7.5. Data Acquisition for *in-vivo* 3D QUS

Studies in phantoms showed that we could successfully extend QUS methods from 2D to 3D. Thus, the next step was implementing these adapted methods on RF echo data from *in vivo* scans of human subjects. To do so, we recruited 15 human subjects (5 of these subjects had fibroadenomas) from a pool of subjects scheduled for core biopsy. The protocol used in the study was UW HSC IRB-approved and HIPAA-compliant. The subjects were scanned with the Siemens S2000 equipped with ABVS-14L5BV transducer in the supine position. Both the breast and contact surface of the compliant, fluid-filled standoff were coated with a thin layer of low-viscosity ultrasound coupling gel. As mentioned earlier, the ABVS system was programmed to move vertically and apply pressure on the breast. Initially, the scanning pod was placed just barely in contact with the breast, and the breast thickness (to the chest wall) was measured. The scanning pod was then lowered until the bag was well-coupled to the breast (at least 20% strain, this was estimated by comparing the thickness from the skin to the chest wall with the bag barely in contact, with the distance when the breast was compressed).

A test sweep of the transducer was performed to determine if there was good coupling between the breast and the bag (no trapped air) and the scan volume was centered over the breast mass. Subjects were asked to hold their breath between volume sweeps (each volume scan took about 16 seconds to complete), but some subjects breathed normally during the acquisition which lead to some motion artifacts. About 21-35 volumes of RF echo data were acquired for each human subject. The black curved phantom used is described in section 7.2. The phantom had the same composition as the phantom used for the second subgroup of the *in vivo* subjects described in Chapter 2.

The analysis was done off line on each slice to estimate QUS parameters of interest for *in vivo* subcutaneous fat (n= 8) and for breast tumors (n=5) and create a C-scan image. Data from volumes at different compression levels for subcutaneous fat were analyzed and results were compared.

### 7.5.1. 3D QUS of *in vivo* subcutaneous breast fat (n= 8)

As discussed in Chapter 3, interpretation of ultrasound images to diagnose solid breast masses generally includes subjectively assessing B-mode image features of the mass and those of the surrounding tissue (i.e. fat, the internal clinical reference point). The echogenicity (how bright is it?) and ultrasound attenuation (does it cast a shadow?) of a mass are qualitatively described using the US BIRADS lexicon<sup>2</sup>, where subcutaneous fat serves as the standard for comparison (see Figure 7.9, IDC10 in Chapter 6).

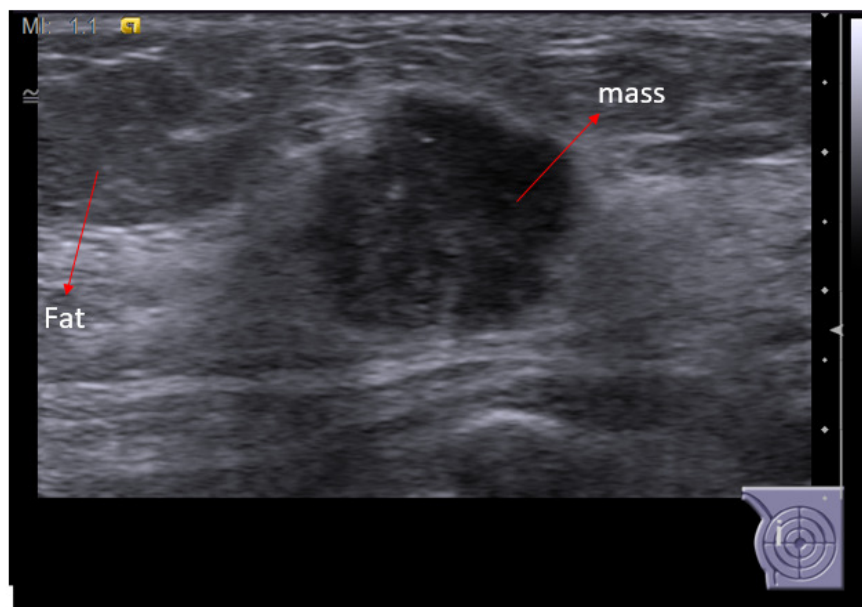


**Figure 7.9.** B-mode image of a mass (IDC10 in Chapter 6) and the surrounding subcutaneous fat

Quantitative ultrasound (QUS) provides acoustic parameters to objectively assess these features; in addition, it can describe tissue microstructure. In Chapter 3, we measured the specific attenuation, the backscatter coefficient, and the effective scatterer diameter for breast fat in two-dimensional (2D) clinical imaging conditions. The results showed that QUS properties of breast fat were consistent among different human subjects. Those findings support the use of fat as a standard for echogenicity comparison with tumors. This study extended the QUS breast fat analysis to include data acquired from the 3D, “whole-breast” ultrasound scanning system to assess whether 3D QUS parameter estimates are consistent with 2D estimates.

RF echo data from 20 slices, each separated by 0.2 mm, covering the same fat lobules were analyzed in the same manner as 2D (see Chapters 2 and 6). For each slice:

- Attenuation coefficients were estimated using the reference phantom method (see Chapter 2).
- Backscatter coefficients were estimated using the reference phantom method after correcting for attenuation in the intervening tissue path with the modified least squares method (see Chapter 2 and 4).
- ESDs were estimated from the BSC using a Gaussian form factor model.

Then, the estimates from the 20 slices were averaged to obtain a single estimate. ESD images were then stacked together to generate a volume and an ESD C-scan image at a depth was generated from this volume.

### 7.5.1.1. Results for 3D QUS of subcutaneous breast fat

Among the 8 fat lobules, the specific attenuation (mean  $\pm$  SD) at 7 MHz was  $0.71 \pm 0.21$  dB $\cdot$ cm $^{-1}$ MHz $^{-1}$ . The average backscatter coefficient was  $0.006 \pm 0.003$  cm $^{-1}$ sr $^{-1}$ . The mean effective scatterer diameter for fat was  $76.5 \pm 10.6$   $\mu$ m. A summary of these QUS estimates for the 8 subjects are shown later (to compare results with 2D). Figure 7.10 show the thick slice (20 image planes, 4 mm) formation of the ESD of subcutaneous breast fat for one subject.

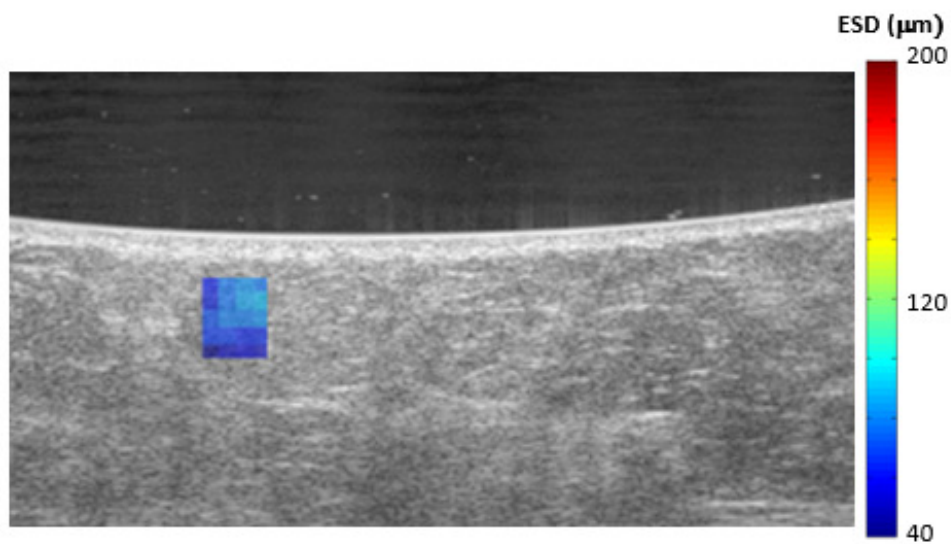


*Figure 7.10. Thick Slice formation of ESD (4mm)*

### 7.5.2. 3D QUS of *in vivo* fibroadenomas (n= 5)

As mentioned before, 3D study had 5 subjects who had fibroadenomas (the same subjects as the first 5 subcutaneous fat lobules in the previous section). The analysis in this section was done for these tumors, QUS parameter estimates from 50 slices (10 mm) were averaged together to generate an estimate and create C-scan image. The analysis was done in the same manner described in the previous section for subcutaneous breast fat. ESD C-scans, and thick

slices were generated for these masses. The ROI size was (by subjective B-mode image assessment) the largest homogeneous region within the tumor boundary outlined by the sonographer at the time of the scan.

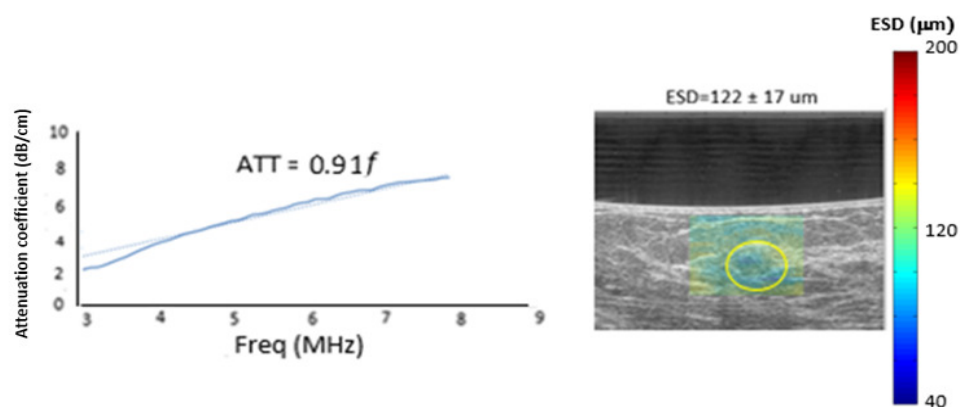
### 7.5.2.1. Results for 3D QUS of fibroadenomas

Table 7.1 show a summary of the QUS parameters estimated from the five subjects having fibroadenomas.

**Table 7.1.** QUS parameters of 5 breast masses scanned with the ABVS system

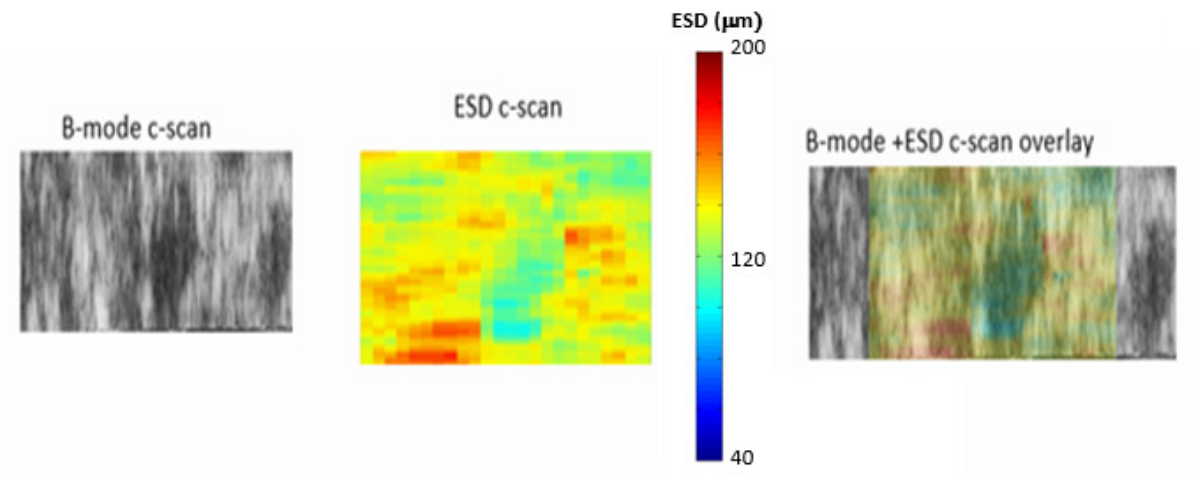
ABVS 3D fibroadenoma				
Subjects	Att ( $\text{dB}\cdot\text{cm}^{-1}\cdot\text{MHz}^{-1}$ )	ESD ( $\mu\text{m}$ )	ESDHI ( $\mu\text{m}$ )	ABSC ( $\text{sr}^{-1}\cdot\text{cm}^{-1}$ )
1	1.1	163	19	0.0080
2	0.95	74	14	0.0241
3	0.77	167	9	0.0122
4	1.12	78	12	0.0425
5	0.91	122	17	0.0064

Figure 7.11 shows an example of the attenuation coefficient versus frequency and the ESD map generated for a fibroadenoma (subject 5, in Table 7.1) scanned with the ABVS system.



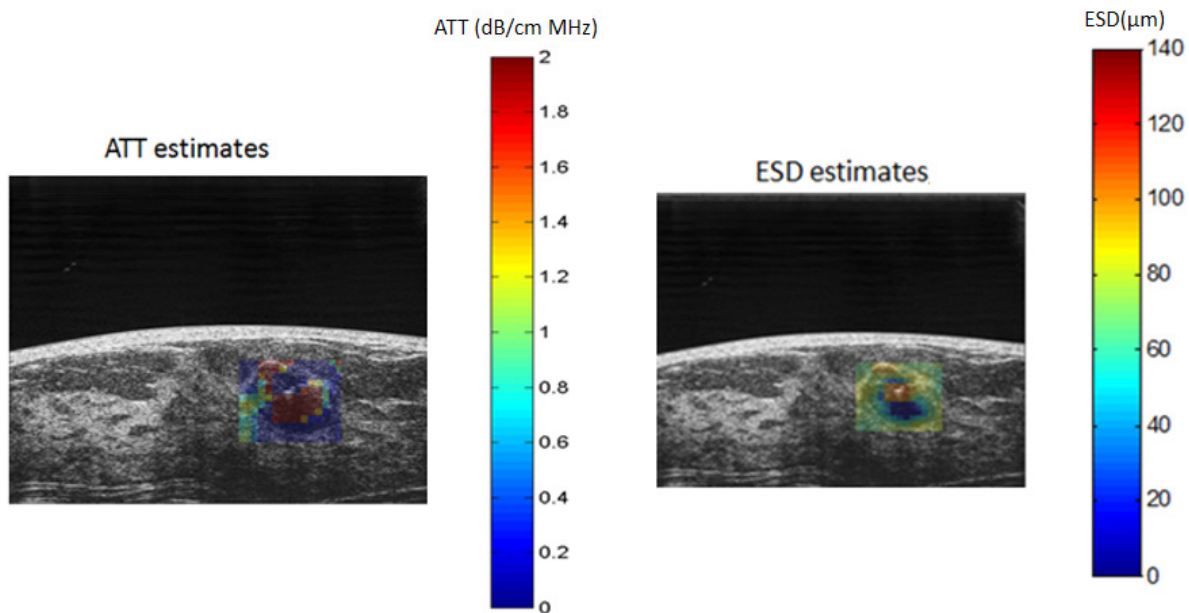
**Figure 7.11.** An example of attenuation and ESD estimated for one human subject with a fibroadenoma (outlined in yellow) scanned with the ABVS system

Figure 7.12 show an ESD C-scan of a fibroadenoma (subject 5, in Table 7.1) scanned with the ABVS system.



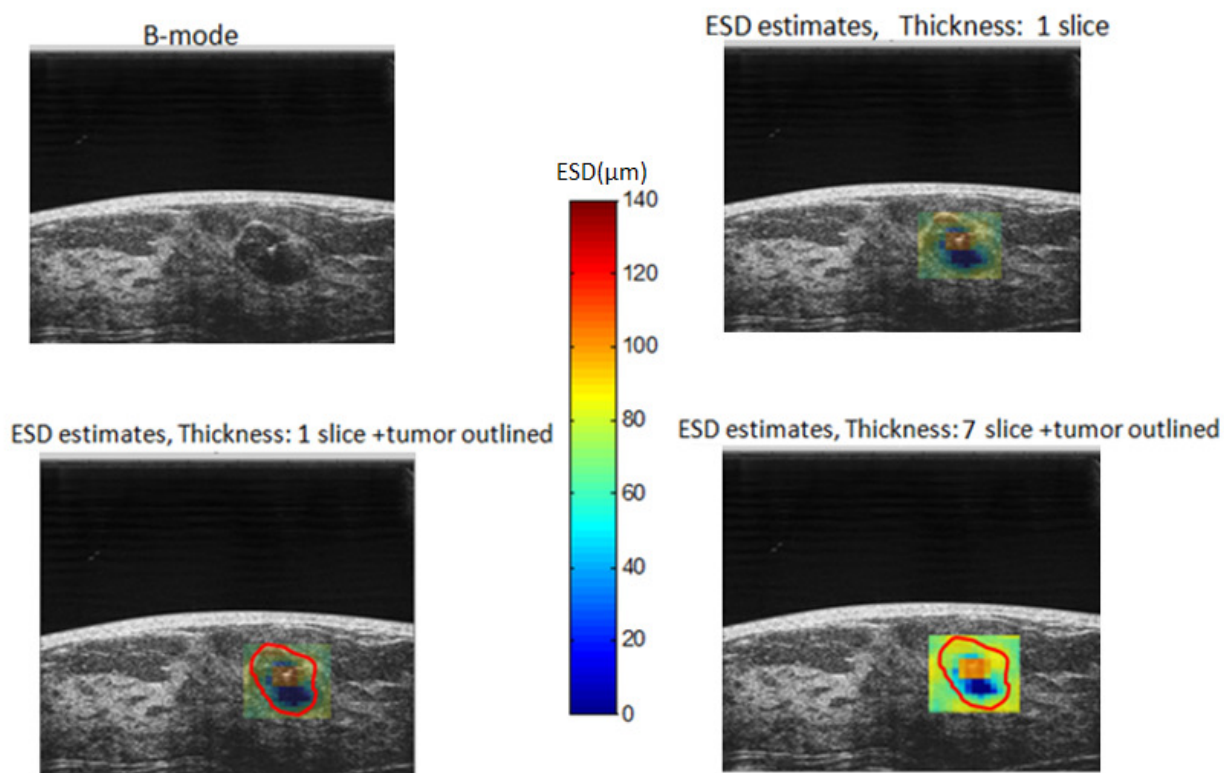
**Figure 7.12.** ESD C-scan of one human subject (subject 5, in Table 7.1) scanned with the ABVS system. Left, B-mode; center, ESD; right, overlay of B-mode and ESD images.

Another interesting subject had a biopsy clip in the middle of the mass. Figure 7.13 shows the ATT and ESD estimated for one slice in that fibroadenoma (subject 4 in Table 7.1). The results show that the QUS estimates are biased due to the presence of the clip, which acts as a coherence source and violates our QUS assumptions.



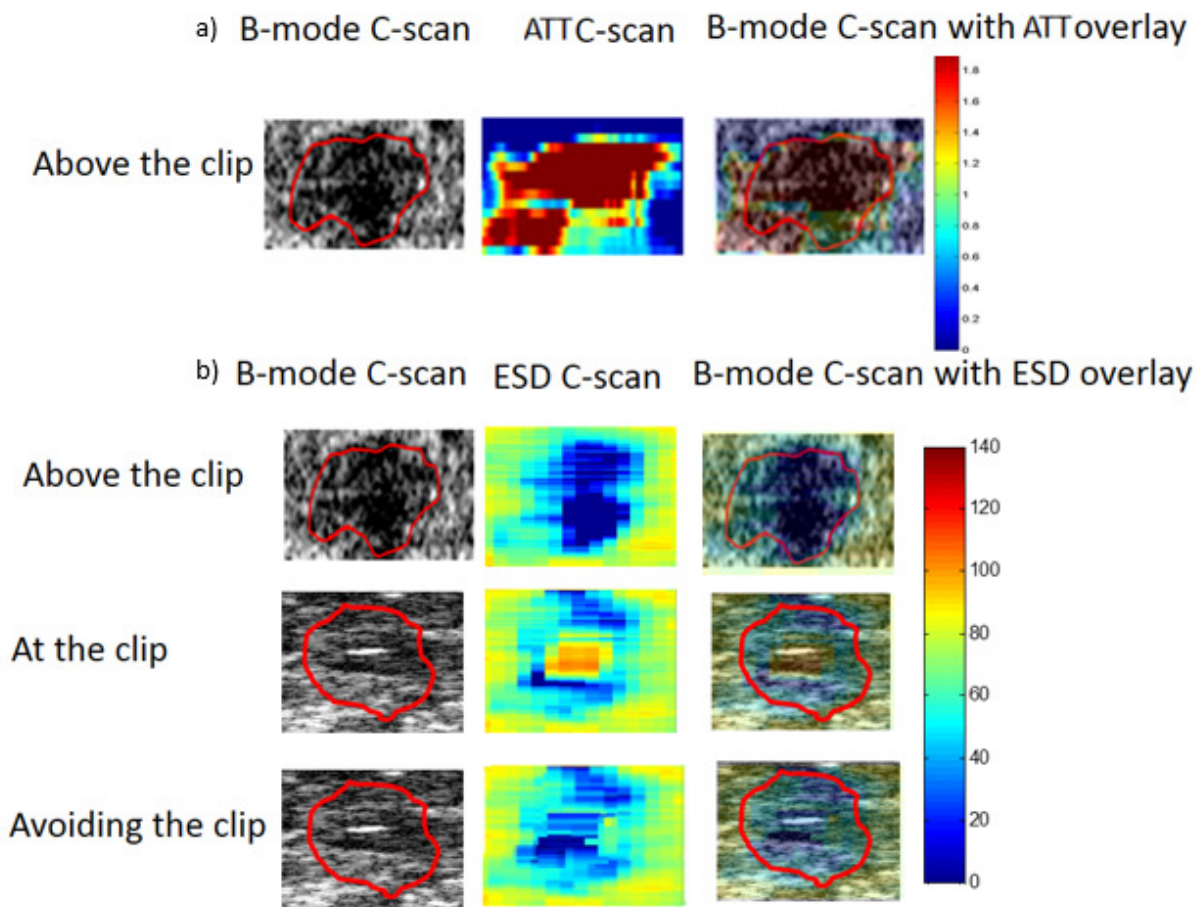
**Figure 7.13.** *ATT and ESD estimates for one slice of a tumor with a clip (subject 4 in Table 7.1)*

Figure 7.14 shows a thick slice formation for the ESD for this subject's tumor. The results show that with 7 slices (1.4 mm thick), the presence of the clip in the ESD estimates is more apparent than with one slice.



**Figure 7.14.** Thick slice formation for the for the ESD estimates in subject 4.

For this subject, we created the ATT C-scan at a depth above the clip. For ESD C-scans, we estimated the value above the clip and at the clip to determine the effect of the presence of coherence. We also estimated the ESD after eliminating the clip (using the same method applied in Chapter 5) and compared the C-scan at the clip with and without avoiding coherence (see Figure 7.15).



**Figure 7.15.** a) B-mode C-scan, ATT C-scan and B-mode C-scan with ATT overlay above the clip, b) the top row: shows B-mode C-scan, ESD C-scan and B-mode C-scan with ESD overlay above the clip, the middle row shows the B-mode C-scan, ESD C-scan and B-mode C-scan with ESD overlay taken at the clip, and the bottom row the B-mode C-scan, ESD C-scan and B-mode C-scan with ESD overlay taken after avoiding it

## 7.6. 2D versus 3D QUS of the breast

In this section, QUS parameters estimated using 2D and 3D data were compared for subcutaneous fat (including a comparison with previously reported data from the literature) and for breast tumors.

### 7.6.1. Results for 2D versus 3D QUS of subcutaneous breast fat

The results in Figure 7.16 show an example of QUS parameters estimated (in subcutaneous fat for one human subject. Results are presented using data acquired with the 18L6 transducer (2D) and with the ABVS-14L5BV transducer (3D). The results show that the parameter estimates are consistent for 2D and 3D data for subcutaneous breast fat. A summary of the results is shown in Table 7.2. Although the linear fit to the attenuation coefficient estimates in this slice in 3D does not describe the data very well, we applied it to facilitate comparison with previously reported data. Also, overall the linear fit works well for most of our *in vivo* data sets.

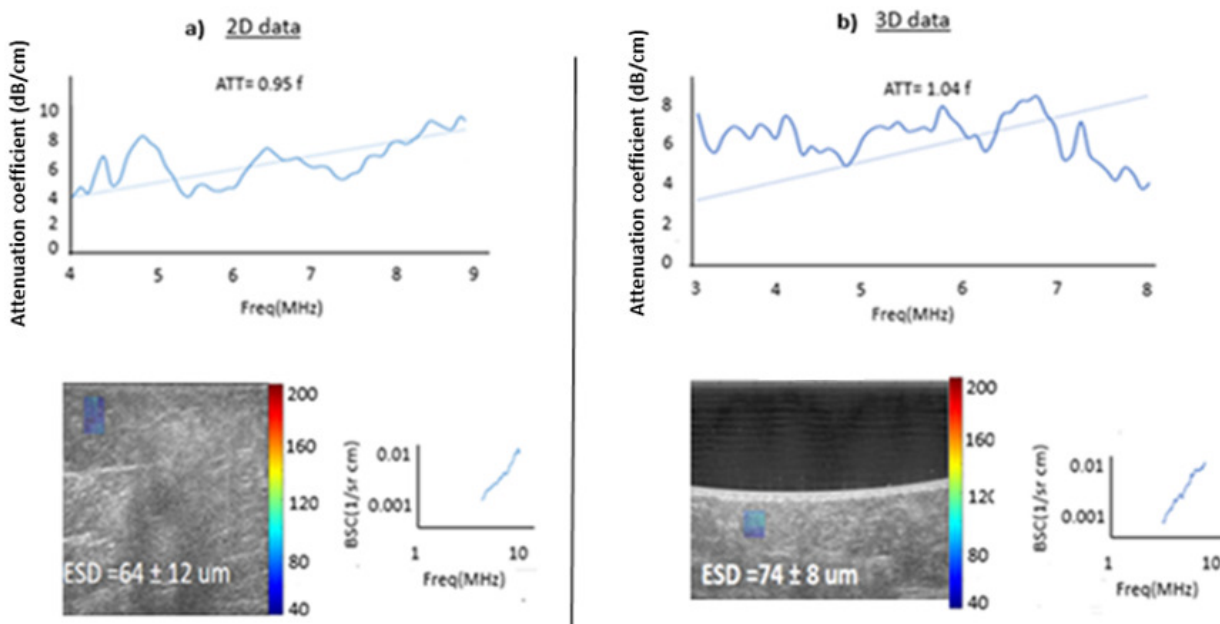


**Figure 7.16.** a) ATT, ESD, and BSC versus frequency estimated in 2D for subcutaneous breast fat, b) 3D QUS parameters estimated for subcutaneous breast fat (in subject 5 Table 7.1), for each subplot the top figures show that attenuation coefficient versus frequency and the bottom figures show the ESD maps and the BSC versus frequency

The results in Figure 7.18 show the BSC estimated for one fat lobule using data acquired with the 18L6 transducer. In 2D, the backscatter coefficient estimates from 5 frames of data

were averaged together. The ROI selected in the fat lobule was 1 cm x 1 cm. Also shown are the BSCs from data acquired with the ABVS-14L5BV transducer. Here BSC estimates from 20 slices were averaged together and the ROI selected in the fat lobule was 1 cm x 1 cm. The results show that the parameter estimates are consistent for 2D and 3D data for subcutaneous breast fat and are in agreement with the previously published data.

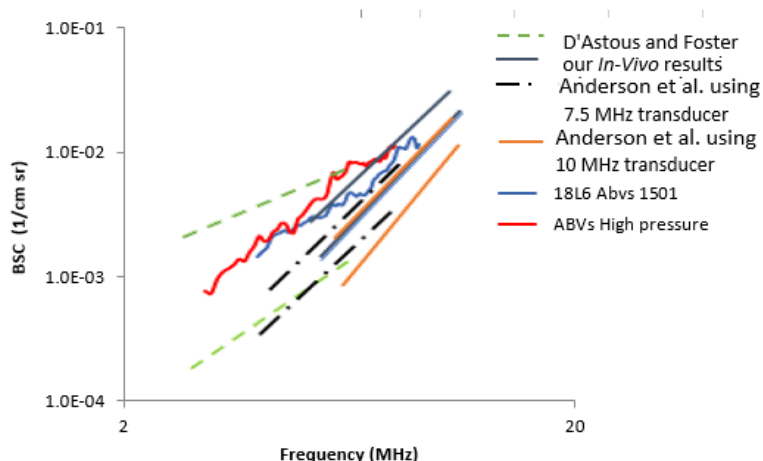


**Figure 7.17.** BSC estimated using data obtained with the 18L6 versus ABVS transducers and previously published data for our previous in-vivo study<sup>3</sup>, D'Astous and Foster<sup>6</sup>, and Anderson et al.<sup>7</sup>

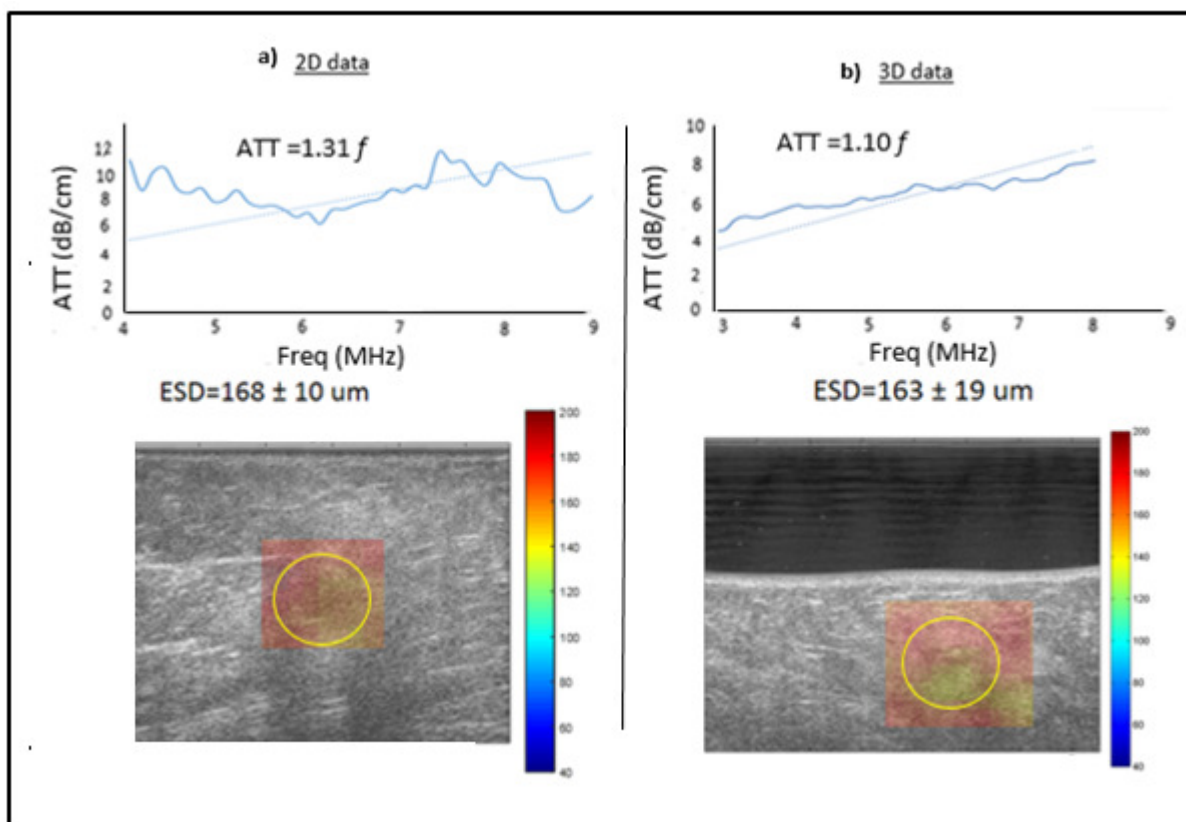
QUS parameters for subcutaneous breast fat, obtained with the 2D and 3D configurations, were in very good agreement. The specific attenuation coefficient (mean  $\pm$  SD) at 7 MHz was  $0.73 \pm 0.23$  dB $\cdot$ cm<sup>-1</sup>MHz<sup>-1</sup> (2D) versus  $0.71 \pm 0.21$  dB $\cdot$ cm<sup>-1</sup>MHz<sup>-1</sup> (3D). These results also are consistent with previously reported values.<sup>3,6,7</sup> The average backscatter coefficient was  $0.007 \pm 0.002$  sr<sup>-1</sup>cm<sup>-1</sup> (2D) versus  $0.006 \pm 0.003$  sr<sup>-1</sup>cm<sup>-1</sup> (3D) somewhat higher than previously reported values.<sup>3,6,7</sup> The mean effective scatterer diameter for fat was  $60.2 \pm 9.5$   $\mu$ m (2D) versus  $76.5 \pm 10.6$   $\mu$ m (3D), the former being consistent with previously reported values.<sup>3,6,7</sup> Table 7.2 summarizes QUS parameters estimated in fat lobules for 2D scans of fat lobules with those for 3D scans in this study. Also shown are our previously published 2D fat data<sup>3</sup> (see Chapter 3).

Table 7.2. 2D versus 3D QUS of Subcutaneous fat

Subcutaneous fat (This study)				
Subjects (3D)	ATT ( $\text{dB cm}^{-1} \text{MHz}^{-1}$ )	ESD ( $\mu\text{m}$ )	ESDHI ( $\mu\text{m}$ )	ABSC ( $\text{cm}^{-1} \text{sr}^{-1}$ )
1	0.74	84.7	8.6	0.008
2	0.84	87.4	12.8	0.006
3	0.84	80.5	7.3	0.009
4	0.47	52.5	6.9	0.002
5	1.04	74.1	8.0	0.007
6	0.70	77.4	12.7	0.003
7	0.72	76.5	13.9	0.004
8	0.37	78.6	14.0	0.007
<b>Average</b>	<b>0.71</b>	<b>76.5</b>	<b>10.5</b>	<b>0.006</b>
<b>Stdev</b>	<b>0.21</b>	<b>10.6</b>	<b>3.1</b>	<b>0.003</b>
Subcutaneous fat (This study)				
Subjects (2D)	ATT	ESD	ESDHI	ABSC
1	0.74	80.3	11.1	0.0083
2	0.88	87.6	14.6	0.005
3	0.92	75.8	9.1	0.008
4	0.43	50.2	8.5	0.004
5	0.95	64.2	12.1	0.008
6	0.81	73.3	10.3	0.003
7	0.74	72.7	18.3	0.005
8	0.35	79.8	15.8	0.007
<b>Average</b>	<b>0.74</b>	<b>73.5</b>	<b>10.8</b>	<b>0.006</b>
<b>Stdev</b>	<b>0.22</b>	<b>16.3</b>	<b>2.8</b>	<b>0.002</b>
Subcutaneous fat previously published 2D data				
Subjects (2D)	ATT ( $\text{dB cm}^{-1} \text{MHz}^{-1}$ )	ESD ( $\mu\text{m}$ )	ESDHI ( $\mu\text{m}$ )	ABSC ( $\text{cm}^{-1} \text{sr}^{-1}$ )
1	0.88	57.6	18.6	0.0032
2	1.04	63.5	17.1	0.0096
3	0.97	50.2	5.4	0.0052
4	0.35	69.8	16.8	0.0036
5	0.94	42.5	7.8	0.0066
6	0.29	75.4	5.1	0.0071
7	0.97	55.5	9.1	0.0066
8	0.52	68.2	6.4	0.0074
9	0.46	68.7	7.4	0.0095
10	0.87	60.8	7.9	0.0074
11	0.53	64.9	7.3	0.0083
12	0.92	65.6	5.7	0.0032
13	0.63	72.1	10.3	0.0071
14	0.86	53.5	8.4	0.0066
15	0.63	70.2	8.9	0.0071
16	0.92	53.3	17.2	0.0054
17	0.95	59.3	2.7	0.0085
18	0.47	62.4	10.8	0.0078
19	0.51	72.1	7.7	0.0083
20	0.86	57.6	18.6	0.0031
21	0.84	46.6	5.9	0.0044
22	0.79	43.5	16.2	0.005
23	0.81	48.6	19.1	0.0091
24	0.45	63.9	12.2	0.0072
<b>Average</b>	<b>0.73</b>	<b>60.2</b>	<b>10.5</b>	<b>0.007</b>
<b>Stdev</b>	<b>0.23</b>	<b>9.5</b>	<b>5.1</b>	<b>0.002</b>

### 7.6.2. Results for 2D versus 3D QUS for an in-vivo breast mass

Figure 7.18 shows the ATT and ESD estimates of a breast mass outlined in yellow. The values reported are for a ROI within the fibroadenoma (subject 1 in Table 7.3) using data obtained from the ABVS system and those obtained from scanning with the 18L6 transducer.



**Figure 7.18.** ATT and ESD for a fibroadenoma (subject 1 in Table 7.1) estimated using a) 2D versus b) 3D data. For each subplot the top figures show that attenuation coefficient versus frequency and the bottom figures show the ESD maps.

Table 7.3 shows a summary of the results for the QUS parameters estimated for the 5 human subjects with fibroadenomas. The results show that the parameters estimated using 3D data agree with the 2D results. The recruitment ID's of these subjects are provided in Appendix B.

**Table 7.3.** QUS parameters estimated for 5 fibroadenomas in 2D and 3D

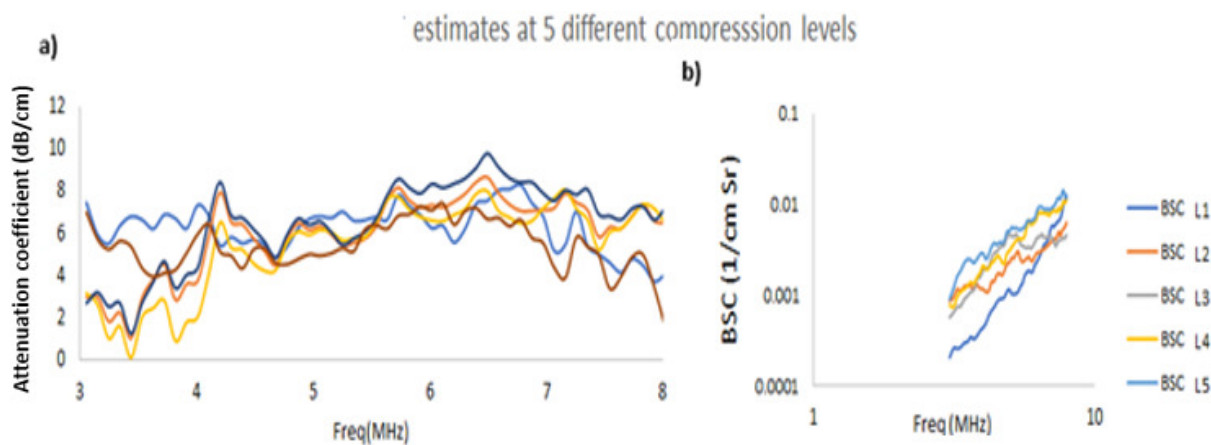
ABVS 3D fibroadenoma				
Subjects	Att (dB·cm <sup>-1</sup> MHz <sup>-1</sup> )	ESD (μm)	ESDHI (μm)	ABSC (cm <sup>-1</sup> sr <sup>-1</sup> )
1	1.1	163	19	0.0080
2	0.95	74	14	0.0241
3	0.77	167	9	0.0122
4	1.12	78	12	0.0425
5	0.91	122	17	0.0064
18L6 2D fibroadenoma				
Subjects	Att (dB·cm <sup>-1</sup> MHz <sup>-1</sup> )	ESD (μm)	ESDHI (μm)	ABSC (cm <sup>-1</sup> sr <sup>-1</sup> )
1	1.31	168	10	0.0061
2	1.61	84	16	0.0102
3	0.78	119	10	0.1223
4	0.95	86.2	17	0.0306
5	1.03	163	19	0.0003

## 7.7. The acoustic properties of subcutaneous breast fat under different compression scenarios

Another aspect that we examined was whether QUS parameter estimates depend on the applied pressure when scanning. Sonographers usually apply relatively high deformation when scanning the breast to flatten tissue planes, (tending to) align Coopers ligaments, and improve acoustic transmission into the breast. If this applied pressure modifies the echogenicity of fat (i.e. the BSC of fat changes with increasing strain), it could lead to biased descriptions of the mass using the BIRAD Lexicon<sup>2</sup>. Therefore, we estimated acoustic properties of subcutaneous breast fat lobules, for five subjects at five different amounts of deformation. Deformation was quantified by percent strain applied, measured using a motion tracking algorithm developed in our group. The starting point was about 0.5% strain, and strains up to 11.8% were tracked.<sup>5</sup>

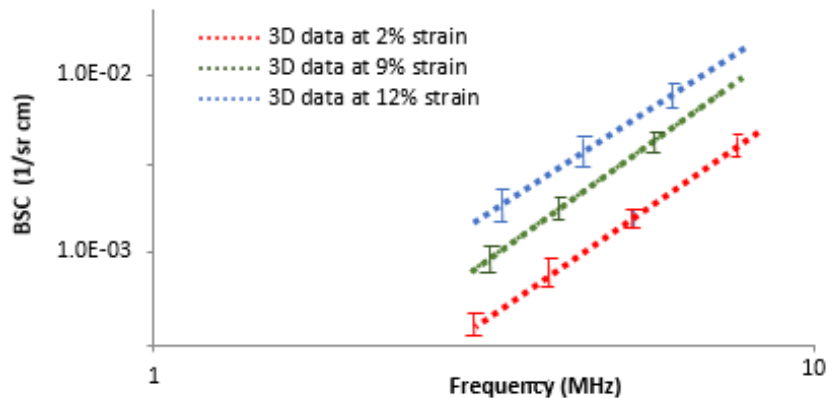
### 7.7.1. Results for 3D subcutaneous breast fat under different levels of compression

Figure 7.19 shows the ATT and the BSC estimates for subcutaneous fat in one human subject (subject 5 in Table 7.1) at 5 different deformations (2.4%, 5.3%, 9.3%, 10.4% and 11.8% strain). The results show that the BSC in breast fat increases with increasing deformation. Thus, the degree of preload on the breast may be an important factor to account for in QUS parameter estimation.



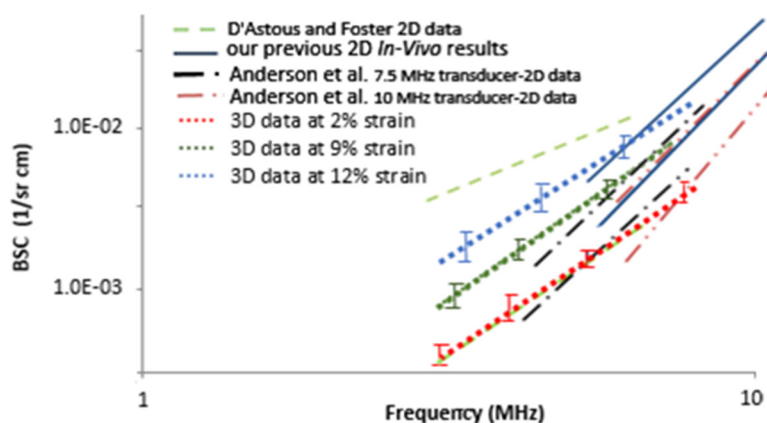
**Figure 7.19.** a) attenuation coefficient versus frequency and b) BSC estimates for subcutaneous fat (for subject 5 in Table 7.1) under different compression scenarios. L1 refers to the first compression level (2.4%), L2 is the second compression level (5.3%), etc.).

To summarize the results, Figure 7.20 shows the mean and standard deviation for the BSC of the breast fat lobules among 5 subjects at 3 different compression levels. The results show that the backscatter coefficient increases with increasing strain level. (Note that these are still small strain levels compared to the typical pre-compression of clinical breast ultrasound.)



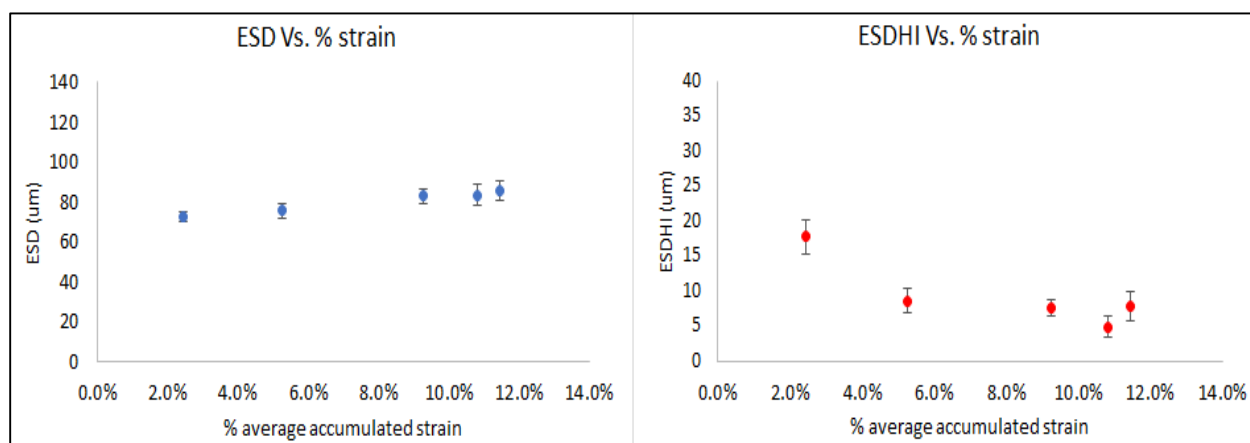
**Figure 7.20.** Mean and standard deviation for the BSC of subcutaneous fat at 3 different compression levels.

Figure 7.21. shows a graphic comparison on a log-log plot of these results with those estimated in our previous study, those of D'Astous and Foster (*ex vivo* data), and those of Anderson et al. (*in vivo* data) using 7.5 and 10 MHz transducers. The upper and lower curves shown are defined by the mean plus and the mean minus one standard deviation of the reported results. The results show that estimates for subcutaneous fat under different compression levels in 3D agree with previously published 2D data.



**Figure 7.21.** BSC results for 3D scans of subcutaneous fat under different compression levels. Also shown are our previously published 2D results, results from D'Astous and Foster<sup>6</sup>, and Anderson et al. results.<sup>7</sup>

We also examined the estimated ESD and ESDHI for different strain levels for the same subject. The results suggest that the ESD increases slightly with increasing applied strain while the ESDHI decreases with increasing strain. This is shown in Figure 7.22.



*Figure 7.22. a) ESD and b) ESDHI versus percent average accumulated strain.*

## 7.8. Discussion

Volume ultrasound RF echo signal data, instead of data from only a single plane, can be obtained by 3D ultrasound scanning systems. After acquisition, data can be analyzed and displayed in different ways, such as displaying the data in planes that are not accessible with typical 2D scanning methods (C-scan planes). Viewing data in different ways might help physicians discover pathology which is otherwise difficult to detect. 3D ultrasound data also enables the visualization of complex tissue structures that might not be seen in typical 2D scanning planes.

Until now the amount of compression applied by the sonographer when scanning a subject has not been considered as a possible source of variability in QUS data or even with conventional subjective image analysis. In our study, the BSC of fat increased with increasing

strain. Thus, preload on the breast may be an important factor to account for in QUS parameter estimation. The range of the BSCs, including those obtained at different compression levels was comparable to the range of values reported by D'Astous and Foster<sup>6</sup> data for *ex vivo* breast fat. Nevertheless, it is feasible that the amount of compression imparted by the transducer might influence BIRADS-based descriptions of a mass.

Data acquired in 3D using the ABVS system were in good agreement with those acquired with the 2D handheld transducer system. The ABVS can scan a region large enough to view the entire breast in a single sweep in many women. Moreover, controlling the applied strain can increase the reproducibility of the QUS parameter estimates.

## 7.9. Conclusions

3D QUS parameter estimates, such as attenuation coefficients and effective scatter diameters, agree well with values obtained with 2D systems, so the 3D approach is very promising. Shapes of masses in the C-scan view may offer insight regarding the nature of a mass. Varying the thickness of the reconstructed slices, can reduce statistical variations beyond the reductions achieved using 2D processing. Since the echogenicity of subcutaneous breast fat increases with increasing strain, controlling the deformation when QUS data are acquired will be an important consideration in future studies.

## 7.10. References

1. Brunke S, Insana M, Dahl J, Hansen C, Ashfaq M, Emert H. An ultrasound research 5 interface for a clinical system. *IEEE Trans. Ultrason. Ferroelectr. Freq. Control* 2007; 54:198-6 210
2. Online American College of Radiology. BI-RADS: Ultrasound, 1st ed. Website. <http://www.acr.org/Quality-Safety/Resources/BIRADS/Ultrasound>. Accessed June 2014.
3. Nasief, H.; Rosado-Mendez, I.; Zagzebski, J.; Hall, T.; Acoustic Properties Of Breast Fat. *J. Ultrason. Med.*, 2015, 34(11). <http://doi.org/10.7863/ultra.14.07039>
4. Wang, Y., Nasief, H.; Kohn, S.; Milkowski, A.; Clary, T.; Barnes,S.; Barbone, P'; and Hall, J.; Three-dimensional ultrasound elasticity imaging on an automated breast volume scanning system, *Ultrasonic imaging*, accepted for publication, May, 2017.
5. Madsen, E.; Berg, W.; Mendelson, E.; Frank, G.; Anthromorphie breast phantom for quantification of investigators for ACRIN protocol 6666, *Radiology* 2006, 239(3), 869-874.
6. D'Astous FT, Foster FS. Frequency-dependence of ultrasound attenuation and backscatter in breast-tissue. *Ultrasound Med Biol* 1986; 12(10):795-808
7. Anderson ME, Soo MS, Trahey GE. In vivo breast tissue backscatter measurements with 7.5- and 10-MHz transducers. *Ultrasound Med Biol* 2001; 27(1):75–81.

## Chapter 8: Contributions and future work

The general goal of this dissertation was to improve the specificity of breast ultrasound imaging. Promising results were reported here from two parallel paths. The first path optimized 2D breast QUS, and the second path introduced 3D QUS. Seven QUS parameters were estimated for each human subject. However, there was a substantial overlap in the parameters estimates for benign and malignant masses.

We built a Bayesian classifier that showed promising results for combining QUS parameters to differentiate fibroadenomas from carcinomas. Being able to differentiate that a mass is a fibroadenoma could in turn reduce the number of unnecessary biopsies of suspicious masses. Classification into these categories (“carcinoma” and “fibroadenoma”) is an important step, but may be insufficient for clinical practice. A more useful classification would include all cancer types, all benign breast masses, and various types of normal tissue. Suggested future study in this area includes introducing more parameters and more tumor types. For training a classifier, an accepted rule of thumb offered by statisticians is that 10 cases of any single mass type are needed per QUS parameter introduced into the classifier. Thus, to robustly test a 5-parameter classifier to select among two categories (benign and carcinoma), and assuming that 10 subjects are needed in each category per parameter, at least 50 subjects per category (at least 100 subjects in total) would be needed. Broadening the number of tissue types (benign tumors and normal tissues) in the ‘non-cancer’ class will require a significantly increased pool of data and thus, will require testing of different classifiers that can tolerate a larger pool of data.

We developed and tested a modified least squares method to compensate for attenuation along the inhomogeneous path above the ROI. Correct compensation for attenuation losses

would lead to more reliable, system-independent estimations of QUS parameters. Future work in this area can include estimating attenuation vs. frequency in media with known values of attenuation frequency dependence (besides  $f^1$ ) and applying this method in other applications (kidney, cervix, liver, etc.).

We developed and examined different methods to detect the presence of anisotropy in QUS parameter estimates since most human subjects showed presence of anisotropy. Thus, it is important to detect isotropy as it would allow spatial compounding techniques. A future study will include testing more data sets and developing more sophisticated approaches to test anisotropy, then compound average data from subjects that showed isotropy. We also tested for coherence in echo signals in phantoms and *in vivo* in the breast and suggested a method to eliminate sources of coherence before estimating QUS parameters. A suggested future study in this area includes further testing this simple approach as well as development and testing of more sophisticated automatic (rather than the manual approach described here) approaches using in-vivo breast data.

We built the first 3D QUS images from an ABVS system that enables complete coverage of suspicious masses, developed 3D parametric images for QUS parameters, and displayed them in unique image planes, such as C-scan image planes that include the plane of breast ductal structures). Using 3D data, we estimated the acoustic properties of subcutaneous breast fat under different compression levels and found that the echogenicity of subcutaneous fat increases with compression. We also varied the thickness of the reconstructed slices to reduce statistical variations. A future study in this area will include a larger number of human subjects that have large tumors and a broad distribution of tissue types, but it will be important to control for the applied deformation during data acquisition. The future study will also examine

the effect of compression on tumor and fat for the same subject and among different subjects. It will also include introducing more parameters to the classifier such as size aspect ratio, shape, margin, etc.

## Appendix A: Reproducibility of the QUS estimates

The purpose of this appendix is to show the reproducibility of the estimated QUS parameters using our QUS methods. Data reported in this section includes results from phantom studies, rat tumor and breast tumors.

### A.1. Reproducibility of QUS estimates in a rodent-mimicking phantom and a rat tumor

The first step in our analysis was to verify the ability to reproduce the estimates obtained from our established QUS methods. Figure A.1 show a schematic of a rodent phantom.<sup>1-4</sup> This phantom consists of three macroscopically uniform sections: two lesion-mimicking, 1.6cm diameter spherical inclusions protruding from a background. The phantom is immersed in a solution of water, propylene glycol and Liquid Germall Plus® (a preservative) and enclosed in an acrylic box. All three sections are composed of mixtures of water, agar, propylene glycol, and Liquid Germall Plus® as well as of different concentrations of graphite powder and different size distributions of glass-bead scatterers. Figure A.2 shows the parametric images of the attenuation coefficient (color encoded representation of the values) for sphere A and B of the rodent phantom and the corresponding. The ATT estimated for sphere A ( $1.02 \text{ dB} \cdot \text{cm}^{-1} \text{MHz}^{-1}$ ) and sphere B ( $1.52 \text{ dB} \cdot \text{cm}^{-1} \text{MHz}^{-1}$ ). These agrees with the expected values,  $1 \text{ dB} \cdot \text{cm}^{-1} \text{MHz}^{-1}$  and  $1.58 \text{ dB} \cdot \text{cm}^{-1} \text{MHz}^{-1}$  for sphere A and B, respectively).

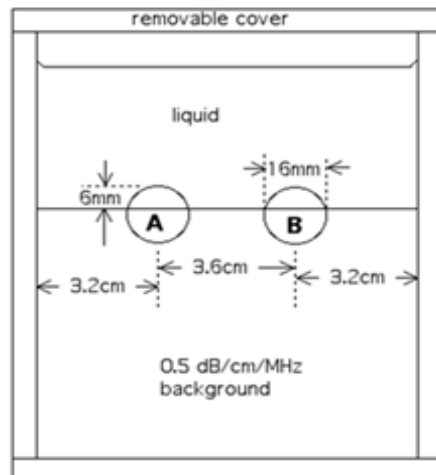


**Figure A.1.** Schematic of the custom made, rodent-lesion mimicking phantom

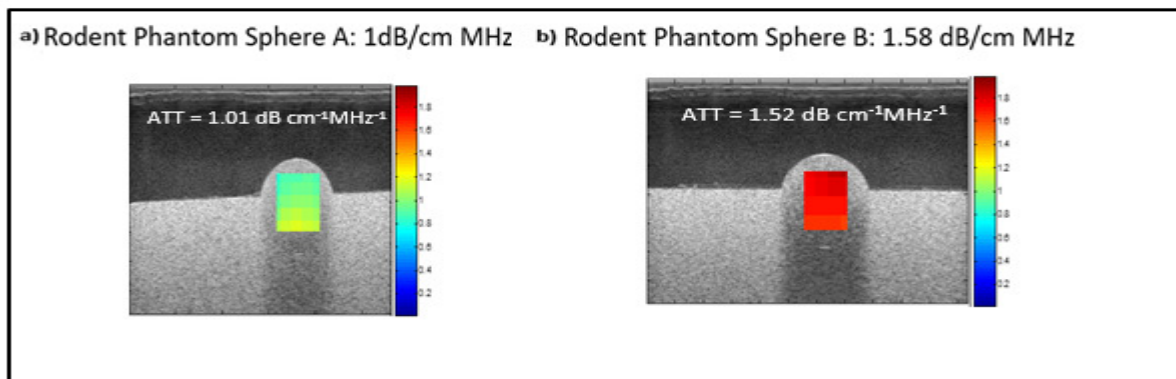


**Figure A.2.** Attenuation maps and attenuation estimates versus frequency for sphere A and B of the rodent phantom. The ATT estimated for each sphere is shown in the Figure (white text) and the expected value is shown for each sphere in black

We also estimated the backscatter coefficient of Sphere A, using the background material of the same phantom as our reference phantom material. The glass bead scatterer size distribution in the background of the phantom is 45-53  $\mu\text{m}$ . The acoustic properties of this phantom were estimated using single-element transducers and a narrow-band substitution method<sup>5</sup> on test samples manufactured at the same time as the reference phantom (see Chapter 2). The sound speed

was 1544 m/s at 2.5MHz. Measured attenuation coefficients at frequencies from 2-10MHz were fit to a linear function of frequency, yielding,  $0.51 \text{ dB}\cdot\text{cm}^{-1}\text{MHz}^{-1}$ . To examine the effect of different paths above the ROI we scanned the background of the rodent phantom with the transducer in direct contact with the background surface and through a saline path. Figure A.3 show the B-mode images and the ROI selected for sphere A and for the reference phantoms.

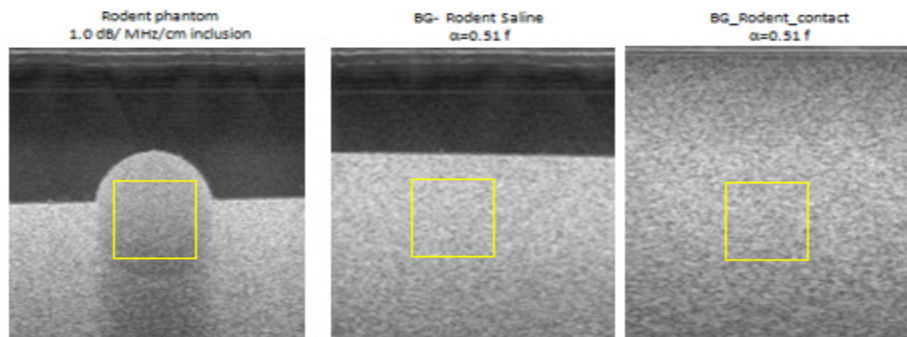


**Figure A.3.** ROI for sphere A and the background of the rodent phantom with the transducer in contact and through a saline path

Figure A.4 shows the power spectra for the sample and the reference and the attenuation-corrected power spectra for the reference phantom data. Figure A.5 shows the results for the backscatter coefficient estimated for the sphere when using the back ground of the phantom (with the transducer in contact and through the saline path) as a reference and the expected BSC from Faran's theory for sphere A.

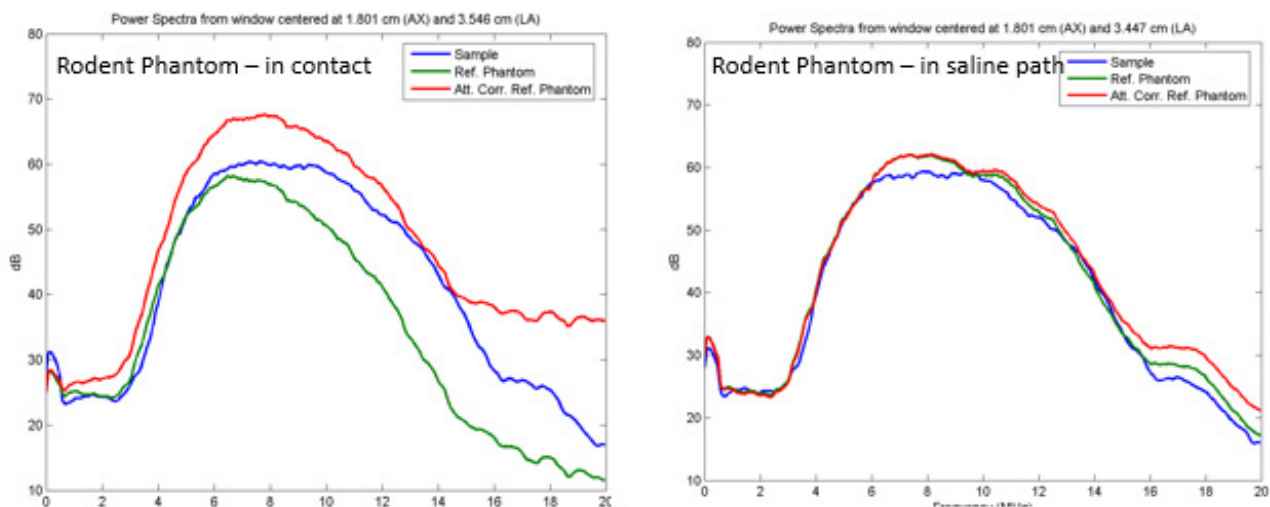


**Figure A.4.** Power spectra of the sample and the reference and the attenuation corrected power spectra for the reference with the transducer in contact and through a saline path

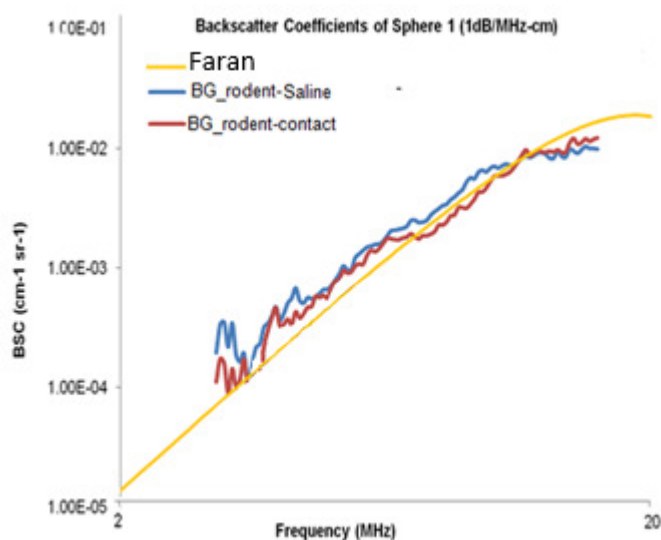


**Figure A.5.** BSC of sphere A using the background of the rodent phantom as the reference phantom material (with transducer in contact and backed off with a saline path)

We also scanned a rat tumor (R3114) from a joint study.<sup>2-3</sup> The rat tumor was scanned with a Siemens S2000 equipped with a 9L4 transducer. The transmit focus was set at 2.25 cm. The analysis was done offline in the same manner described in Chapter 2. The reference phantom used for the study was the same “BRP phantom” used for the second subgroup of the *in vivo* data (see

Chapter 2). Figure A.6 show the B-mode image of the rat tumor and the backscatter estimated for the rat tumor.

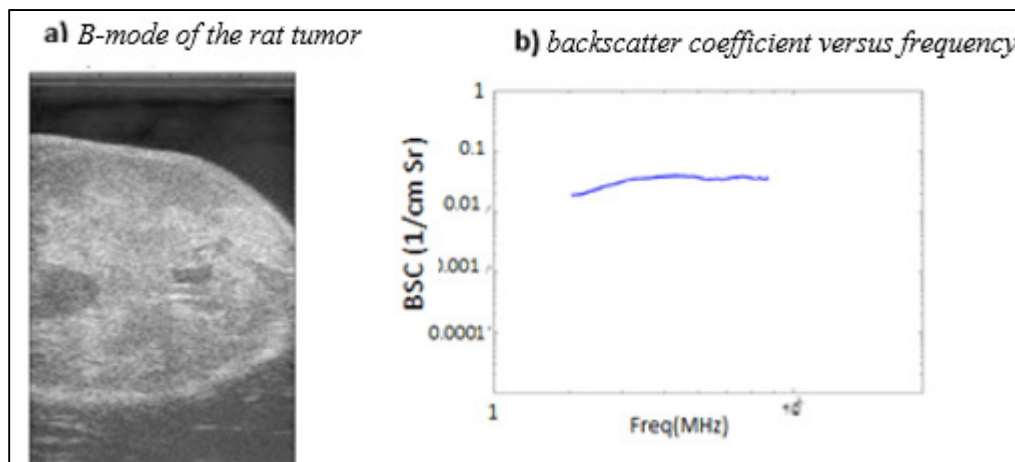


**Figure A.6.** a) B-mode of the rat tumor phantom, and b) the backscatter coefficient versus frequency estimated for the rat tumor.

## A.2. Reproducibility of results on breast masses

To further examine our ability to reproduce the attenuation coefficient estimated in *in vivo* breast masses, we asked two graduate students (who were experienced in QUS data analysis, had published papers reporting research involving estimating QUS parameters in the breast) to estimate the attenuation coefficient in the tumor. Each user, independently performed the analysis and obtained parameter estimates (the same data were analyzed by each “user” using the same MATLAB script). Users were free to choose what they consider the largest homogeneous ROI within the tumor boundaries and provide the estimated ATT to “user 1” to compare the results. The location of the ROI might have varied among the users (user 2 and 3 didn’t keep the information about the exact location of their ROIs). Figure A.7 shows examples summarizing the attenuation estimates from the 3 users, the ROI shown were selected by “user 1” and used in this dissertation. The tumors included were fibroadenomas (FA4, FA3, and FA24 in Chapter 6),

adenocarcinoma (ACA in Chapter 6), and invasive ductal carcinomas (IDC 3, and IDC10 in Chapter 6).

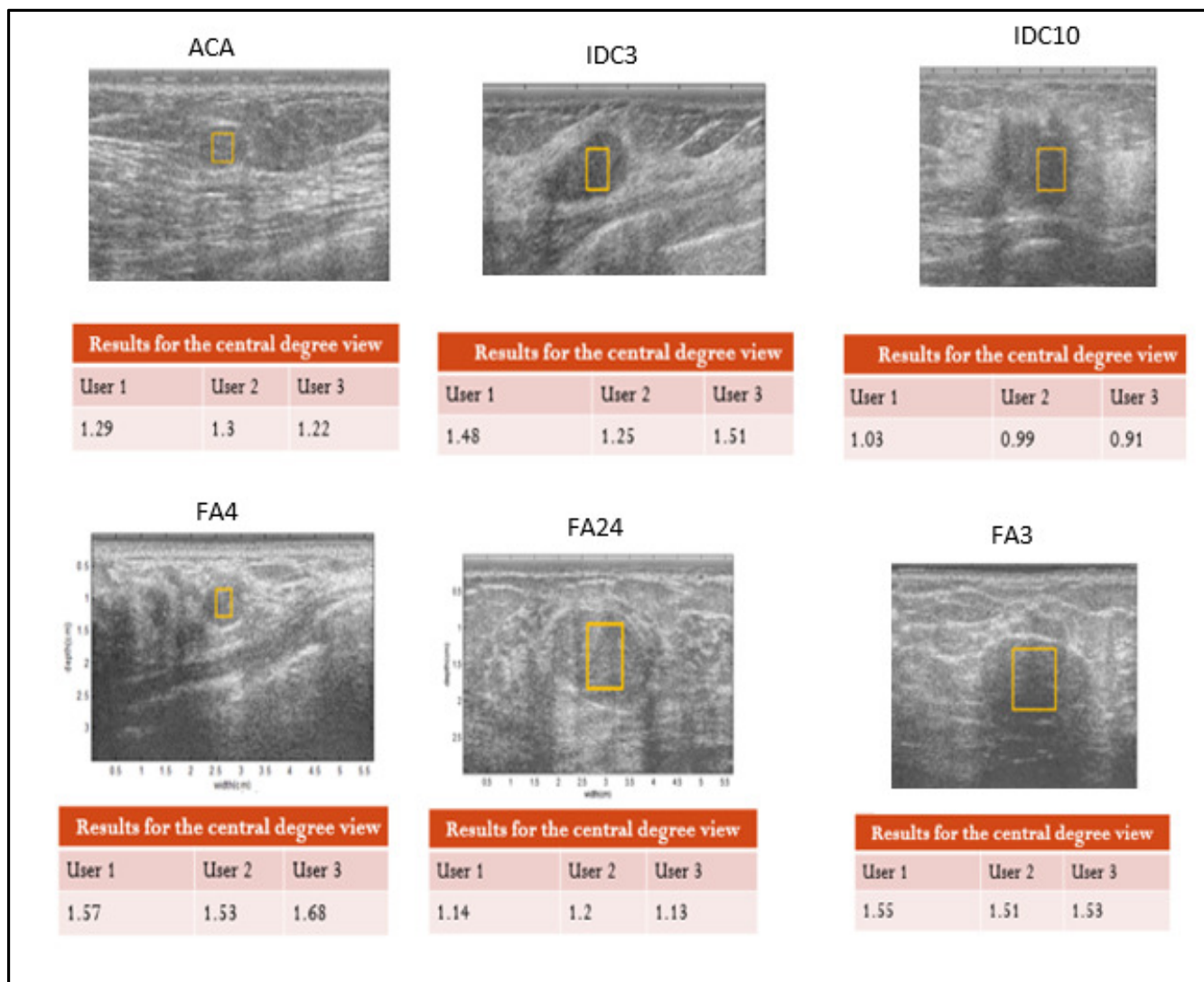


**Figure A.7.** Example showing the reproducibility of data among different users for different human subjects (ACA: adenocarcinoma, IDC: ductal carcinoma, FA: fibroadenoma). Numbers represented in the tables show the ATT estimated from each user in  $\text{dB}\cdot\text{cm}^{-1}\text{MHz}^{-1}$ .

### A.3. References

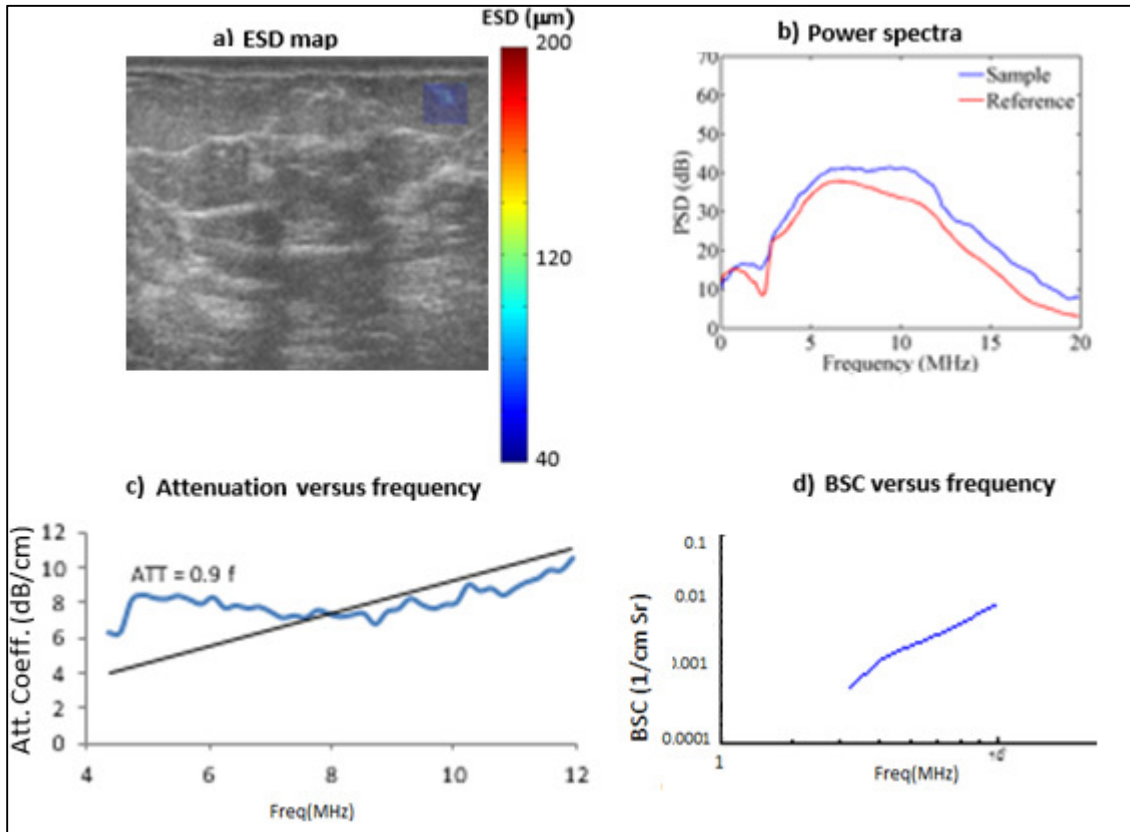
1. Nam, K.; Rosado-Mendez, I.; Wirtzfeld, L.; et al. Ultrasonic Attenuation and Backscatter Coefficient Estimates of Rodent-Tumor-Mimicking Structures: Comparison of Results among Clinical Scanners. *Ultrason Imaging* **2011**;33(4):233-250.
2. Wirtzfeld, L.; Ghoshal, G.; Hafez, Z.; et al. Cross-Imaging Platform Comparison of Ultrasonic Backscatter Coefficient Measurements of Live Rat Tumors. *J Ultrasound Med.* **2010**;29(7):1117-1123.
3. Oelze, M.; Zachary, J.; O'Brien, Jr., W., Parametric imaging of rat mammary tumors in vivo for the purpose of tissue characterization. *J Ultrasound Med.* **2002**; 21:1201-1210.
4. Madsen, E.; Dong, F.; Frank, G. ; Garra, B. ; Wear, K.; Wilson, T.; Zagzebski, J.; Miller, H.; Shung, K.; Wang, S.; et al. Interlaboratory comparison of ultrasonic backscatter, attenuation, and speed measurements. *J Ultrasound Med.* **1999** Sep; 18(9): 615–631.
5. Nam, K.; Rosado-Mendez, I.; Rubert, N.; Madsen, E.; Zagzebski, J.; Hall, T.; Ultrasound attenuation measurements using a reference phantom with sound speed mismatch. *Ultrason Imaging* **2011**; 33(4):251-63.

## **Appendix B: Additional examples for *in vivo* breast fat and masses**

This appendix shows summary figures that contain examples of the QUS parameters estimated for *in vivo* breast fat and breast tumor. It also reports additional results for anisotropy using the power law fit to attenuation and the backscattered power difference method (see Chapter 5). The derivation of the method used to calculate the uncertainty in the estimates obtained from the power law fit is summarized in this appendix. The graphical user interface built using 43 human subjects and leave one out method to differentiate fibroadenoma and carcinoma is also shown and additional examples for 3D QUS in the breast.

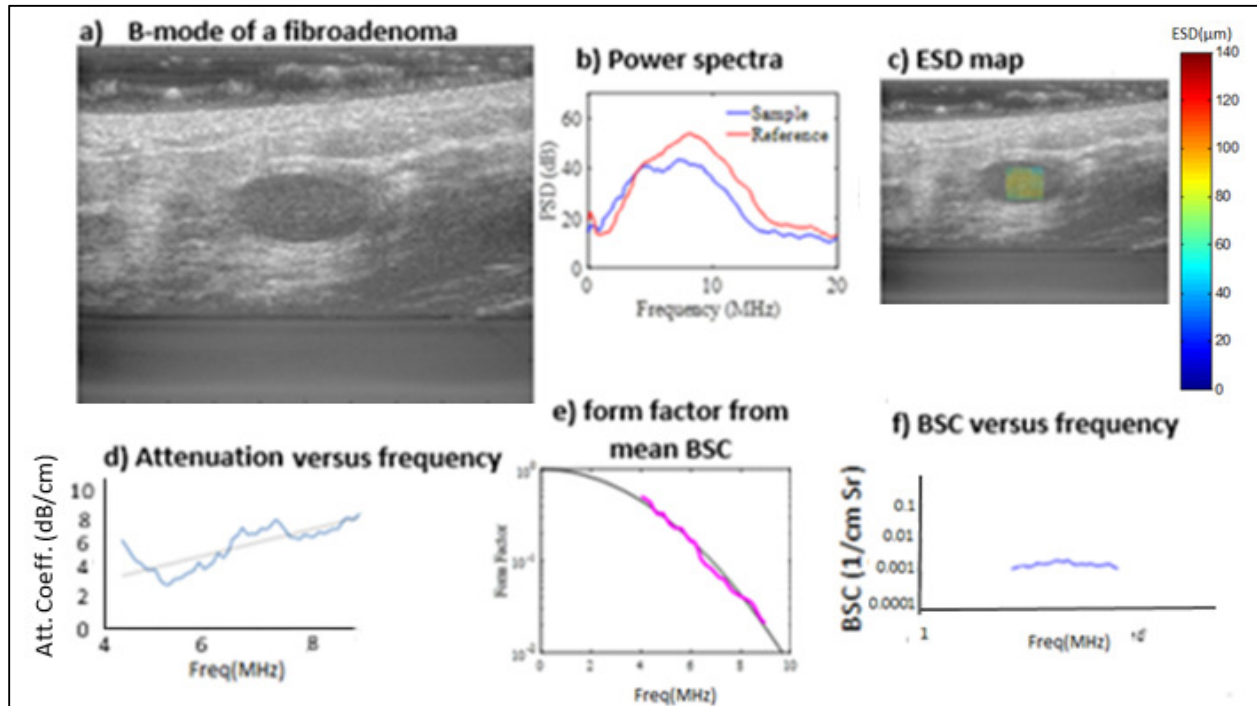
### **B.1. QUS parameter estimates after optimization of the QUS methods**

In this section, examples of the QUS parameters estimated for subcutaneous fat and for a breast tumor are shown below. For these data, correction for attenuation for the inhomogeneous tissue path above the ROI was done using the MLSM (see Chapter 4). Figure B.1 shows the ATT and BSC estimated for a ROI within the subcutaneous breast fat for one human subject (scanned with 18L6 transducer and Siemens S2000, subject 16 Table 7.2 for the published 2D fat data) at the central degree view.



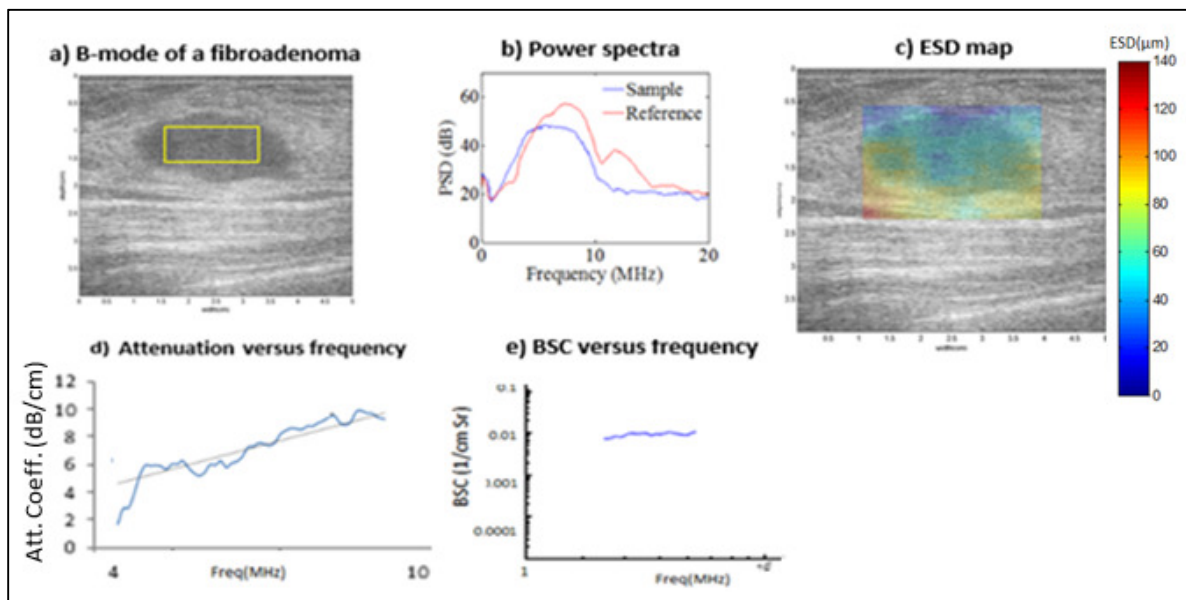
**Figure B.1.** QUS of subcutaneous breast fat a) ESD map, b) power spectra for the sample and the reference, c) attenuation coefficient versus frequency, and d) BSC versus frequency

Figure B.2 shows the ATT, BSC, ESD map estimated for a ROI within the tumor boundary for a fibroadenoma (FA23 in Chapter 6), and experimental form factor versus the best-fit model form factor for the central degree view.



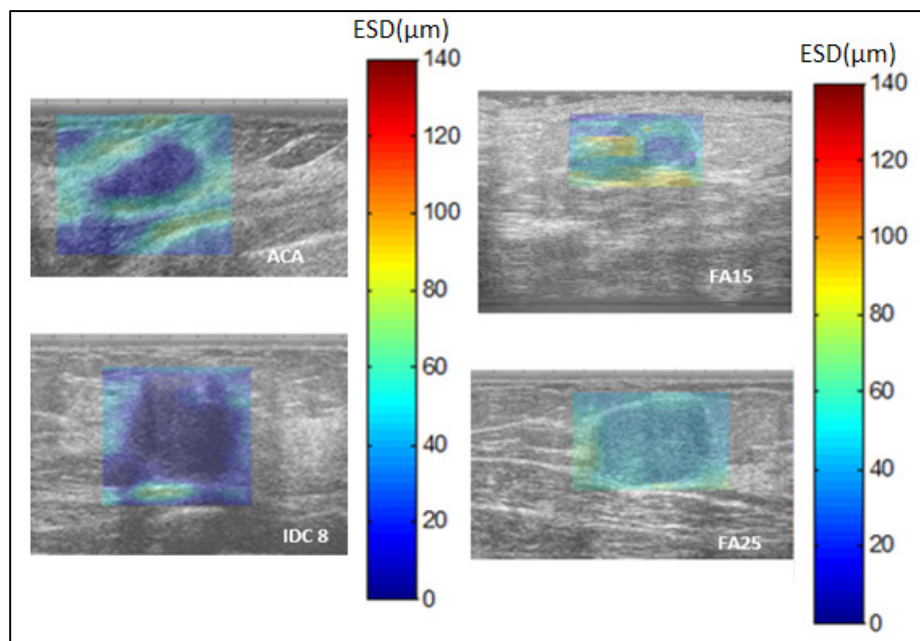
**Figure B.2.** QUS parameter estimation for central degree view for a fibroadenoma (FA23) a) the B-mode image, b) the power spectra of the sample and the reference, c) ESD map, d) attenuation versus frequency, e) form factor from mean BSC, f) BSC versus frequency

Figure B.3 shows an example of the creation of large ESD parametric images that go beyond the mass boundary (a fibroadenoma, FA21 in Chapter 6), and the QUS parameter estimated for that mass. Note that QUS parameters are estimated using a ROI within the tumor boundary (outlined in yellow).



**Figure B.3.** QUS parameters estimated and creation of large parametric images of ESD of a fibroadenoma (FA21)

Figure B.4 shows large ESD parametric images for four human subjects (2 fibroadenomas; FA15 and FA25 in Chapter 6, and 2 carcinomas; ACA and IDC 8 in Chapter 6).



**Figure B.4.** Large parametric images of ESD of two carcinomas (ACA and IDC 8) and two fibroadenoma (FA 15 and FA25)

## B.2. Detecting anisotropy

Figure B.5 shows an example of the beam steered data of an infiltrating ductal carcinoma (IDC3 in Chapter 6) captured from the Siemens S2000 machine in research mode, Figure B.6 shows an example of the beam steered data captured from the Siemens S2000 machine in clinical mode, of a ductal carcinoma in situ (DCIS1 in Chapter 6) and Figure B.7 shows an example of beam steered data generated using off-line analysis on raw RF echo signal data.

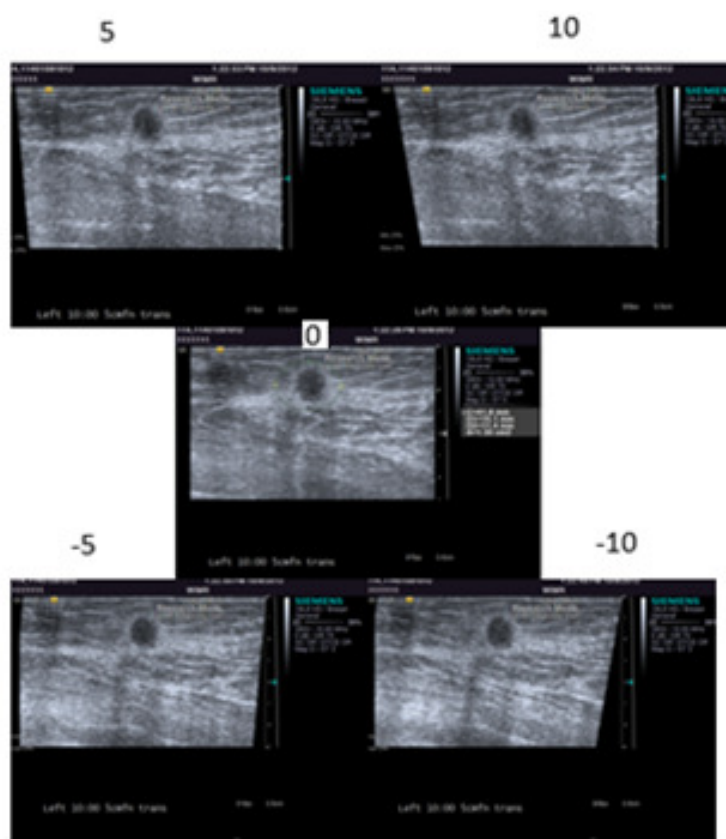


**Figure B.5.** Beam steered B-mode images from -10 to 10 degrees captured from the S2000 in research mode for an infiltrating ductal carcinoma

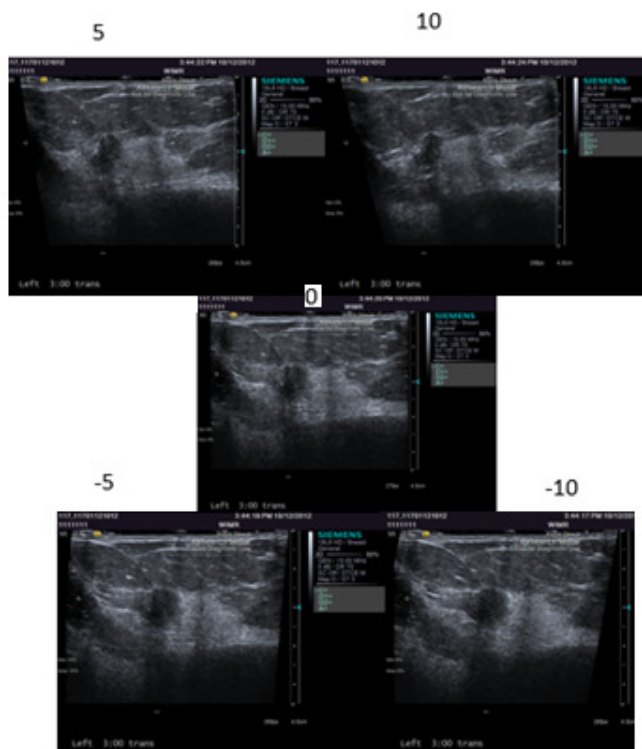


**Figure B.6.** Beam steered B-mode images from -10 to 10 degrees with an increment of 5 degrees for a ductal carcinoma in situ (DCIS1) captured from the S2000 in clinical mode for a fibroadenoma

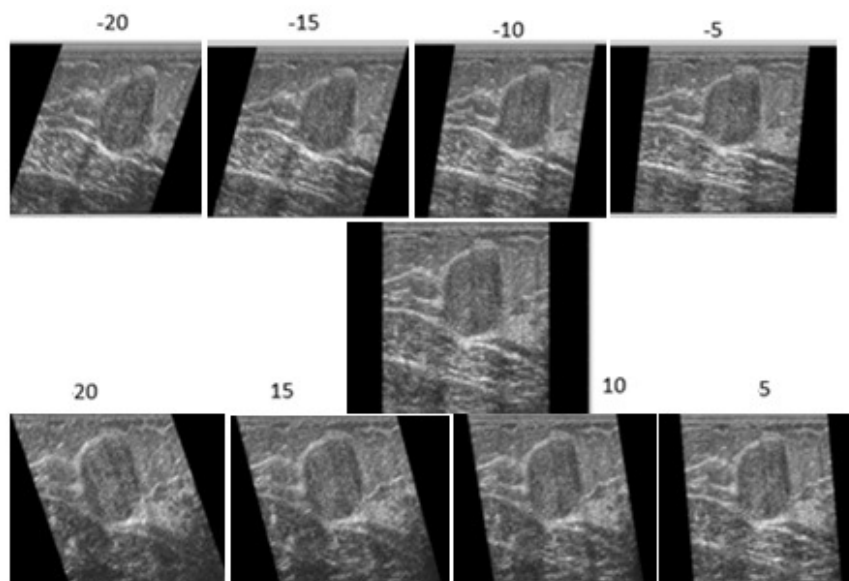


**Figure B.7.** example of beam steered B-mode images (steered from -20 to 20 degrees) generated offline from the RF data acquired from the S2000 in research mode for a fibroadenoma (FA20 in Chapter 6)

Figure B.8 shows a summary of QUS parameter estimated for one human subject (adenocarcinoma, ACA in Chapter 6) for -5 to +5 beam steering angles, the associated B-mode image, and the power spectra at each beam steering angle.

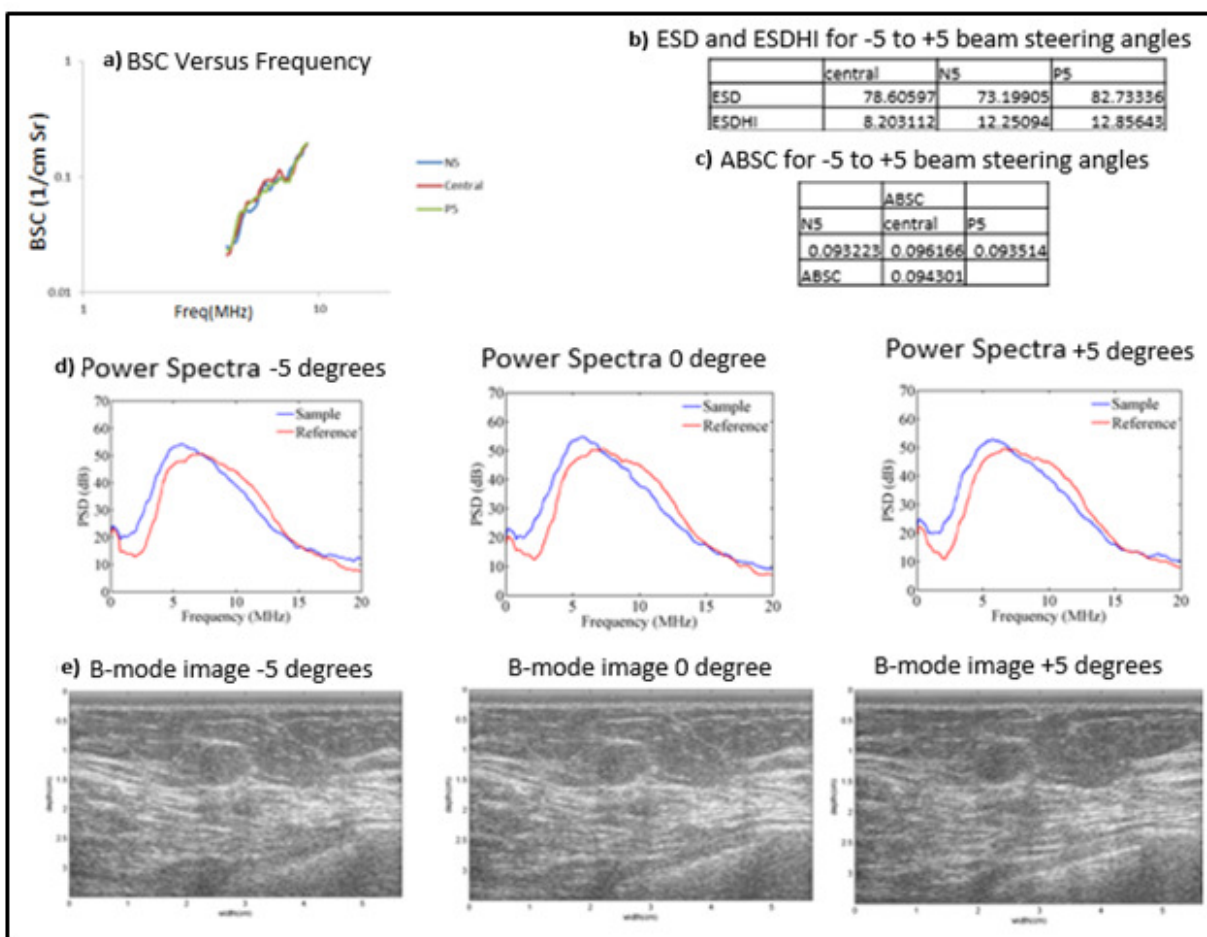


**Figure B.8.** QUS parameter estimated for different beam steering angles for an adenocarcinoma (ACA in Chapter 6), a) BSC versus frequency, b) table showing ESD and ESDHI estimates for -5 to +5 degrees, c) table showing BSC estimates for -5 to +5 degrees, d) Power spectra for -5, 0, and +5 degrees, and e) B-mode images for -5, 0, and +5 beam steering angles

### B.2.1. Power law method

To better judge anisotropy, we limited our study to large tumors that didn't show evidence of coherence (by visual evaluation) over different beam steering angles. The section below shows

how the power law fit to attenuation approach was implemented to judge anisotropy. Figure B.9 shows the attenuation coefficient versus frequency for an intracystic papillary carcinoma (IPC in Chapter 6).

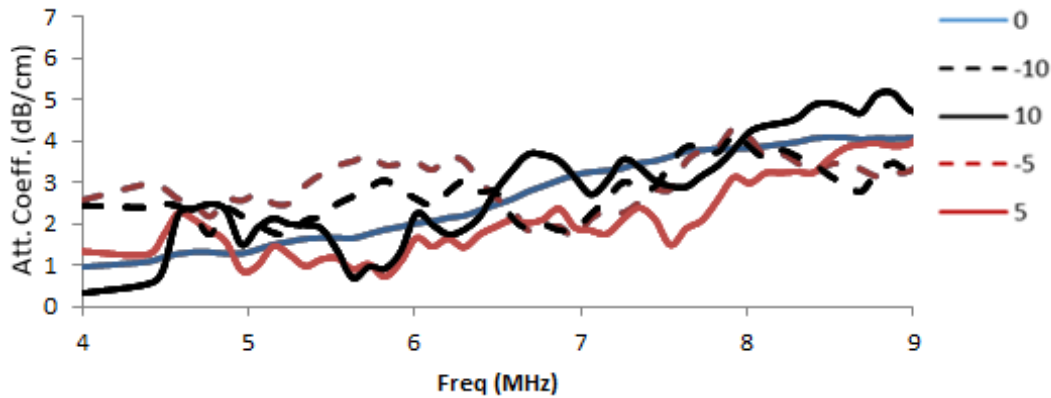


**Figure B.9.** shows an example of attenuation coefficient versus frequency for different beam steering angles for an intracystic papillary carcinoma (IPC)

The power law fit of the attenuation coefficient is modeled as  $\alpha(f) = \alpha_o f^n$ . We started by computing the power law fit to the attenuation estimates as shown in Figure B.10 (P5 is positive 5 degrees, N5 is negative 5 degrees, central is zero degrees, P10 is positive 10 degrees, and N10 is negative 10 degrees' view). This gives us an estimate of  $\alpha_o$  and  $n$  for each beam steering angle, such that

$$\hat{\alpha}(f) \approx \tilde{\alpha}_o f^{\tilde{n}} \quad (1)$$

where  $\hat{\alpha}(f)$  denotes the estimated attenuation coefficient and  $\tilde{\alpha}_o$  and  $\tilde{n}$  are the parameters of the power law fit.

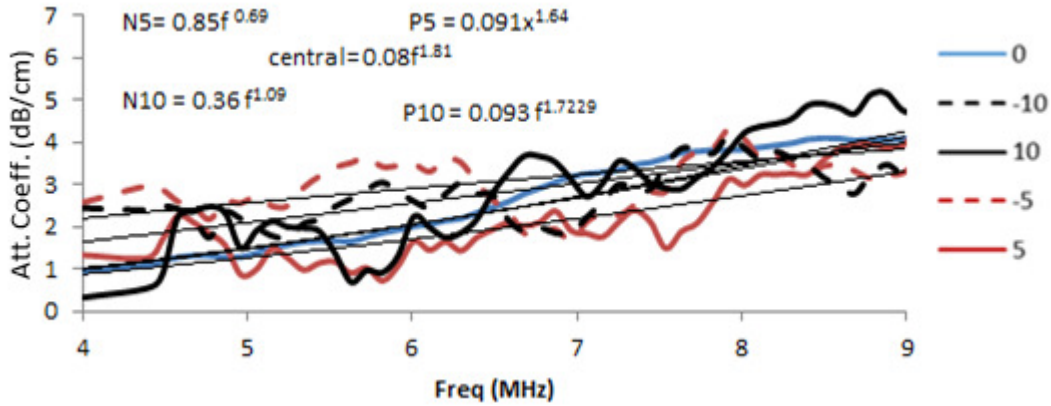


**Figure B.10.** shows an example of power law fits to attenuation for different beam steering angles for the intracystic papillary carcinoma (IPC) shown in Figure B.10

Then, we calculated the value at 6MHz from the power law fit and normalize it to the value at the central degree view by division. In order to determine the standard errors, we applied the delta method. The question was what is the uncertainty in  $\hat{\alpha}(f)$  given the uncertainty in  $\tilde{\alpha}_o$  and  $\tilde{n}$ ?

The general form of the delta method state that if  $z = f(x,y)$  then,

$$\sigma_z^2 = \left(\frac{\partial f}{\partial x}\right)^2 \sigma_x^2 + \left(\frac{\partial f}{\partial y}\right)^2 \sigma_y^2 + 2\left(\frac{\partial f}{\partial x} \frac{\partial f}{\partial y}\right) \sigma_{x,y}^2 \quad (2)$$

To simplify the analysis, we assumed that the covariance between  $x$ ,  $y$  is small and can be neglected. Thus, taking the derivative of equation 1 with respect to  $\tilde{\alpha}_o$  and  $\tilde{n}$  yields:

$$\frac{\partial \hat{\alpha}}{\partial \tilde{\alpha}_o} = f^{\tilde{n}} \quad \text{and} \quad \frac{\partial \hat{\alpha}}{\partial \tilde{n}} = \tilde{\alpha}_o f^{\tilde{n}} \ln(f) \quad (3)$$

The uncertainty in  $\hat{\alpha}$  is evaluated at a specific frequency within the power law fit range (i.e. 6 MHz) is

$$\sigma_{\hat{\alpha}}^2 = (f^{\tilde{n}})^2 \sigma_{\tilde{\alpha}_o}^2 + (\tilde{\alpha}_o f^{\tilde{n}} \ln(f))^2 \sigma_{\tilde{n}}^2 \quad (4)$$

To obtain the uncertainty we need the value for  $\sigma_{\tilde{\alpha}_o}^2$  and  $\sigma_{\tilde{n}}^2$ . To obtain these values we used the excel LINEST function of the log of the attenuation coefficient and frequency

(EXP (INDEX (LINEST (LN (attenuation coefficient), LN (frequency), , ),1,2)) (5)

Table B.1. shows an example of the values obtained for the power law fit parameters  $\bar{\alpha}_o$  (alpha o) and  $\bar{n}$  (n), and  $\sigma_{\bar{\alpha}_o}^2$  (sigma alpha o) and  $\sigma_{\bar{n}}^2$  (sigma n) for the tumor shown above.

**Table B.1.** Example for the sigma n and sigma alpha 0 obtained for different beam steering angles

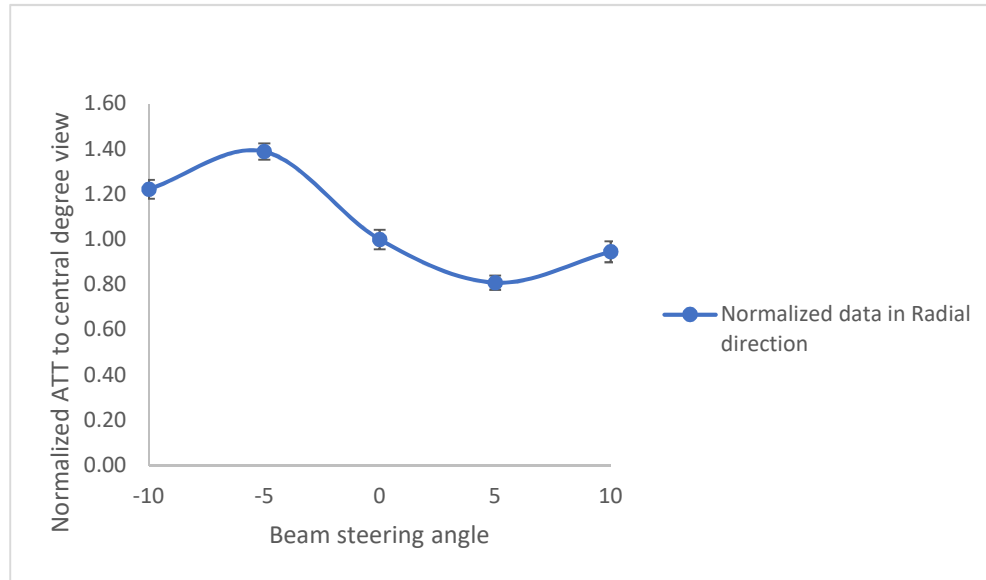
	alpha o	n	sigma n	sigma alpha o
-10	0.35	1.11	0.02	0.05
-5	0.83	0.70	0.02	0.03
0	0.08	1.82	0.04	0.08
5	0.09	1.65	0.05	0.01
10	0.09	1.72	0.01	0.02

Table B.2 shows an example of attenuation coefficient value calculated from the power law fit at 6 MHz and the normalized value to the central degree view (normalization is done by division).

**Table B.2.** ATT values at 6 MHz and the normalized values to the central degree view for the IPC shown above

Beam steering angle	6MHz Value	Normalized Data in Radial Direction
-10	2.55	1.25
-5	2.90	1.42
0	2.04	1.00
5	1.70	0.83
10	2.05	1.00

Figure B.11 shows an example of normalized attenuation values versus beam steering angles and uncertainty in the estimates for one human subject at the radial direction.



*Figure B.11. The resultant normalized ATT to the central degree view (shown in Table B.2) with the standard error values for the IPC*

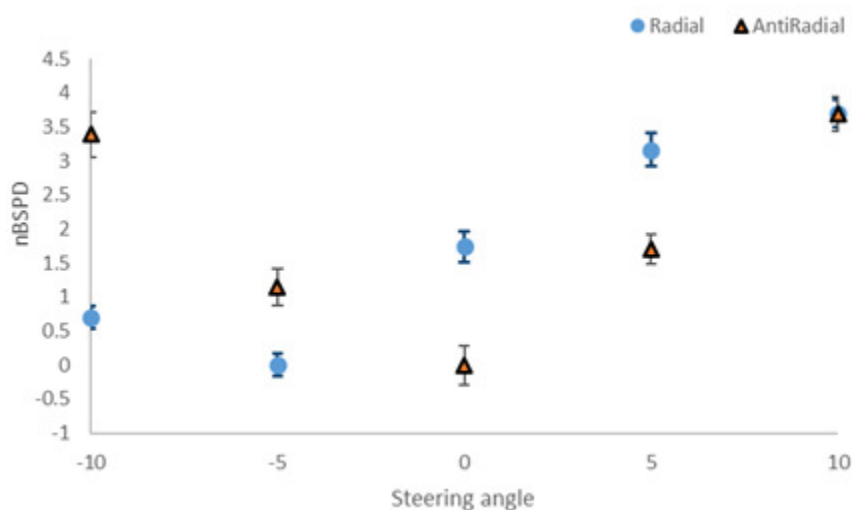
### **B.2.2. BSPD method for detecting anisotropy in the power spectra of backscattered echo signals**

Table B.3 show an example of the BSPD method used to detect anisotropy in the backscatter echo signals of the intracystic papillary carcinoma (IPC). The data from different beam steering angles were normalized to the maximum value and the normalization in this method was done by subtraction.

**Table B.3.** The BSPD method to detect anisotropy in the power spectra of backscattered echo signals

Beam steering angle	0	-5	-10	5	10
BSPD	-2.94	-1.2	-1.9	-4.38	-4.9
nBSPD	1.74	0	0.7	3.18	3.7
	<0	>0			
	0.7	6.88			
aBSPD	-6.18				
mBSPD	1.864				

Figure B.12 show examples of the normalized BSPD value for different beam steering angles for the intracystic papillary carcinoma (IPC).



**Figure B.12.** Examples for the BSPD method in detecting anisotropy

### B.3. Bayesian classifier GUI for 43 human subjects

Figure B.13 shows the GUI built for the Bayesian classifier for the 43 human subjects utilizing the leave one out method for training and four QUS parameters (ATT, ESD, ESDHI). Estimates for the new test subject are plugged into the GUI and the data point is plot in the corresponding 2D and 3D graphs. A category is displayed as either fibroadenoma or carcinoma, an example of each is shown in Figure B.14 and Figure B.15.

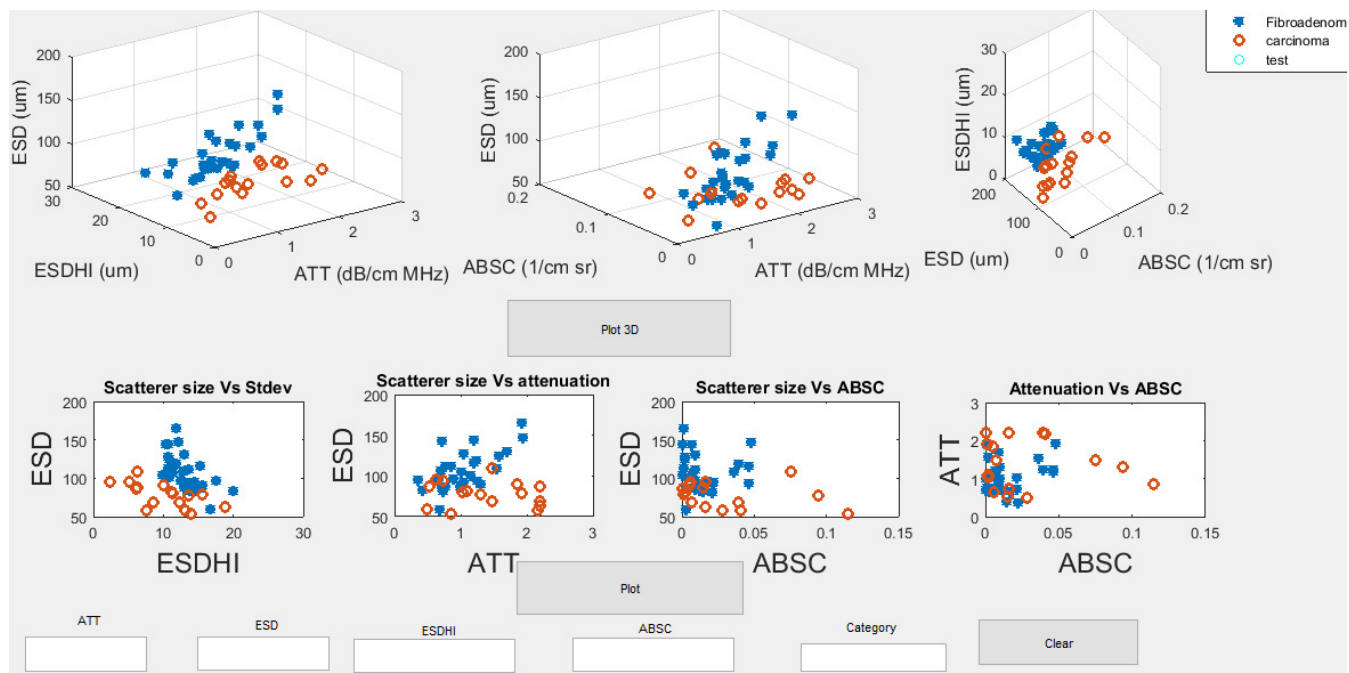


**Figure B.13.** Example of the GUI built for the Bayesian classifier

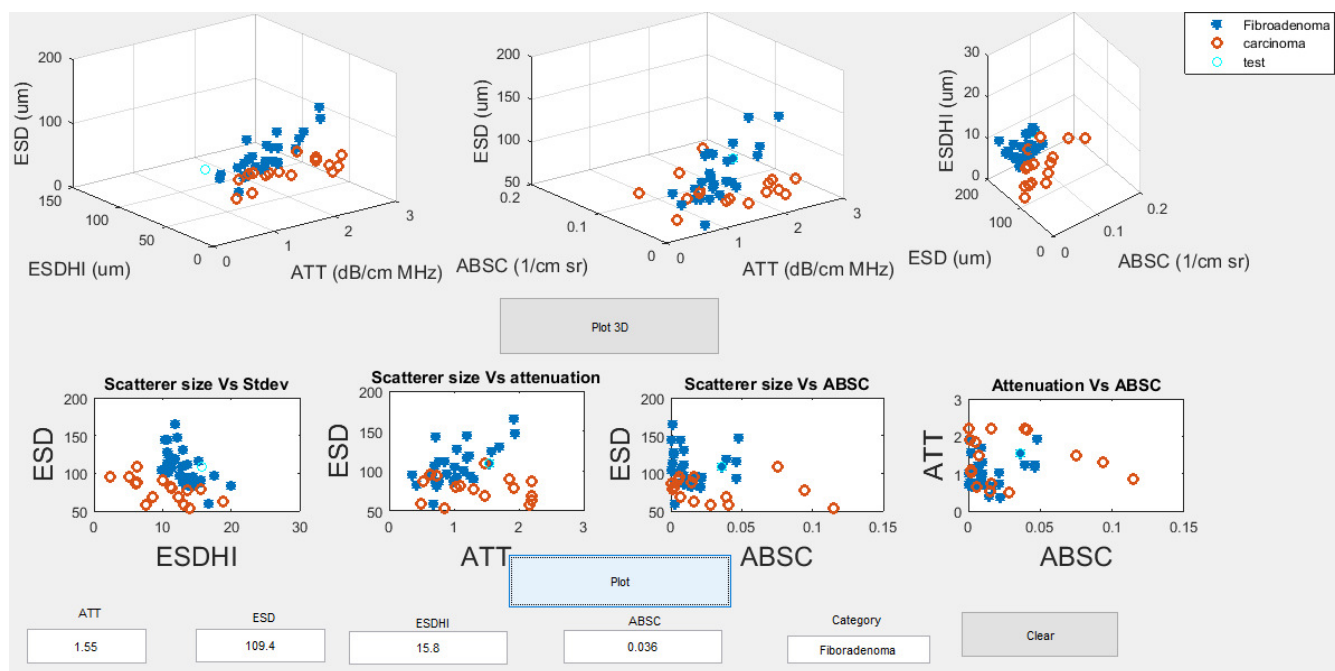


**Figure B.14.** Example of the GUI built for the Bayesian classifier differentiating a fibroadenoma (FA3 in Table 6.2, see Chapter 6)

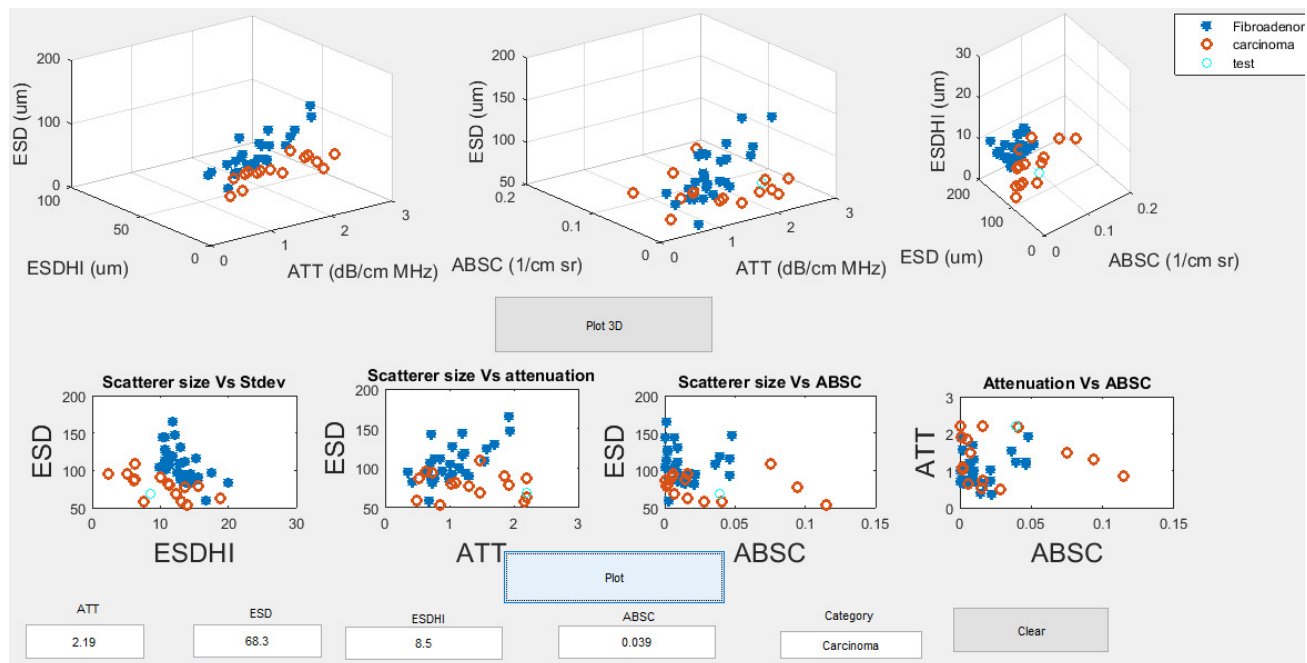


**Figure B.15.** Example of the GUI built for the Bayesian classifier differentiating a carcinoma (IDC 2 in Table 6.3, see Chapter 6)

## B.4. 3D data

Figure B.16 shows an example of the ESD estimates for data acquired from the ABVS system and the ESD C-scan of the tumor (ABVS1401, subject 1 in Table 7.2). The ESD for this mass was  $167 \pm 9 \mu\text{m}$ .

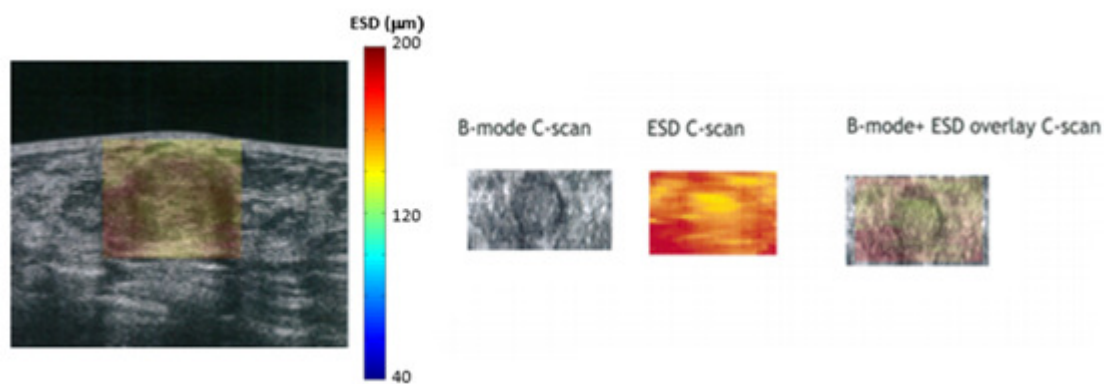


**Figure B.16.** QUS parameters estimated using the ABVS system and the ESD C-scan for a fibroadenoma (ABVS 1401, subject 1, Table 7.2)

Table B.4 shows the subject number used in Chapter 7 for the ABVS data for the subcutaneous fat and the breast masses and the corresponding subject naming used during recruitment. The first 5 subjects in the subcutaneous fat are the same subjects with masses, the other 3 subjects used for subcutaneous fat analysis didn't have breast mass

**Table B.4.** *Subject ID used in chapter 7 and the subject ID from recruitment for subcutaneous fat and breast masses*

<b>subcutaneous fat</b>	
<b>Subject ID in chapter 7</b>	<b>Subject ID from recruitment</b>
1	ABVS1401
2	ABVS 0701
3	ABVS 1201
4	ABVS 0901
5	ABVS 1501
6	ABVS 0301
7	ABVS 1301
8	ABVS 0401
<b>Breast masses</b>	
1	ABVS1401
2	ABVS 0701
3	ABVS 1201
4	ABVS 0901
5	ABVS 1501